Springer Series in Materials Science 298

Horst Biermann
Christos G. Aneziris *Editors*

Austenitic TRIP/TWIP Steels and Steel-Zirconia Composites

Design of Tough, Transformation-Strengthened Composites and Structures

Springer Open

Springer Series in Materials Science

Volume 298

The Springer Series in Materials Science covers the complete spectrum of materials research and technology, including fundamental principles, physical properties, materials theory and design. Recognizing the increasing importance of materials science in future device technologies, the book titles in this series reflect the state-of-the-art in understanding and controlling the structure and properties of all important classes of materials.

More information about this series at http://www.springer.com/series/856

Horst Biermann · Christos G. Aneziris
Editors

Austenitic TRIP/TWIP Steels and Steel-Zirconia Composites

Design of Tough, Transformation-Strengthened Composites and Structures

Springer Open

Editors
Horst Biermann
Institut für Werkstofftechnik
TU Bergakademie Freiberg
Freiberg, Sachsen, Germany

Christos G. Aneziris
Institut für Keramik, Glas- und Baustofftechnik
TU Bergakademie Freiberg
Freiberg, Sachsen, Germany

ISSN 0933-033X ISSN 2196-2812 (electronic)
Springer Series in Materials Science
ISBN 978-3-030-42602-6 ISBN 978-3-030-42603-3 (eBook)
https://doi.org/10.1007/978-3-030-42603-3

This Springer imprint is published by the registered company Springer Nature Switzerland AG
The registered company address is: Gewerbestrasse 11, 6330 Cham, Switzerland

Preface

The fundamental development of new materials is an essential basis for scientific knowledge and economic success. This awareness motivates research into forward-looking technologies for the production of resource-saving materials. New material properties, such as those made possible by composite materials, are of central importance for new, durable products and safety components, particularly in the areas of mobility and mechanical engineering. This motivates the vision of the marriage of modern high-performance steels of the highest strength and formability with damage-tolerant ceramics as a prime example of innovative manufacturing technologies for a new class of high-performance composites.

In concrete terms, this book aims to combine new high-alloy TRIP steels (TRIP: TRansformation-Induced Plasticity) with zirconium dioxide ceramics on powder metallurgical routes and via melt infiltration to form new composite materials, the "TRIP-Matrix Composites". Groundbreaking new processes are used, such as the production and combination of metalloceramic paper, hollow and solid spheres and filigree honeycomb bodies, which enable excellent formability and a largely free geometric design of lightweight components for mobility applications.

This book is the final publication of the Collaborative Research Centre (SFB 799) "TRIP-Matrix Composite—Design of tough, transformation-reinforced composites based on Fe and ZrO_2". The Collaborative Research Centre funded by the German Research Foundation (DFG) ran from 2008 to 2020 at the Technische Universität Bergakademie Freiberg, Germany. The chapters contained in this book provide an overview of the most important results of the projects of the Collaborative Research Centre in the completed funding periods and at the same time present current, in some cases still unpublished results.

The book is thematically divided into three sections, (i) the synthesis of TRIP-Matrix Composites, (ii) the characterisation of the materials produced and (iii) simulation and modelling. In these three sections, new and innovative materials and their synthesis pathways were explored.

Powder metallurgical processes were an important focus of several projects, see Chaps. 1 and 5–9. An essential contribution to the production of the new composite materials is the development of new high-alloy austenitic stainless steels and steel

powders with excellent properties, which serve as matrix for the composite materials, as described in Chaps. 2 and 3, respectively. The melting metallurgical marriage of the steels with ZrO_2 presented in Chap. 4 also resulted in new effects and promising approaches. Finally, the joining of composite materials was also investigated, see Chap. 10.

The characterisation of the new composites and the steel alloys is described in Chap. 11 with respect to the microstructure and in Chaps. 12–14 for the uniaxial, quasi-static, dynamic, fracture mechanical, cyclic as well as multi-axial mechanical properties. A special insight into the kinetics of the occurring deformation and damage mechanisms is provided by the methods of in situ investigation of the new materials described in Chaps. 15 and 16. Corrosion research (Chap. 17) also plays an important role for later applications.

An integral part of the description of the material properties are the projects for modelling the processes (Chap. 18) and the thermodynamics of the phases involved (Chap. 19), the coupled thermodynamic-mechanical modelling (Chap. 20) and the continuum mechanical and multi-scale modelling of the behaviour of ZrO_2 (Chap. 21) and of TRIP steels (Chap. 22), as well as the micromechanical simulations (Chaps. 23 and 24). In these projects, new approaches for the description of materials and processes were developed and applied to the materials produced in the Collaborative Research Centre.

As speaker and deputy speaker, we would like to thank all current and former members of the Collaborative Research Centre for their constant support. The successful work would not have been possible without the dedicated cooperation of all scientists who worked on or supported the projects. We would also like to thank other contributors, all technical and administrative staff as well as the countless students for their outstanding cooperation.

Due to the excellent scientific work, the Collaborative Research Centre has been able to produce the basis for many scientific qualification theses, from habilitations and doctorates to student theses. In this way, numerous scientific careers have been established over 12 years and many graduates have been shaped scientifically. This young talent work was also promoted within the framework of a graduate school, which taught many soft skills in addition to professional qualifications.

We would also like to thank the public relations team, which made the scientific results available to a broad public and thus made an important contribution to the reputation of the Technische Universität Bergakademie Freiberg. This public relations work has also interested many students in the special research areas of the Collaborative Research Centre and thus drawn their attention to the university's courses of study.

We would also like to highlight the support of the industrial board.

Our special thanks go to the German Research Foundation for the trust it has placed in us and for funding (project number: 54473466), in particular to E. Effertz, S. Isernhagen and R. Nickel from the Collaborative Research Centres Department, F. Fischer, B. Jahnen and X. Molodova from the Materials Science and Engineering Department and Mrs. Hammel and Mrs. C. Niebus from the administration centre. We are also deeply indebted to all the experts who have

followed our work with interest as referees as well as to the members of the Senate Committee of the German Research Foundation.

Finally, we would like to thank Mrs. A. Beier and P. Michel, whose work in the office of the Collaborative Research Centre ensured the smooth running of all financial aspects and the organisation of all events.

Freiberg, Germany

Horst Biermann
Christos G. Aneziris

Contents

Contributors

Christos G. Aneziris Institute of Ceramic, Glass and Construction Materials, Technische Universität Bergakademie Freiberg, Freiberg, Germany

Christine Baumgart Institute of Materials Engineering, Technische Universität Bergakademie Freiberg, Freiberg, Germany

Harry Berek Institute of Ceramic, Glass and Construction Materials, Technische Universität Bergakademie Freiberg, Freiberg, Germany

Horst Biermann Institute of Materials Engineering, Technische Universität Bergakademie Freiberg, Freiberg, Germany

Sebastian Borrmann Institute of Mechanics and Fluid Dynamics, Technische Universität Bergakademie Freiberg, Freiberg, Germany

Anja Buchwalder Institute of Materials Engineering, Technische Universität Bergakademie Freiberg, Freiberg, Germany

Michael Budnitzki Institute of Mechanics and Fluid Dynamics, Technische Universität Bergakademie Freiberg, Freiberg, Germany

Andreas Burgold Institute of Mechanics and Fluid Dynamics, Freiberg, Germany

Humberto Chaves Institute of Mechanics and Fluid Dynamic, Technische Universität Bergakademie Freiberg, Freiberg, Germany

Sabine Decker Institute of Materials Engineering, Technische Universität Bergakademie Freiberg, Freiberg, Germany

Claudia Dommaschk Foundry Institute, Technische Universität Bergakademie Freiberg, Freiberg, Germany

Matthias Droste Institute of Materials Engineering, Technische Universität Bergakademie Freiberg, Freiberg, Germany

Ralf Eckner Institute of Materials Engineering, Technische Universität Bergakademie Freiberg, Freiberg, Germany

Olga Fabrichnaya Institute of Materials Science, Technische Universität Bergakademie Freiberg, Freiberg, Germany

Sergey Guk Institute for Metal Forming, Technische Universität Bergakademie Freiberg, Freiberg, Germany

Lars Halbauer Institute of Materials Engineering, Technische Universität Bergakademie Freiberg, Freiberg, Germany

Michael Hauser Institute of Iron and Steel Technology, Technische Universität Bergakademie Freiberg, Freiberg, Germany

Sebastian Henkel Institute of Materials Engineering, Technische Universität Bergakademie Freiberg, Freiberg, Germany

Claudia Heuer Institute of Ceramic, Glass and Construction Materials, Technische Universität Bergakademie Freiberg, Freiberg, Germany

Qiuliang Huang Institute of Iron and Steel Technology, Technische Universität Bergakademie Freiberg, Freiberg, Germany

Rudolf Kawalla Institute for Metal Forming, Technische Universität Bergakademie Freiberg, Freiberg, Germany

Björn Kiefer Institute of Mechanics and Fluid Dynamics, Technische Universität Bergakademie Freiberg, Freiberg, Germany

Volodymyr Kietov Institute of Materials Engineering, Technische Universität Bergakademie Freiberg, Freiberg, Germany

Markus Kirschner Institute for Metal Forming, Technische Universität Bergakademie Freiberg, Freiberg, Germany

Iurii Korobeinikov Institute of Iron and Steel Technology, Technische Universität Bergakademie Freiberg, Freiberg, Germany

Lutz Krüger Institute of Materials Engineering, Technische Universität Bergakademie Freiberg, Freiberg, Germany

Meinhard Kuna Institute of Mechanics and Fluid Dynamics, Technische Universität Bergakademie Freiberg, Freiberg, Germany

Robert Lehnert Institute of Materials Engineering, Technische Universität Bergakademie Freiberg, Freiberg, Germany

Marcel Mandel Institute of Materials Engineering, Technische Universität Bergakademie Freiberg, Freiberg, Germany

Stefan Martin Institute of Materials Science, Technische Universität Bergakademie Freiberg, Freiberg, Germany

Javad Mola Material Design and Structural Integrity Lab, Osnabrück University of Applied Sciences, Osnabrück, Germany

Mykhaylo Motylenko Institute of Materials Science, Technische Universität Bergakademie Freiberg, Freiberg, Germany

Sebastian Neumann Institute of Mechanics and Fluid Dynamics, Technische Universität Bergakademie Freiberg, Freiberg, Germany

Marie Oppelt Institute of Ceramic, Glass and Construction Materials, Technische Universität Bergakademie Freiberg, Freiberg, Germany

Ulrich Prahl Institute for Metal Forming, Technische Universität Bergakademie Freiberg, Freiberg, Germany

Stefan Prüger Institute of Mechanics and Fluid Dynamics, Technische Universität Bergakademie Freiberg, Freiberg, Germany

Markus Radajewski Institute of Materials Engineering, Technische Universität Bergakademie Freiberg, Freiberg, Germany

David Rafaja Institute of Materials Science, Technische Universität Bergakademie Freiberg, Freiberg, Germany

Paul Rähmer Albert Hoffmann GmbH, Eschweiler, Germany

Mohan Kumar Rajendran Institute of Mechanics and Fluid Dynamics, Technische Universität Bergakademie Freiberg, Freiberg, Germany

Ivan Saenko Institute of Materials Science, Technische Universität Bergakademie Freiberg, Freiberg, Germany

Stefan Sandfeld Institute of Mechanics and Fluid Dynamics, Technische Universität Bergakademie, Freiberg, Germany

Rüdiger Schwarze Institute of Mechanics and Fluid Dynamics, Technische Universität Bergakademie Freiberg, Freiberg, Germany

Andreas Seupel Institute of Mechanics and Fluid Dynamics, Freiberg, Germany

Rachel Strobl Institute of Mechanics and Fluid Dynamics, Freiberg, Germany

Christiane Ullrich Institute of Materials Science, Technische Universität Bergakademie Freiberg, Freiberg, Germany

Olena Volkova Institute of Iron and Steel Technology, Technische Universität Bergakademie Freiberg, Freiberg, Germany

Anja Weidner Institute of Materials Engineering, Technische Universität Bergakademie Freiberg, Freiberg, Germany

Christian Weigelt Institute of Ceramic, Glass and Construction Materials, Technische Universität Bergakademie Freiberg, Freiberg, Germany

Andreas Weiß Institute of Iron and Steel Technology, Technische Universität Bergakademie Freiberg, Freiberg, Germany

Marco Wendler Institute of Iron and Steel Technology, Technische Universität Bergakademie Freiberg, Freiberg, Germany

Carl H. Wolf Institute of Materials Engineering, Technische Universität Bergakademie Freiberg, Freiberg, Germany

Gotthard Wolf Foundry Institute, Technische Universität Bergakademie Freiberg, Freiberg, Germany

Chapter 1
Ceramic Casting Technologies for Fine and Coarse Grained TRIP-Matrix-Composites

Claudia Heuer, Marie Oppelt and Christos G. Aneziris

Abstract The present contribution focuses on the development of composite materials using innovative *ceramic casting technologies*. Within this work different processing routes, the relevance of their process parameters as well as the resulting mechanical and microstructural characteristics are discussed. The successfully developed TRIP-matrix foams as well as full beads reinforced with 5 and 10 vol.% zirconia achieve higher compressive strengths and energy absorption during deformation in comparison to the pure metal materials as references. The functionally graded beads allowed a compression of up to 20% with corresponding specific energy absorption of 10.7 kJ/kg. In a further approach, metal-matrix composites have been generated via *paper-manufacturing technology*. The partial replacement of cellulose fibers by commercially available zirconia fibers resulted in fiber reinforced TRIP-matrix composites with an increased tensile strength of approx. 33% as compared to the pure metal material as reference. Large-size ceramic matrix composites with high potential for applications requiring sufficient wear and thermal shock resistance have been successfully prepared via *pressure slip casting*. The last topic is concerned with the development of yttria-stabilized zirconia fibers with a tailored phase composition (monoclinic-tetragonal-cubic) via *electrospinning*.

1.1 Introduction

The increasing technological demand within the last decades led to the development of composites significantly enlarging the application field of conventional materials. The research efforts are not only concerned with innovative material systems but also with novel fabrication technologies, always with the aim to create composites with

C. Heuer (✉) · M. Oppelt · C. G. Aneziris
Institute of Ceramic, Glass and Construction Materials, Technische Universität Bergakademie Freiberg, Agricolastr. 17, 09599 Freiberg, Germany
e-mail: claudia.heuer@ikgb.tu-freiberg.de

H. Biermann and C. G. Aneziris (eds.), *Austenitic TRIP/TWIP Steels and Steel-Zirconia Composites*, Springer Series in Materials Science 298,
https://doi.org/10.1007/978-3-030-42603-3_1

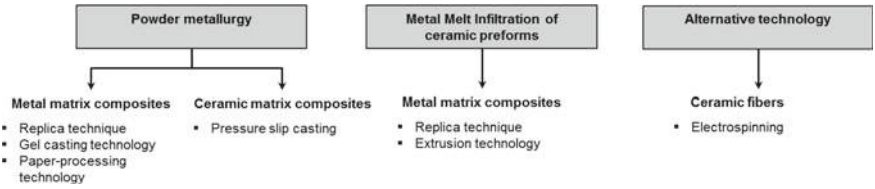

Fig. 1.1 Flowchart of the applied casting technologies

superior mechanical, thermal, thermo-mechanical, wear- and damping-related properties. Within the frame of the Collaborative Research Center 799—TRIP-matrix-composites based on metastable austenitic steel and magnesia partially stabilized zirconia are of interest. The combination of metastable austenitic steel with transformation induced plasticity with magnesia partially stabilized zirconia is advantageous in terms of high strength and specific energy absorption. [1, 2] Both materials exhibit a martensitic phase transformation triggered upon exposure to external stresses.

The present work focuses on the development of metal matrix and ceramic matrix composites using innovative casting technologies that are typically employed for the fabrication of ceramic components (Fig. 1.1). A main emphasis is the development *of metal matrix composites* (*MMC*) using the replica technique, the gel casting and the paper technology. Furthermore, the infiltration of ceramic preforms by TRIP-steel melts was studied. The preforms are prepared using the replica technique or extrusion technology. *Ceramic matrix composites* (*CMC*) are generated using the pressure slip casting technology. In addition to that electrospinning has been applied for the development of zirconia fibers with tailored phase compositions. Within the present work the different processing routes, the relevance of their process parameters and the resulting microstructural and mechanical characteristics will be illustrated and discussed.

1.2 Experimental Details

This work is divided into four main parts; the first one deals with the development of TRIP-matrix composites by replica technique, gel casting and paper-processing technology. The second part concerns the metal melt infiltration of ceramic preforms (obtained via replica technique and extrusion). The development of ceramic matrix composites by pressure slip casting was the third part of the study. Finally, an alternative technology for the fabrication of zirconia fibers is introduced. The following section will provide information on the raw materials as well as on the methods of characterization. The sample preparation for the mentioned technologies will be illustrated.

1.2.1 Raw Materials

1.2.1.1 Magnesia Partially Stabilized Zirconia

Within the present work three different types of fused cast magnesia partially stabilized zirconia (Saint Gobain, USA) have been used. The zirconia powders are hereinafter referred to as Mg-PSZ (fine) with $d_{50} = 1.3$ µm, Mg-PSZ (coarse) with $d_{50} = 3.0$ µm and Mg-PSZ (new) with $d_{50} = 4.3$ µm. The chemical compositions of the different Mg-PSZ powders are summarized in Table 1.1.

1.2.1.2 Austenitic Stainless TRIP-Steel

Three different types of austenitic stainless steel powder (TLS Technik Bitterfeld, Germany) have been utilized in the present work. The commercially available AISI 304 (X5CrMnNi18-1-10) with a mean particle size of 33 µm has been employed for the development of MMCs via replica technique. The other steel powders following referred to as X8CrMnNi16-7-3 ($d_{50} = 21.9$ µm) and X3CrMnNi16-7-6 ($d_{50} = 25$ µm) had a substantially higher manganese content, which partially replaced nickel. The true densities were determined to be 7.83 g/cm^3 (X5CrMnNi18-1-10), 7.78 g/cm^3 (X8CrMnNi16-7-3) and 7.83 g/cm^3 (X3CrMnNi16-7-6), respectively. During the investigations several steel batches have been used having minor differences in their chemical composition, see Table 1.2.

1.2.1.3 Alumina

Calcined and reactive alumina powders were used for the pressure slip casting of alumina based composites. The fine and coarse grained powders had mean particle

Table 1.1 Chemical compositions of the zirconia powders in wt.%

	ZrO_2	MgO	HfO_2	SiO_2	Al_2O_3	TiO_2
Mg-PSZ (fine)	Bal.	3.37	1.73	2.43	0.63	0.14
Mg-PSZ (coarse)	Bal.	2.82	1.74	0.41	0.38	0.13
Mg-PSZ (new)	Bal.	1.85	1.85	0.10	1.58	0.13

Table 1.2 Chemical compositions of the steel powders in wt.%

	Fe	Cr	Mn	Ni	C	Si	S
PMX5CrMnNi18-1-10	Bal.	17.50–18.10	1.13–1.30	7.8–8.74	0.03–0.05	0.40–0.55	0.01–0.02
PMX8CrMnNi16-7-3	Bal.	15.60–16.70	6.02–7.14	3.04–3.50	0.04–0.08	0.80–0.93	0.00–0.01
PMX3CrMnNi16-7-6	Bal.	15.90–16.30	7.10–7.20	6.60–6.90	0.02–0.03	1.00–1.16	0.01

sizes ranging from 0.2 μm to 3 mm and were provided by Almatis (Ludwigshafen, Germany) and Martinswerke (Bergheim, Germany), respectively.

1.2.1.4 Raw Materials for Electrospinning

For the development of nanofibers via electrospinning high purity zirconyl chloride octahydrate (Sigma Aldrich Steinheim, Germany), yttrium (III) nitrate hexahydrate (Sigma Aldrich Steinheim, Germany) and magnesium nitrate hexahydrate served as precursor materials for the synthesis of zirconia fibers stabilized with 3 mol.% yttria and 8 mol.% magnesia, respectively. Granular polyvinylpyrrolidone (PVP) with an average M_w of $1.3 \times 1\,0^6$ g/mol (Sigma Aldrich Steinheim, Germany) was employed as polymeric component. The starting materials were dissolved in deionized water and ethanol with a purity of ≥99.8% (Carl Roth Karlsruhe, Germany), respectively. Triton X (Sigma Aldrich Steinheim, Germany) was used as non-ionic surfactant.

1.2.2 Sample Preparation

1.2.2.1 Development of TRIP-Matrix Composites via Powder Metallurgy

Aneziris et al. [3] produced open cell foam structures via ***replica technique*** from 30 ppi (pores per inch) polyurethane foams with dimensions of 50 × 50 × 20 mm^3. Two different compositions based on 100 vol.% steel powder (0Z) and 90 vol.% steel powder and 10 vol.% Mg-PSZ powders (10Z) were evaluated. The composition of the impregnation slurries is shown in Table 1.3. The polyurethane foams were fully immersed in the slurry, afterwards the excess slurry was removed with the aid of a manual roller mill. After this first impregnation step the filters were dried at 90 °C for 1 h. In a second coating step the dried foams were sprayed with a spraying slurry based on the same composition as the impregnation slurry, see Table 1.3. The spraying slurry was prepared using a ViscoJet stirrer system. The spray coating was performed with the aid of a SATAjet B spraying gun 1.0 E nozzle type. In a further version, a dense coating (hereafter indicated by the letter "J" in the slurry compositions) of approx. 1.5 mm thickness was applied on the 50 × 20 mm^2 side surfaces for both slurry compositions. The corresponding samples were designated to as 0ZJ and 10ZJ. After drying the samples have been sintered at 1350 °C for 2 h in an electrical furnace Linn HT 1600 GT Vac with $MoSi_2$-heating elements in 99.9.% argon atmosphere.

Full and hollow TRIP-matrix composite beads were prepared with the aid of gel casting. The composition of the slurries with a powder to water ratio of 70:30 is given in Table 1.4. For the generation of full beads calcium chloride was chosen as hardener and the prepared aqueous hardener solution contained 0.8 wt.% calcium chloride [4]. For the fabrication of hollow beads calcium hydroxide had to be applied

Table 1.3 Composition of the slurries for replica technique in wt.% [3]

	Type	Supplier	0Z	10Z
Raw materials				
Austenitic TRIP- steel powder	PMX5CrMnNi18-1-10	TLS Technik, GER	94.99	87.67
ZrO_2	Mg-PSZ (coarse)	Saint Gobain, USA	–	7.32
Additives				
Antifoam	Axilat DF 581 B	C.H. Erbslöh, GER	0.11	0.11
Surfactant	PPG P400	Sigma-Aldrich, GER	0.55	0.55
Binder	Optapix PAF 35	Zschimmer and Schwarz, GER	1.66	1.66
Dispersant	Darvan C	R.T. Vanderbilt, USA	0.47	0.47
Binder	Ligninsulfonate T11B	Otto Dille, GER	1.66	1.66
Stabilizer	Axilat RH 50 MD	C.H. Erbslöh, GER	0.56	0.56
		Total	100	100
Dispersing fluid				
Water (coating)	Deionized		9.5	9.5
Water (spraying)	Deionized		19.2	19.2

Table 1.4 Composition of the slurries used for gel casting in wt.% [7]

	Type	Supplier	0Z	5Z	10Z	20Z	100Z
Raw materials							
Austenitic TRIP-steel powder	PMX8CrMnNi 16-7-3	TLS, GER	68.47	65.00	61.83	54.62	–
ZrO_2	Mg-PSZ (coarse)	Saint Gobain, USA	–	3.47	6.64	13.85	68.47
Additives							
Sodium alginate	FD 175	C.E. Roeper, GER	0.42	0.42	0.42	0.42	0.42
Plasticizer	Darvan C	R.T. Vanderbilt, USA	0.69	0.69	0.69	0.69	0.69
Stabilizer	KM2000	Zschimmer and Schwarz, GER	0.42	0.42	0.42	0.42	0.42
Dispersing fluid							
Water	Deionized		30	30	30	30	30

Table 1.5 Composition of the feedstocks excluding water in vol.%

	Type	Supplier	0Z	10Z	3ZF	6ZF
Raw materials						
Austenitic TRIP-steel powder	PMX3CrMnNi 16-7-6	TLS Technik, GER	78.5	71.2	78.5	78.5
ZrO_2	Mg-PSZ (new)	Saint Gobain, USA	–	7.9	–	–
ZrO_2-Fibers	Yttria-stabilized	Final GmbH, GER	–	–	2.5	5.0
Cellulose	–	Zellstoff Pöls AG, AT	14.5	14.1	12.0	9.5
Additives						
Starch	–	Südstärke Chemie, GER	7.0	7.0	7.0	7.0

as hardener in a 1.0 wt.% aqueous hardener solution [5]. The prepared slurries were added dropwise into the hardener solutions and thus solidification took place. Additionally, functionally graded beads were prepared as described by Oppelt et al. [6]. The wet green beads were removed from the hardener solution and dried for 24 h at 40 °C. After debinding, the beads were sintered in an inert atmosphere (Ar 5.0) in an XGraphit furnace (XERION Ofentechnik Freiberg, Germany) with a heating rate of 1 K/min up to 660 °C with a dwelling time of 60 min at 660 °C, followed by a heating rate of 5 K/min up to 1350 °C and a dwelling time of 120 min at 1350 °C. The cooling rate was 5 K/min.

The development of TRIP-matrix composites via ***paper-manufacturing technology*** comprised several steps. The pulp suspension contained 0.27 wt.% cellulose fibers and 0.01 wt.% cationic starch. In order to obtain the feedstock, a 90 wt.% aqueous suspension containing stainless steel, magnesia partially stabilized zirconia, and 0.17 wt.% anionic starch were added to the pulp suspension. In context of the development the cellulose pulp fibers have been partially replaced (2.5 and 5 vol.%) by commercially available yttria-stabilized zirconia fibers. Thus, fiber reinforced TRIP-matrix composites were prepared. The composition of the feedstock excluding water is given in Table 1.5. Square paper sheets with 200 mm in length were then formed on a laboratory sheet-forming device. The green sheets were stepwise dried starting from 40 °C up to 110 °C within 24 h. Subsequently, the dried paper sheets were calendered on a rolling mill applying a line load of 30 kN/mm at a roller speed of 0.1 m/s. The calendered sheets were thermally treated using an debinding and sintering process developed by Wenzel [8].

1.2.2.2 Development of TRIP-Matrix Composites via Metal Melt Infiltration of Ceramic Preforms

Open cell foam structures based on magnesia-partially stabilized zirconia for the infiltration with TRIP-steel melts were prepared using the ***replica technique***. The

fabrication of these foam structures comprises two coating steps as mentioned before. The impregnation of the polyurethane foams was done according to the description in Sect. 1.2.2.1. The spray coating procedure was modified and performed airstream assisted. The impregnated foam was therefore placed into a tubular sample holder connected to a vacuum unit. The distance between sample holder and spraying gun was set to 27 cm for all experiments; the pressure of the compressed air was maintained at 0.3 MPa. The mass flow of the slurry was set to 80 g/min and the foams were sprayed for 8 s. A detailed description of the experimental setup is given elsewhere [9]. The spraying slurries were prepared with different powder to water ratios. The spraying slurries contained 40 wt.% water, 45 wt.% and 55 wt.% water, respectively After coating, the foams were dried at 110 °C. Debinding and sintering was performed in an oxidizing atmosphere. Debinding took place at 500 °C with a heating rate of 1 K/min and a holding time of 60 min. Sintering was performed at 1600 °C with a heating rate of 5 K/min and a dwell time of 120 min.

The ***extrusion technology*** was applied as a further option for the fabrication of porous ceramic preforms, honeycombs and randomly arranged spaghetti-filters, which have been casted with TRIP-steel melt. The preparation and the extrusion of the different plastic feeds are described in detail by Wenzel and Aneziris [10] and Schärfl et al. [11]. Honeycomb specimens with 196 cpsi (channels per square inch) and a wall thickness of 250 μm as well as randomly arranged full strand-spaghetti-filters with a strand diameter of 1 mm have been prepared. Both extruded ceramic preform types were sintered in an electrical heating furnace with $MoSi_2$-heating elements in oxidizing atmosphere. The heating rate was 1 K/min to 350 °C with a holding time of 90 min and then 3 K/min to 1650 °C with a holding time of 120 min.

Subsequently, the ceramic preforms were infiltrated by a ***Cast*** X5CrMnNi16-7-7 steel melt in order to obtain bulk TRIP-matrix composites. Therefore, the preforms were preheated to 1000 °C with a holding time of 10 h and then placed in an unheated sodium silicate bonded SiO_2 sand mold. The samples were fixed to the bottom of the mold. The experimental setup is discussed in detail by Weider and Eigenfeld [12]. The steel casting took place with a temperature of 1600 °C in oxidizing atmosphere. A constant height of the feeder was guaranteed due to an inclined drainage for excess steel.

1.2.2.3 Development of Ceramic Matrix Composites via Pressure Slip Casting

Slip preparation comprised several steps, starting with the addition of the organic additives Welan Gum and Konjac flour in deionized water for 10 min using a Heidolph homogenizer DIAX 600 (Heidolph Instruments Schwabach, Germany). Subsequently, the solid fractions and the additive-water mixture have been homogenized for 15 min in an intensive laboratory mixer RV02 (Maschinenfabrik Gustav Eirich Hardheim, Germany) to obtain the slurries. Casting was performed in a modified industrial pressure slip casting device DGM80D (Dorst Technology Kochel am See, Germany). The suspension was pumped from a receiver tank into a polyurethane

mould (200 × 200 × 38 mm^3) at a pressure of 0.1–0.15 MPa. The pressure was then increased to 2 MPa and held constant for the whole casting time of 25 min. Afterwards, the pressure was released and the green specimens have been demoulded. The casted bodies were subsequently dried up to 110 °C. Debinding took place in an oxidizing atmosphere with a heating rate of 1 K/min up to 400 °C and a dwelling time of 90 min at 400 °C. Sintering was conducted in a XGraphit furnace (XERION Ofentechnik Freiberg, Germany) with a heating rate of 5 K/min to 1450 °C and a holding time of 120 min and an argon flow rate of 2.5 l/min at an excess pressure of 5 mbar.

1.2.2.4 Development of Ceramic Fibers Using Electrospinning

With the aid of the *electrospinning technology yttria-stabilized zirconia fibers* have been developed. First, a 18 wt.% precursor solution was prepared by dissolving $ZrOCl_2 \cdot 8\ H_2O$ and $Y(NO_3)_3 \cdot 6\ H_2O$ in deionized water in a ratio that corresponds to the final composition ZrO_2–3 mol.% Y_2O_3. In a second step, a 7 wt.% polymeric solution was obtained by dissolving the granular PVP in ethanol. The polymeric solution was stirred on a magnetic stirrer at 500 rpm for 30 min. The polymeric solution was then poured stepwise into the precursor solution with a 3:1 weight ratio. Finally, 0.5 wt.% Triton X was added and the stock solution was further stirred at 250 rpm for 240 min. The electrospinning was conducted using an electrospinning device NE 300 (Inovenso Istanbul, Turkey) with a bottom-up configuration and a 4-nozzles feeding unit, each nozzle having an inner diameter of 0.8 mm. The processing temperature and relative humidity were kept constant at 23 °C and 40%, respectively. The stock solution was fed at 3.5 ml/h with a high precision syringe pump (New Era Pump Systems Farmingdale, USA). The electrospinning was carried out at a voltage of 24 kV using a DC power supply at a distance between needle tip and collector of 75 mm. The fibers were collected on a drum that was covered with alumina foil and which was rotating at 300 rpm. The sintering of the nanofibers was performed at different temperature of 700, 1100, 1350 and 1650 °C.

1.2.3 Characterization of the Composite Materials

1.2.3.1 Rheological Characterization of the Slurries

The rheological properties of the slurries developed for the gel-casting of metal beads as well as for the impregnation and spraying of polyurethane foams were investigated using a rotational viscometer Haake RheoStress 150 (ThermoHaake Karlsruhe, Germany). The rheological experiments were carried out under shear control. For the gel-casting the slurries were investigated with a given shear rate of 1–500 s^{-1} in 150 s. After a holding time of 100 s at 500 s^{-1} the shear rate was decreased again. The slurries for the impregnation of the polyurethane foams were

investigated with given shear rates of 1–200 s^{-1} or 1000 s^{-1} in 300 s. After a holding time of 60 s at 200 s^{-1} and 1000 s^{-1} respectively it was stepwise decreased to 1 s^{-1}.

1.2.3.2 Thermal Analysis

Highly relevant aspects for the development of composite materials containing TRIP-steel are investigations on the thermal decomposition behavior of the temporary additives. Differential scanning calorimetry (DSC) combined with thermo-gravimetric measurements (TG) were performed using a STA 409 (NETZSCH Waldkraiburg, Germany). During decomposition experiments the DSC/TG device was flushed with synthetic air. For the fabrication of metal beads using gel-casting the decomposition behavior of sodium alginate was of fundamental importance. The chosen heating rate was 10 K/min to 1000 °C. For the paper-derived TRIP-matrix composites the decomposition behavior of the cellulose pulp fibers was investigated up to 800 °C with a heating rate of 1 K/min.

1.2.3.3 Physical Properties

The linear shrinkage after sintering was calculated according to DIN EN 993-10. For the full and hollow metal beads, the pressure slip-casted ceramic matrix composites as well as for the zirconia preforms obtained by extrusion the open porosity, the pore size distribution as well as the bulk density were investigated with the aid of a mercury porosimeter (PASCAL series, Porotec Hofheim am Taunus, Germany). The thickness of the paper-derived TRIP-matrix composites was determined after processing and calendering at five different positions for each sheet using a digital vernier caliper and an analogue dial gauge. The bulk density was determined from weight and volume measurements before and after sintering. The volume of the samples was determined by displacement in mercury volume meter. The theoretical density of the composite mixtures was calculated according to the rule of mixture using the density of the initial powders as measured by helium pycnometry.

1.2.3.4 Mechanical Properties

The mechanical properties of the different composites were determined. Compressive deformation tests have been performed on a 500 kN servohydraulic testing device type MTS 880 (MTS Systems Eden Prairie, USA) with a displacement rate of 0.016 mm/s for the TRIP-matrix composite foams prepared via ***replica technique***. For the hollow and full TRIP-matrix composite beads the compressive deformation strength was measured with a testing machine TT 2420 (TIRA Schalkau, Germany) arranged with a measuring equipment for single granules. 20 beads of each composition have been tested to failure with a displacement rate of 0.05 mm/s. In case of functionally graded beads the compressive strength was determined with a measuring

device for single granules and a displacement rate of 0.002 mm/s with a load cell of 10 kN. For these metal matrix composites the specific energy absorption (SEA) was calculated according to (1.1) and (1.2). SEA_V is defined as specific energy absorption per volume (V) unit, SEA_m refers to mass (m) unit, respectively.

$$SEA_V = \frac{W}{V} \quad SEA_m = \frac{W}{m} \tag{1.1}$$

$$W = \int_0^{S_b} P \mathrm{d}S \tag{1.2}$$

W is the total energy absorbed during sample deformation, P the load, S the displacement, and S_b is the strain at end of experiment according to Jacob et al. [13].

The tensile strength of the as-fabricated and calendered paper-derived materials was determined according to DIN EN ISO 1924-2 on a servohydraulic testing machine TT 28100 (TIRA Schalkau, Germany). The clamping length was 65 mm and the sample width was 10 mm. The crosshead speed for the as-fabricated samples was 5 mm/min, and for the calendered samples 3 mm/min. Different crosshead speeds had to be applied in order to ensure sample fracture within 5–30 s as given by the standard.

The tensile strength of the paper-derived TRIP-matrix composites after sintering was determined according to DIN EN ISO 6892-1. It was investigated on as-sintered samples with the following dimensions (before sintering): $l_0 = 150$ mm, $l_c = 115$ mm, $b = 20$ mm, $b_0 = 10$ mm, with a transition radius of 60 mm (DIN 50125 shape H). Tensile loading tests were also performed on the servohydraulic testing machine TT 28100 (TIRA Schalkau, Germany) at a clamping length of 98 mm. The test length was 70 mm at a crosshead speed of 2.35 mm/min.

Flexural strength (DIN EN 993-6, DIN EN 843-1) and Young's modulus by static flexure (DIN EN 843-2, Method A) were determined on a servohydraulic universal testing device type TT 28100 (TIRA Schalkau, Germany) with a support distance of 125 mm and a crosshead speed of 0.15 N/mm for the pressure slip casted ceramic matrix composites as well as for the zirconia preforms obtained by extrusion.

1.2.3.5 Microstructural Characterization

Microstructural characterization was conducted by digital microscopy VHX-2000 (Keyence, Germany) and scanning electron microscopy XL30 ESEM (Philips, Germany) equipped with energy dispersive X-ray spectroscopy technology (EDS). Phase identification was done using electron back scatter diffraction (EBSD) analysis (Philips XL30 with EBSD system TSL from Edax/Ametek). For EBSD analysis the samples were polished up to 1 μm grain. Final polishing for 20 h was realized using a VibroMet2 with a SiO_2-suspension MasterMet2 (0.02 μm grain size) (Buehler, USA). To avoid electric charging all samples were sputtered with Pt using

a sputter coater (Edwards, England). The crystallographic data used for phase determination were taken from ICDD-database. Detailed information are given in Berek et al. [14], Oppelt et al. [4, 5], Wenzel et al. [10, 15, 16] and Hasterok et al. [9]. Important features of the developed composites have been studied with the aid of a microfocus X-ray computed tomograph CT-ALPHA (Procon X-ray Sarstedt, Germany) equipped with a 160 kV X-ray source and a Hamamatsu detector with 2040 × 2040 pixels. For the open cell foam structure based on magnesia partially stabilized zirconia the homogeneity of the applied spray coatings was studied [9]. In case of the pressure slip casted ceramic matrix composites the homogenous distribution of the steel particles and the coarse alumina grains in the ceramic matrix was evaluated [8]. The deformation behavior of the open cell foam structures based on TRIP-steel and Mg-PSZ was evaluated using of X-ray tomography [3]. With the aid of a Zeiss Xradia 510 Versa X-ray microscope (XRM) the functionally graded beads were investigated with special regard to the formation of transition zones and the formation of cracks between the different layers [6].

1.3 Results and Discussion

1.3.1 Development of TRIP-Matrix Composites via Powder Metallurgy

1.3.1.1 Open Cell Foam Structures Based on TRIP-Steel/Mg-PSZ

TRIP-matrix composite foams have been prepared using the replica technique. In addition to the conventional coating procedure a dense coating (jacket) has been applied onto the side surfaces of the polyurethane foam template and the mass gain of the foams was registered (see Table 1.6). The linear shrinkage and the bulk density of the sintered foam structures are summarized in Table 1.7. The addition of zirconia particles in the steel matrix led to higher shrinkages. The MMCs without and with dense coating are displayed in Fig. 1.2a, b. The thickness of the dense coating has been determined to be 1.5 mm. SEM micrographs of the typical surface regions of the samples are shown in Fig. 1.3. During thermal treatment, the TRIP-steel matrix formed a nearly dense structure with only a few pores.

Table 1.6 Mass gain of the TRIP-matrix composite foams (mean values of 3 samples, with a standard deviation of less than 5%)

		0Z	10Z	0ZJ	10ZJ
Mass after impregnation	g	35.7	36.2	60.8	62.7
Mass after spraying	g	44.2	46.0	68.6	71.8
Mass after sintering	g	41.3	43.2	64.9	68.1

Table 1.7 Bulk density and linear shrinkage of the TRIP-matrix composite foams (mean values of 3 samples, with a standard deviation of less than 3%)

		0Z	10Z	0ZJ	10ZJ
Density	g/cm^3	1.1	1.2	1.7	1.8
Linear shrinkage in height	%	13.8	14.7	13.3	15.4
Linear shrinkage in width	%	10.9	11.2	9.5	10.6

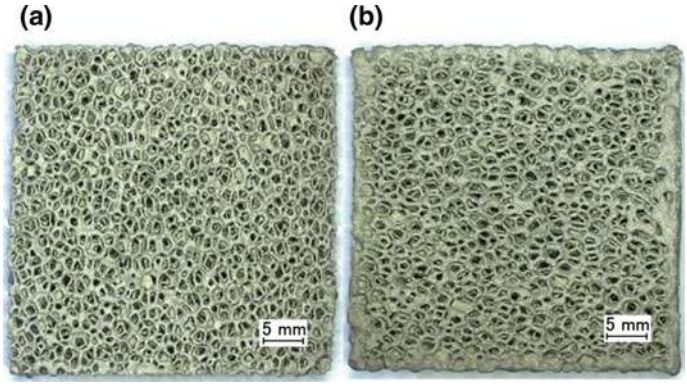

Fig. 1.2 Digital image of the TRIP-matrix composite foams **a** without dense coating (jacket) and **b** with dense coating (jacket) [3]

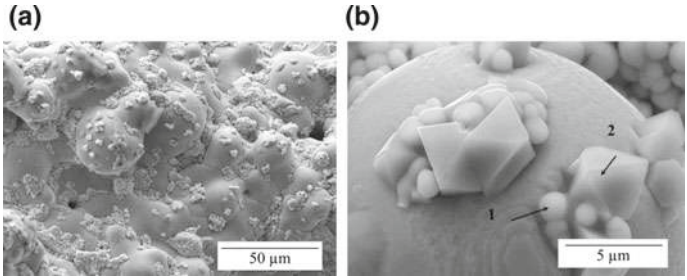

Fig. 1.3 SEM micrographs of the surface region of the composite with the composition 10ZJ [3]

With the aid of EDS measurements magnesia partially stabilized zirconia particles have been identified (see position 1 in Fig. 1.3b). The formation of spinel-type structures (see position 2 in Fig. 1.3b) has also been registered. These spinel-type structures have been analyzed by EDS. The results are summarized in Table 1.8.

Due to the significant differences in particle size between steel ($d_{50} = 30\ \mu m$) and zirconia ($d_{50} = 3.0\ \mu m$) clusters of zirconia particles were found between the steel particles. Berek et al. [17] investigated the phase composition of these reinforcing magnesia partially stabilized zirconia particles and found that approx. 80% of the

zirconia particles transform into the monoclinic state during thermal treatment up to 1350 °C in argon atmosphere. At the grain boundaries of the zirconia particles precipitates containing Mg are found.

The influence of compressive stress on the structure of TRIP-matrix composite foams was investigated by in situ CT, see Fig. 1.4. A compressive strain of 45% led to apparently broken cells. During deformation the cubic and tetragonal ZrO_2 (that is remaining after thermal treatment) is transformed into the monoclinic phase within the first 5% of compressive strain.

Figure 1.5 displays the compressive stress-strain curves of the developed TRIP-matrix composite foams; the corresponding values of the mass- and volume-specific energy absorption calculated according to (1.1) and (1.2) as a function of the compressive strain are presented in Table 1.9. It has to be mentioned that the calculated stress is the force divided by the nominal cross section after sintering (technical stress). The stress-strain curves of the TRIP-matrix composite foam structures with a dense coating (jacket) 0ZJ and 10ZJ show a large regime of strain hardening, followed by a plateau-like behavior with a flow stress of above 45 MPa at approximately 15% strain, followed by a long plateau stress in which deformation occurs at almost constant stress. The successive collapse of cell walls and struts of the cellular structure accounts for this long plateau which is typical for metallic foams. The reference material 0ZJ shows lower yield strength in comparison to the reinforced composite 10ZJ. In case of the samples without any dense coating similar behavior is registered, but with significantly lower yield strengths.

Table 1.8 Chemical composition (EDS) of spot 2 in Fig. 1.3b (oxides in wt.%, spinel-type structure)

MgO	Al_2O_3	ZrO_2	V_2O_5	Cr_2O_3	MnO	Fe_2O_3	NiO	TiO_2	SiO_2
2.78	26.45	5.43	1.33	34.20	25.51	2.59	0.47	0.80	0.42

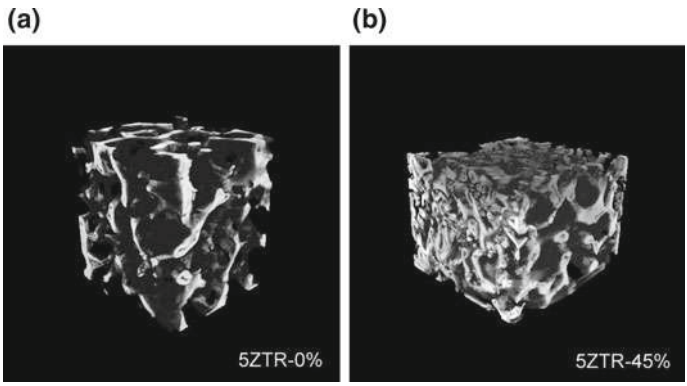

Fig. 1.4 3D CT images of a typical TRIP-matrix composite foam **a** before and **b** after 45% compressive strain [17]

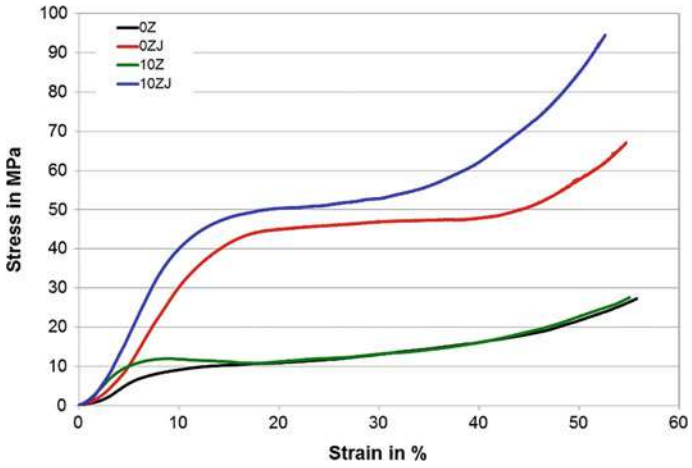

Fig. 1.5 Compressive stress-strain curves of the TRIP-matrix composite foams and the reference materials [3]

Table 1.9 Specific energy absorption (SEA) at 1, 2, 10, 20 and 50% compressive strain

	1% strain		2% strain		10% strain		20% strain		50% strain	
	kJ/kg	MJ/m^3	kJ/kg	MJ/m^3	kJ/kg	MJ/m^3	kJ/kg	MJ/m^3	kJ/kg	MJ/m^3
0Z	0.003	0.004	0.010	0.012	0.44	0.50	1.35	1.53	5.32	6.01
10Z	0.006	0.007	0.028	0.034	0.68	0.84	1.60	1.96	5.32	6.52
0ZJ	0.003	0.005	0.010	0.018	0.68	1.21	2.92	5.23	10.99	19.70
10ZJ	0.004	0.007	0.017	0.031	0.99	1.87	3.49	6.57	13.07	24.61

Strain hardening of the TRIP-matrix composite foams starts at smaller strains compared to the non-reinforced reference material and is independent if there is a dense side coating or not. This is of great importance and in accordance with the EBSD analysis. Thus, the reinforcement effect of magnesia partially stabilized zirconia in TRIP-matrix composites seems to be proven. This has also been observed for the mass and volume specific energy absorption, respectively. The specific energy absorption is higher in the composite foams as compared to the pure steel reference material especially up to a strain of 10% for all structures. The 10ZJ composite foam keeps its better performance in comparison to the reference material up to 50% compressive strain. The plotted results are average values of 5 samples with a deviation of approximately 5%.

1.3.1.2 Full or Hollow TRIP-Matrix Composite Beads and Functionally Graded Beads Using Gel-Casting

For the development of full and hollow beads an established additive system containing Darvan C and KM 2000 [8, 16] has been investigated in combination with sodium alginate. The sodium alginate was used for initial experiments since it is widely applied in food industry. Furthermore, sodium alginate has been successfully utilized for the fabrication of ceramic beads based on alumina [18]. Comprehensive rheological measurements have been carried out with a rotational viscometer (Haake RheoStress 150) with a given shear rate of 1–500 s^{-1} in 150 s with subsequent dwell of 100 s at maximum shear rate. The initial slurry had a powder to water ratio of 70:30. The addition of 0.3, 0.4, 0.7 and 1.0 wt.% sodium alginate based on the solid content was tested. Different powder to water ratios of 80:20 and 55:45 were tested at a fixed sodium alginate content of 0.4 wt.%. The different viscosity curves are displayed in Fig. 1.6a, b. All investigated slurries show a shear thinning behavior. For the slurries containing 0.3 and 0.4 wt.% sodium alginate a significant increase in viscosity can be recognized at shear rates below 50 s^{-1}. Slurries with 0.7 and 1.0 wt.% sodium alginate are not applicable in gel casting. Sodium alginate is a polysaccharide incorporating water in its structure; therefore highly viscous slurries are obtained that are not droppable through a cannula. Similar results are obtained if the water content is reduced to 20 wt.%. Taking the results of the rheological measurements into consideration, the optimum amount of sodium alginate is 0.4 wt.% for full beads and 0.7 wt.% for hollow beads. In addition to the rheological characterization of the slurries experiments relating to the possible size of the composite beads have been carried out. In this context, different syringe cannulas have been tested and beads with diameters ranging from 1.6 to 2.7 mm were fabricated. It has been verified that completely spherical composites are obtained with a cannula having a diameter of 1.1 mm. Subsequently, all further experiments were conducted with this cannula diameter. The sphericity of the composites does not only depend on the diameter of the cannula, but also on the distance between the injector and the

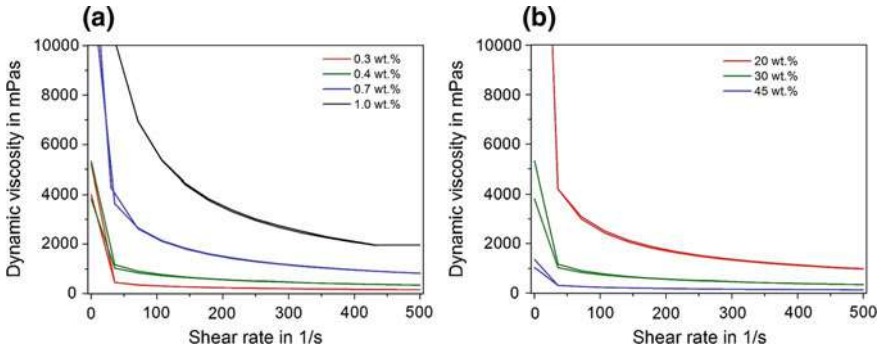

Fig. 1.6 Viscosity curves of the gel-casting slurries **a** with varying sodium alginate content at a powder to water ratio of 70:30; **b** with varying water content at a sodium alginate content of 0.4 wt.%

hardener solution. For the fabrication of spherical samples, the distance should be 13 mm (at a cannula diameter of 1.1 mm). At a greater distance the beads flattened and at a smaller distance "raindrop shaped" composites were produced as shown in Fig. 1.7. Hence, the level of the hardener solution should be continuously controlled during experiment. Depending on the chemical composition of the hardener solution hollow ($Ca(OH)_2$) or full beads ($CaCl_2$) can be produced as illustrated in Fig. 1.8 [5].

The wet green beads have been removed from the hardener solution after casting and subsequently dried. The full beads have been conventionally dried for 12 h at 40 °C. The development of a drying procedure for the hollow beads was more challenging. The shells of the hollow beads collapse due to their weight if conventional or vacuum drying procedures are used. The differences are illustrated in Fig. 1.9a, b.

Therefore, the hollow beads had to be freeze-dried. For the freeze-drying procedure the hollow beads were placed in a freeze-dryer. The hollow beads were frozen to −89 °C and the surrounding pressure reduced to under 6.11 mbar. According to the vapour pressure curve for ice and water, the frozen water sublimates directly from the solid to the gaseous phase without reaching the liquid state. With this drying method, the cavity within the hollow beads can be retained during the drying process and moisture is completely removed after 12 h.

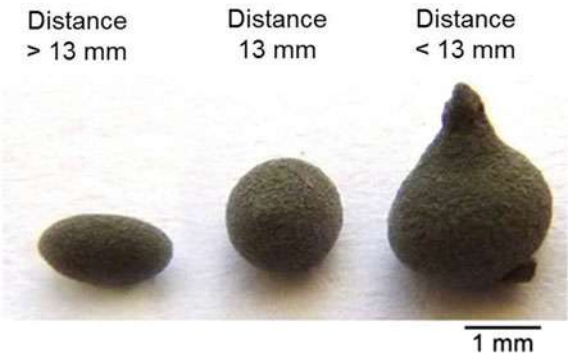

Fig. 1.7 Shape of composite beads as function of the distance between injector to hardener solution [4]

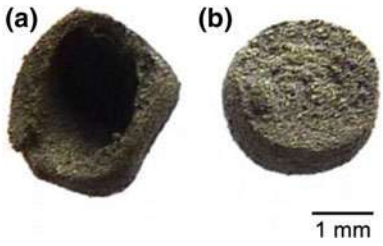

Fig. 1.8 Hollow (**a**) and full (**b**) composite beads [5]

The debinding of the green full and hollow beads is an essential processing step in the development of TRIP-matrix composite beads. Within the present work sodium alginate (gelation agent) as well as Darvan C and KM 2000 (binder system) were used as temporary additives. The thermal removal of the organic additives is not only a critical step in terms of defect-free debinding, but also in terms of the residual carbon content affecting the chemical and phase composition of the TRIP-steel powders [19]. The decomposition behavior of the sodium alginate in synthetic air at a heating rate of 10 K/min is displayed in Fig. 1.10a. Three exothermic peaks can be recognized at 250, 360 and 650 °C with the corresponding total mass loss of 41%, 45% and 59%, respectively. At 800 °C the decomposition is completed. For the evaluation of the debinding parameters the knowledge of the oxidation tendency of the ***PM***X8CrMnNi16-7-3 and ***PM***X3CrMnNi16-7-6 steel powders is essential. The results of the thermogravimetric measurements are shown in Fig. 1.10b. The increase in mass has been registered for both types of steel powder. The ***PM***X3CrMnNi16-7-6 steel powder possesses a lower oxidation resistance in comparison to the ***PM***X8CrMnNi16-7-3 steel powder.

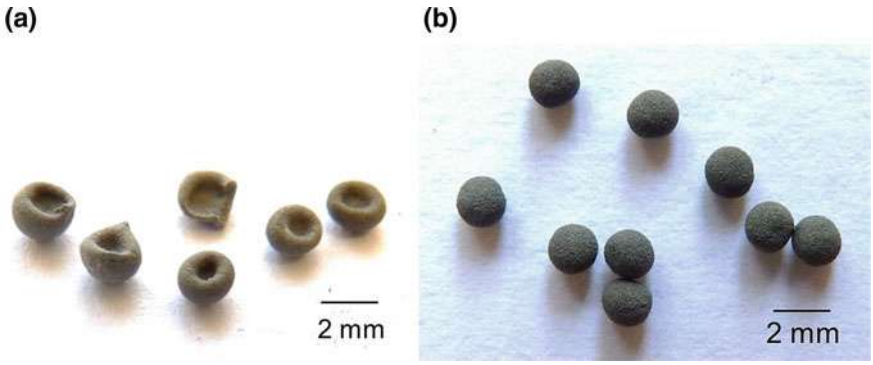

Fig. 1.9 Green hollow beads **a** conventionally dried **b** freeze-dried [7]

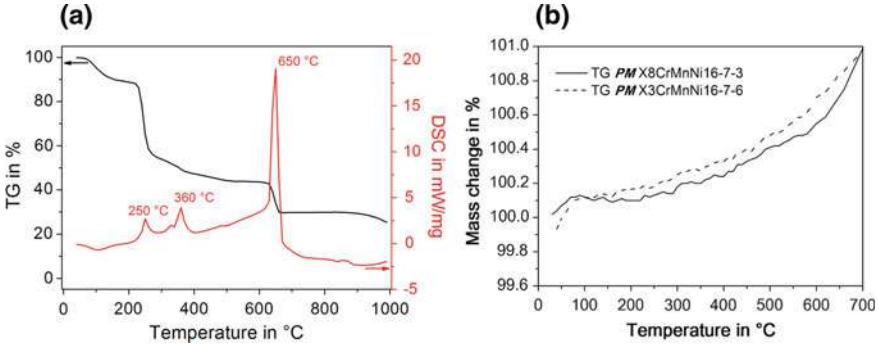

Fig. 1.10 Thermal analysis of **a** sodium alginate and **b** applied steel powders at a heating rate of 10 K/min in synthetic air [4, 8]

The oxidation rate significantly increases at temperatures above 400 °C. Within the present work the debinding temperature was set to 660 °C, which is a reasonable compromise between the binder removal and the oxidation of the steel powder. Based on the DSC/TG-analyses, the debinding experiments were conducted at 660 °C with varying dwell time at 250 °C and 660 °C, respectively. The heating rate was set to 1 K/min for a defect-free debinding of the composite beads. The residual carbon content as well as the oxygen content were determined in order to evaluate the debinding success (see Table 1.10). Using the above discussed debinding conditions, the carbon content can be reduced from 0.33 wt.% in the green beads to 0.048% in the binder-free beads. Within the present work the TRIP-matrix composite beads were sintered at 1350 °C as suggested by Weigelt [19]. The dwell time at maximum temperature was set to 120 min. The sintering was conducted with excess pressure of 5×10^{-4} MPa in order to reduce the evaporation of alloying elements. Argon 5.0 was chosen as flushing gas.

Figure 1.11a represents a SEM micrograph of a full bead containing 20 vol.% zirconia (20Z). These beads were characterized by a rough surface. The zirconia particles were evenly distributed within the steel matrix. Nevertheless poor densification of the composite during sintering led to a high porosity. A microstructural overview of the hollow beads is given in Fig. 1.11b. According to Oppelt and Aneziris [5] hollow beads are obtained if the hardener solution is highly alkaline.

Table 1.10 Results of the debinding experiments as a function of the thermal treatment (mean values of 3 measurements)

Dwell time in min at		Carbon content in wt.%	Oxygen content in wt.%
250 °C	660 °C		
15	0	0.049 ± 0.004	11.50 ± 3.61
15	15	0.048 ± 0.002	7.13 ± 3.17
15	30	0.048 ± 0.003	6.80 ± 1.91
30	0	0.053 ± 0.005	7.37 ± 1.55
30	15	0.053 ± 0.003	4.23 ± 1.06
30	30	0.051 ± 0.006	7.17 ± 1.80

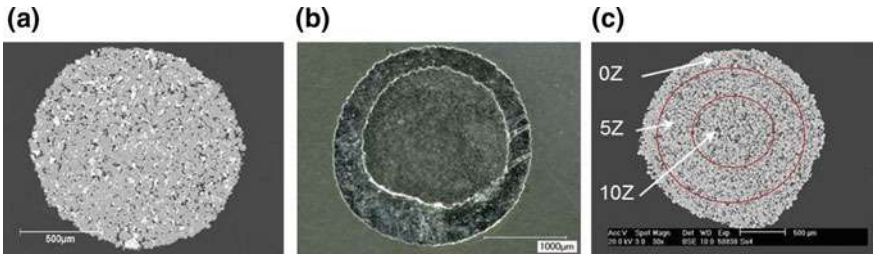

Fig. 1.11 Polished section micrographs of **a** single bead (SEM-micrograph) and **b** hollow bead (LOM-micrograph) and **c** functionally graded bead (SEM-micrograph)

In alkaline solutions the sodium alginate is readily soluble and forms an incoherent sodium alginate sol. If this sol gets in contact with bivalent Ca-ions the water insoluble calcium alginate gel is formed due to the ion exchange of Na^+ and Ca^{2+}. During fabrication the alginate containing slurries are added dropwise into the hardener solution. Upon contact with the calcium hydroxide containing hardener solution the drop surface solidifies and a solid shell is formed. This shell inhibits the further incorporation of Ca^{2+}-ions into the alginate structure. The transition from sodium alginate sol to calcium alginate gel proceeds exclusively within the shell and a cavity is formed. As a result of the fabrication process these cavities are irregularly shaped. Within the present study 94% of the examined hollow beads show pronounced cavities. Figure 1.11c shows an example for the prepared functionally graded beads. A full bead with the composition 10Z was coated with a slurry of the composition 5Z and finally a layer of the composition 0Z was applied. The initial bead had a diameter of 1.8 mm. The layer thicknesses were determined to be 76 ± 21 µm (1st layer) and 63 ± 5 µm (2nd layer). The microstructural differences are visible at higher magnifications (see Fig. 1.12). Since the sintering conditions are equal for all types of beads it can be assumed that the pH value of the hardener solution as well as the type of hardener agent influences the solidification process during casting. At neutral or low alkaline pH (using $CaCl_2$, pH = 7.2) the ion exchange from Na^+ to Ca^{2+} takes place at lower rates. Therefore the transition from sodium alginate sol to calcium alginate gel is decelerated and the resulting beads have a higher porosity in comparison to the hollow beads. In case of the hollow beads a better densification of the material is recognized. As stated above at higher alkaline pH (using $Ca(OH)_2$, pH = 13.4) the ion exchange as well as the transition from sol to gel takes place at higher rates. For the development of the functionally graded beads a different approach was chosen. The different layers were sprayed onto a full bead. The composition of the spraying slurries was adopted from the spray coating procedure for the development of TRIP-matrix composite foams. In Fig. 1.12c a functionally graded bead is shown. The 2nd coating had the composition 0Z and is characterized by a high residual porosity.

For all types of TRIP-matrix composite beads precipitation can be found at the steel/steel grain boundaries. The chemical and phase composition of these precipitations have been analyzed using EDS/EBSD. The results are displayed in Fig. 1.13. The lattice parameters of the considered phases for EBSD-analysis are given by

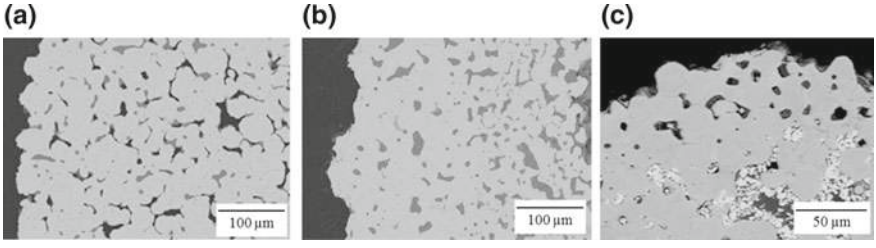

Fig. 1.12 SEM micrographs of **a** single bead, 0Z and **b** hollow bead, 0Z and **c** functionally graded bead, 10Z-5Z-0Z at higher magnifications [6]

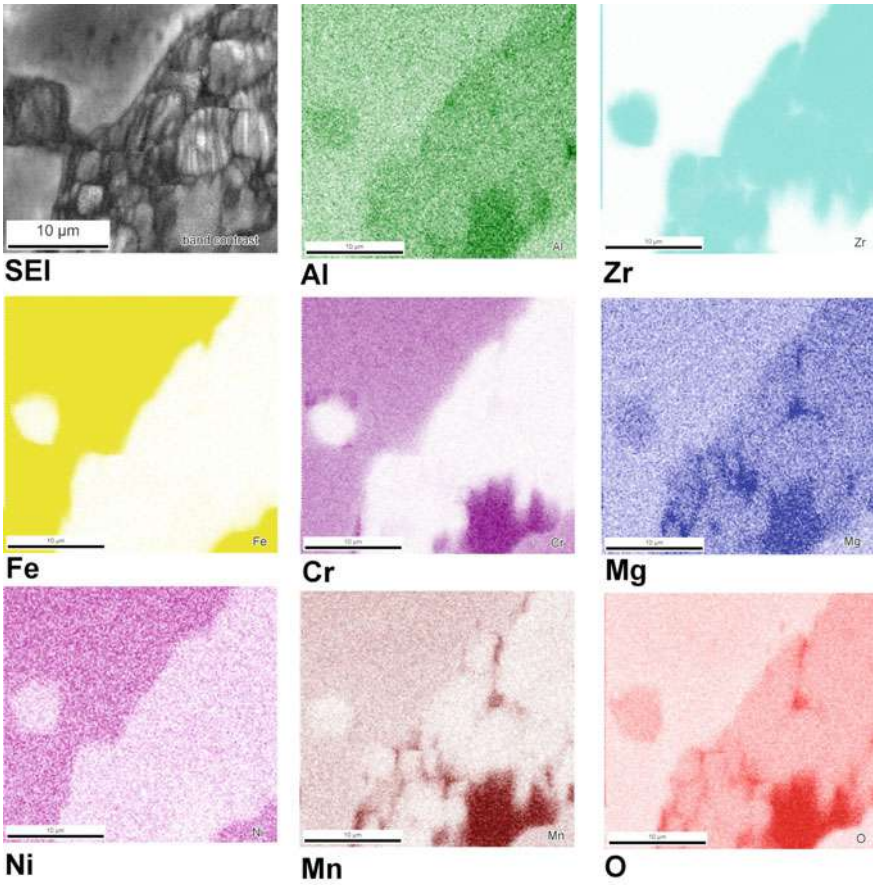

Fig. 1.13 EDS mapping of a full TRIP-matrix composite bead, composition 20Z (polished surface) [4]

Oppelt [7]. The steel matrix can be clearly distinguished due to the presence of Fe and Ni. The zirconia particles can be recognized due to the Zr-distribution pattern. Mixed spinel formation during sintering occurred due to diffusion processes [10] and is indicated by the distribution of Al, Mg, O, Mn and Mg, Cr. At the grain boundaries steel/steel three different types of precipitates Mn–Cr–O, Mn–Si–O and Cr–C have been found. By means of EBSD the precipitations could be identified as $MnCr_2O_4$, Mn_2SiO_4 and Cr_7C_3. The formation of carbides has been reduced due to optimization of the thermal processes.

The physical properties of the different TRIP-matrix composite beads are summarized in Table 1.11. For the full beads it can be recognized that the shrinkage increases if zirconia particles are incorporated in the steel matrix. Due to the chosen hardener agent ($CaCl_2$) the transition from sodium alginate sol to calcium alginate gel during casting is decelerated. The fabricated full beads therefore have high

Table 1.11 Properties of the TRIP-matrix composite beads, after sintering at 1350 °C

	Shrinkage %	Bulk density g/cm^3	Open porosity %	Compressive strength MPa	Strain at failure %	Total specific energy absorption kJ/kg
Full beads						
0Z	5.7 ± 0.1	4.1	11.3	398.3 ± 17.3	29.4 ± 0.8	11.5 ± 0.4
5Z	16.7 ± 0.0	–	5.9	344.4 ± 18.1	13.5 ± 0.7	6.3 ± 0.4
10Z	22.0 ± 0.1	4.7	3.7	359.1 ± 15.1	16.6 ± 0.2	7.9 ± 0.4
20Z	16.1 ± 0.1	6.1	15.0	240.3 ± 13.5	16.5 ± 0.2	3.9 ± 0.1
Hollow beads						
0Z	38.7 ± 5.9	5.6	10.2	61.4 ± 3.2	15.6 ± 3.1	2.4 ± 0.4
5Z	26.1 ± 2.6	4.9	9.0	98.8 ± 12.7	15.3 ± 2.2	3.7 ± 0.2
10Z	24.5 ± 5.4	4.8	12.7	104.0 ± 30.3	10.4 ± 4.5	1.5 ± 0.5
Functionally graded beads (10Z-95Z-0Z)						
dipped	24.4 ± 4.8	6.8	23.0	49.6 ± 4.9	4.6 ± 0.8	0.4 ± 0.1
sprayed	27.0 ± 1.8	7.7	10.1	551.3 ± 59.3	21.5 ± 3.0	13.7 ± 3.5

porosities in the green stage (35–47%). After sintering the composition 10Z has the lowest open porosity of 3.7% and the highest shrinkage of 22.0%. For the hollow beads shrinkages ranging from 24.5% (10Z) to 38.7% (0Z) have been determined. It has to be noted that the cavities of the hollow beads are reduced during thermal treatment. Therefore a higher overall shrinkage was measured. The hollow beads containing 5 and 10 vol.% zirconia show higher open porosities in comparison to the full beads. The functionally graded beads (FGS) were prepared by dip or spray coating of composites beads with the initial composition 10Z. Hence, the shrinkages of the FGS correspond to the shrinkage of the full beads with the composition 10Z. The difference in open porosity can be attributed to the choice of coating procedure. With the aid of spray coating a fine spray is generated and it presumably closed the open pores of the initial bead. This effect has not been recognized for the dip coated material. The mechanical properties of the different TRIP-matrix composite beads are also summarized in Table 1.11. The functionally graded beads (spray coating) exhibit the highest compressive strength with 551 MPa. The compressive strength of the reference material (full bead) with the composition 0Z was determined to be 399 MPa. This material also shows the highest strain at failure with 30%, whereas the functionally graded beads (spray coating) have a strain at failure of 21.5%. The functionally graded beads also show the highest total specific energy absorption with 13.7 kJ/kg, followed by the reference material with 11.5 kJ/kg. In Table 1.12 the specific energy absorption of the different TRIP-matrix composite beads is displayed as a function of compression strain. The full beads with the composition 0Z and the functionally graded beads (spray coated) allow a compression of up to 20%. At this compression the FGSs show the highest specific energy absorption with 10.7 kJ/kg.

At a compression of up to 15% all zirconia reinforced beads have a higher specific energy absorption compared to the reference material 0Z. Oppelt [7] has found that the reinforcing zirconia particles in the TRIP-matrix show a stress-assisted phase transformation. In Fig. 1.14, the results of the compressive testing are given for all developed TRIP-matrix composite beads. The full beads have a 4 times higher strength in comparison to the hollow beads. Up to a compression of 15% the full beads of the composition 5Z and 10Z show a significant higher strength than the reference material 0Z. The highest strength has been determined for the functionally graded beads even at compression above 15%.

1.3.1.3 TRIP-Matrix Composites via Paper-Manufacturing Technology

Square paper sheets with 200 mm in length have been formed on a laboratory sheet-forming device. Figure 1.15 shows the microstructure of as-fabricated and calendered green sheets. In contrast to the processing of pre-ceramic paper, where both filler particles and pulp fibers develop a negative surface charge in water, the steel particles used as fillers remained non-charged in water. Coagulation and flocculation therefore only took place for pulp fibers in the suspension due to the addition of organic additives. Figure 1.15a illustrates the domination of that fiber-to-fiber bonds. During wet paper processing via filtration, the steel particles were incorporated in between the fiber network, and steel clusters could be found. The solids retention was greater than 90 wt.%. The as-fabricated paper had a high porosity and surface roughness (Fig. 1.15c), which could be significantly reduced by calendering at 30 kN/mm (Fig. 1.15b, d). During calendering the steel particles deformed plastically due to the high surface load and may have undergone a martensitic phase transformation, which was reversible upon heat treatment.

Table 1.12 Specific energy absorption (SEA_m) in kJ/kg at 5, 10, 15 and 20% strain

	5% strain	10% strain	15% strain	20% strain
Full beads				
0Z	0.19 ± 0.02	1.11 ± 0.06	2.73 ± 0.18	5.22 ± 0.22
5Z	0.74 ± 0.01	3.34 ± 0.13	–	–
10Z	0.75 ± 0.01	3.39 ± 0.22	7.27 ± 0.18	–
20Z	0.29 ± 0.01	1.27 ± 0.03	3.08 ± 0.3	–
Hollow beads				
0Z	0.26 ± 0.05	1.14 ± 0.06	2.08 ± 0.40	–
5Z	0.39 ± 0.02	1.45 ± 0.14	3.14 ± 0.30	–
10Z	0.57 ± 0.05	1.51 ± 0.53	–	–
Functionally graded beads (10Z-95Z-0Z)				
dipped	0.34 ± 0.04	–	–	–
sprayed	0.64 ± 0.19	2.95 ± 0.54	6.89 ± 0.90	10.7 ± 0.23

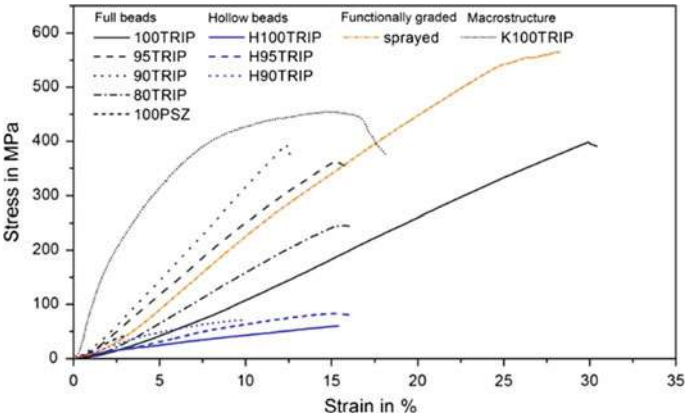

Fig. 1.14 Stress-strain curves for the different TRIP-matrix composite beads [7]

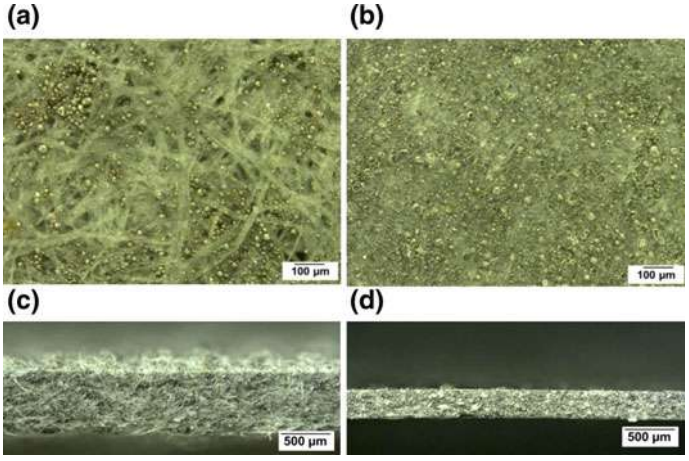

Fig. 1.15 LOM micrographs of a green paper sheet, composition 0Z, **PM**X8CrMnNi16-7-3. Top surface view: **a** uncalendered, **b** calendered at 30 kN/mm. Cross-sectional view: **c** uncalendered, **d** calendered at 30 kN/mm [15]

The properties of the green composites are summarized in Table 1.13. In the as-fabricated state, the fibers were loosely arranged with many interspaces, whereas calendering led to the firm embedding of the fibers between the filler particles. In consequence, the total porosity and the surface roughness are decreased due to calendering, which also increases the tensile strength of the calendered samples. The calendered sheets therefore offer enough stability to be further processed (e.g. punching of samples for determination of tensile strength after sintering, preparation of corrugated cardboard structures).

Table 1.13 Properties of the TRIP-matrix paper composites in green state

Recipe		0Z	5Z	10Z
Thickness as-fabricated	mm	1.00 ± 0.05	0.97 ± 0.05	0.97 ± 0.06
Thickness after calendering	mm	0.31 ± 0.03	0.31 ± 0.01	0.31 ± 0.1
Tensile strength as-fabricated	N/mm^2	6.1 ± 0.9	5.3 ± 0.6	5.2 ± 0.5
Tensile strength after calendering	N/mm^2	13.2 ± 1.7	14.0 ± 2.9	15.6 ± 3.2

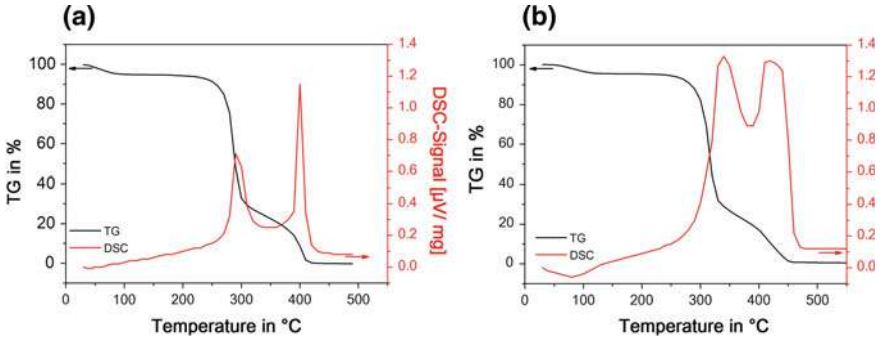

Fig. 1.16 DSC/TG analysis of the cellulose fibers in oxidizing atmosphere applying different heating rates: **a** 1 K/min, **b** 5 K/min [15]

The debinding of the calendered paper sheets is an essential processing step in the development of TRIP-matrix composites by paper-manufacturing technology. The total organic quantity of the as-fabricated paper sheets was 40–45 vol.%. The thermal removal of the organic additives is therefore not only a critical step in terms of defect-free debinding, but also in terms of residual carbon (resulting from an insufficient debinding) affecting the chemical and the phase composition of the TRIP-steel matrix. The thermal decomposition behavior of the cellulose pulp fibers at heating rates of 1 and 5 K/min are summarized in Fig. 1.16. For both heating rates, two exothermic peaks can be distinguished. At a heating rate of 5 K/min, the peaks are shifted to higher temperatures and appear less pronounced. At a heating rate of 1 K/min, the maxima of both exothermic reactions are given at 290 and 400 °C. The decomposition was completed at 420 °C. At a heating rate of 5 K/min, the exothermic reactions shifted to 340 and 430 °C, respectively, and the reaction was completed at 460 °C.

As a result of the DSC/TG analyses the debinding rate was set to 0.5 K/min. The maximum debinding temperature was set to 460 °C, with a dwell time of 90 min. The carbon content for the composition 0Z after debinding was determined to be 0.044%, which corresponds to the carbon content of the initial steel powder. The microstructure of the sintered sample 5Z is displayed in Fig. 1.17. The paper manufacturing technology requires the use of cellulose pulp fibers, which are thermally removed by a debinding process, leaving pores within the material. The sintering at

1350 °C with a dwell time of 60 min did not result in a sufficient densification of the steel matrix. The incorporated zirconia particles form agglomerates, which are embedded in the interstices of the steel particles and the process derived pores. It can be furthermore recognized that no interfacial reaction occurred between the zirconia particles and the surrounding steel matrix. Nevertheless, precipitates are formed at the grain boundaries steel/steel.

The chemical as well as the phase composition of the precipitates has been analyzed using EDS/EBSD. According to the EDS mappings two different types of precipitates have formed during sintering as shown in Fig. 1.18a, b. In the center of the investigated sample the precipitates are composed of chromium, manganese, and carbon and were identified as trigonal $(Cr, Mn, Fe)_7C_3$. The second type of precipitation was occasionally found at the sample edges. These precipitates are composed of manganese, silicon, and oxygen and have been identified as orthorhombic Mn_2SiO_4. The manganese silicate is surrounded by an iron, chromium, carbon rich area that was identified as trigonal $(Cr, Mn, Fe)_7C_3$. The potential of the paper-derived TRIP-matrix composites regarding the desired deformation-assisted austenite to martensite phase transformation is significantly lowered due to the presence of carbides. The influence of the sintering atmosphere on the formation of carbides is discussed in [8]. In a further investigation the calendered paper sheets have been sintered in a purified argon atmosphere with the aim to prohibit the formation of carbide precipitations. The resulting microstructure is shown in Fig. 1.19. Obviously, the incorporated zirconia particles form agglomerates and they are embedded within the pores. The formation of carbide precipitates has not been registered. According to EDS/EBSD the steel matrix shows segregations with higher concentrations of chromium and lower concentrations of nickel than the surrounding matrix. Furthermore, the material contains randomly dispersed oxide precipitations that were most likely formed during heat treatment. These oxide precipitations have been identified as orthorhombic $(Mg, Mn)_2SiO_4$.

If the thermal treatment was conducted in a non-purified atmosphere, the mechanical properties of the paper-derived metal-matrix composites were deteriorated due

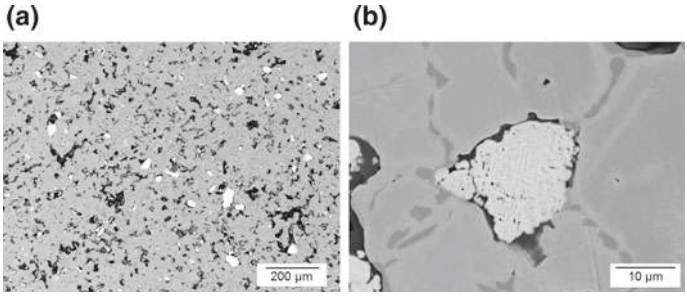

Fig. 1.17 SEM micrographs (BSE-mode) of the sintered composites prepared by paper-manufacturing technology (light grey: zirconia, dark grey: steel matrix with precipitations) [8]

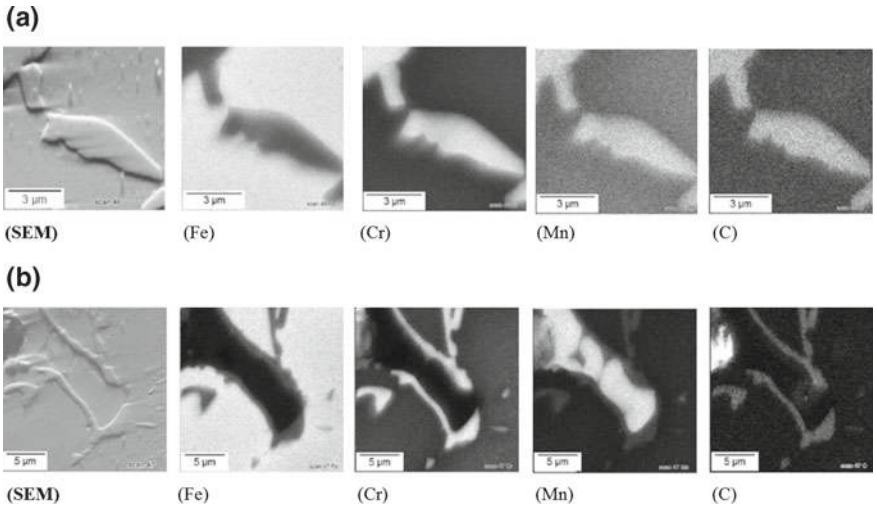

Fig. 1.18 EDS mapping of the reference material 0Z at the grain boundaries, sintered at 1350 °C, **a** in the center of the sample, **b** at the edge of the sample [8]

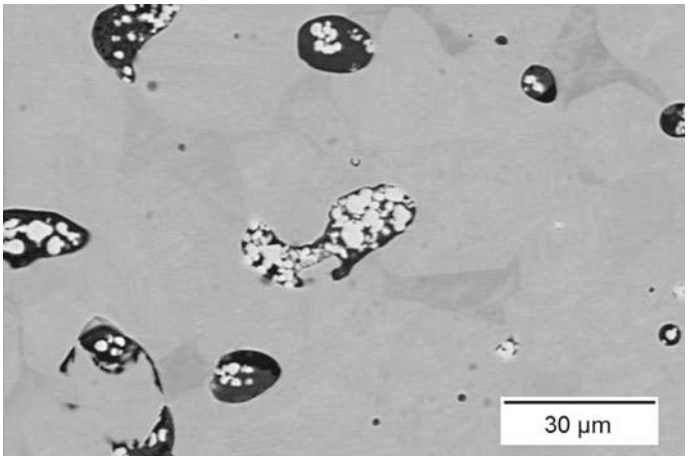

Fig. 1.19 SEM micrograph (BSE-mode) of the paper-derived TRIP-matrix composite 10Z sintered in a purified argon atmosphere [8]

to the presence of carbides. The highest tensile strength was determined for the reference material 0Z with 176.6 ± 12.1 MPa at a total porosity of 66%. The composition 5Z (5 vol.% zirconia) showed a lower tensile strength of 123.3 ± 3.1 MPa. For the composite 10Z (10 vol.% zirconia) a tensile strength of 103.3 ± 14.4 MPa was determined. The materials failed at a maximum strain of 0.6% and showed brittle fracture behavior.

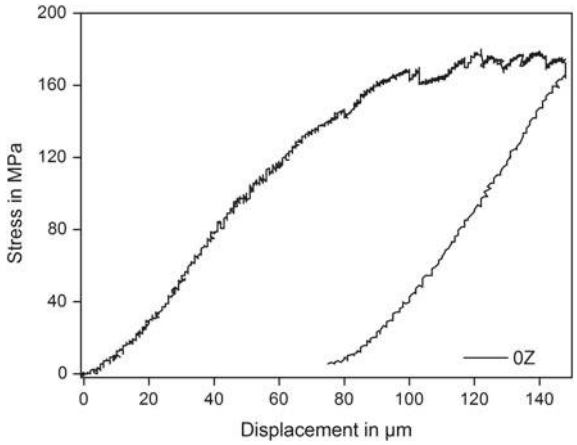

Fig. 1.20 Stress-displacement curve of the reference material 0Z during tensile load testing [8]

An in situ tensile test was carried out for the reference material 0Z in a scanning electron microscope MIRA 3 XMI (Tescan, Czech Republic) in order to characterize the deformation and damage behavior of the material under quasi-static load at a crosshead speed of 1 µm/s. The evolution of the microstructure was registered as a function of the crosshead displacement. The corresponding stress-displacement curve is shown in Fig. 1.20.

Figure 1.21a shows the microstructure of the reference material 0Z in its initial state. The carbide precipitates are clearly visible at the grain boundaries. Pores are filled with Mn_2SiO_4. At a crosshead displacement of 110 µm the carbide precipitates start to break, and cracks are initiated on macroscopic scale (see Fig. 1.21b, c). The single cracks joined to a large main crack when the crosshead displacement is further increased, see Fig. 1.21d. The crack tip passes along the carbide grain boundaries toward bigger pores. The precipitates debond from the steel matrix and fracture in a transgranular manner.

In case of the paper-derived TRIP-matrix composites sintered in a purified argon atmosphere significant higher tensile strength has been determined. A purified atmosphere and the optimized composition of the paper-sheets led to tensile strength of 170.6 ± 18.7 for the composition 0Z and 142.4 ± 10.5 MPa for the composition 10Z at total porosities of 26%. The incorporation of commercially available zirconia fibers led to further improvements of the mechanical performance. At a fiber incorporation of 3 vol.% the tensile strength was determined to be 207.0 ± 17.4 MPa at a total porosity of 25%. However, these optimized TRIP-matrix composites showed also a brittle fracture behavior.

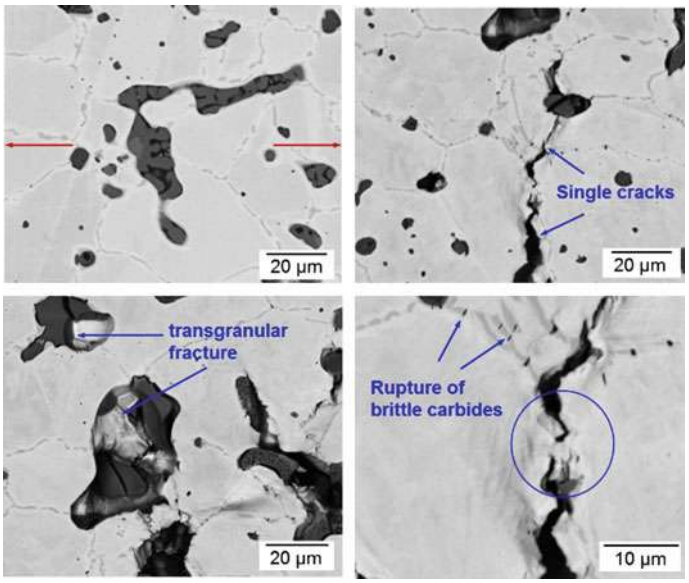

Fig. 1.21 SEM micro-graphs of the reference material (0Z) during tensile loading at different displacements (red arrows: load direction) [8]

1.3.2 Development of TRIP-Matrix Composites via Metal Melt Infiltration of Ceramic Preforms

1.3.2.1 Open Cell Foam Structures Based on Magnesia-Partially Stabilized Zirconia

Open cell foam structures based on magnesia partially stabilized zirconia have been prepared using the replica technique. In a preliminary study an adequate additive system has been developed. Comprehensive rheological measurements have been carried out. In Fig. 1.22 the viscosity curves for the different spraying slurries are displayed. According to literature [20] typical shear rates for spray processes are 10^3–10^5 s^{-1}. At a shear rate of 1000 s^{-1} the viscosities of the slurries have been determined to be 126 mPas (40 wt.% water), 100 mPas (45 wt.% water) and 63 mPas (55 wt.% water). These low viscosities favor the formation of a fine spray during the spray coating procedure. The appropriate additive system additionally assists to keep the slurries stable in idle state. It was recognized that the conventional spray coating procedure led to a poor coating of the foam struts especially in the foam center. If the spray coating procedure was done air stream assisted, a better deposition of the spray droplets on the polyurethane foams has been established. In addition to that less pore blocking has been registered. With the aid of computer tomography the homogeneity of the coatings has been analyzed [9]. In Fig. 1.23, a comparison between conventional and airstream assisted coating procedure is given.

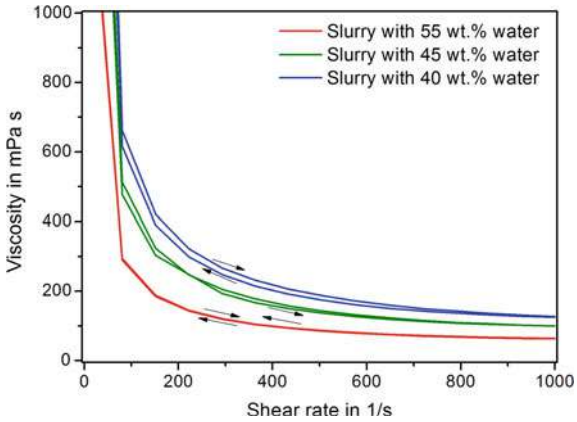

Fig. 1.22 Viscosity curves of the zirconia slurries at different powder to water ratios [9]

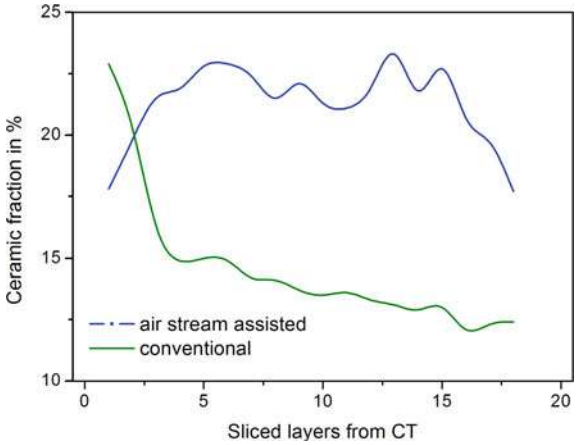

Fig. 1.23 Homogeneity of coated open foam cell structures using the different spray coating procedures [9]

For the conventional spray coating, the ceramic portions are mainly deposited on the surface of the open cell foam structures. In the first layer of the foam it was determined to be 22% and decreases to 15%. In the center of the open cell foam structure the ceramic portion is negligible. Quite different results have been found if the spraying procedure was done air stream assisted. It can be seen that the ceramic fraction was always greater than 20% throughout the considered volume of the open cell foam structure.

The influence of the solid content of the spraying slurry on the homogeneity of the spray coating has also been investigated. The slurry with 55 wt.% water had a

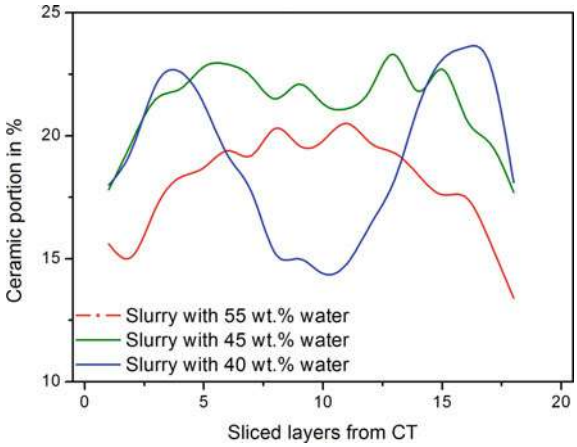

Fig. 1.24 Influence of the solid content of the spraying slurry on the homogeneity of the spray coating [9]

viscosity of 63 mPas and a yield stress of 13 Pa. Due to the low viscosity the slurry easily penetrates the foam structures.

As it can be seen in Fig. 1.24 the ceramic portion in the middle of the foam was determined to be greater than 20%. However, the ceramic portion is rather small on the upper surface of the sprayed foam. Presumably the yield stress of the slurry is exceeded due to the air pressure of the spray. For the slurry with 40 wt.% water a different effect can be seen. On the upper surface of the open cell foam structure the ceramic fraction was determined to be greater than 22%. Due to the higher yield stress the slurry strongly adheres onto the struts of the top surface and is not transported deeper into the structure. The best distribution of the ceramic fraction throughout the entire foam structure has been achieved if the slurry with 45 wt.% water was used for the spray coating procedure. Due to the yield stress of 20 Pa, the slurry remains on the struts. The viscosity of this slurry was determined to be 100 mPas and is therefore able to deeply infiltrate the foam structure.

The sintered open cell foam structures were infiltrated by a ***Cast*** X5CrMnNi16–7–7 steel melt in order to obtain TRIP-matrix composites. The phase composition of the infiltrated foam structures has been analyzed with the aid of EBSD. In Fig. 1.25, a SEM micrograph of the polished sample surface is presented. According to the EBSD-phase analysis the infiltrated foam structure contained 4.5% monoclinic zirconia, 49.8% tetragonal zirconia and 45.7% cubic zirconia. Thus, approximately 50% of the ceramic material is able to transform stress-assisted. No martensite has been detected by EBSD-analysis; the analyzed part consisted of 100% austenite.

1.3.2.2 Extrusion Technology for Honeycombs and Randomly Arranged Spaghetti-Filters

Ceramic preforms of honeycomb or spaghetti filter type have been prepared via extrusion technology. After sintering at 1650 °C in oxidizing atmosphere the preforms have been infiltrated by a ***Cast*** X5CrMnNi16-7-7 steel melt in order to obtain TRIP-matrix composites. For a sufficient infiltration the preforms had to be preheated to 1000 °C. The honeycombs were joined by a cold joining technique. Schärfl et al. [11] prepared spaghetti filters with a diameter of 70 mm and a height of 120 mm in one piece. Wenzel et al. [10] extruded spaghetti filter discs of with a diameter of 50 and 25 mm height. Before infiltration, these filters were stack to give a preform of 120 mm height. For the honeycomb structures as well as for the spaghetti filters an incomplete infiltration was registered. The metal melt froze during casting, presumably due to the high ceramic portion as well as due to the dense arrangement of the strands/honeycombs. A sufficient infiltration has been obtained if the hollow spaghetti filters have been used, see Fig. 1.26. It can be seen that the hollow strands are infiltrated. Presumably the thermal shock at the beginning of the steel casting caused the cracking of the hollow zirconia strands; moreover there is a significant density gradient between zirconia and steel. At the interface between zirconia and steel a crack network has been formed.

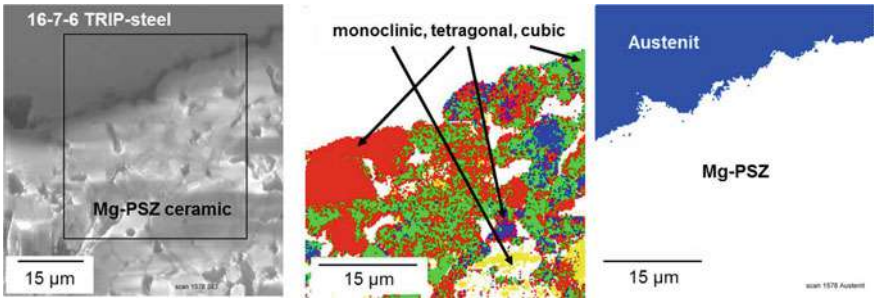

Fig. 1.25 SEM micrograph of the infiltrated open cell foam structure and the corresponding results of the EBSD-analysis [9]

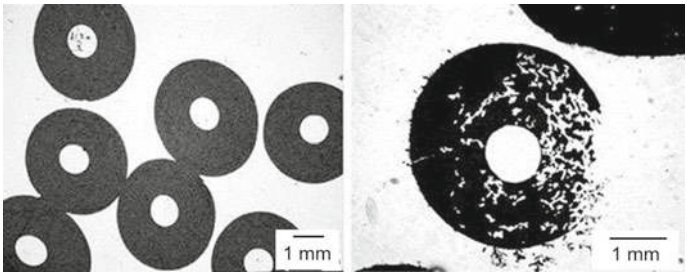

Fig. 1.26 LOM micrograph showing infiltrated hollow rods [11]

1.3.3 Development of Ceramic Matrix Composites via Powder Metallurgy

Another focus of the present work was the fabrication of ceramic matrix composites using pressure slip casting. The developed materials were based on zirconia and alumina with additions of up to 20 vol.% TRIP-steel powder (**PM** X8CrMnNi16-7-3). The zirconia matrix composites were cast as fine and coarse grained components, whereas the alumina matrix composites were only cast as coarse grained components. In a previous studies [16] an organic binder system containing KM 1001, KM 2000 and Optapix PAF 35 has been successfully established for the rheological stabilization of zirconia-steel slurries. For the casting of large components ($200 \times 200 \times 38$ mm^3) two additional binders, Welan gum and Konjac flour, had to be applied in order to guarantee the dimensional stability of the cast green bodies after demoulding. Due to the adjustment of the solid content as well as the optimization of the particle packing the casting times for these large components could be set to 90 min (fine grained slurries) and to 25 min (coarse grained slurries). The maximum casting pressure was 2 MPa. After drying the cast components were sintered at 1550 °C in argon atmosphere. The microstructure of the CMCs for the components containing 80 vol.% alumina (coarse) or 80 vol.% zirconia (fine) is exemplarily shown in Fig. 1.27. The homogenous distribution of the steel particles within the matrix materials has been verified with the aid of the microfocus X-ray computed tomograph. As a result of the casting technology and the sintering temperatures the pressure slip casted ceramic matrix composites features open porosities of $\geq$27%.

The wear behavior of the pressure slip casted composites has been investigated. Therefore the surfaces of the materials have been polished using different grinding media down to 1 μm grain size. Wear tests have been performed using a pin-on-disc tribometer with a WC-Co pin at room temperature under a normal force of 50 N and at a sliding speed of 0.05 m/s and a maximum sliding distance of 200 m. The wear tracks are at least 4 mm in width and can be clearly distinguished from the untreated surface as shown in Fig. 1.28. The wear resistance of the test specimens is characterized by their mass loss and the wear rates of the materials as given in

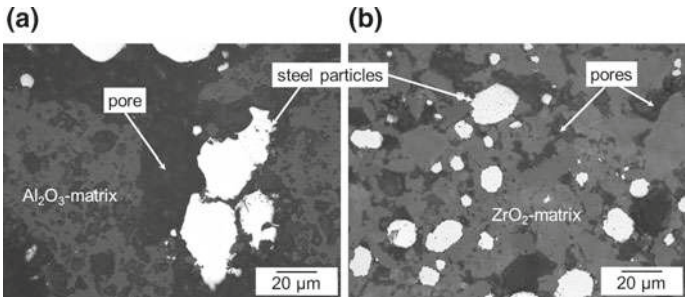

Fig. 1.27 LOM micrograph of pressure slip casted CMCs of the compositions **a** 80 vol.% alumina coarse and **b** 80 vol.% zirconia fine

Table 1.14. All investigated materials present severe wear with wear rates in the order of 10^{-1} to 10^{-4} mm^3/Nm. The wear tracks are characterized by abrasion, adhesion as well as fracture processes. Especially the coarse grained zirconia matrix composites are characterized by severe abrasive wear. The finer zirconia matrix material was significantly worn off; as a result also the coarser grains broke out of the matrix. For the coarse alumina composites identical wear mechanisms have been identified. With the aid of EDS the deposition of the counter body material tungsten carbide-cobalt in the wear track was registered. The fine grained zirconia matrix composites are

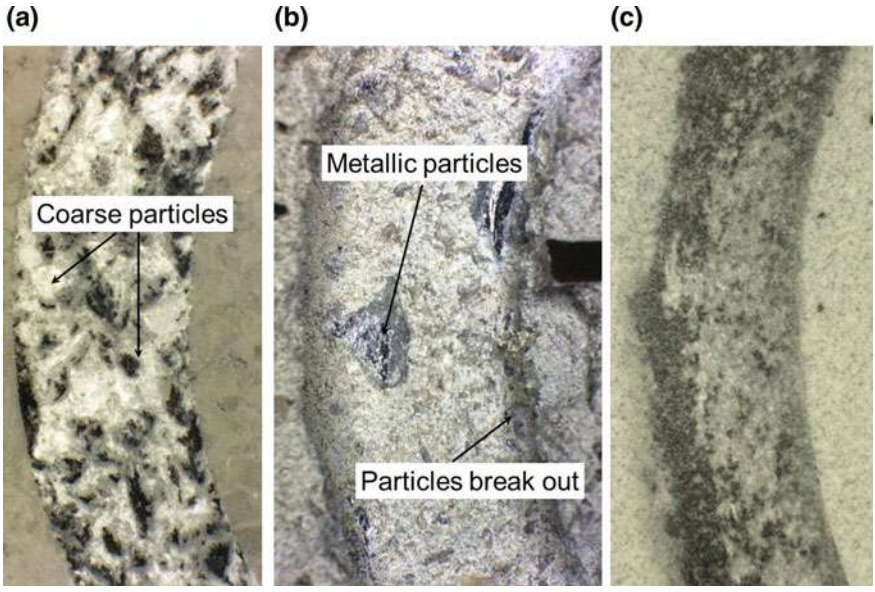

Fig. 1.28 Wear tracks of **a** 100 vol.% alumina (coarse), **b** 90 vol.% zirconia (coarse), **c** 100 vol.% zirconia (fine)

Table 1.14 Mass loss and wear rate of the investigated ceramic matrix composites

Matrix material	Metal fraction	Mass loss g	Wear rate 10^{-2} mm^3/Nm
Alumina (coarse)	0	0.015 ± 0.009	0.050 ± 0.024
	10	0.033 ± 0.032	0.103 ± 0.117
	20	0.014 ± 0.009	0.037 ± 0.027
Zirconia (coarse)	0	1.949 ± 1.322	49.099 ± 33.318
	10	1.233 ± 0.405	11.828 ± 38.863
	20	0.853 ± 0.421	7.789 ± 3.847
Zirconia (fine)	0	0.008 ± 0.011	0.024 ± 0.025
	10	0.027 ± 0.034	0.081 ± 0.028
	20	0.034 ± 0.001	0.076 ± 0.022

characterized by less material abrasion. The continuous stresses may cause surface fatigue in such a way that occasionally larger fragments of the material break out. In these areas the material abrasion is enhanced due to the rough surfaces. The wear behavior of the pressure slip casted composites is similar to existing results in literature. It may be significantly improved if the sintering parameters will be optimized, e.g. performing of the sintering at higher temperatures (1650–1700 °C). However, a compromise between sintering temperatures of the ceramic material and the reinforcing metal particles has to be found.

1.3.4 Development of Ceramic Components Using Alternative Technologies

Intensive research work has been conducted in terms of the development of partially stabilized zirconia fibers using the electrospinning technology. The fibers were prepared from polyvinylpyrrolidone (PVP), $ZrOCl_2 \cdot 8\ H_2O$ and $Y(NO_3)_3 \cdot 6\ H_2O$. The appearance of the as-spun fibers with a mean fiber diameter of 225 nm is displayed in Fig. 1.29. The thermal decomposition behavior has been studied with the aid of DSC/TG-analysis. Three different peaks have been identified and the corresponding total weight loss was determined to be 80%. The first weight loss of 15% from room temperature to 200 °C is caused by the removal of water and ethanol. The second weight loss (47%) is related to exothermic reactions as shown by the DSC curve, see Fig. 1.30. The exothermic peaks at 358, and 400 °C are associated with the decomposition of the PVP. From 400 to 504 °C there was a weight loss of approx.

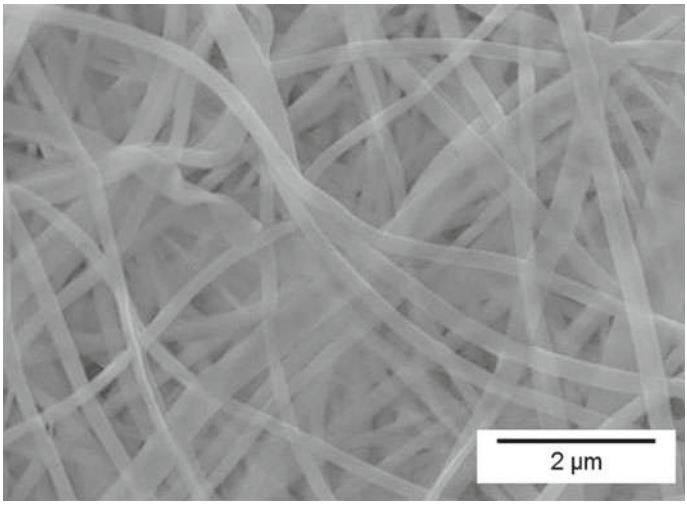

Fig. 1.29 SEM micrograph of the as-spun fibers with a mean fiber diameter of 225 nm

19%, which can be assigned to the transition from $ZrOCl_2$ to ZrO_2 and the further decomposition of PVP.

The as-spun fibers have been sintered at 700, 1100, 1350 and 1650 °C with heating rates of 1 K/min and 10 K/min. The evolution of the crystalline structure has been analyzed using X-ray diffraction. If the sintering was conducted at 700 °C only tetragonal zirconia has been identified, see Fig. 1.31. With increasing sintering temperature the peaks become tapered. Sintering at 1100 °C with a heating rate of 1 K/min led to a decrease of the tetragonal phase in intensity and a monoclinic pattern appears, see

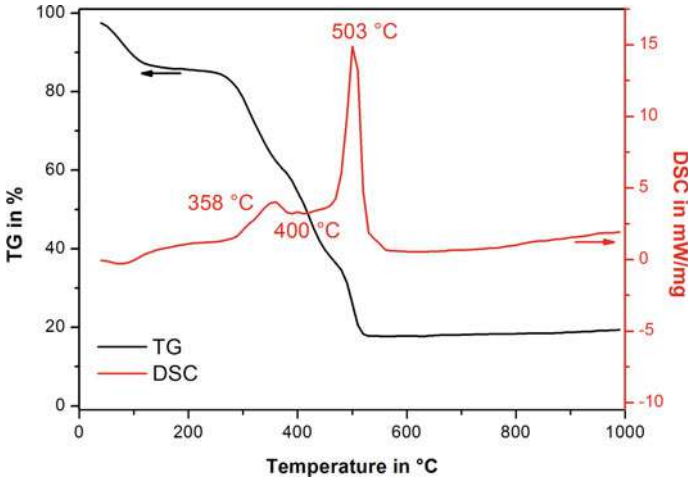

Fig. 1.30 DSC/TG-analysis of the as-spun fibers

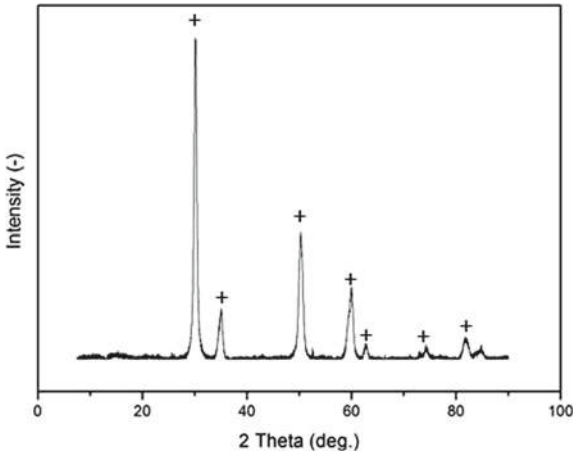

Fig. 1.31 X-ray diffraction pattern of the yttria stabilized zirconia fibers after sintering at 700 °C, tetragonal phase indicated by +

Fig. 1.32. These results are consistent with the observations made by Davies et al. [21] and may be attributed to the coarsening of the zirconia grains/fibers. If the heating rate has been increased to 10 K/min (at the same sintering temperature) the formation of a monoclinic phase and coarsening of the zirconia fibers/grains could not be registered, see Figs. 1.32b and 1.33. At sintering temperatures of 1350 and 1650 °C the tetragonal phase dominates, since the thermal treatment has been conducted in the tetragonal solid solution field. At sintering temperatures of 1350 °C, the fiber structure disappears as shown in Fig. 1.34. The final microstructure is characterized by a high open porosity.

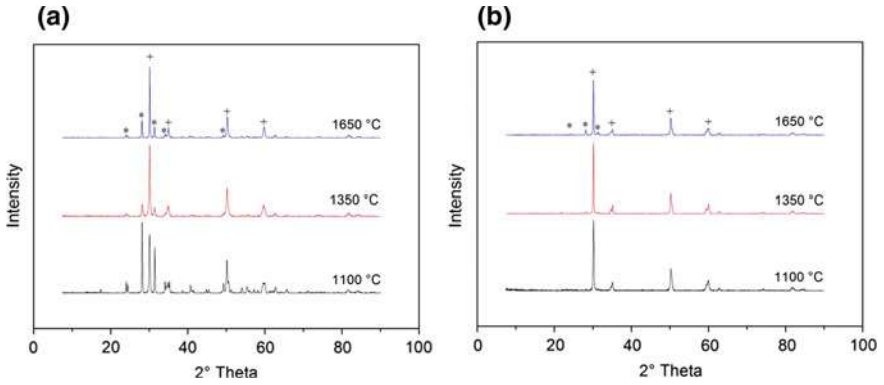

Fig. 1.32 X-ray diffraction patterns of the yttria-stabilized zirconia fibers as a function of the sintering conditions, **a** heating rate of 1 K/min **b** heating rate 10 K/min, (monoclinic phase indicated by *, tetragonal phase indicated by +)

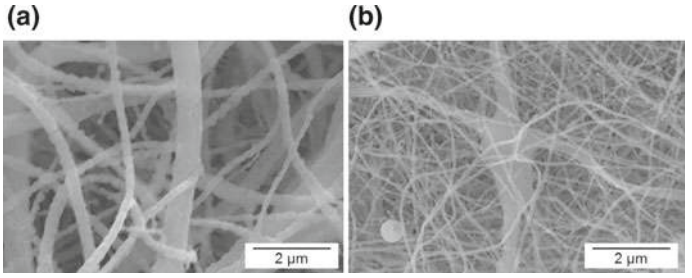

Fig. 1.33 SEM micrographs of the yttria-stabilized zirconia fibers, sintered at 1100 °C with a heating rate of **a** 1 K/min and **b** 10 K/min

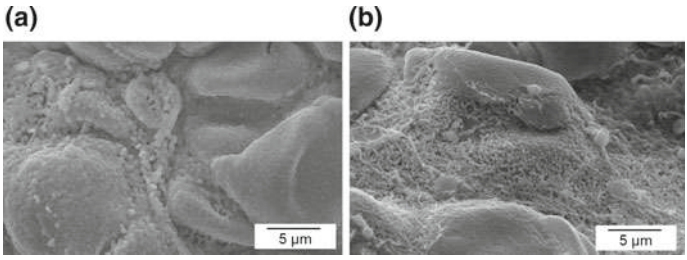

Fig. 1.34 SEM micrographs of the yttria-stabilized zirconia fibers, sintered at 1350 °C with a heating rate of **a** 1 K/min and **b** 10 K/min

1.4 Summary

The present work focused on the development of metal matrix composites and ceramic matrix composites using ***innovative casting technologies*** that are typically employed ***for the fabrication of ceramic components***.

The ceramic processing route of polyurethane foams at room temperature has been applied for the development of open cell foam structures based on austenitic stainless TRIP-steel and TRIP-steel/zirconia composite materials. Advantages have been achieved in terms of higher compressive stresses as well as energy absorption during deformation. Particularly, the supplement of the TRIP-matrix composite with a dense coating (jacket) at the foam macrostructures led to a light structure design with excellent energy absorption values. Due to EBSD-analysis the stress-induced martensitic phase transformation of metastable tetragonal zirconia has been identified at compressive strains below 2%.

Full and hollow beads based on austenitic stainless TRIP-steel have been developed using the gel casting technology. A major success was the development of functionally graded beads prepared via ***gel casting*** in combination with a specific heat treatment. The developed full beads (composition 10Z) as well as the functionally graded beads have compressive strengths of approx. 380 MPa at a compression of 15%. The pure metal reference material (0Z) shows a significantly lower strength of 150 MPa at the same compression. At about 15% compression the full TRIP-matrix beads collapse. The functionally graded beads have a good integrity up to 30% compression and have a significantly higher strength. At small deformation, the stress level of macroscopic bead structures is well above single beads, but then fails due to the poor joining strength. Therefore, the joining between the beads should be optimized to combine the properties of the particle-reinforced beads and functionally graded beads with the good properties of the spherical macrostructures. The functionally graded beads as well as the particle-reinforced beads with 5 and 10 vol.% zirconia show greatest potential within the group of metal beads obtained by gel casting in terms of energy absorption.

Paper-derived metal matrix composites have been developed using the ***paper-manufacturing technology***. Initially sintered TRIP-matrix composites were characterized by a strong carbide formation, resulting in a brittle fracture behavior of these materials. The crack initiation always started from the precipitates and the cracks propagated along the grain boundaries. The highest tensile strength was determined for the zirconia-free reference material with 177 MPa at a total porosity of 66%. A further sintering approach concerned the purification of the flushing gas Argon 5.0 and the improvement of the sealing performance of the furnace. As a result the formation of carbide precipitations was prevented. In a further development, cellulose pulp fibers have been successfully replaced by commercially available zirconia fibers. The resulting fiber reinforced TRIP-matrix composites showed improved tensile strength of 207 MPa, which was approx. 33% higher than for the zirconia-free reference material at a significantly lower porosity. The easy casting technology of the paper-derived metal matrix composites, the possibility to tune the functional properties as well as the raw material selection allows a wide range of applications e.g. as filter material, heat exchanger or catalyst material.

Open cell foam structures based on magnesia partially stabilized zirconia were prepared using the ***replica technique***. If the spray coating procedure was done airstream assisted the homogeneity of the ceramic struts was significantly improved. The optimized slurry based on magnesia partially stabilized zirconia contained 45 wt.% water. After the infiltration of the sintered foam structures the TRIP-matrix composite contained 4.5 vol.% monoclinic zirconia, 49.8 vol.% tetragonal zirconia and 45.7 vol.% cubic zirconia. Thus, approximately 50 vol.% of the ceramic material is able to transform stress-assisted. The steel matrix consisted of 100% austenite.

Another emphasis of the present work was the fabrication of ceramic matrix composites using ***pressure slip casting***. After successful casting the composites were sintered at 1550 °C in argon atmosphere and the homogenous distribution of the steel particles within the matrix materials has been verified. As a result of the casting technology and the sintering temperatures the pressure slip casted ceramic matrix composites had open porosities of $\geq$27%. Within this work package the wear behavior of the composites has been investigated using a pin-on-disc test. The wear behavior of the pressure slip casted composites was similar to existing results in literature and will be improved if the sintering parameters are optimized. Moreover, the pressure slip casted ceramic matrix composites have a high potential for applications at elevated temperatures, since they show a good resistance to thermal shock [16].

A further challenge was the development of zirconia fibers with a tailored phase composition via ***electrospinning***. Fibers were successfully prepared from polyvinylpyrrolidone (PVP), $ZrOCl_2 \cdot 8\,H_2O$ and $Y(NO_3)_3 \cdot 6\,H_2O$. Up to a sintering temperature of 1100 °C single zirconia fibers can be obtained. Due to the addition of varying amounts of yttrium (III) nitrate hexahydrate the phase composition was successfully tailored.

Acknowledgements The authors gratefully acknowledge the financial support of the Deutsche Forschungsgemeinschaft (DFG, German Research Foundation) for funding this research project A1

within the frame of the Collaborative Research Center (CRC) 799—TRIP-Matrix-Composites—project number 54473466.

We would like to thank our former colleagues Dr.-Ing. Wolfgang Schärfl and Dipl.-Ing. Manuel Hasterok for their contribution to the subproject A1. For the experimental support we would like to acknowledge the support of Dipl.-Ing. Anna Schneider and M.Sc. Christian Krumbiegel. Moreover, we like to thank our colleagues of the CRC 799, particularly Dr.-Ing. Anja Weidner, Dr.-Ing. Anke Dalke, Dr.-Ing. Katja Pranke and Dipl.-Ing. Christine Baumgart. We greatly appreciate the support of our colleagues at the Chair of Ceramics, in particular Dr.-Ing. Christian Weigelt, Dr.-Ing. habil. Harry Berek, Dr.-Ing Christiane Biermann and M.Eng. Ashish Pokhrel.

References

1. C. Aneziris, W. Schärfl, H. Biermann, U. Martin, Int. J. Appl. Ceram. **6**, 727 (2009)
2. C.G. Aneziris, H. Biermann, P. Scheller, TU Bergakademie Freiberg, German Patent, DE10 2007 044 160, 19 June 2008
3. C.G. Aneziris, H. Berek, M. Hasterok, H. Biermann, S. Wolf, L. Krüger, Adv. Eng. Mater. **12**, 197 (2010)
4. M. Oppelt, C. Wenzel, C.G. Aneziris, H. Berek, Metall. Mater. Trans. B. **45**, 2000 (2014)
5. M. Oppelt, C.G. Aneziris, J. Alloys. Compd. **634**, 43 (2015)
6. M. Oppelt, T. Leißner, H. Berek, C. Baumgart, L. Krüger, U. Peuker, C.G. Aneziris, Adv. Eng. Mater. **21**, 1 (2018)
7. M. Oppelt, Dissertation, Technische Universität Bergakademie Freiberg (2018)
8. C. Wenzel, Dissertation, Technische Universität Bergakademie Freiberg (2016)
9. M. Hasterok, C. Wenzel, C.G. Aneziris, U. Ballaschk, H. Berek, Steel Res. Int. **82**, 1032 (2011)
10. C. Wenzel, C.G. Aneziris, Steel Res. Int. **82**, 1057 (2011)
11. W. Schärfl, H. Berek, C.G. Aneziris, M. Weider, A. Yanina, Adv. Eng. Mater. **13**, 480 (2011)
12. M. Weider, K. Eigenfeld, Steel Res. Int. **82**, 1064 (2011)
13. G.C. Jacob, J.F. Fellers, S. Simunovic, J.M. Starbuck, J. Compos. Mater. **36**, 813 (2002)
14. H. Berek, C.G. Aneziris, M. Hasterok, H. Biermann, S. Wolf, L. Krüger, Solid State Phenom. **172–174**, 709 (2011)
15. C. Wenzel, C.G. Aneziris, K. Pranke, Metall. Mater. Trans. A. **47**, 160 (2016)
16. C. Wenzel, C. G. Aneziris, Mater. Sci. Eng., B **176**, 32 (2011)
17. H. Berek, C.G. Aneziris, M. Hasterok, H. Biermann, S. Wolf, L. Krüger, Adv. Eng. Mater. **13**, 1037 (2011)
18. C.G. Aneziris, W. Schärfl, TU Bergakademie Freiberg, German Patent, DE10 2007 001 724 A1, 11 July 2008
19. C. Weigelt, Dissertation, Technische Universität Bergakademie Freiberg (2013)
20. J.S. Reed, *Principles of Ceramic Processing*, 2nd edn. (Wiley, New York, 1995)
21. E. Davies, A. Lowe, J. Am. Ceram. Soc. **91**, 1115 (2008)

Chapter 2
Design of High Alloy Austenitic CrMnNi Steels Exhibiting TRIP/TWIP Properties

Qiuliang Huang, Marco Wendler, Javad Mola, Andreas Weiß, Lutz Krüger and Olena Volkova

Abstract This chapter is centered on the development of austenitic high strength cast CrMnNi steels with excellent strength-ductility combination by triggering TWIP and TRIP effects. Special attention is given to obtain a high yield strength and a good formability. For this purpose, three generations of steels were developed. The 1st generation is comprised of cast X3CrMnNi16-7-x steels. Their Ni concentration was varied in order to manipulate the stacking fault energy of austenite and change the operative deformation mechanisms. Based on the mechanical properties of the 1st generation steels, the 2nd generation steels were developed with a composition similar to the X3CrMnNi16-7-6 steel. Interstitial alloying elements were added to take advantage of solid solution strengthening and precipitation hardening effects. The substitutional alloy contents were carefully adjusted to ensure the occurrence of TRIP/TWIP effects during plastic deformation. For the 3rd generation, two steels from the 2nd generation, X16CrNiMnN15-3-3 and X16CrNiMnN19-4-3, were treated with tailored quenching and partitioning (Q&P) processing routines to further increase

Q. Huang (✉) · M. Wendler · A. Weiß · O. Volkova
Institute of Iron and Steel Technology, TU Bergakademie Freiberg, Freiberg, Germany
e-mail: qhuang@iest.tu-freiberg.de

M. Wendler
e-mail: marco.wendler@iest.tu-freiberg.de

A. Weiß
e-mail: weiss@iest.tu-freiberg.de

O. Volkova
e-mail: volkova@iest.tu-freiberg.de

J. Mola
Material Design and Structural Integrity Lab, Osnabrück University of Applied Sciences, Osnabrück, Germany
e-mail: j.mola@hs-osnabrueck.de

L. Krüger
Institute of Materials Engineering, TU Bergakademie Freiberg, Freiberg, Germany
e-mail: krueger@ww.tu-freiberg.de

H. Biermann and C. G. Aneziris (eds.), *Austenitic TRIP/TWIP Steels and Steel-Zirconia Composites*, Springer Series in Materials Science 298,
https://doi.org/10.1007/978-3-030-42603-3_2

the strength, especially the yield strength. The developed Q&P cast steels exhibited an outstanding strength-ductility combination, e.g. a yield strength over 1000 MPa and a total elongation exceeding 20% for the steel X16CrNiMnN15-3-3 containing 0.12 wt% N.

2.1 Introduction

Conventional austenitic stainless steels such as AISI 304 have been widely accepted in industry due to their outstanding properties such as superior toughness and extraordinary formability [1]. They are usually used in the annealed state and exhibit relatively low strength. Therefore, efforts have been made to develop metastable austenitic steels with low stacking fault energy (SFE) to enhance the strength-ductility combination by introducing transformation-induced and twinning-induced plasticity (TRIP and TWIP) effects during deformation of the steels [2–4].

To enable martensitic transformation at a certain temperature, the Gibbs free energy of martensite must be lower than that of austenite. The temperature, where the Gibbs free energies of the two phases are equal, is usually denoted as T_0 [5]. In practice, a sufficient undercooling below T_0 is often required to supply the interfacial energy between the austenite and the martensite nuclei as well as the elastic strain energy associated with the transformation [6]. Under external loading, deformation can proceed via martensitic transformation, twinning and other plasticity mechanisms. The occurrence of these mechanisms depends on the chemical composition and temperature, as they both influence the SFE [7–10]. It is commonly accepted that a SFE below 20 mJm^{-2} favors the transformation of austenite into martensite by either the sequence $\gamma \rightarrow \varepsilon \rightarrow \alpha'$ or direct $\gamma \rightarrow \alpha'$ transformation [11, 12]. The deformation-induced transformation to martensite is regarded to be responsible for the so-called TRIP effect [13].

When SFE increases to a value between 20 and 40 mJm^{-2}, the formation of mechanical twins is often observed [14]. The twins have different crystal orientations with respect to the matrix and hence, they reduce the effective glide distance of dislocations. The latter leads to an enhanced strain hardening, especially in the presence of a high twin density. This mechanism in TWIP steels is described as the dynamic Hall-Petch effect [15]. With an even higher SFE, where dissociation of perfect dislocations is energetically unfavorable, deformation proceeds mainly by the wavy glide of perfect dislocations [16]. It results in dislocation cell structures with almost dislocation-free interiors [17].

Decreasing SFE enhances the planar slip of dislocations, which promotes the formation of deformation bands with numerous stacking faults (SF) localized on parallel {111} planes of austenite. At a given strain rate, the associated ductility increases significantly compared to steels with high SFE, where wavy glide serves as the dominant deformation mechanism [18]. Table 2.1 summarizes the temperature dependence of austenite SFE [19]. SFE can also be modified by careful adjustment of the alloy content. The Cr, Si, and Mn addition in Fe–Cr–Ni austenitic stainless steels

Table 2.1 Variation of austenite SFE with temperature ($d\gamma_{SF}/dT$) [19]

Alloys (wt%)	$d\gamma_{SF}/dT$ ($mJm^{-2}\ K^{-1}$)	Temperature range (°C)	References
Fe–18Cr–14Ni–4Si	0.04	$-123 \leq T \leq 127$	[7]
Fe–18.3Cr–10.7Ni	0.05	$25 \leq T \leq 325$	[7, 23]
Fe–7.8Cr–12Ni	0.05	$-150 \leq T \leq 100$	[24]
Fe–17.8Cr–14.1Ni	0.06	$-180 \leq T \leq 27$	[7, 8]
Fe–15.9Cr–12.5Ni	0.08	$-115 \leq T \leq 100$	[7, 8]
Fe–18.7Cr–16.9Ni	0.10	$25 \leq T \leq 325$	[7, 23]
Fe–18Cr–7Ni–0.18C	0.10	$20 \leq T \leq 330$	[7, 25]
Fe–19.9Mn–4Cr–0.48C	0.08	$27 \leq T \leq 127$	[26]

was found to lower SFE and promote the planar dislocation arrays, while the Ni and C alloying raises SFE and encourages a cellular dislocation arrangement [20]. There is no consensus regarding the effect of N on SFE. In an Fe–21Cr–6Ni–9Mn steel, SFE reduces from 53 mJm^{-2} at 0.21 wt% N to 33 mJm^{-2} at 0.24 wt% N [21]. Further increase in N content up to 0.52 wt% does not vary the SFE. In the Fe–18Cr–10Mn steel, on the contrary, SFE increases from 10 mJm^{-2} at 0.39 wt% N to 23 mJm^{-2} at 0.69 wt% N [22].

The present work focuses on developing CrMnNi cast stainless steels as the matrix for novel composite materials, TRIP-Matrix-Composites, for the Collaborative Research Center 799. Efforts, including varying the Ni content, addition of different interstitial contents, and application of tailored quenching and partitioning (Q&P) processing routines, were made to achieve a high strength combined with a high ductility in the cast CrMnNi stainless steels.

2.2 Experimental Methods

The steels were all melted in a VIM12 vacuum induction melting and casting facility (ALD Vacuum Technologies GmbH) and cast in water-cooled copper molds as illustrated in Fig. 2.1. Details about the production of the steels can be referred to [27–29].

Hollow specimens with a length of 10 mm, an outer diameter of 4 mm and an inner diameter of 2 mm were used for dilatometry experiments on Bähr 805 A/D dilatometer with a cryogenic unit, which enabled subzero quenching to −130 °C. The as-quenched α'-martensite fraction ($f^{Q}_{\alpha'}$) was determined by subtracting the δ-ferrite fraction estimated by optical microscopy from the ferromagnetic phase fraction quantified by magnetic measurements. The latter was obtained based on the measured magnetization after corrections for the effect of alloying elements on the magnetization of pure iron. The accuracy is therefore dependent on the accuracy of the corrections for the effect of chemical composition and is usually within ±1 vol%.

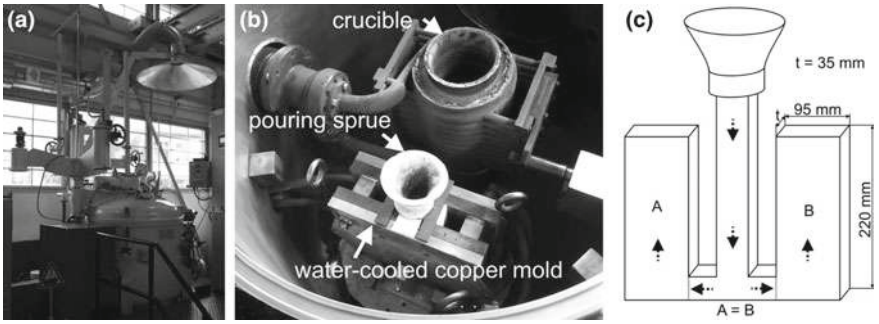

Fig. 2.1 **a** VIM 12 vacuum induction melting and casting facility used for the fabrication of the cast steels; **b** Components inside the furnace chamber; **c** Schematic view of the cast mold with arrows indicating the flow direction of the melt during casting [29]

The mechanical properties of the steels were evaluated by tensile testing on a Zwick 1476 universal testing machine at various temperatures. Tensile specimens with a gauge diameter of 6 mm and a gauge length of 30 mm were machined according to ISO 6892-1. The tensile direction was parallel to the height of ingots A and B in Fig. 2.1c. To minimize the adiabatic heating of tensile specimens, the crosshead displacement speed was set to 1 mm min^{-1}. This corresponds to an initial strain rate of 4×10^{-4} s^{-1}. For each alloy, three specimens were tested at each temperature. Strain-induced α'-martensite fraction ($f_{\alpha'}^{\text{ind.}}$) was determined by subtracting the α'-martensite fraction ($f_{\alpha'}$) in the undeformed grip section from the α'-martensite fraction in the uniformly-deformed gauge section. After $f_{\alpha'}^{\text{ind.}}$ values at various testing temperatures are obtained, the first temperature where $f_{\alpha'}^{\text{ind.}}$ becomes 1 vol% is determined as M_d.

Besides optical microscope, microstructures were examined using a Zeiss ULTRA 55 GEMINI-type field emission scanning electron microscope (FESEM) equipped with an AMETEK-EDAX analysis system for chemical composition and elemental distribution analysis. The deformed microstructures were characterized by electron backscatter diffraction (EBSD) measurements and electron contrast channeling imaging (ECCI). The step size for EBSD examinations was 0.1–0.2 μm and the camera (DIGIVIEW) output rate was 70 frames per second. ECCI was performed using an angle-selective backscatter electron detector (ASB) and a large aperture in the high current mode. The precipitation of carbides was verified by selected area electron diffraction (SAED) and Fast-Fourier Transformation (FFT) of high-resolution images in a Jeol JEM-2200FS transmission electron microscope (TEM). Efforts were made to avoid martensitic transformation during sample preparation by grinding and polishing at 80 °C and final electropolishing. The fracture surfaces of tested tensile specimens were examined using the secondary electron (SE) detector at an acceleration voltage of 10 kV.

2.3 Austenitic CrMnNi Cast Steels

For the 1st generation steels, the SFE was modified by varying the Ni content in cast X3CrMnNi16-7 steels from 3 to 9 wt%. Tensile testing at various temperatures reveals pronounced TRIP effect at RT in the cast steels with 3 and 6 wt% Ni.

2.3.1 Constitution and Special Methods

The chemical compositions of the 1st generation CrMnNi steels are shown in Table 2.2. To determine martensite start (M_s) temperatures, dilatometry cycles involving heating under vacuum to 1050 °C at 10 K/s and cooling to −130 °C at 10 K/s after a holding time of 30 min were performed [30]. Prior to tensile tests, tensile specimens were solution annealed at 1050 °C for 30 min under vacuum to reduce the compositional inhomogeneity of substitutional elements generated during solidification. Tensile tests were done at temperatures ranging from −196 to 250 °C.

2.3.2 Initial Microstructures of 16-7-3/6/9 Steels

The microstructures of the cast steels were predicted based on Schaeffler diagram (Fig. 2.2) with Cr− and Ni-equivalents (Cr_{eq} and Ni_{eq}) calculated according to the following equations proposed for cast austenitic stainless steels [32]:

$$\begin{aligned} Cr_{eq} = {} & \%Cr + \%Mo + 4\%Ti + 4\%Al + 1.5\%Si \\ & + 1.5\%\,V + 0.9\%Nb + 0.9\%Ta + 0.5\%W \end{aligned} \tag{2.1}$$

$$\begin{aligned} Ni_{eq} = {} & \%Ni + 30\%C + 18\%N + 0.5\%Mn \\ & + 0.3\%\,Co + 0.2\%Cu - 0.2\%Al \end{aligned} \tag{2.2}$$

The microstructures and phase fractions of the cast steels are demonstrated in Fig. 2.3. With increasing Ni content, the fractions of α'-martensite and δ-ferrite decrease until a fully austenitic microstructure is obtained for the 9% Ni alloy. The SFE of the steels at RT is calculated according to the empirical relationship in (2.3)

Table 2.2 Chemical compositions of the 1st generation CrMnNi steels in wt% [31]

Steels	Steel ID	Cr	Mn	Ni	Si	C	N
Cast X3CrMnNi16-7-3	16-7-3	16.40	7.00	3.10	1.00	0.03	0.01
Cast X3CrMnNi16-7-6	16-7-6	16.20	7.10	5.90	1.10	0.03	0.01
Cast X3CrMnNi16-7-9	16-7-9	16.40	6.90	9.00	1.09	0.03	0.01

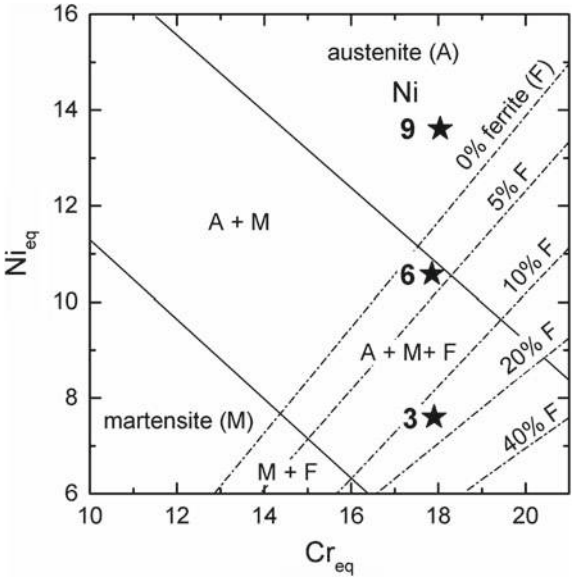

Fig. 2.2 Position of 16-7-3/6/9 steels in Schaeffler diagram based on (2.1)–(2.2)

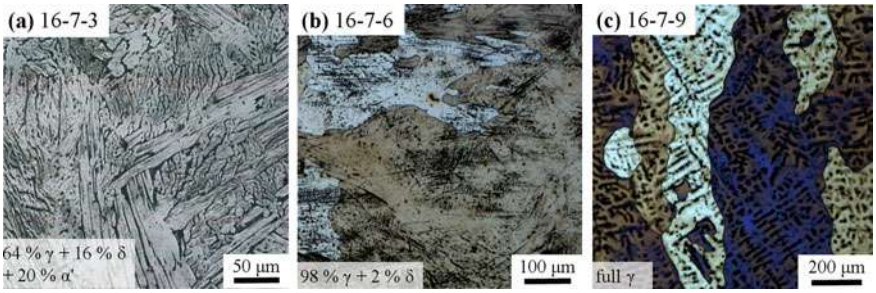

Fig. 2.3 Optical micrographs and phase fractions of the steels **(a)** 16-7-3, **(b)** 16-7-6 and **(c)** 16-7-9 solution annealed at 1050 °C for 30 min. Note that the straight lines (black) in some austenitic regions of (**b**) represent deformation bands induced in the first solidified regions (dendrite cores) during the metallographic preparation. The depletion of alloying elements and the low stability of austenite in such regions may lead to the formation of preparation-induced martensite. The samples were etched with Beraha I solution [34]

[33]. The calculated SFEs and the M_s temperatures determined using dilatometry are shown in Table 2.3.

$$\begin{aligned}\mathrm{SFE} = {} & 39 + 1.59\%\mathrm{Ni} - 1.34\%\mathrm{Mn} + 0.06\%\mathrm{Mn}^2 - 1.75\%\mathrm{Cr} + 0.01\%\mathrm{Cr}^2 \\ & + 15.21\%\mathrm{Mo} - 5.59\%\mathrm{Si} + 26.27(\%\mathrm{C} + 1.2\%\mathrm{N})(\%\mathrm{Cr} + \%\mathrm{Mn} + \%\mathrm{Mo})^{1/2} \\ & + 0.61[\%\mathrm{Ni}(\%\mathrm{Cr} + \%\mathrm{Mn})]^{1/2} - 60.69(\%\mathrm{C} + 1.2\%\mathrm{N})^{1/2} \end{aligned} \quad (2.3)$$

2.3.3 Mechanical Properties of 16-7-3/6/9 Steels

The stress-strain curves of the cast steels are indicated in Fig. 2.4. The associated mechanical properties and the $f_{\alpha'}$ values are summarized in Fig. 2.5. Analogous to M_s temperatures, M_d temperatures calculated based on $f_{\alpha'}^{\text{ind.}}$ in Fig. 2.5d reduce with raised Ni contents (120 → 60 → 30 °C). With decreasing tensile test temperature from 250 °C to M_d temperature the elongation increases (Fig. 2.5b) due to the reduced SFE, which promotes the propagation of SFs and restricts climb and cross slip of dislocations [35]. Below M_d temperature, where strain-induced α'-martensite formation can be triggered, elongation decreases as a result of the early occurrence of α'-martensite during tensile tests and the accompanied obstruction of planar dislocation motion in the austenite. Intersection points of slip bands, SFs, ε-martensite and twins may act as nucleation sites for the strain-induced α'-martensite formation.

The elongation of the 16-7-9 steel decreases first below 20 °C and then increases again when the temperature drops from −70 to −196 °C. The latter increase is related to an attenuated α'-martensitic transformation below Néel temperature (T_N), which enhances the plasticity. The influence of T_N on α'-martensite formation is discussed in detail in Sect. 2.4.3.

Owing to the presence of a high $f_{\alpha'}^{Q}$ in the undeformed condition, the 16-7-3 steel (Fig. 2.5d) exhibited almost always the smallest $f_{\alpha'}^{\text{ind.}}$ (Fig. 2.5c) but the highest total $f_{\alpha'}$ after tensile tests (Fig. 2.5d). This explains the higher ultimate tensile strength (UTS) of the 16-7-3 steel compared to 16-7-6 and 16-7-9 steels (Fig. 2.5a). The presence of 16 vol% δ-ferrite in the initial microstructure of the 16-7-3 steel might have also contributed to its higher strength as ferrite often offers a higher strength than austenite. In contrast, the fully austenitic 16-7-9 steel provides the lowest tensile strength.

At RT, the UTS and total elongation (TE) are 1013 MPa and 23% for the 16-7-3 steel, 765 MPa and 53% for the 16-7-6 steel, and 550 MPa and 72% for the 16-7-9 steel, respectively. Due to the higher Ni content and SFE of the 16-7-9 steel compared to the other two steels, the α'-martensitic transformation was almost fully suppressed during testing at RT. In contrast, a pronounced TRIP effect was observed in both 16-7-3 and 16-7-6 steels. The products of UTS and TE are 23.3, 40.5 and 39.6 GPa% for the 16-7-3, 16-7-6, and 16-7-9 steels, respectively.

To examine the formability of steels at RT, an austenitic cast steel with a chemical composition similar to the 16-7-6 steel, namely X4CrMnNi16-7-7, was cold rolled in 22 passes to reduce the thickness from 14.3 mm to 0.7 mm. The total reduction

Table 2.3 M_s temperatures and SFE based on (2.3) for 16-7-3/6/9 steels [31]

Steel ID	M_s (°C)	SFE at RT (mJm^{-2})
16-7-3	61	10
16-7-6	1	16
16-7-9	−47	22

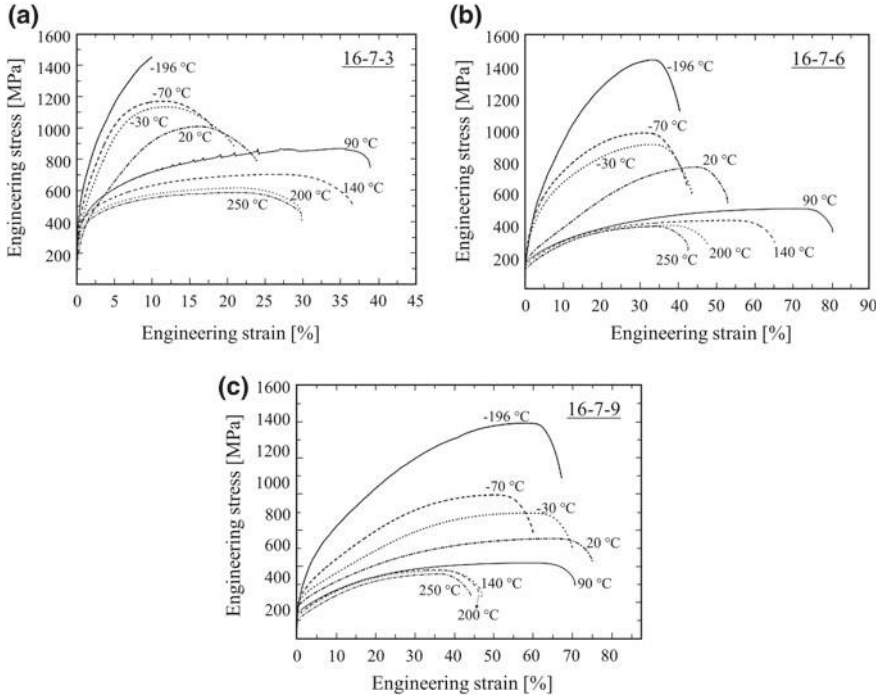

Fig. 2.4 Stress-strain curves of **a** 16-7-3, **b** 16-7-6, and **c** 16-7-9 steels tested at various temperatures [31]

ratio was 95%. Between consecutive passes, the steel was allowed to cool down to RT. As shown in Fig. 2.6a, the TRIP effect occurred already in the second pass. After the final pass, 21 vol% strain-induced α'-martensite was formed, which increased the hardness from 143 to 515 HV. In spite of its coarse cast dendritic microstructure, the ingot could be successfully rolled without any intermediate annealing.

The outstanding mechanical properties of the cast steels of the present study, regardless of their cast microstructure which is usually characterized by a coarse grain size and poor ductility [36], can be attributed to the low SFE of the steels ranging between 10 and 22 mJm^{-2}. At these SFE values, plastic deformation proceeds by planar glide of partial dislocations and may be aided by TRIP/TWIP effects. The formation of deformation bands, strain-induced α'-martensite and mechanical twins fragments the coarse cast structure and decreases the grain size of the initial austenite. They serve as obstacles to dislocation motion and hence, reduce the dislocation mean free path. The associated enhanced strain hardening postpones the necking of the material according to the Considère criterion. In this way, the drawback of a coarse cast structure is partly compensated.

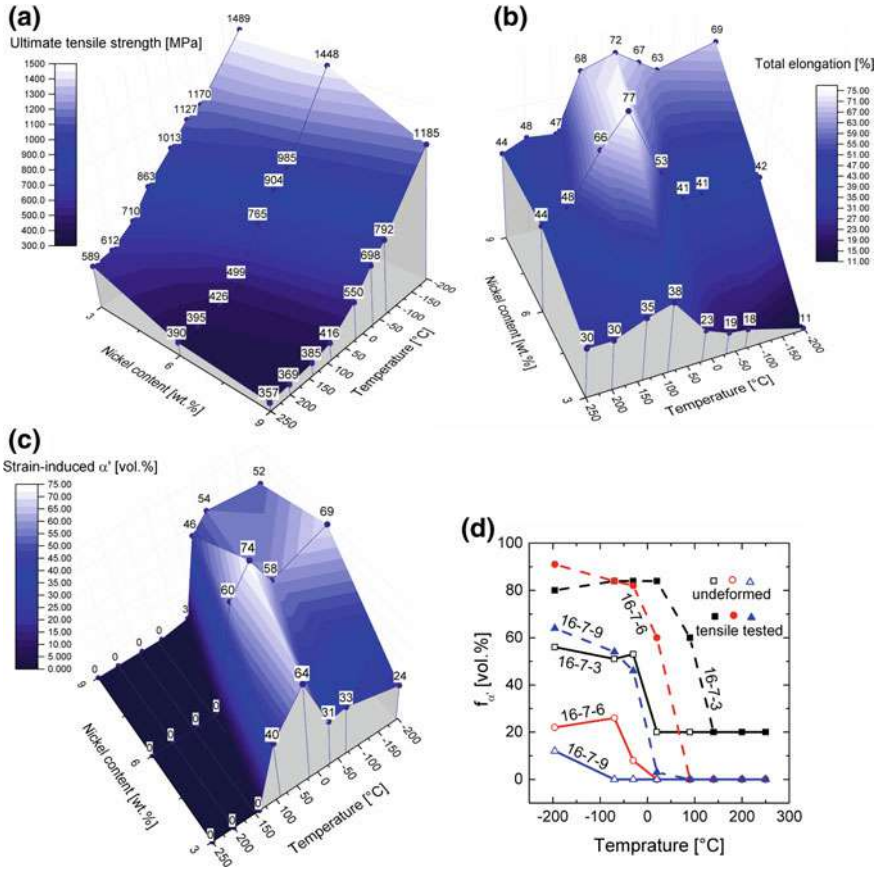

Fig. 2.5 **a** UTS, **b** TE, **c** $f_{\alpha'}^{\text{ind.}}$, and **d** $f_{\alpha'}^{Q}$ (open symbols) and total $f_{\alpha'}$ after tensile tests (solid symbols) at various Ni contents and temperatures

2.3.4 *Conclusions for the 1st Generation Steels*

The mechanical properties of the 1st generation cast stainless steels consisting of X3CrMnNi16-7-3/6/9 were investigated in the temperature range of −196 to 250 °C. In general, all steels exhibited a tensile behavior typical for austenitic steels with deformation-induced plasticity mechanisms. At decreasing tensile temperatures, the tensile elongation increases to a peak value before it reduces at temperatures below $M_d^{\gamma \rightarrow \alpha'}$. The temperature corresponding to the peak elongation decreases at higher Ni content. In addition, the grain fragmentation resulting from the formation of deformation bands, strain-induced α'-martensite and mechanical twins compensates the disadvantages of the coarse cast structures in the studied steels and results in their excellent mechanical properties at RT.

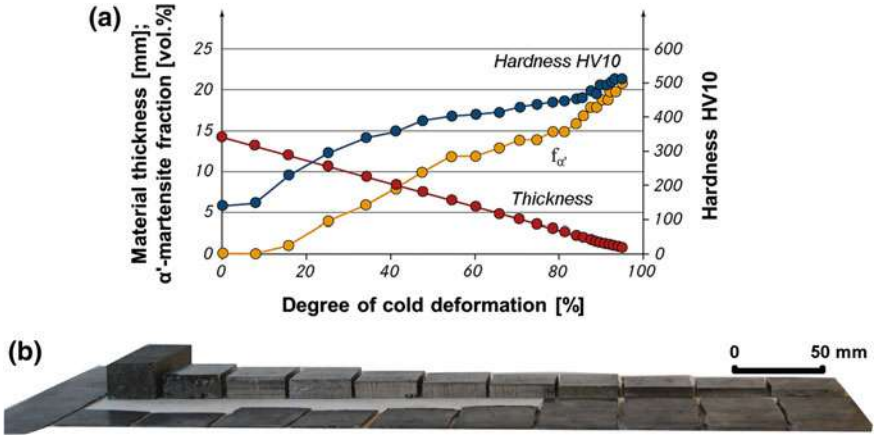

Fig. 2.6 **a** The variation in thickness, $f_{\alpha}{}'$ and hardness of an X4CrMnNi16-7-7 cast ingot during 22 passes of cold rolling; **b** Pictures showing thickness reduction during rolling [37]

2.4 Austenitic CrMnNi–C–N Cast Steels

Although the steels studied in the first period, especially 16-7-6, provide excellent strength-ductility combination, their strength level at RT remains low (below 1000 MPa). Therefore, the target for the 2nd generation was to achieve a high strength, especially yield strength (YS), by the addition of interstitial alloying elements to make use of their solid solution strengthening effect as well as precipitation hardening by the formation of carbides, nitrides and carbo-nitrides. To counterbalance the austenite stabilizing effect of interstitial alloying, the substitutional contents were modified to facilitate the occurrence of TRIP effect during plastic deformation.

2.4.1 Constitution and Special Methods

Two series of steels with compositions shown in Tables 2.4 and 2.5 were produced. In both series, the N content is maintained nearly constant (target N contents of either 0.10 wt% in Series I and 0.15 wt% in Series II) while C contents are varied between 0.05 and 0.25 wt% in steps of 0.05 wt%. To achieve high N contents of nearly 0.15 wt% in Series II, their Cr contents were raised to 19 wt% to increase the N solubility in the liquid steel [38]. In short, Series I steels with the designation X(0.05-0.25)CrNiMnN15-3-3 are denoted as Cr15NC10.X and Series II steels with the designation X(0.05-0.25)CrNiMnN19-4-3 are referred to as Cr19NC15.X, where X indicates the C concentration in wt% times hundred. The molten steels were cast in a copper mold with a cross section dimension of 95 × 35 mm^2.

Table 2.4 Chemical compositions of interstitially-alloyed X(0.05–0.25) CrNiMnN15-3-3 steels in wt% and the respective SFEs based on (2.1) [39]

Steel	Steel ID	Cr	Ni	Mn	Si	N	C	SFE (mJm^{-2})
Cast X5CrNiMnN15-3-3	Cr15NC10.05	14.90	2.86	3.11	0.51	0.103	0.052	12
Cast X10CrNiMnN15-3-3	Cr15NC11.10	15.20	2.89	3.20	0.48	0.107	0.100	14
Cast X16CrNiMnN15-3-3	Cr15NC12.16	14.90	2.91	2.97	0.53	0.122	0.155	18
Cast X20CrNiMnN15-3-3	Cr15NC11.20	15.10	3.23	2.99	0.49	0.106	0.200	20
Cast X25CrNiMnN15-3-3	Cr15NC13.25	14.90	3.03	3.02	0.57	0.132	0.250	24

Table 2.5 Chemical compositions of interstitially-alloyed X(0.05–0.25) CrNiMnN19-4-3 steels in wt% and the respective SFEs based on (2.1) [19]

Steel	Steel ID	Cr	Ni	Mn	Si	N	C	SFE (mJm^{-2})
Cast X5CrNiMnN19-4-3	Cr19NC14.05	18.90	4.02	2.90	0.53	0.140	0.051	14
Cast X10CrNiMnN19-4-3	Cr19NC15.10	19.20	3.97	3.09	0.53	0.149	0.097	17
Cast X16CrNiMnN19-4-3	Cr19NC14.16	19.20	4.11	3.20	0.50	0.140	0.156	21
Cast X20CrNiMnN19-4-3	Cr19NC16.21	19.30	4.09	3.15	0.54	0.162	0.208	26
Cast X25CrNiMnN19-4-3	Cr19NC15.26	19.10	4.17	3.06	0.49	0.146	0.264	30

The addition of interstitial elements inevitably introduces precipitates such as $M_{23}C_6$ carbides and M_2N nitrides (M denotes Fe and Cr) during cooling of the ingots. These precipitates would reduce the solute interstitial contents of steels. Hence, the steels were solution annealed at temperatures above their full dissolution points prior to the tensile tests. The full dissolution temperatures increase at higher interstitial contents as predicted by phase diagrams in Fig. 2.7. The applied solution annealing temperatures as marked in Fig. 2.7 were chosen based on the results obtained by dilatometry and Thermo-Calc. Annealing was performed for 30 min followed by water quenching to RT to suppress the re-formation of precipitates.

The influence of T_N temperature on the α'-martensite formation was investigated using Cr15NC10.X steels. T_N of the alloys were calculated by extrapolating the available thermodynamic database of Thermo-Calc version S [40] to temperatures below RT. The sensitivity of T_N to the C concentration was quite low. The calculated T_N temperatures were −132 °C and −128 °C for the steels Cr15NC13.25 and Cr15NC10.05, respectively. To determine the effect of the antiferromagnetic to paramagnetic transition of austenite at T_N on the formation of α'-martensite, solution annealed cylindrical specimens with a dimension of Ø6 mm × 3.5 mm were

quenched to temperatures between −196 °C and RT and held for 10 min. The spontaneous α'-martensite fractions were subsequently quantified by magnetic saturation measurements.

2.4.2 Initial Cast Microstructures of the Steel Series

The used ingot mold had a cross section of 95 × 35 mm^2 different from the 50 × 50 mm^2 employed for the 1st generation steels. The increased contact area of the liquid steel with the mold, arising from the rectangular shape of the cross section, boosted the heat dissipation into the mold and resulted in the refinement of dendrites during solidification. As indicated in Fig. 2.8, the primary dendrite spacing of the cast ingots was significantly finer than those of the 1st generation steels, leading to a less pronounced microsegregation of main alloying elements.

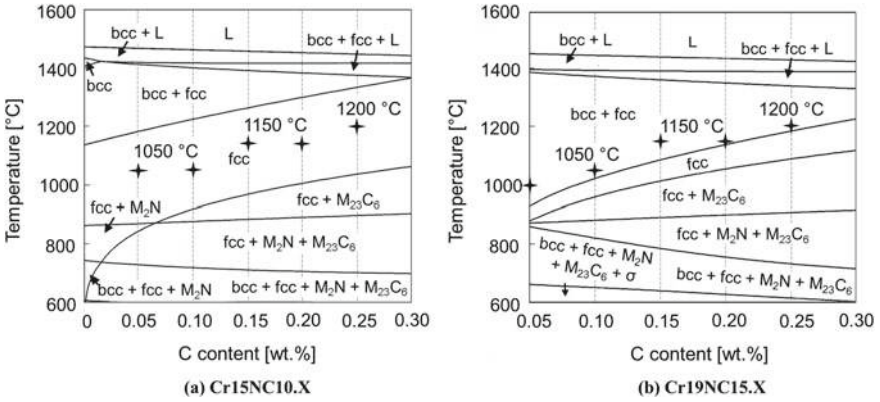

Fig. 2.7 Phase diagrams of **a** Cr15NC10.X [39] and **b** Cr19NC15.X [19] steels. Symbols indicate solution annealing temperatures prior to tensile tests

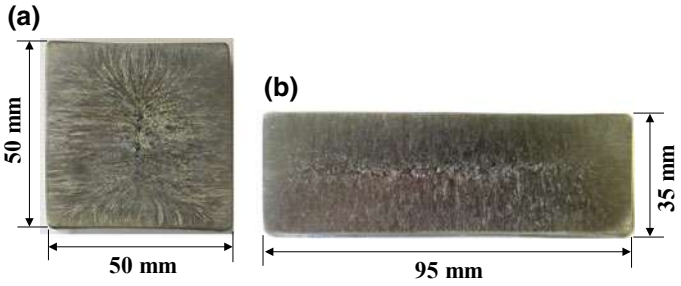

Fig. 2.8 Cross sections of **a** 16-7-6 and **b** Cr15NC11.20 cast ingots

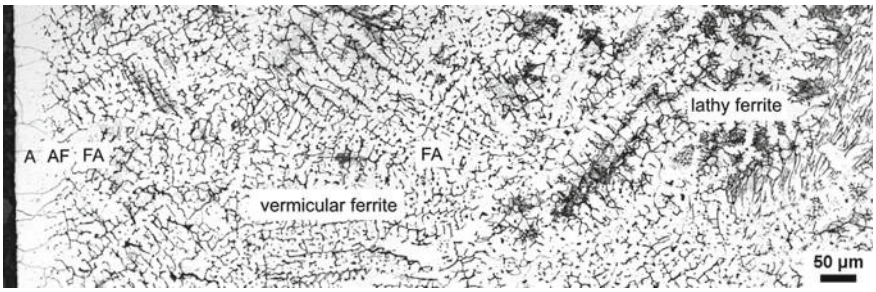

Fig. 2.9 Varied solidification mode from the outer surface (left) towards the core (right) of the Cr19NC14.16 ingot: A → AF → FA. V_2A reagent was used as etchant [19]

All the cast ingots exhibit pronounced dendritic microstructures and heterogeneous phase distribution as exemplified by Cr19NC14.16 in Fig. 2.9. At the outer layer of the ingot, due to the enormous undercooling of the melt generated by its direct contact with the cold mold, austenite forms at first with segregation of ferrite stabilizer Cr in the melt. The solidification heat release in the front reduces the undercooling of the melt. Along with the enriched Cr content in the melt, the solidification mode changes from primary Austenite (A) to Austenite-Ferrite (AF). Therefore, from the outer layer towards the center, the solidification mode varies in sequence: primary Austenite (A) → Austenite-Ferrite (AF) → Ferrite-Austenite (FA). The solidification modes were estimated according to substitutional distributions obtained from energy-dispersive X-ray spectroscopy (EDS) analysis.

The microstructures and corresponding phase fractions of the cast steels are revealed in Figs. 2.10 and 2.11. With increasing C contents, the microstructure of Cr15NC10.X steels at RT varies in sequence: $\gamma + \alpha' + \delta \rightarrow \gamma + \alpha' \rightarrow \gamma$. For the Cr19NC15.X steel, on the other hand, the sequence changes with increasing C contents from $\gamma + \delta$ to γ.

2.4.3 *Austenite ↔ α′-Martensite Transformation Behavior*

As illustrated in Fig. 2.12, the M_s, A_s, and A_f temperatures of Cr15NC10.X steels decrease all linearly at higher interstitial contents [39]. Figure 2.13 shows the $f_{\alpha'}^{Q}$ of Cr15NC10.X steels at various temperatures. With decreasing temperature, $f_{\alpha'}^{Q}$ in all steels initially increases and then decreases below a certain temperature. The transition temperatures, ranging from −81 to −141 °C as marked by crosses, are in the vicinity of T_N (between −132 and −128 °C). This phenomenon has been reported in [41]. At T_N, the magnetic state of austenite changes from paramagnetic to antiferromagnetic. This is accompanied by changes in the physical properties, such as a reduction in the elastic modulus, thermal conductivity and thermal expansion coefficient [42]. The associated magnetic ordering also reduces the entropy of austenite [43], so that the free energy of austenite increases at a smaller rate with decreasing

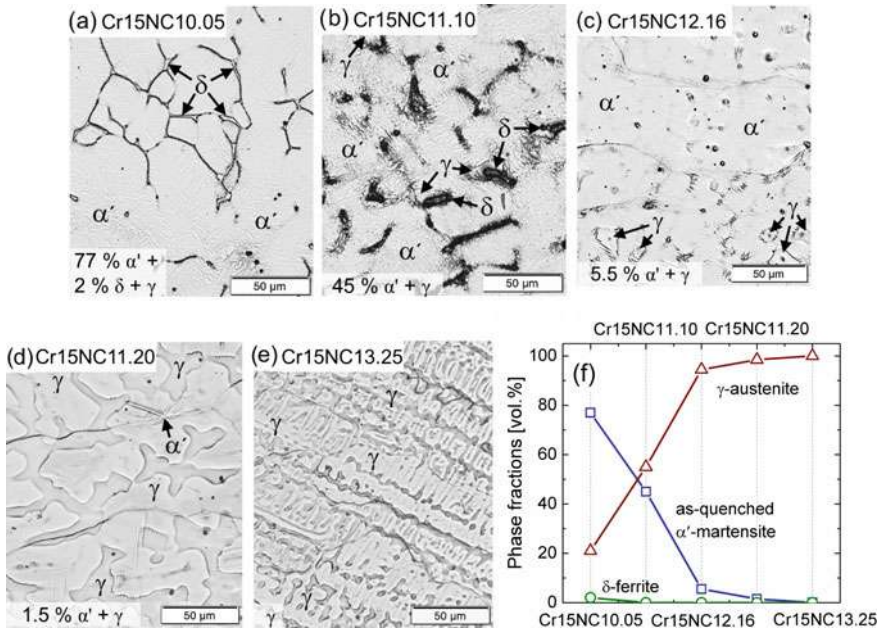

Fig. 2.10 **a**–**e** Microstructures and **f** phase fractions of cast Cr15NC10.X steels. Etchant: HNO_3 Adapted from [19]

temperature. As a consequence, the absolute difference between the free energy of austenite and α'-martensite is reduced. In other words, the chemical driving force for α'-martensitic transformation is lowered. Hence, $f^{Q}_{\alpha'}$ stops increasing even in the presence of a high austenite fraction (e.g. Cr15NC11.20). In addition, the decayed kinetics of isothermal α'-martensitic transformation [44] leads to a decrease in $f^{Q}_{\alpha'}$ below T_N. Therefore, the reduction in $f_{\alpha'}$ after passing through a peak at cryogenic temperatures can be attributed to the reduction in both the chemical driving force and the kinetics of transformation at temperatures below T_N.

For the Cr19NC15.X series, even after a cryogenic treatment in liquid nitrogen, it was not possible to introduce as-quenched α'-martensite in the solution annealed cast steels.

2.4.4 *Mechanical Properties of Cr15NC10.X Steel Series*

The stress-strain curves and associated mechanical properties are exemplified by those tested at RT and 200 °C as shown in Fig. 2.14. In Fig. 2.15, the mechanical properties and $f^{\text{ind.}}_{\alpha'}$ are presented as functions of the tensile test temperature. The M_s temperatures of steels are also marked by vertical dash-dotted lines. In most steels, YS improves from RT to 100 °C due to the precipitation of fine transition carbides

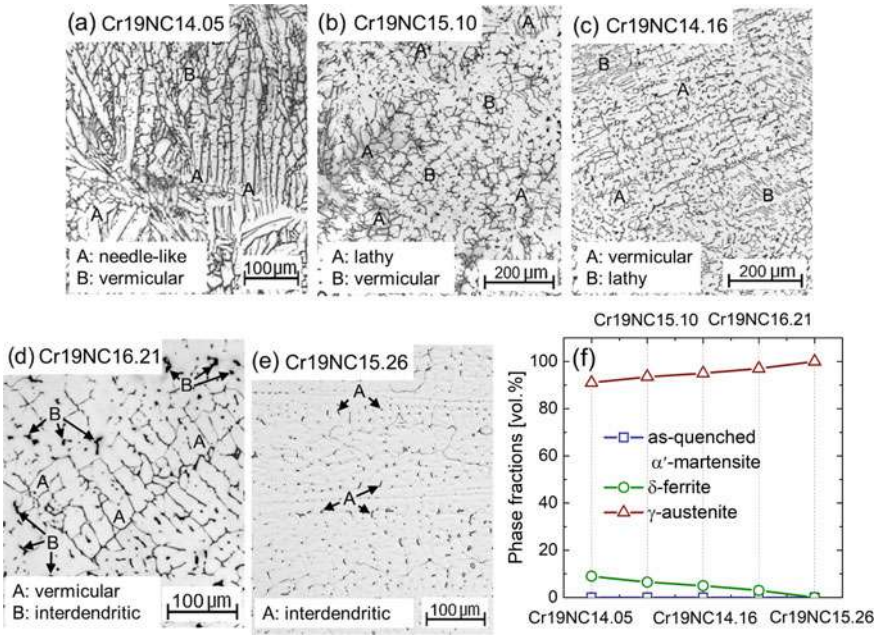

Fig. 2.11 **a**–**e** Microstructures and **f** phase fractions of cast Cr19NC15.X steels. Etchant: HNO_3. Adapted from [19]

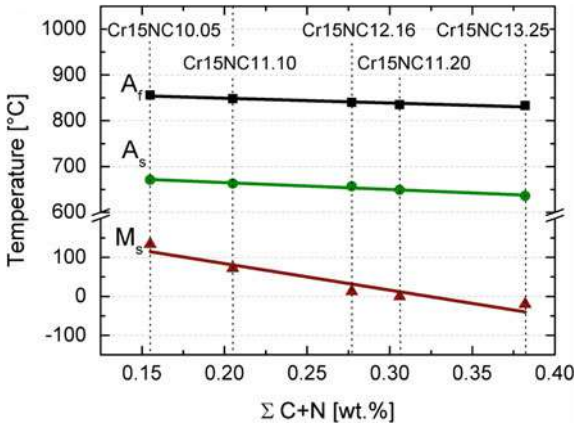

Fig. 2.12 M_s, A_s, A_f temperatures of Cr15NC10.X steels [39]

and nitrides in the α'-martensitic constituent, while TE and UE increase as a result of improved austenite stability against α'-martensitic transformation. Accordingly, $f_{\alpha'}^{\text{ind.}}$ decreases, except for the steels with 0.05–0.16 wt% C when temperature increases from −40 °C to RT. The latter variation is due to the raised $f_{\alpha'}^{Q}$ at −40 °C compared

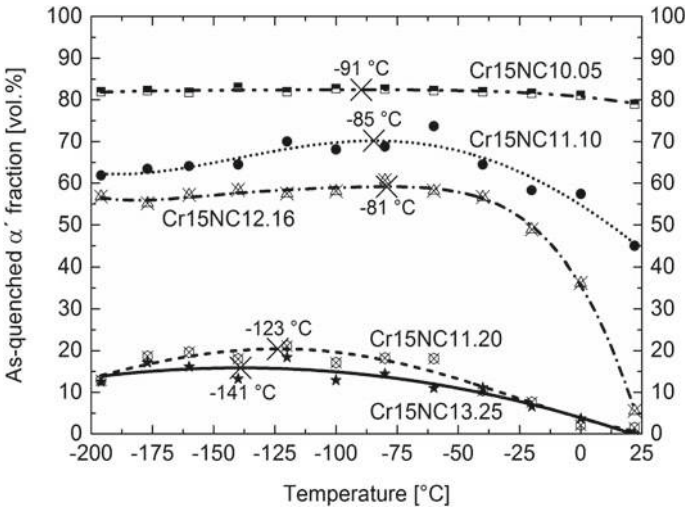

Fig. 2.13 $f_{\alpha'}^{Q}$ of Cr15NC10.X steels after holding for 10 min at various temperatures [39]. The crosses mark the temperatures associated with maximum $f_{\alpha'}^{Q}$

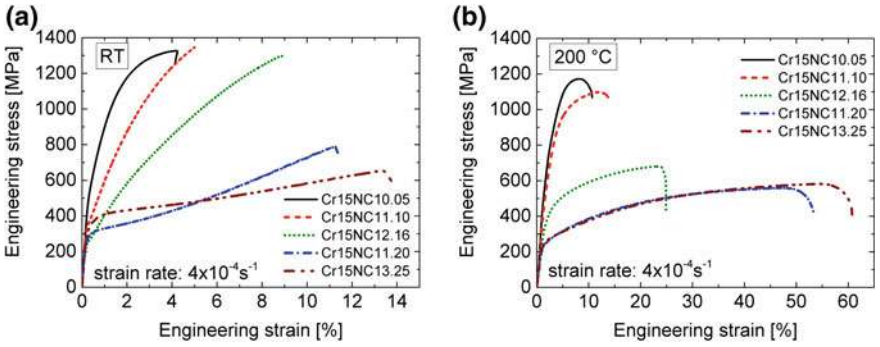

Fig. 2.14 The stress-strain curves of Cr15NC10.X steels at RT (**a**) and at 200 °C (**b**) [39]

to RT. Namely, the lower initial fractions of retained austenite at −40 °C resulted in a smaller $f_{\alpha'}^{\text{ind.}}$ than that tensile tested at RT.

The high stability of austenite at 200 °C is primarily a result of a raised SFE. Nevertheless, in alloys containing as-quenched α'-martensite such as Cr15NC10.05 and Cr15NC11.10, the thermal stabilization of austenite might have also contributed to its enhanced stability [45]. Although the temperature is too low for the long-range diffusion of C and N in the austenite, it is sufficiently high for them to diffuse from the supersaturated α'-martensite to the $\gamma - \alpha'$ phase boundaries. For instance, the diffusion distance of C in the α'-martensite is 4–20 nm at 200 °C within the timeframe of 20 min necessary for the temperature equalization of the tensile test specimens

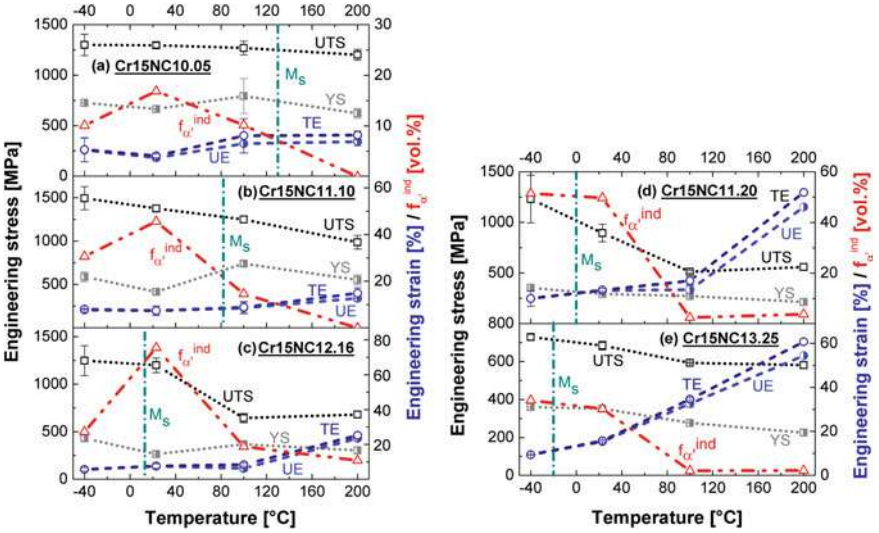

Fig. 2.15 Mechanical properties, $f_{\alpha'}^{\text{ind.}}$ and $M_s^{\gamma \rightarrow \alpha'}$ temperatures of Cr15NC10.X [19]

before tensile loading [39]. The enrichment of C atoms at phase boundaries reduces the potential nucleation sites for α'-martensite and hence, improves the resistance of austenite against α'-martensitic transformation. This effect was confirmed by quenching two solution annealed Cr15NC11.10 samples in liquid nitrogen. One of them was thermally treated at 200 °C for 20 min before quenching in liquid nitrogen. After quenching, the sample held at 200 °C showed a $f_{\alpha'}$ of only 46 vol% compared to 63 vol% α'-martensite formation in the sample without treatment at 200 °C. Due to the local interstitial content change leading to thermal stabilization of austenite, the M_d temperatures could not be determined.

2.4.5 Mechanical Properties of Cr19NC15.X Steel Series

Figure 2.16 shows the stress-strain curves of the Cr19NC15.X steels deformed at −40 and 200 °C. The S-shape curves at −40 °C imply the deformation-induced α'-martensite formation. In contrast, no noticeable increase in work hardening can be detected at 200 °C. At −40 °C, YS increases from 372 MPa at 0.05 wt% C to 413 MPa at 0.26 wt% C. This is due to the solid solution strengthening effect of C. The highest UTS of 1326 MPa combined with a TE of 44% is achieved in the case of the Cr19NC14.16 steel. In stable austenitic steels, an increase in the SFE is expected to decrease the elongation. This behavior can be justified by the dominance of wavy glide mode and the reduced planarity of dislocation glide. Nevertheless, at 200 °C, where $f_{\alpha'}^{\text{ind.}}$ equals zero in all alloys, the tensile elongation enhances as the C concentration and thereby the SFE of austenite increases [46]. Consistent with the

enhanced elongation, the ECC images of the deformed steels in Figs. 2.17a, c and e reveal a higher density of deformation bands at higher C contents.

The improved ductility at higher C contents can be attributed to the increasing segregation of substitutional elements including Cr, Mn and Ni. The higher Ni_{eq} alters the solidification mode from FA to AF [47]. For Fe–Cr–Ni alloys, the distribution coefficients between the primary δ-ferrite and the melt are 0.95–1.05 for Cr and 0.7–0.8 for Ni [48]. The distribution coefficients between the primary austenite and the melt, on the other hand, are 0.7–0.8 for Cr and 0.95 for Ni [48]. Due to the much higher Cr content of the studied steels compared to their Ni content, the change of solidification mode from FA to AF promotes the substitutional segregation, primarily Cr segregation, to the interdendritic regions. This was also confirmed by EDS analysis. The associated inhomogeneity of the chemical composition in turn leads

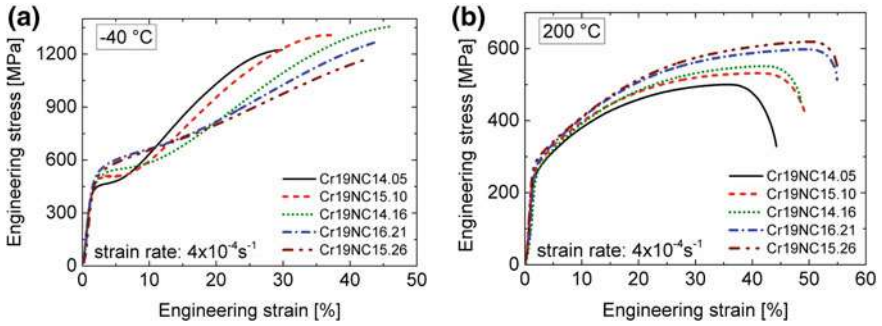

Fig. 2.16 Stress-strain curves of Cr19NC15.X steels at −40 °C (**a**) and at 200 °C (**b**) [19]

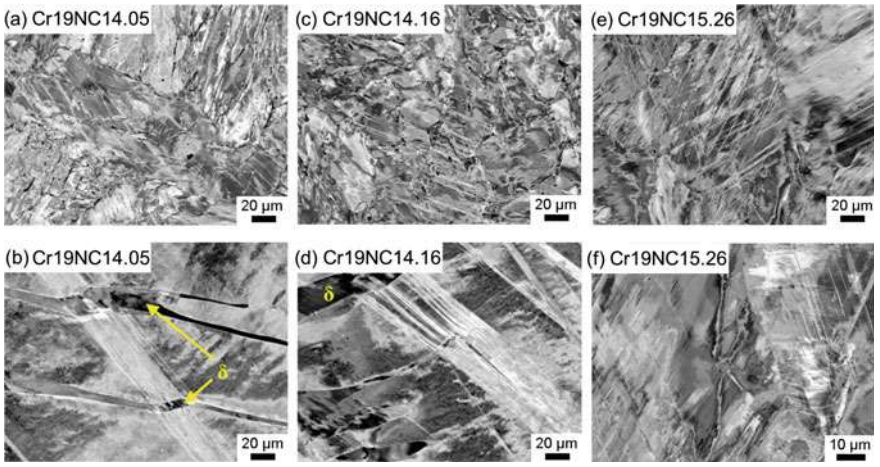

Fig. 2.17 ECC images of indicated steels strained to **a**, **b** 42%, **c**, **d** 48%, and **e**, **f** 55% at 200 °C. The samples were taken from the uniformly deformed regions in gauge section [19]

to regions with varying SFE and local variations in the plastic deformation accommodation mechanism. As shown in Fig. 2.17e for the Cr19NC15.26 steel, multiple deformation mechanisms were activated in one austenite grain. The diversification of deformation mode results in the enhanced tensile elongation.

Different interaction behavior was observed between slip bands and δ-ferrite depending on the thickness of δ-ferrite. According to Fig. 2.17b, it appears that at small thickness, although deformation bands stop at the phase boundaries, the deformation propagate to the adjacent austenite region and activate further slip bands. At high thickness (Fig. 2.17d), the strain is accommodated by the thick δ-ferrite and no further slip bands are generated in the next austenite region.

The temperature dependences of mechanical properties in Cr19NC15.X series as well as $f_{\alpha'}^{\text{ind.}}$ and M_d temperatures are summarized in Fig. 2.18. At higher temperatures, YS decreases nearly linearly, while UTS decreases with a stronger dependence on $f_{\alpha'}^{\text{ind.}}$. M_d decreases from 106 °C at 0.05 wt% C to 46 °C at 0.26 wt% C.

The maximum TE is achieved at temperatures where pronounced twinning occurs. This is exemplified in Fig. 2.19 by the Cr19NC14.16 steel tested at 60 °C and the Cr19NC15.26 steel tested at 80 °C. The elongation peaks of Cr19NC16.21 and Cr19NC15.26 steels are clearly broadened, especially Cr19NC15.26 with the maximum TE of approximately 65% at 40–80 °C. This is related to the coexistence of regions with various austenite stabilities as a result of pronounced substitutional segregation under AF solidification mode. Local variations in the stability/SFE is in turn associated with local variations in the temperature dependence of ductility. Accordingly, the overall temperature dependence of ductility is the weighted average of the different regions. This can in turn result in a broadened elongation peak. In

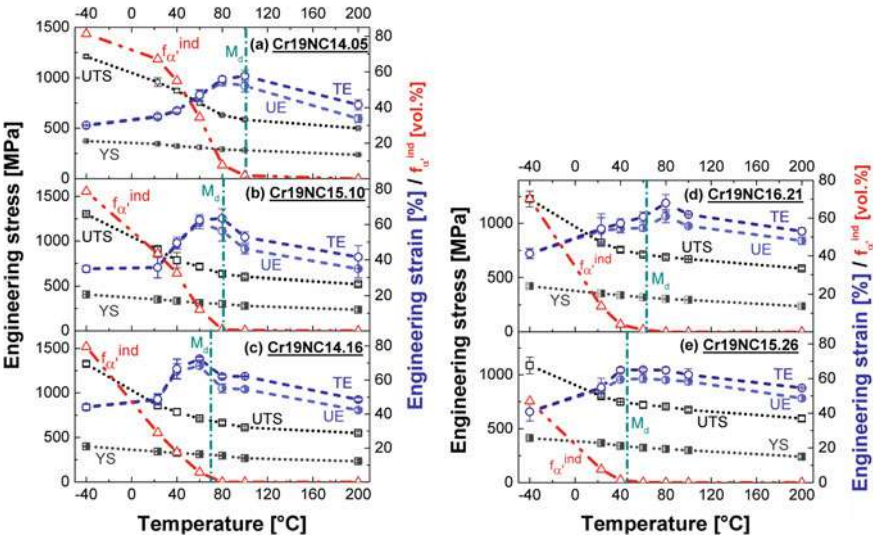

Fig. 2.18 Mechanical properties, $f_{\alpha'}^{\text{ind.}}$ and $M_d^{\gamma \rightarrow (\text{SF}, \varepsilon) \rightarrow \alpha'}$ temperatures in Cr19NC15.X [19]

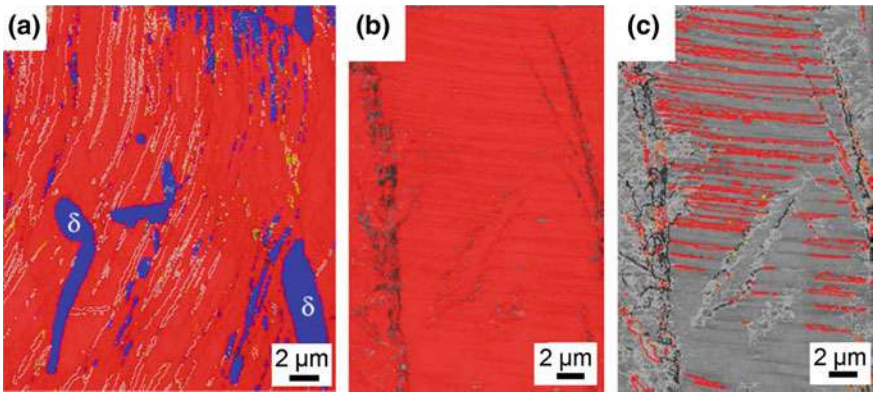

Fig. 2.19 Phase maps of **a** Cr19NC14.16 steel tested at 60 °C [28] and **b** Cr19NC15.26 tested at 80 °C [19]; **c** Map of Σ3 twin boundaries (red lines) superimposed with image quality map corresponding to the phase map in (**b**) [19]. In (**a**) and (**b**): red: austenite, blue: δ-ferrite or α'-martensite, yellow: ε-martensite, white: twin boundaries, grey: not indexed

addition, pronounced substitutional segregation in a cast Fe–14.3Cr–5.5Mn–5.5Ni–0.5Si–0.37N–0.02C steel was found to result in an enhanced ductility at cryogenic temperatures despite the occurrence of a high $f_{\alpha'}^{\text{ind.}}$ [49]. α'-martensitic transformation mostly started in the dendritic regions depleted from substitutional alloying elements. Nevertheless, the formation of fresh α'-martensite at temperatures below M_d was compensated by the enhanced glide planarity and ductility of the surrounding interdendritic regions, leading to an enhancement of TE.

2.4.6 *Conclusions for the 2nd Generation Steels*

The 2nd generation steels consist of interstitially-alloyed cast stainless steels Cr15NC10.X and Cr19NC15.X with C concentrations ranging from 0.05 to 0.25 wt%. The following conclusions were drawn:

1. Upon quenching, $f_{\alpha'}^{Q}$ stops increasing in the vicinity of T_N before the exhaustion of austenite. This is due to the decreased chemical driving force for transformation and the reduced kinetics of transformation at temperatures below T_N.
2. The phase constituents, SFE, M_s and M_d temperatures, as well as mechanical properties at RT of Cr15NC10.X and Cr19NC15.X steels are summarized in Tables 2.6 and 2.7.
3. At 200 °C, strain-induced α'-martensitic transformation was fully suppressed in Cr19NC15.X steels. Both strength and ductility enhance at increasing C concentrations. The improved ductility was attributed to more pronounced substitutional segregation generated during primary austenitic solidification.

Table 2.6 Summarized properties of Cr15NC10.X steels

X	0.05	0.10	0.15	0.2	0.25
Cast microstructure	$\gamma + \alpha' + \delta$	$\gamma + \alpha'$	$\gamma + \alpha'$	$\gamma + \alpha'$	γ
$f_{\alpha'}$ of cast (vol%)	77	45	5.5	1.5	0
SFE (mJm^{-2})	12	14	18	20	24
M_s (°C)	135	82	13	0	−20
YS at RT (MPa)	665	415	263	293	352
UTS at RT (MPa)	1296	1377	1199	895	684
TE at RT (%)	4	7	8	13	15
UTS × TE (GPa%)	5.2	9.6	9.6	11.6	10.3

Table 2.7 Summarized properties of Cr19NC15.X steels

X	0.05	0.10	0.15	0.2	0.25
Cast microstructure	$\gamma + \delta$	$\gamma + \delta$	$\gamma + \delta$	$\gamma + \delta$	γ
δ fraction of cast (vol%)	9	6.5	5	3	0
SFE (mJm^{-2})	14	17	21	26	30
M_d (°C)	100	81	70	63	46
YS at RT (MPa)	345	351	342	355	368
UTS at RT (MPa)	956	903	861	822	801
TE at RT (%)	35	36	48	54	55
UTS × TE (GPa%)	33.5	32.5	41.3	44.4	44.1

4. The prominent substitutional segregation at 0.20 and 0.26 wt% C in Cr19NC15.X also leads to the broadening of the elongation peak in the diagrams exhibiting the temperature dependent average mechanical properties.

2.5 Q&P Processing of Austenitic CrMnNi-C-N Cast Steels

The 2nd generation steels exhibit either a high YS with a low TE due to a large $f_{\alpha'}^{Q}$ (e.g. an average YS of 650 MPa and an average TE of 9% for the Cr15NC11.10 steel) or a low YS with an excellent TE (e.g. an average YS of 325 MPa and an average TE of 60% for the Cr19NC14.16 steel). Clearly, a high YS demands the presence of tempered α'-martensite. Therefore, Q&P processing was applied for the 3rd generation steels to obtain austenitic-martensitic microstructures to ensure an adequate combination of strength and ductility. Ever since its proposal in 2003 [50], Q&P processing has been widely applied to low-alloy and stainless steels [51–53]. It involves partial transformation of austenite into α'-martensite, followed by heating to a higher temperature, where the diffusion of the supersaturated C and N

from fresh α'-martensite into austenite is enabled [54]. The final microstructure consists of C-enriched austenite and C-depleted α'-martensite. Two steels with medium C contents, Cr15NC12.16 and Cr19NC14.16, were selected for the application of Q&P processing. The 3rd generation steels are denoted as AMC based on their final microstructures containing Austenite and tempered α'-Martensite with embedded Carbides.

2.5.1 Constitution and Special Methods

The Q&P processing routine for the Cr15NC12.16 steel with a composition given in Table 2.4 is illustrated in Fig. 2.20a. It involves solution annealing at 1150 °C followed by quenching to RT and subsequently to a subzero temperature above T_N to create a sufficiently high $f_{\alpha'}^{Q}$. Based on the $f_{\alpha'}^{Q}$ values presented in Fig. 2.13, −130 °C was selected for subzero quenching. The resulting microstructure consisted of 58 vol% α'-martensite and 42 vol% austenite. It was then partitioned at 450 °C for 3 min. In contrast, no α'-martensite could be obtained in Cr19NC14.16 steel (composition shown in Table 2.5) even when quenched in liquid nitrogen. Hence, α'-martensite was introduced by deformation below M_d subsequent to quenching from 1150 °C (Fig. 2.20b). The pre-strained specimens were then partitioned at 450 °C for 3 min. This process is referred to as Quenching-Deformation-Partitioning (QDP) processing. As shown in Fig. 2.18c, the steel Cr19NC14.16 possesses an M_d temperature of 70 °C. At lower testing temperatures, a smaller strain is required to generate strain-induced α'-martensite. Hence, pre-straining was performed at −40 °C. The degree of pre-straining required to induce a desirable $f_{\alpha'}^{\text{ind.}}$ was determined by a tensile test at −40 °C with in situ magnetic measurement to estimate the $f_{\alpha'}^{\text{ind.}}$ evolution according to the procedure described in [55]. In addition, interrupted tensile testes at engineering strains of 5, 15 and 25% were performed to quantify $f_{\alpha'}^{\text{ind.}}$ with ex situ magnetic measurements. The C and N enrichment in the austenite during

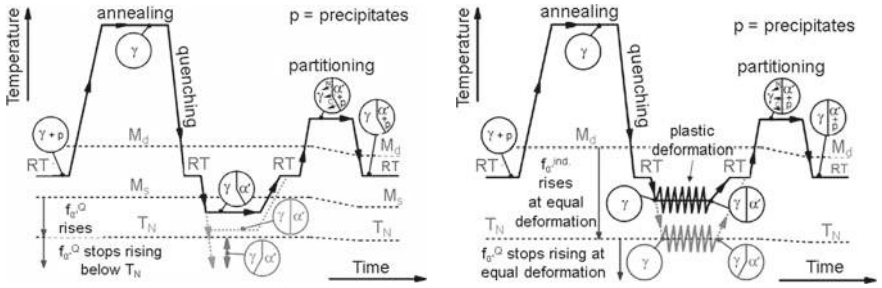

Fig. 2.20 Schematic illustrations of **a** Q&P processing for Cr15NC12.16 steel [27] and **b** QDP processing for Cr19NC14.16 steel [28]

partitioning was studied based on the variations in the austenite lattice parameter. This was done by X-ray diffraction (XRD) measurements using Cu Kα radiation in a Seifert-FPM RD7 diffractometer.

2.5.2 Q&P Processing of Cr15NC12.16 Steel

The microstructure of Cr15NC12.16 steel quenched to −130 °C is demonstrated in Fig. 2.21a. Due to the low austenite stability prior to partitioning, α'-martensitic transformation occurs during specimen preparation for metallography (preparation-induced α'-martensite), leading to a $f^{Q}_{\alpha'}$ of over 58 vol% based on an optical microscopy estimation. The remaining untransformed austenite in the micrograph represents the chemically-stabilized interdendritic regions. Based on the EDS analysis of the region marked in Fig. 2.21a as shown in Figs. 2.21b–d, elements including Cr, Mn and Ni are enriched in the austenitic regions. The segregation is most pronounced for Cr and least for Ni.

Based on the diffusion equation proposed by Ågren [56], the diffusion distance of C in austenite upon holding at 450 °C for 3 min is 693 nm. As N atoms have a higher diffusion coefficient at 450 °C than C atoms, i.e. 5.21×10^{-11} cm^2 s^{-1} versus 1.46×10^{-11} cm^2 s^{-1} [57], it is assumed, that the stabilization of austenite could be more significant by N. Substitutional elements are assumed to be immobile in both phases during the applied partitioning conditions [58]. During partitioning, M_3C carbides formed in α'-martensite, indicating a reduction in the interstitial content available for the partitioning process. Figure 2.22a shows the SAED pattern of an M_3C-type carbide in a martensitic matrix. Figure 2.22b shows a high resolution TEM micrograph of another M_3C-type carbide with a size of approximately 20 nm.

As a result of the enriched interstitial content, austenite peak profiles determined by XRD shift towards lower angles after partitioning. This is exemplified by the $(311)_\gamma$ peak in Fig. 2.23. The asymmetric peak profiles could be related to the non-uniform interstitial enrichment of austenite arising from differences in the size and distribution of austenitic regions. An increase in the solute C content by 1 at.% was

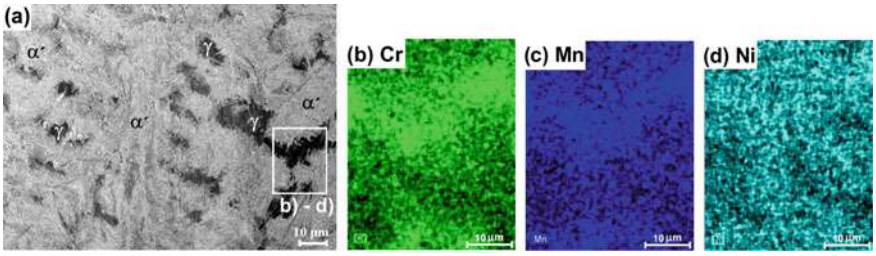

Fig. 2.21 **a** Optical micrograph of Cr15NC12.16 steel quenched to −130 °C; **b–d** Distribution of substitutional alloying elements Cr, Mn and Ni in the region demarcated in (**a**) [27]

reported to expand the austenite lattice parameter by 0.00045 nm [59]. Accordingly, assuming a similar austenite lattice dilatation effect for N, the peak shift in Fig. 2.23 implies an increase in the interstitials content of austenite by 0.1 wt%. In other words, the average interstitial content of austenite increased from 0.28 to 0.38 wt% after partitioning.

The stress-strain curves of the solution annealed steel are demonstrated in Fig. 2.24a. After Q&P processing, both UTS and TE were greatly improved (Fig. 2.24b). Because of the high tempered $f_{\alpha'}$ and the dispersed fine M_3C carbides, a YS of 1050 MPa and a UTS of 1550 MPa were achieved at RT. Furthermore, the coexistence of tempered α'-martensite with C-stabilized austenite resulted in a TE of 22% (Fig. 2.24c). The phase fractions of the tested Q&P specimens are shown in

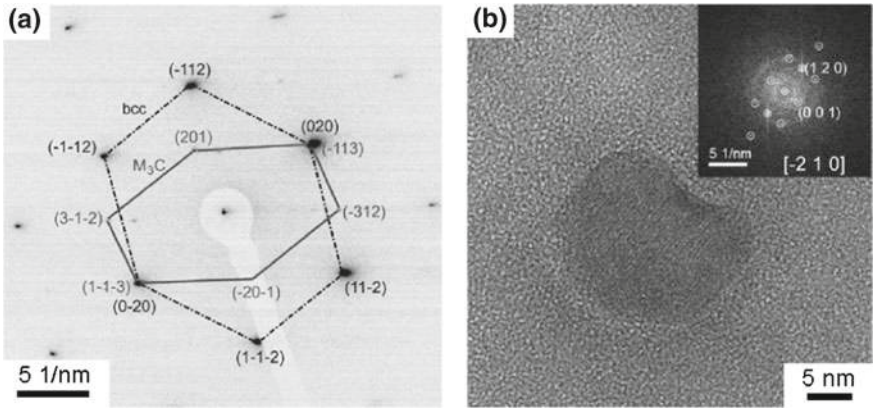

Fig. 2.22 **a** A SAED pattern of an M_3C-type carbide embedded in tempered α'-martensite. The zone axes are $[201]_{\alpha'}$ and $[17\text{-}2]_{M3C}$, respectively; **b** High resolution TEM image of an M_3C-type carbide and the corresponding FFT image with a $[-210]_{M3C}$ zone axis for the carbide [27]

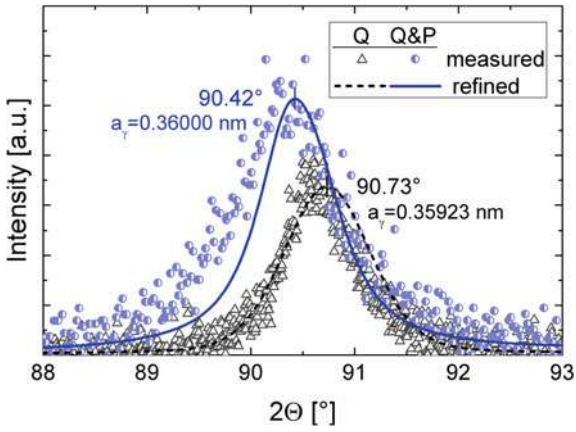

Fig. 2.23 XRD $(311)_\gamma$ peak profiles of Cr15NC12.16 in the as-quenched condition (Q) and after partitioning (Q&P) [27]

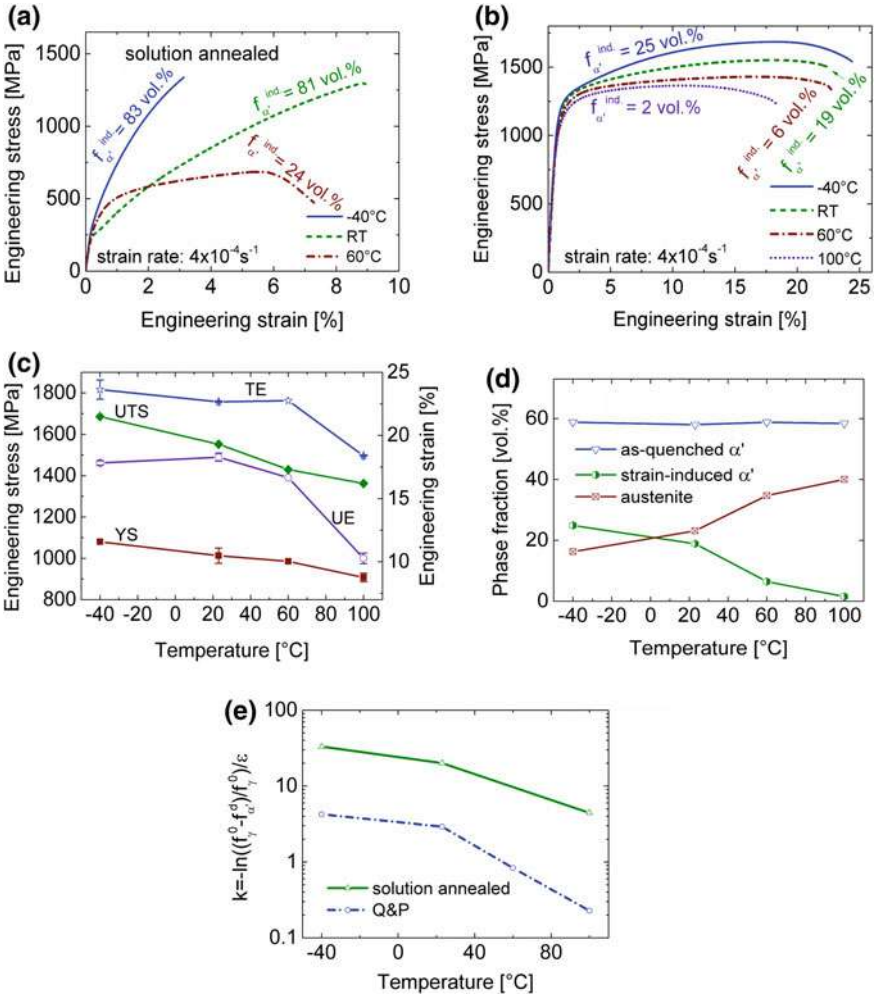

Fig. 2.24 The stress-strain curves of the Cr15NC12.16 steel in the solution annealed condition (**a**), and after quenching to −130 °C and partitioning at 450 °C (**b**); **c** average mechanical properties and **d** phase fraction evolution of AMC Cr15NC12.16; **e** mechanical stability of austenite in the solution annealed and Q&P conditions [27]

Fig. 2.24d. The formation of strain-induced α'-martensite inside the austenite deformation bands and at their intersections reduces the mean free path of dislocations (Fig. 2.25a) and hence, improves the strength as well. This justifies the increase in the strain hardening rate at lower temperatures. Within the slip bands in the austenite deformed at 60 °C (Fig. 2.25b), less α'-martensite was formed compared to that tested at RT. At 100 °C with $f_{\alpha'}^{\text{ind.}}$ equal to zero, the strain hardening rate is relatively low.

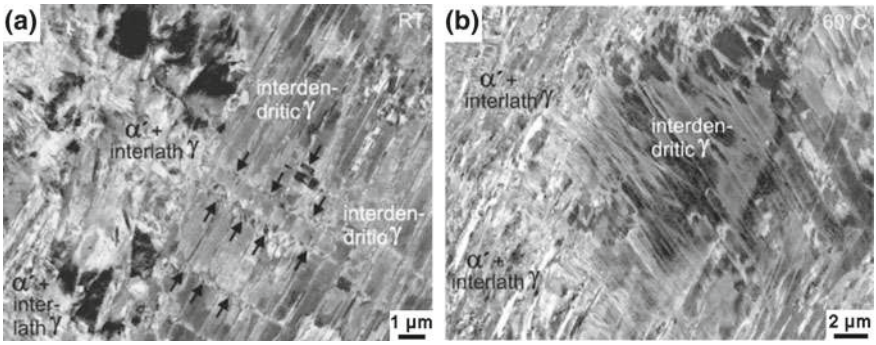

Fig. 2.25 ECC images of AMC Cr15NC12.16 steel tensile tested at RT (**a**) and 60 °C (**b**) [27]. The arrows mark strain-induced α'-martensite platelets in the deformation bands

The average mechanical stability of austenite was quantified using the following equation proposed by Sugimoto et al. [60]:

$$k = -\ln\left(\left(f_{\gamma}^{\circ} - f_{\alpha'}^{\text{ind.}}\right)/f_{\gamma}^{\circ}\right)/\varepsilon \tag{2.4}$$

where, f_{γ}° is the initial austenite fraction, ε is the applied true strain, and k is a parameter that is inversely proportional to the mechanical stability of austenite. k calculated using global strain is shown in Fig. 2.24e. The enriched interstitial contents after partitioning indeed improved the austenite stability as confirmed by a much smaller k in the Q&P condition. The mechanical stability at −40 °C in partitioned condition nearly equals that of the solution annealed steel at 100 °C.

Similar to [49], TE of the AMC Cr15NC12.16 steel increases even at temperatures below M_d, where the $f_{\alpha'}^{\text{ind.}}$ increases. This can be attributed to various austenite stabilities in the dendritic and interdendritic regions. Apart from the elemental redistribution between liquid and solid phases during solidification, Q&P Processing increases the chemical inhomogeneity and the inequality of the austenite stability in different regions. As the α'-martensitic transformation upon quenching leads to the fragmentation of austenite, the quenched microstructure consists of martensitic laths and austenitic regions with various sizes. Fine interlath austenite exhibits the highest stability against strain-induced martensitic transformation [61, 62]. Furthermore, the adjacent α'-martensite prevents them from noticeable straining during tensile test. Apart from the morphology, small austenitic regions, especially interlath austenite with a large interfacial area with the surrounding α'-martensite, experiences a more significant interstitial enrichment during partitioning.

Figure 2.26 shows the inverse pole figures (IPF) of austenite and α'-martensite phases in the AMC Cr19NC14.16 steel tested at RT. Figure 2.26a reveals the presence of two interdendritic austenitic regions marked by ellipses, which were only partially transformed into α'-martensite, indicating their superior austenite stability compared to the surrounding dendritic regions. The strong variant selection for the strain-induced α'-martensite within the marked areas in Fig. 2.26b distinguishes this type

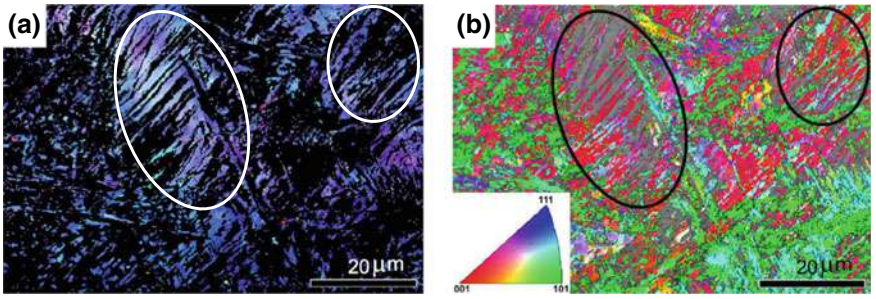

Fig. 2.26 IPF maps of (**a**) austenite and (**b**) α'-martensite in AMC Cr15NC12.16 tested at RT with tensile direction vertical in the plane of view [27]. Colors indicate crystal directions horizontal in the plane of view

of α'-martensite from as-quenched α'-martensite, which often consists of a larger number of α'-martensite variants.

2.5.3 QDP Processing of Cr19NC14.16 Steel

$f_{\alpha'}$ evolutions during tensile testing at −40 °C of the solution annealed Cr19NC14.16 steel were quantified by in situ and ex situ magnetic measurements. As shown in Fig. 2.27a, both types of results are in reasonable agreement. Using these data, the coefficients α and β in the equation proposed by Olson and Cohen for the evolution of $f_{\alpha'}^{\text{ind.}}$ were determined [63]. With the exponent n equal to 4.5 [64], α and β were fitted to be 7.49 and 2.09, respectively. Engineering strains of 0.15 and 0.25, associated with 25 and 56 vol% strain-induced α'-martensite, respectively, were selected for the pre-straining of the solution annealed Cr19NC14.16 steel at −40 °C. The two QDP steels are accordingly denoted as QDP_15% PS and QDP_25% PS. The pre-strained

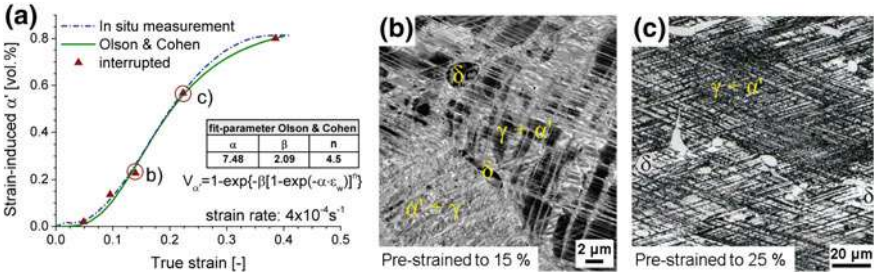

Fig. 2.27 **a** $f_{\alpha'}^{\text{ind.}}$ evolution during the tensile testing of the solution annealed Cr19NC14.16 steel as quantified by in situ and ex situ magnetic measurements and an Olson-Cohen fit to the data using the listed fitting parameters; **b**, **c** ECC images corresponding to engineering strains of 0.15 and 0.25 [28]

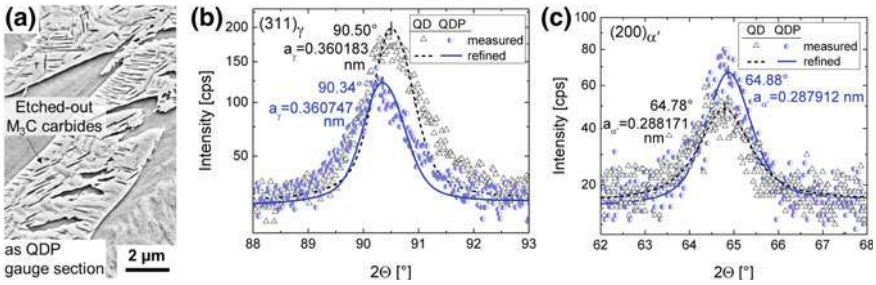

Fig. 2.28 **a** SEM image of electrolytically-etched α'-martensite in the final microstructure of the QDP_25% PS Cr19NC14.16 steel; **b** $(311)_{\gamma}$ and **c** $(200)_{\alpha'}$ peak profiles before and after partitioning [28]

microstructures are shown in Fig. 2.27b, c. In both conditions, a high density of slip bands are visible on multiple sets of {111} glide planes with α'martensite present within the bands and at their intersections.

Subsequent to partitioning, M_3C carbides also formed in the α'-martensite phase of the QDP AMC Cr19NC14.16 steel (Fig. 2.28a). According to $(311)_{\gamma}$ peak profiles, the interstitial content partitioned into the austenite is estimated to be 0.28 wt% for the QDP_25% PS (Fig. 2.28b). Concurrently, the depletion of interstitial contents in α'-martensite results in the shift of its $(200)_{\alpha'}$ peak to a higher angle (Fig. 2.28c).

In Fig. 2.29, the stress-strain curves of the AMC Cr19NC14.16 steel are compared with those in the solution annealed condition (quenched to RT). Due to the absence of α'-martensite formation during tensile tests, the solution annealed steel provides a generally low tensile strength, except at −40 °C. TE of the solution annealed steel ranges from 44 to 73%. With the introduction of α'-martensite and a subsequent partitioning, tensile strength of the AMC Cr19NC14.16 steel is clearly enhanced at the expense of tensile elongation. The premature failure of QDP_15% PS at 60 and 100 °C is associated with severe localized deformation in the transition zone from gauge section to the grip section of tensile specimens as shown in Fig. 2.30a. Based on magnetic measurements, with an applied pre-strain of 15%, strain-induced α'-martensite only formed in the gauge section, while the transition and the grip sections retained a γ-δ microstructure. The absence of α'-martensitic constituent provided no opportunity to enhance austenite stability by interstitial partitioning. Furthermore, as shown in Fig. 2.19a for the solution annealed condition, it is expected that the QDP steel exhibits a pronounced TWIP effect in the transition area at 60 °C, leading to a facilitated localized deformation and an early fracture. In contrast, the heavier pre-straining in QDP_25% PS caused strain-induced α'-martensite formation even in the gauge to grip transition zone (Fig. 2.30b). This enabled interstitial enrichment of austenite in such regions during partitioning. The associated strengthening and the enhancement of austenite stability in such regions inhibited localized deformation and premature failure of the QDP_25% PS steel at 60 and 100 °C. Compared to Q&P Cr15NC12.16, the work hardening rate of QDP_25% PS is smaller as shown in Fig. 2.29c. Its negligible work hardening can be explained on one hand by the absence

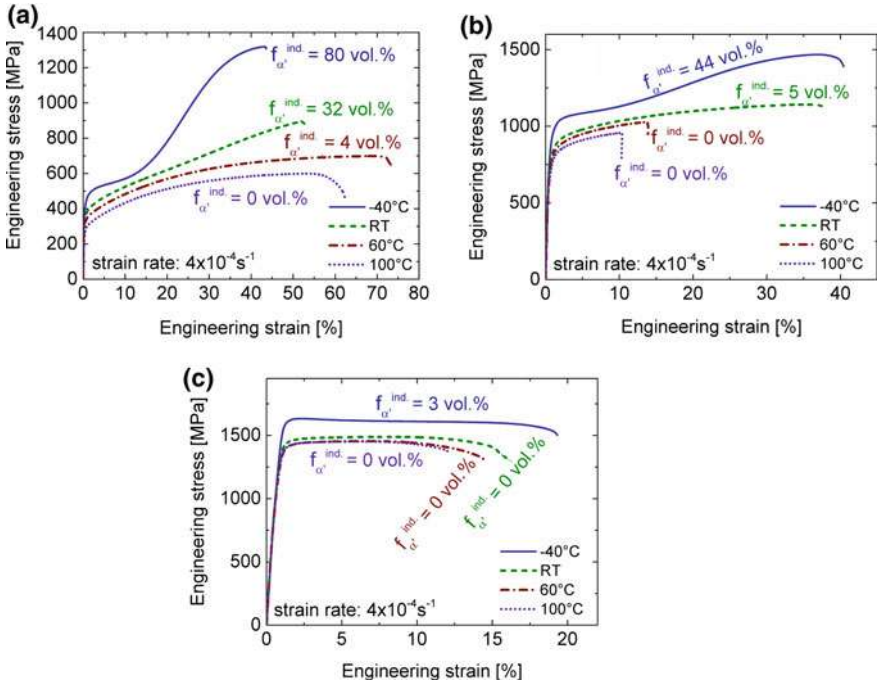

Fig. 2.29 Stress-strain curves of Cr19NC14.16 steel in various conditions [19, 28]: **a** Solution annealed and quenched to RT; **b** QDP_15% PS; **c** QDP_25% PS

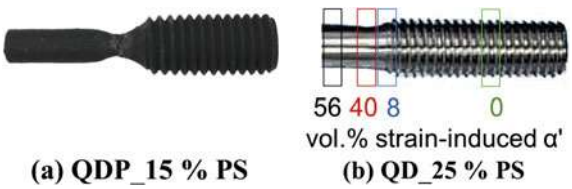

Fig. 2.30 Tensile specimens of **a** QDP_15% PS tested at 60 °C [19] and **b** QD_25% PS tested at 60 °C with $f_{\alpha'}^{ind.}$ at different areas

of $f_{\alpha'}^{ind.}$ and on the other hand by the recovery of SFs during partitioning. They were generated at −40 °C in the course of pre-straining and then narrowed/annihilated at 450 °C due to raised SFE [65]. Such constricted SFs in the pre-existing deformation bands can widen upon further deformation at lower temperatures without necessity of activating new glide systems.

The phase fraction evolution and the mechanical properties of AMC Cr19NC14.16 steel are summarized in Fig. 2.31. M_d temperature decreases from 70 °C in the solution annealed condition to nearly RT and −40 °C after QDP_15% PS and QDP_25% PS processing, respectively. The lower M_d of the latter can be attributed to the higher interstitial enrichment in the austenite due to a larger $f_{\alpha'}^{ind.}$.

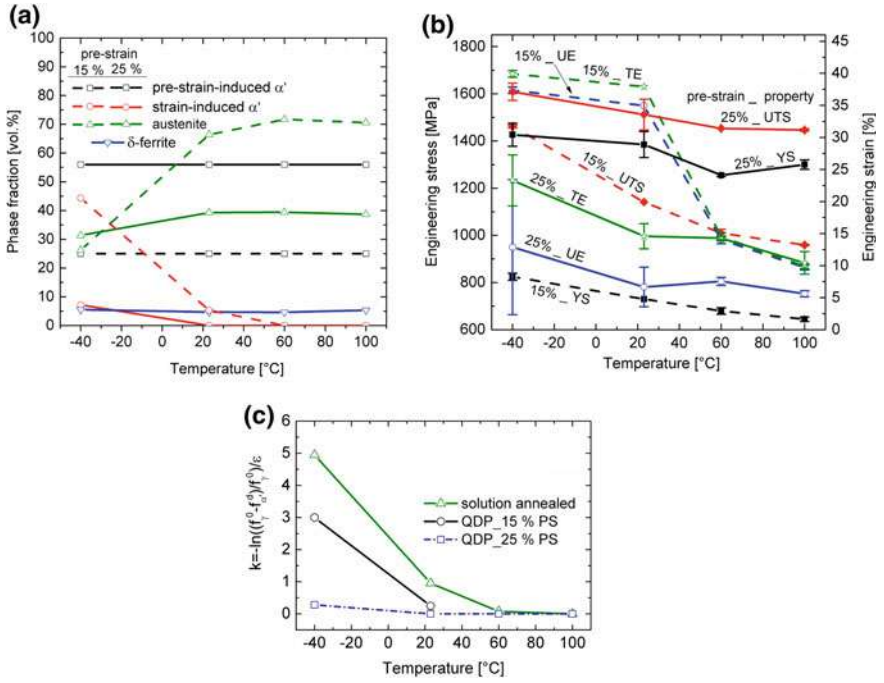

Fig. 2.31 **a** Evolution of phase fractions, **b** mechanical properties and **c** calculated k parameter of AMC Cr19NC14.16 tested at various temperatures [19]. Due to the localized deformation in the gauge to grip transition zone, k values for QDP_15% PS at 60 and 100 °C are not given. k values for the solution annealed condition are shown for comparison

Both steels exhibit excellent tensile strength, which increases at lower temperature. QDP_15% PS steel provides a YS of 644–824 MPa and a UTS of 960–1461 MPa, while QDP_25% PS steel exhibits a YS of 1300–1426 MPa and a UTS of 1446–1608 MPa. Similar to the Q&P-processed AMC Cr15NC12.16 steel, a concurrent enhancement of tensile strength and elongation at temperatures below M_d was observed. This can be explained by the occurrence of elemental segregation during solidification and the inhomogeneous interstitial enrichment of austenite in the partitioning step. The mechanical stability of austenite, expressed in terms of the k-parameter is shown in Fig. 2.31c. Due to the occurrence of localized deformation in the transition zone, this parameter was not determined for the QDP_15% PS steel tested at 60 and 100 °C. As a result of the interstitial enrichment, the mechanical stability of austenite was significantly improved after QDP Processing.

The fracture surfaces of QDP_25% PS tested at RT and −40 °C are illustrated in Fig. 2.32. Both specimens exhibit a ductile cup-and-cone fracture surface (Figs. 2.32a, d). At RT, intensive dimples formed often around inclusions (Fig. 2.32b), especially around Al_2O_3 inclusions based on the EDS analysis. Parallel aligned dendrites were observed, such as those hundreds μm long marked by ellipses in Fig. 2.32b. Their longitudinal direction denotes their growth direction during solidification and reveals the thickness direction of the cast ingot, namely the heat

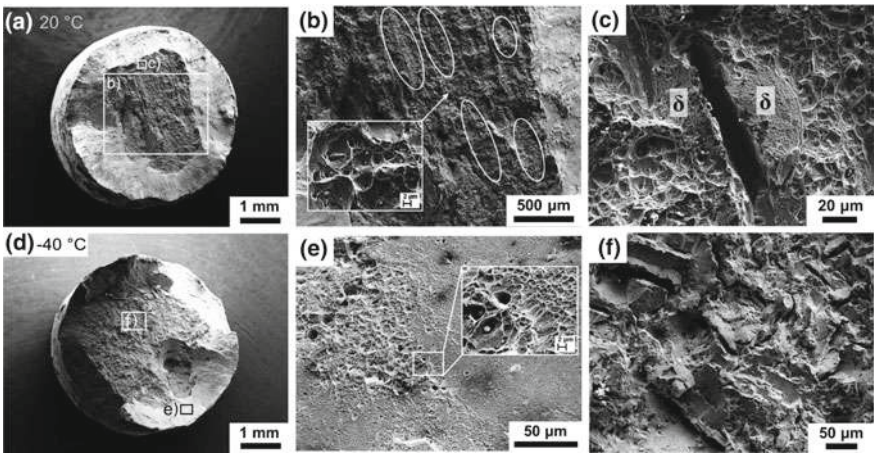

Fig. 2.32 Fracture surfaces of QDP_25% PS tested at RT (**a**–**c**) and at −40 °C (**d**–**f**) [28]: **a**, **d** overview of the entire fracture surface; **b**–**c**, **e**–**f** magnified view of the regions marked by rectangles in **a**, **b**. **b**, **e** dimples formation; **c**, **f** decohesion

dissipation direction (Fig. 2.8). Material decohesion was only observed occasionally in the central fracture region. As shown in Fig. 2.32c, the separation initiates very likely within δ-ferrite or at prior austenite/ferrite boundaries. At −40 °C, pronounced formation of dimples with various sizes was observed as well (Fig. 2.32e). Compared to the test at RT, cracks due to the decohesion at grain boundaries were more obvious as exemplified in Fig. 2.32f. This is to some extent due to the higher tensile elongation at −40 °C. In other words, the damage tolerance evaluated by the ductility was even higher than at RT, which can be ascribed to the enhanced glide planarity of austenite.

2.5.4 Conclusions for the 3rd Generation Steels

The 3rd generation steels were developed by treating Cr15NC12.16 and Cr19NC14.16 steels with tailored Q&P processing. The aim was to improve the tensile strength, especially YS, without significant loss of ductility. Following conclusions can be drawn:

1. The processing parameters and mechanical properties at RT of AMC Cr15NC12.16 and Cr19NC14.16 steels are presented in Table 2.8.
2. After partitioning at 450 °C for 3 min, M_3C carbides formed in α'-martensite, leading to an interstitial loss that competed with the interstitial enrichment in the austenite.
3. The high fractions of α'-martensite strengthened by M_3C carbides enhanced YS significantly. The YS exceeded 900 MPa for the Q&P Cr15NC12.16 and

Table 2.8 Summarized processing parameters and mechanical properties at RT of AMC Cr15NC12.16 and Cr19NC14.16 steels

Steels	Cr15NC12.16	Cr19NC14.16	
Method to create α'-martensite	Quench to −130 °C	15% pre-strain at −40 °C	25% pre-strain at −40 °C
$f_{\alpha'}$ prior to partitioning (vol%)	58	25	56
YS at RT (MPa)	1013	730	1385
UTS at RT (MPa)	1550	1141	1510
TE at RT (%)	22	38	15
UTS × TE (GPa%)	34.1	43.4	22.7

QDP_25% PS steels. The latter reaches even 1426 MPa due to the additional work hardening in the course of pre-straining.

4. After partitioning, both strength and ductility increase at lower temperatures. The enhanced ductility in spite of the formation of strain-induced α'-martensite is attributed to the chemical composition inhomogeneities, which originated from the solidification and was reinforced during the Q&P processing.
5. Deformation was mostly accommodated by the planar glide of dislocations in the austenite phase of partitioned steels. In QDP steels, the constriction of the pre-straining-induced SFs in the subsequent partitioning step and their easy separation during further deformation at lower temperatures excludes the need for activating new glide system. This leads to a negligible work hardening rate.

2.6 Conclusions

This chapter focuses on the development of cast CrMnNi stainless steels exhibiting excellent strength-ductility combination with the aid of TRIP/TWIP effect. Figure 2.33 summarizes the mechanical properties of the three generation steels presented in this chapter. The 1st generation steels include interstitial-free 16-7-3/6/9 steels with SFEs ranging from 10–22 mJm^{-2}. Regardless of their coarse cast microstructures, both 16-7-6/9 steels provided an excellent product of UTS and TE of approximately 40 GPa% due to the dynamic Hall-Petch effect by the formation of deformation bands, twins and strain-induced α'-martensite. Nevertheless, their YS was mostly below 400 MPa due to the almost fully austenitic microstructures. Therefore, interstitially-alloyed steels Cr15NC10.X and Cr19NC15.X were produced for the 2nd generation steels, aiming at solid solution strengthening, second phase strengthening by introducing as-quenched α'-martensite, and precipitation hardening. Within the studied C content range of 0.05–0.25 wt%, YS decreased and TE increased at higher C contents in the Cr15NC10.X steel series. Accordingly, YS in excess of 600 MPa was mostly accompanied by a TE of less than 10%. The

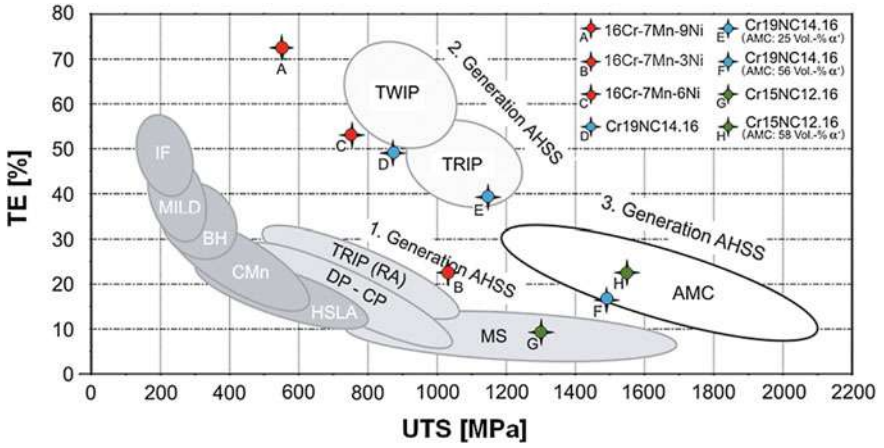

Fig. 2.33 Mechanical properties of steels presented in this chapter compared to those of advanced high strength steels (AHSS) [19]

enhanced ductility and reduced strength at higher C contents was due to the increase in the fraction and stability of austenite. Cr19NC15.X steel series with almost fully austenitic microstructures exhibited excellent ductility but YS below 450 MPa. To further enhance the YS, Q&P and QDP processing were applied to the Cr15NC12.16 and Cr19NC14.16 steels, respectively, to develop the 3rd generation steels. For the former, 58 vol% α'-martensite was created by quenching from 1150 °C to RT and then to −130 °C, while for the latter with an M_s temperature below −196 °C, 25 and 56 vol% α'-martensite were introduced by tensile straining at −40 °C to strains of 15% and 25%. Partitioning was then performed at 450 °C for 3 min. Due to the high fractions of α'-martensite with embedded fine M_3C carbides, AMC Cr15NC12.16 steel and QDP_25% PS exhibited excellent YS above 900 MPa in the temperature range of −40 to 200 °C. The QDP_25% PS steel exhibited an especially high YS of 1426 MPa at −40 °C owing to the additional work hardening in the course of pre-straining. The chemical segregation generated during solidification is intensified during Q&P processing, which results in an enhanced ductility even at tensile temperatures below M_d temperature where deformation-induced α'-martensitic transformation takes place. As indicated in Table 2.8, the product of UTS and TE at RT reaches 34, 43 and 23 GPa% for Q&P Cr15NC12.16, QDP Cr19NC14.16 with 15% and 25% pre-straining, respectively.

Acknowledgements The authors would like to thank Dr. A. Jahn for the research on the 1st generation steels. Sincere thanks are due to the colleagues at the Institute of Iron and Steel Technology (IEST) and the Institute of Materials Science (IWW) for their support and assistance on the experiments: Dr. R. Rahimi, Ms. C. Ullrich and Dr. C. Schimpf for the SEM, ECCI and XRD measurements; Dr. M. Motylenko for the TEM examinations; Mr. M. Hauser for the tensile tests with in situ magnetic measurements; Dr. T. Kreschel und Mr. G. Franke for the heat treatments; Mrs. G. Schubert for the dilatometry experiments and hardness tests; Mr. P. Neuhold for producing the steels; Mr. G. Schade for the tensile tests; Mrs. I. Grahl and Mrs. J. Kreschel for the metallographic

sample preparation and light optical microscope observations; Mr. M Block for the machining of specimens; and all the student assistants for the magnetic measurements.

This work was funded by the Deutsche Forschungsgemeinschaft (DFG, German Research Foundation)—Projektnummer 54473466—SFB 799 under the subproject A2. The financial support is gratefully acknowledged. The authors would also like to thank Prof. P. R. Scheller, the previous director of IEST, for his support on preparing the A2 subproject proposal. Special thanks are extended to all the colleagues from SFB 799 for the valuable and fruitful scientific discussions.

References

1. M. Naghizadeh, H. Mirzadeh, Metall. Mat. Trans. A **47**, 4210 (2016)
2. S.H. Bak, M.A. Abro, D.B. Lee, Metals **6**, 169 (2016)
3. E. Polatidis, W.-N. Hsu, M. Šmíd, T. Panzner, S. Chakrabarty, P. Pant, H. Van Swygenhoven, Scr. Mater. **147**, 27 (2018)
4. I. Karaman, H. Sehitoglu, Y.I. Chumlyakov, H.J. Maier, JOM **54**, 31 (2002)
5. L. Kaufman, M. Cohen, Prog. Met. Phys. **7**, 165 (1958)
6. G.B. Olson, M. Cohen, Metall. Trans. A **7**, 1897 (1976)
7. L. Rémy, A. Pineau, B. Thomas, Mater. Sci. Eng. **36**, 47 (1978)
8. F. Lecroisey, B. Thomas, Phys. Stat. Sol. (a) **2**, K217 (1970)
9. T. Yonezawa, K. Suzuki, S. Ooki, A. Hashimoto, Metall. Mat. Trans. A **44**, 5884 (2013)
10. M. Wendler, A. Weiß, L. Krüger, J. Mola, A. Franke, A. Kovalev, S. Wolf, Adv. Eng. Mater. **15**, 558 (2013)
11. A. Dumay, J.-P. Chateau, S. Allain, S. Migot, O. Bouaziz, Mater. Sci. Eng. A **483**, 184 (2008)
12. A. Saeed-Akbari, L. Mosecker, A. Schwedt, W. Bleck, Metall. Mat. Trans. A **43**, 1688 (2012)
13. D. Fahr, Dissertation, University of California, 1969
14. S. Martin, S. Wolf, U. Martin, L. Krüger, Solid State Phenom. **172–174**, 172 (2011)
15. B.C. De Cooman, O. Kwon, K.-G. Chin, Mater. Sci. Technol. **28**, 513 (2012)
16. H.-J. Kestenbach, Philos. Mag. **36**, 1509 (1977)
17. M. Pozuelo, J.E. Wittig, J.A. Jiménez, G. Frommeyer, Metall. Mat. Trans. A **40**, 1826 (2009)
18. J. Mola, in *Austenitic Stainless Steels—New Aspects*, eds. by W. Borek, T. Tanski, Z. Brytan (InTech, 2017), pp. 7–28
19. M. Wendler, Dissertation, Technische Universität Bergakademie Freiberg, 2017
20. R.E. Schramm, R.P. Reed, Metall. Trans. A **6**, 1345 (1975)
21. R. E. Stoltz, J. B. Vander Sande, Metall. Trans. A **11**, 1033 (1980)
22. T.-H. Lee, E. Shin, C.-S. Oh, H.-Y. Ha, S.-J. Kim, Acta Mater. **58**, 3173 (2010)
23. R.M. Latanision, A.W. Ruff, Metall. Trans. **2**, 505 (1971)
24. F. Lecroisey, A. Pineau, Metall. Mat. Trans. B **3**, 391 (1972)
25. F. Abrassart, Metall. Trans. **4**, 2205 (1973)
26. L. Rémy, A. Pineau, Mater. Sci. Eng. **26**, 123 (1976)
27. M. Wendler, C. Ullrich, M. Hauser, L. Krüger, O. Volkova, A. Weiß, J. Mola, Acta Mater. **133**, 346 (2017)
28. M. Wendler, M. Hauser, M. Motylenko, J. Mola, L. Krüger, O. Volkova, Adv. Eng. Mater. **21**, 1800571 (2019)
29. M. Wendler, M. Hauser, E.F. Sandig, O. Volkova, Metall. Mat. Trans. B **49**, 581 (2018)
30. A. Jahn, A. Kovalev, A. Weiß, P.R. Scheller, Steel Res. Int. **82**, 1108 (2011)
31. A. Jahn, A. Kovalev, A. Weiß, S. Wolf, L. Krüger, P.R. Scheller, Steel Res. Int. **82**, 39 (2011)
32. A. Weiss, H. Gutte, M. Radtke, P. Scheller, WO/2008/009722 (25 January 2008)
33. Q.-X. Dai, A.-D. Wang, X.-N. Cheng, X.-M. Luo, Chin. Phys. (Overseas Edition) **11**, 596 (2002)
34. A. Jahn, Dissertation, Technische Universität Bergakademie Freiberg, 2012

35. R. Rahimi, C. Ullrich, V. Klemm, D. Rafaja, B.C. De Cooman, H. Biermann, J. Mola, Mater. Sci. Eng., A **649**, 301 (2016)
36. Y. Maehara, Y.S.U. Tani, K. Gunti, Trans. ISIJ **25**, 8 (1985)
37. A. Weiss, M. Wendler, H. Gutte, H. Biermann, Int. J. Foundry Res. **65**, 2 (2013)
38. Y. Kobayashi, H. Todoroki, N. Shiga, T. Ishii, ISIJ Int. **52**, 1601 (2012)
39. M. Wendler, M. Hauser, O. Fabrichnaya, L. Krüger, A. Weiß, J. Mola, Mater. Sci. Eng. A **645**, 28 (2015)
40. J.-O. Andersson, T. Helander, L. Höglund, P. Shi, B. Sundman, Calphad **26**, 273 (2002)
41. M. Hauser, M. Wendler, O. Fabrichnaya, O. Volkova, J. Mola, Mater. Sci. Eng. A **675**, 415 (2016)
42. Y.S. Zhang, X. Lu, X. Tian, Z. Qin, Mater. Sci. Eng. A **334**, 19 (2002)
43. A. Sato, E. Chishima, Y. Yamaji, T. Mori, Acta Metall. **32**, 539 (1984)
44. G. Ghosh, V. Raghavan, Mater. Sci. Eng. **80**, 65 (1986)
45. O.N. Mohanty, Mater. Sci. Eng. B **32**, 267 (1995)
46. P.J. Brofman, G.S. Ansell, Metall. Trans. A **9**, 879 (1978)
47. J.W. Fu, Y.S. Yang, J.J. Guo, W.H. Tong, Mater. Sci. Technol. **24**, 941 (2008)
48. T. Koseki, M.C. Flemings, Metall. Mat. Trans. A **27**, 3226 (1996)
49. J. Mola, M. Wendler, A. Weiß, B. Reichel, G. Wolf, B.C.D. Cooman, Metall. Mat. Trans. A **46**, 1450 (2015)
50. J. Speer, D.K. Matlock, B.C. De Cooman, J.G. Schroth, Acta Mater. **51**, 2611 (2003)
51. R. Eckner, L. Krüger, C. Ullrich, M. Wendler, O. Volkova, Int. J. Fract. **215**, 139 (2019)
52. J. Mola, B.C.D. Cooman, Metall. Mat. Trans. A **44**, 946 (2013)
53. Q. Huang, C. Schröder, H. Biermann, O. Volkova, J. Mola, Steel Res. Int. **87**, 1082 (2016)
54. J.G. Speer, F.C. Rizzo Assunção, D.K. Matlock, D.V. Edmonds, Mater. Res. **8**, 417 (2005)
55. M. Hauser, M. Wendler, S.G. Chowdhury, A. Weiß, J. Mola, Mater. Sci. Technol. **31**, 1473 (2015)
56. J. Ågren, Scr. Mater. **20**, 1507 (1986)
57. H. Oettel, H. Schumann, *Metallografie: mit einer Einführung in die Keramografie* (Wiley, 2011)
58. L. Yuan, D. Ponge, J. Wittig, P. Choi, J.A. Jiménez, D. Raabe, Acta Mater. **60**, 2790 (2012)
59. T. Minemura, A. Inoue, T. masumoto, Trans. ISIJ **21**, 649 (1981)
60. K.-I. Sugimoto, M. Kobayashi, S.I. Hashimoto, Metall. Mater. Trans. A **23**, 3085 (1992)
61. A. Rosen, R. Jago, T. Kjer, J. Mater. Sci. **7**, 870 (1972)
62. K. Nohara, Y. Ono, N. Ohashi, Tetsu-to-Hagane **63**, 772 (1977)
63. G.B. Olson, M. Cohen, MTA **6**, 791 (1975)
64. J. Talonen, H. Hänninen, P. Nenonen, G. Pape, Metall. Mat. Trans. A **36**, 421 (2005)
65. Q. Huang, B.C.D. Cooman, H. Biermann, J. Mola, Metall. Mat. Trans. A **47**, 1947 (2016)

Chapter 3
Tailoring of Thermophysical Properties of New TRIP/TWIP Steel Alloys to Optimize Gas Atomization

Iurii Korobeinikov, Humberto Chaves and Olena Volkova

Abstract This work is dedicated to the optimization of the inert gas atomization process applied for production of steel powders. One aim is the optimization of melt parameters with the target to reduce the particle size of atomized powder. A second aim is focused on the atomization equipment optimization. In order to study thermophysical properties of steel melts the development of a new research units was accomplished: Maximum Bubble Pressure device for measurement of the surface tension and density of liquid steels and alloys, patented vibrating finger viscometer, dedicated to the investigation of low-viscosity fluids under the conditions of high temperatures and high reactivity of the studied media; density measurement cell based on the Archimedean principle for the precise estimation of steel alloys density. Then, the effect of thermophysical properties on the inert gas atomization of high-alloy steels was studied. The effects of alloying with Mn and Ni were studied as well as microalloying with S, P, Se on the surface tension and viscosity of liquid steels. Surface tension and viscosity modification of the alloys led to considerable reduction of the size of inert gas atomized powders. Alloying with N allowed finding effect on the powder phase structure.

I. Korobeinikov (✉) · O. Volkova
Institute of Iron and Steel Technology, Technische Universität Bergakademie Freiberg, Freiberg, Germany
e-mail: Iurii.Korobeinikov@iest.tu-freiberg.de

O. Volkova
e-mail: volkova@iest.tu-freiberg.de

H. Chaves
Institute of Mechanics and Fluid Dynamic, Technische Universität Bergakademie Freiberg, Freiberg, Germany
e-mail: Humberto.Chaves@imfd.tu-freiberg.de

H. Biermann and C. G. Aneziris (eds.), *Austenitic TRIP/TWIP Steels and Steel-Zirconia Composites*, Springer Series in Materials Science 298,
https://doi.org/10.1007/978-3-030-42603-3_3

3.1 Surface Tension and Density of the TRIP/TWIP Steels

The main target of the research from the very beginning was a development of new steel grades which may be used as a steel matrix of the steel-ceramic composites. The solid state subproject has developed 3 Cr–Mn-Ni steels with varying Ni content: 16%Cr7%Mn3%Ni (in Table 3.1 and further it refers to **16-7-3**), 16%Cr7%Mn6%Ni (**16-7-6**) and 16%Cr7%Mn9%Ni (**16-7-3**). As long as these 3 new TRIP/TWIP-effect steel grades were developed, the thermophysical properties of them in a liquid state had to be investigated (Table 3.1). The primary objective of such investigation is to deliver insights on the surface tension and density of the new alloys, as well as their infiltration into ceramics capabilities.

Institute of Iron and Steel Technologies (IEST) was already equipped with a high-temperature microscope capable for the measurement of wetting angle and surface tension with the classical sessile drop method. It is well known from the literature that Mn-containing steels in a liquid state intensively lose manganese due to evaporation. At the same time, classical sessile drop method features high surface to volume ratio of the investigated liquid sample. Therefore, it was decided to widen the range of applied methods for estimation of thermophysical properties of Mn-containing steels in order to have better validity of obtained results. One of the best alternative methodologies for the estimation of surface tension is a classical maximum bubble pressure technique (MBP). Among its' features are low surface to volume ratio and low sensitivity to the atmosphere around the sample.

Maximum bubble pressure technique is a well-established method for measuring of a surface tension applicable for a variety of liquids ranging from alcohols at room temperatures to liquid metals and oxides at temperatures well above their melting points. A detailed description of the technique can be found in dedicated literature [1, 2]. The main idea of the method is to measure maximum pressure in the bubble blown in the liquid. The bubble is typically blown through the capillary of a precisely defined inner diameter and with a sharpened tip. Maximum pressure of the gas inside the bubble of a defined diameter indicates the surface tension of the studied liquid. Pressure in the bubble is measured by the sensor attached to the other side of the capillary (to gas supply system). Pressure in the bubble is defined as:

$$P_{\max} = \frac{2\sigma}{r_{\text{capillary}}} + \rho * g * h \tag{3.1}$$

where σ is a surface tension, r is a radius of the bubble (inner radius of the capillary), ρ is a density of the liquid, g is an acceleration of free fall, h is an immersion depth.

The surface tension is then calculated as:

$$\sigma = 0.5 * p_{\max}(h = 0) * r_{\text{capillary}} \tag{3.2}$$

The density of the studied liquid (ρ) is calculated as a slope of the linear regression ($\Delta p_{\max}/\Delta h$) and acceleration of free fall:

Table 3.1 Chemical composition of the samples, modified after [3]

	C	Si	Cr	Mn	Ni	Al	Mo	N	O_{tot}	S	P
	%							Mass ppm			
16-7-3	0.027	0.89	15.4	7.25	3.03	0.0010	0.095	147	61	57	151
16-7-6	0.036	0.92	15.6	7.34	5.73	0.0020	0.101	167	69	80	146
16-7-9	0.035	0.95	15.9	7.37	9.20	0.0033	0.105	135	57	70	133

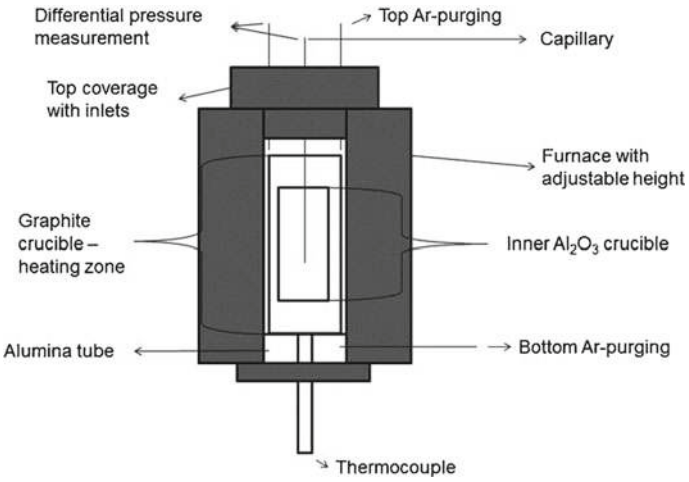

Fig. 3.1 Scheme of the maximum bubble pressure measurement cell [3, 4]

$$\rho = \frac{\Delta p_{\max}}{\Delta h * g} \tag{3.3}$$

The maximum bubble pressure unit had a scheme as shown in the Fig. 3.1. The sample is molten inside the alumina crucible placed in a graphite heating element. Graphite heating element is inductively heated by the copper coil imbedded in ceramic walls of the furnace. The inner volume of the furnace is continuously flushed with argon 5.0 (99.999% purity) from the liquid storage tank. Presence of carbon in the heating zone of the furnace ensures the elimination of the oxygen around the sample. Temperature control of the sample is executed via a thermocouple attached to the bottom of the ceramic crucible. Alumina capillary of 1.0 mm inner diameter is sealed with the zero press rings to the argon supply tube. Immersion of the capillary inside the sample is done by moving of the furnace in a vertical direction. The precision of the capillary position is controlled with 0.005 mm error with the use of WayCon system. For one temperature point a total of approximately 200 bubbles were measured—ca. 10 bubbles with a step of 1 mm between 10 and 20 mm depth along the immersion and subtraction of the capillary.

As a reference, the samples were also investigated with the use of a drop weight method. This method allows deriving the surface tension of the liquid from the weight of the droplet passing through the orifice of known diameter. Principal scheme of the measurement cell is shown on Fig. 3.2. Steel melt is pressed out of the alumina crucible through the ZrO_2 capillary by a stamp (piston) and forms a droplet on the orifice of the capillary surrounded by Ar gas (99.999% purity). As soon as gravity force exceeds the surface tension force, the droplet detaches from the capillary tip. The weight of the droplets is measured with the use of high precision balance. Thus, the (3.4) is used for the estimation of the surface tension of the sample.

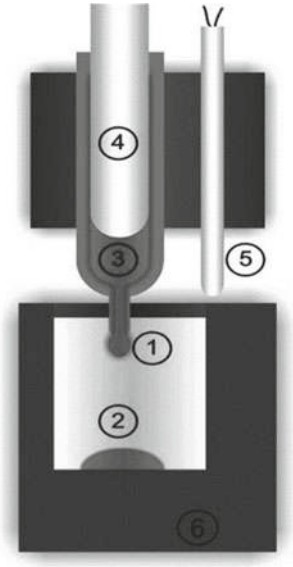

Fig. 3.2 Scheme of the drop weight method for the investigation of surface tension of liquid metals. (1) capillary, (2) crucible, (3) liquid metal bath, (4) stamp, (5) thermocouple, (6) precision balance, modified after [3]

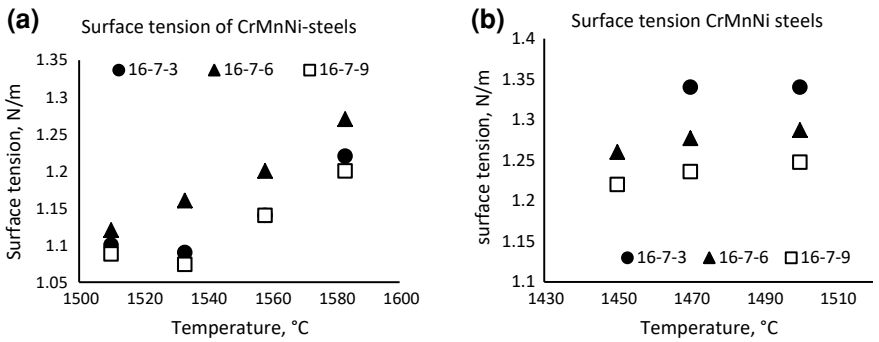

Fig. 3.3 The surface tension of Cr–Mn–Ni-steels determined by **a** the maximum bubble pressure method (MBP) and **b** drop weight method (DWM), based on [3]

$$\sigma = \frac{m * g}{2 * \pi * r * \psi} \tag{3.4}$$

where m is mass of drop, g is an acceleration of free fall, r is a radius of the drop (radius of the capillary), and ψ is a correction factor.

Experiments showed that the surface tension of the investigated alloys is relatively low—in the range of 1.1–1.3 N/m (Fig. 3.3). Drop weight method gave higher values of surface tension than MBP technique. Another significant fact revealed by this

Table 3.2 Temperature coefficient of surface tension $d\sigma/dT$ for investigated steel types, based on [3]

	MBP (Nm^{-1} K^{-1})	DWM (Nm^{-1} K^{-1})
16-7-3	$+1.7 \times 10^{-3}$	$+7.0 \times 10^{-5}$
16-7-6	$+2.0 \times 10^{-3}$	$+5.1 \times 10^{-4}$
16-7-9	$+1.7 \times 10^{-3}$	$+4.2 \times 10^{-4}$

study was that the surface tension of these alloys rose with the temperature increase (Table 3.2). Measurement with the MBP technique also delivered the first data on the density of the new TRIP/TWIP alloys (Fig. 3.4). Besides that, the wettability of samples on the ZrO_2 ceramics was investigated (Fig. 3.5).

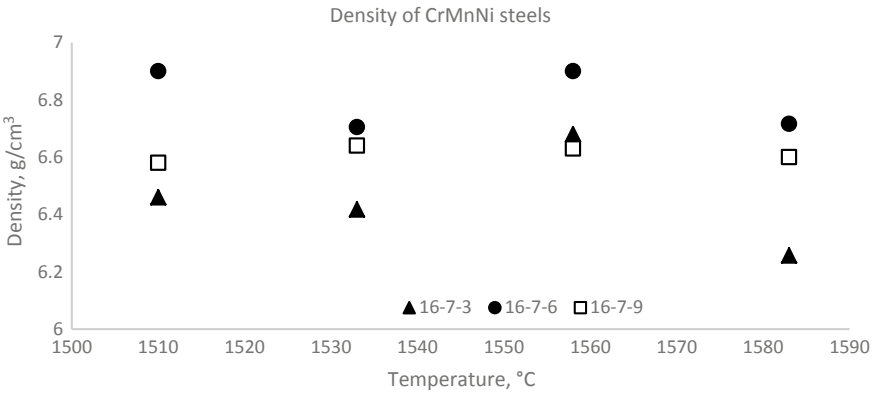

Fig. 3.4 Density of selected Cr–Mn–Ni-steels determined by the maximum bubble pressure method (MBP), based on [3]

Fig. 3.5 Wettability of investigated steel grades on ZrO_2 under Ar 5.0 atmosphere (<2 mass ppm O_2), 1550 °C; based on [3]

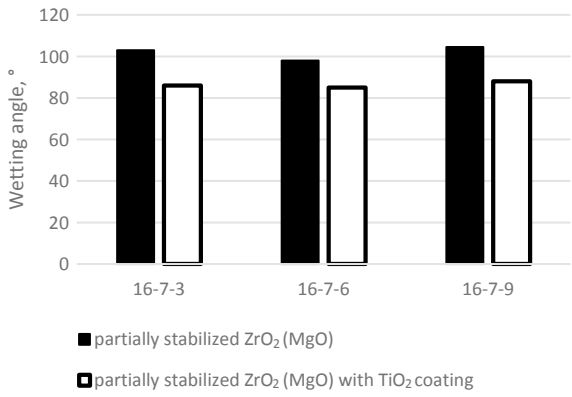

Also, maximum bubble pressure unit was tested on metallurgical slags with the excellent results what showed a capability to their measure surface tension and density [5]. In order to withstand interaction with the slag, the measurement cell was modified—the capillary and crucible were made of molybdenum.

3.2 Control of Atomization by the Thermophysical Properties of the Atomized Media

The next research focus was targeted towards investigations of various alloying options of the TRIP/TWIP steels 16-7-3, 16-7-6, and 16-7-9. Besides that, the MBP measurement cell was updated with new capillaries. Preliminary tests showed that ZrO_2 ceramic is more corrosion-resistant at high temperatures. Particular interest to this issue was paid due to substantial contents of Mn in these steel alloys.

New yttria-partially stabilized ZrO_2 capillaries were applied for the measurement of surface tension and density of the TRIP/TWIP alloys together with the reference steel grade AISI 304 and electrolytic copper. A surface tension and a density of copper and 304 steel was rather correctly estimated with the applied measurement cell. Remarkably, that a surface tension results of 16-7-3, 16-7-6 and 16-7-9 are in a good agreement with the results obtained in previous work [3] (Fig. 3.6).

This study showed the effect of nickel on the surface tension of liquid steel. Increase of nickel content from 6 to 9% led to a small decrease of a surface tension

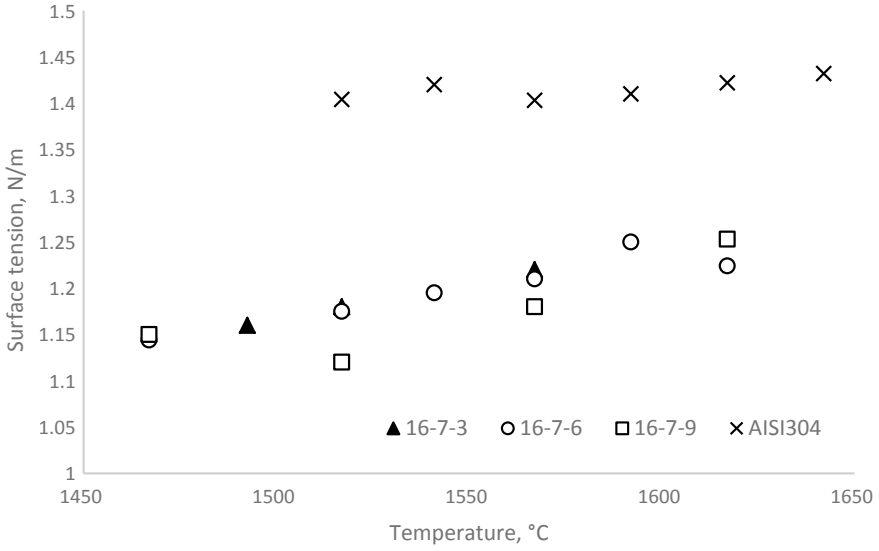

Fig. 3.6 Surface tension of and of TRIP/TWIP alloys compared to AISI 304 (Cr–Ni on the plot) steel, based on [6]

(Fig. 3.7a). Moreover, the experiments allowed to gain more accurate data on the density of the new alloys (Fig. 3.7b).

Later measurements of the surface tension of TRIP/TWIP steels have shown similar results [7]. It is a notable fact that surface tension values measured with maximum bubble pressure technique are higher than those measured with the sessile drop technique (Fig. 3.8). Simultaneously, a benchmark study was accomplished with the electromagnetic levitation technique (EML) in the DLR facility (Cologne, Germany). It allowed confirming the surface tension of TRIP (16-7-3) steel at temperatures around their liquidus line. However, the features of the EML technique

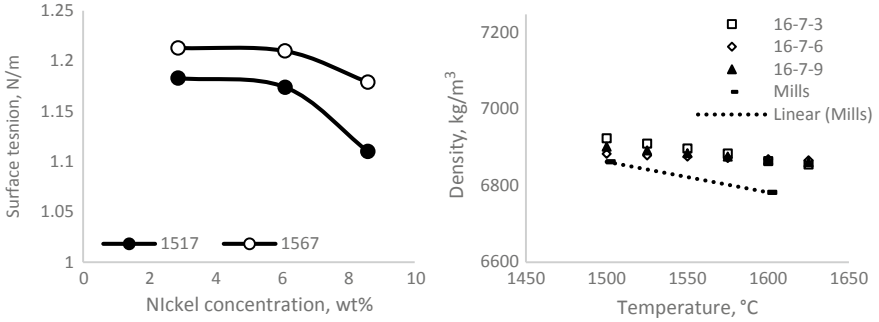

Fig. 3.7 **a** Effect of nickel on the surface tension of steel. **b** Density of 16-7-3, 16-7-6 and 16-7-9 steels measured with MBP technique, based on [6]

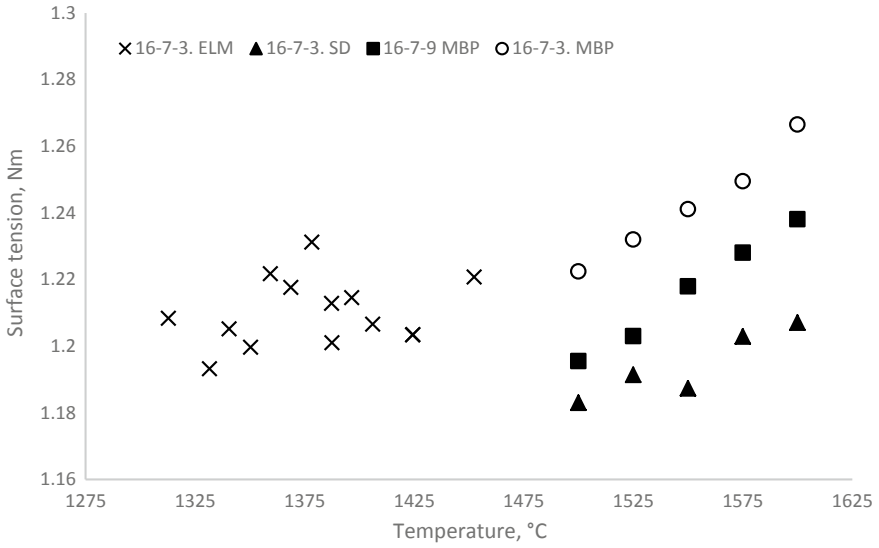

Fig. 3.8 Surface tension of 16-7-3 and 16-7-9 steels measured with maximum bubble pressure (MBP), sessile drop (SD) and electromagnetic levitation (EML) techniques, Modified after [7]

have led to severe evaporation of manganese. 16-7-3 sample has lost nearly 4 out of 7 wt% of manganese.

Chemical analysis of the samples before and after the experiments showed the remarkable loses of sulphur. This phenomenon could explain the positive surface tension coefficient.

Besides Ni, the effects of Mn, S, Se, P on the surface tension of CrNiMn alloys were investigated (Table 3.3) [8]. As can be seen in Fig. 3.9, manganese at low concentrations (until 5%) significantly reduces the surface tension of the CrMnNi alloy. Further growth of Mn concentration led to a minor surface tension reduction. Furthermore, the effect of Mn concentration on surface tension diminished with temperature increase.

Alloying with up to 0.22% phosphorus (Table 3.4) did not reveal a clear trend of the effect on surface tension. The surface tension of alloy 16-7-6 slightly rose when phosphor content increased from 0.02 to 0.05% and further remained stable (Fig. 3.10). At higher temperature (1600 °C) the surface tension of an investigated alloy deviated on ± 0.03 N/m around 1.21 N/m.

Among other surface-active elements, selenium is known for its strong effect on the surface tension of liquid iron [9, 10]. Therefore, a series of Se-microalloyed steels on base of 16-7-6 composition was prepared on VIM-12 unit (Table 3.5). Same as in case of P, Mn, and Ni, the surface tension of the alloys was measured with the MBP technique. The results of experiments, presented in Fig. 3.12, showed that even a minimum amount of Se (0.009%) led to significantly lower ST values than steel alloyed with a comparable amount of sulphur (Fig. 3.11).

3.2.1 Investigation of the Effect of Surface Tension on Inert Gas Atomization

Inert gas atomization is one of the variants of a metal powder production. Its main advantages are the sphericity, surface cleanness and controlled chemical composition of the final powder. Among disadvantages are relative complexity of the equipment and high cost of the obtained metal powders. Currently, inert gas atomization technology is the primary source of high-quality powders for the emerging metal 3d-printing industry. The principle of the gas atomization is based on the disintegration of the liquid metal stream by the gas jet/jets which is well described in the literature [11, 12]. In the present project the inert gas atomization unit VIGA-1B (ALD-Vacuum Technologies) was used. Principal scheme of the atomizer is given in Fig. 3.13. Sample of metal is inductively heated and melted in a 1 litre tundish located in the upper chamber of the atomizer. Upper chamber can provide vacuum, argon or nitrogen atmosphere. When the liquid is heated to a target temperature, the stopper rod is lifted and metal can flow thru a zirconia nozzle out of the tundish. A stream of metal meets super-sonic close-coupled confined gas jet, streaming out of the steel ring nozzle. Sprayed liquid droplets rapidly solidify while falling into the bottom of the

Table 3.3 Chemical composition of Mn-alloyed samples, modified after [8]

Alloy	C	Si	Cr	Mn	Ni	Al	Mo	N	O_{tot}	S	P
	%							ppm			
V_Mn_1	0.041	1.06	15.9	0.15	6.12	0.0202	0.060	250	36	11	170
V_Mn_2	0.046	1.04	16.0	2.95	6.02	0.0249	0.077	229	42	25	191
V_Mn_3	0.042	1.1	16.1	4.81	5.96	0.0262	0.086	231	37	102	221
V_Mn_4	0.039	0.99	16.0	9.86	5.86	0.0265	0.112	300	16	87	145
V_Mn_5	0.040	0.98	16.1	15.3	5.78	0.0160	0.192	255	25	105	190
V_Mn_6	0.072	0.81	16.3	24.8	5.73	0.0054	0.352	398	20	117	–

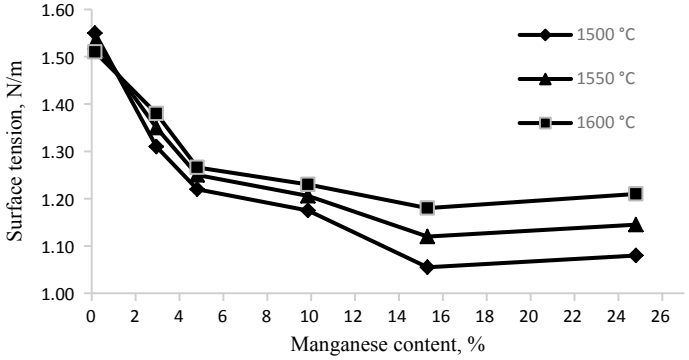

Fig. 3.9 Surface tension of CrMnNi alloy as a function of Mn content and temperature measured with MBP technique, modified after [8]

atomization vessel. After cooling of the unit, a fine powder is collected from the powder can (trap).

For the atomization of metals argon gas was used in VIGA-1B. Gas was supplied from the liquid storage tank and was re-gasified before injection into the ring nozzle. Gas pressure was 26 bar. In all the experiments the gas flow rate was kept constant and was equal to the technical maximum for the atomization unit.

The main target was to investigate the effect of thermophysical properties of the liquid alloys on the inert gas atomization. One of the easiest characteristics for modification of the molten steel is surface tension. To date, a vast amount of literature data is available on the surface-active elements, which can be applied for steel. Sulphur is known for its strong reducing effect on a surface tension of iron and iron-based alloys [10, 15]. Therefore, a series of alloys based on 16-7-9 steel was prepared with variable sulphur content in the range of 114–984 mass ppm S (Table 3.6). The surface tension of the alloyed steels was measured with the application of MBP-technique. Figure 3.11 shows that surface tension temperature curves lay substantially lower with the growth of sulphur content in the alloy. As a result, the surface tension of the 16-7-9 alloy at the target atomization temperature of 1600 °C dropped from 1250 to 1050 mN m^{-1} what was a 16% reduction.

Further these sulphur-alloyed steels together with 304 steel (which has much higher surface tension due to lower Mn-content) were atomized at a constant gas pressure and mass flow rate. Analysis of the median particle size (d_{50}) of the obtained powders (Fig. 3.14) showed a clear and strong dependence of d_{50} on the surface tension of the atomized metal.

Thus, sulphur alloying has shown a remarkable effect on the atomization. Sulphur itself is known as one of the least desirable trump element for most of the steel applications. With this regard, it was decided to check the possibility of d_{50} reduction with other surface active elements. As was given above, selenium showed further tremendous reduction of the surface tension of steel alloy with already low surface tension (Figs. 3.14 and 3.15a).

Table 3.4 Chemical composition of the samples alloyed with phosphorus, modified after [8]

	C	Si	Cr	Mn	Ni	Al	Mo	N	O_{tot}	S	P
	%							ppm			
P200	0.032	1.02	15.9	6.87	5.95	0.0234	0.078	227	17	136	182
P400	0.031	1.09	16.0	6.91	5.99	0.0152	0.077	249	27	114	423
P500	0.034	1.02	15.9	6.98	5.94	0.0096	0.081	260	16	111	505
P1000	0.031	1.09	16.0	6.90	5.90	0.0105	0.083	255	14	118	1210
P1500	0.036	0.93	15.8	7.06	6.01	0.0099	0.077	268	32	116	1600
P2000	0.033	1.00	16.1	6.92	5.80	0.0061	0.084	290	19	112	2160

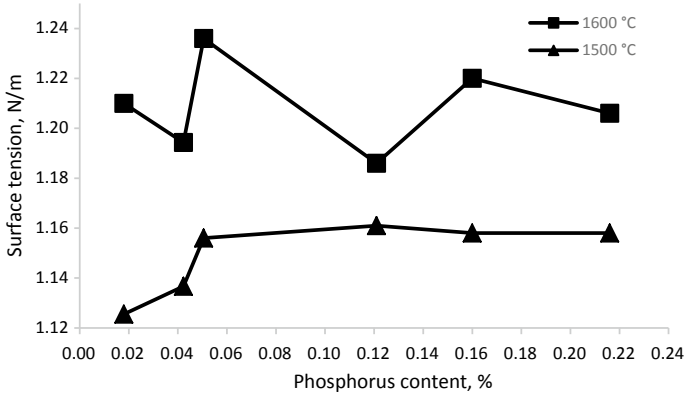

Fig. 3.10 Surface tension of CrMnNi alloy (16-7-6) as a function of phosphorus content measured with MBP technique, modified after [8]

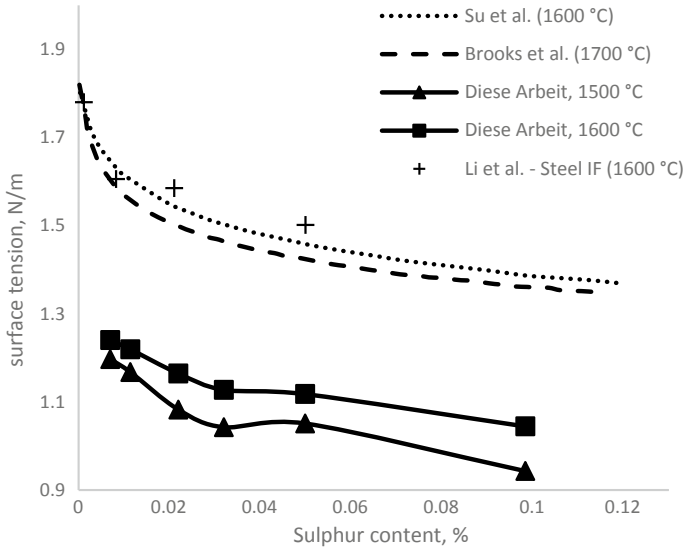

Fig. 3.11 Surface tension of 16-7-9 alloy as a function of sulphur content, modified after [8]

Results of atomizations of Se-alloyed steels showed the same trend on the reduction of median particle size due to a surface tension reduction (Fig. 3.15b). However, data points had higher scatter compared to S-alloyed powders.

Table 3.5 Chemical composition of samples alloyed with selenium, modified after [8]

	C	Si	Cr	Mn	Ni	Al	Mo	N	O_{tot}	S	P	Se
	%							ppm				
V_Se_1	0.030	0.99	16.1	6.94	5.96	0.0081	0.095	219	34	70	187	190
V_Se_2	0.028	0.98	15.8	7.06	5.94	0.0051	0.097	326	24	40	163	934
V_Se_3	0.029	1.01	16.1	7.14	5.98	0.0237	0.079	292	33	97	73	90
V_Se_4	0.023	1.00	16.1	7.02	5.96	0.0130	0.090	301	20	90	109	304
V_Se_5	0.026	1.05	16.0	6.97	6.10	0.0297	0.097	275	17	76	81	637

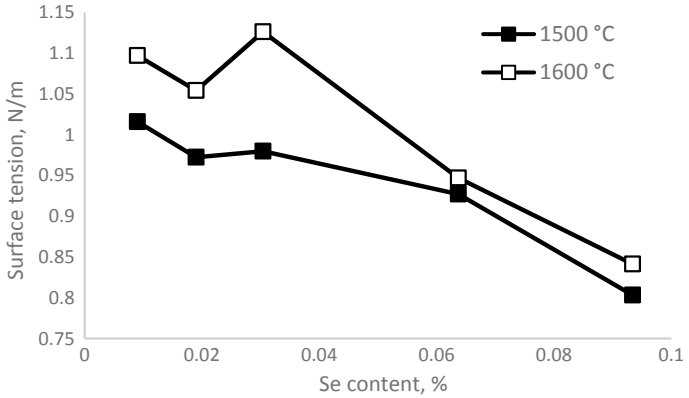

Fig. 3.12 Surface tension of 16-7-6 alloy as a function of selenium content measured with MBP technique, based on [8]

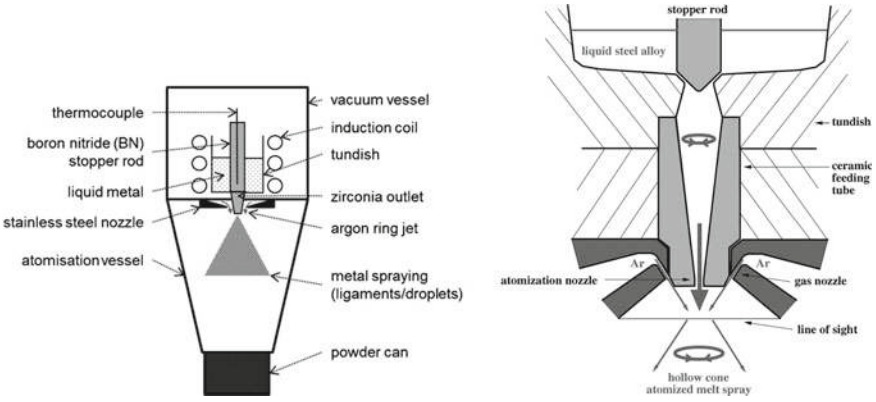

Fig. 3.13 Scheme of the inert gas atomization unit VIGA-1B [13, 14]

3.2.2 Effect of the Viscosity of Liquid Metal on the Inert Gas Atomization

It is known from literature, that atomization process is affected by the viscosity of the atomized liquid. In order to investigate this phenomenon, it was necessary to alloy the atomized steels with viscosity modifier. One of the studies accomplished in the framework of CRC 799 has indicated improvement of flowability of the phosphorus-alloyed steel [16]. Moreover, addition of phosphorus did not affect the surface tension—another parameter influencing atomization. Therefore, phosphorus was an ideal alloying element to study the modification of viscosity while other melt parameters being fixed.

Table 3.6 Chemical composition of the samples alloyed with sulphur, modified after [8]

	C	Si	Cr	Mn	Ni	Al	Mo	N	O_{tot}	S	P
	%							ppm			
16-7-9 S1	0.037	1.09	16.1	6.98	9.17	0.0063	0.082	215	21	114	111
16-7-9 S2	0.020	0.87	16.0	6.93	8.80	0.0040	0.078	222	11	220	173
16-7-9 S3	0.036	1.00	15.9	7.14	8.98	0.0063	0.084	240	9	320	71
16-7-9 S5	0.037	1.01	15.8	6.90	9.12	0.0056	0.090	214	10	499	61
16-7-9 S10	0.035	1.02	16.0	6.88	9.04	0.0049	0.080	241	14	984	36

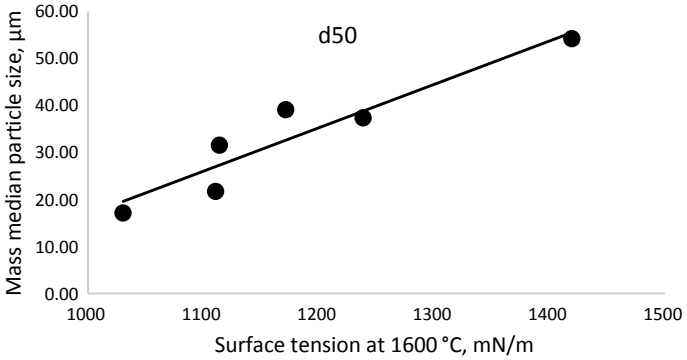

Fig. 3.14 Surface tension of sulphur-alloyed steel (**a**) and the effect of surface tension on the median particle size of the atomized powder (**b**), based on [13]

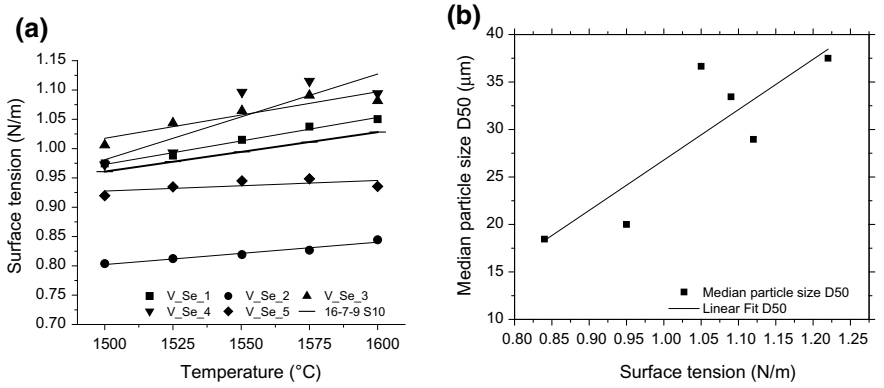

Fig. 3.15 Surface tension reduction by Se-alloying (**a**), modified after [8], the effect of surface tension on the median particle size d_{50} (**b**)

However, viscosity research required a high-precision viscosity measurement device. High precision was required in order to address even minor changes of such low-viscous liquids as molten Fe-alloys. It is known that steels have a viscosity only slightly higher than water. Beside that, it should be measured at temperatures well above 1450 °C. Additionally, alloys of interest contained 7% of Mn, what posed additional challenge to selection of materials for measurement instrument. All the above mentioned topics illustrates that the development of the viscosity measurement device was not a trivial task.

An entirely new device capable of low viscosity measurements was developed and patented [17]. Figure 3.16 shows the scheme of the unit and its' measurement head. Vibrating finger viscometer has a unique resonance oscillating head with the amplitude controlled by a laser micrometer. The amplitude is provided by the neodymium magnet excited by a field coil. As soon as a vibrating finger, attached to the oscillating

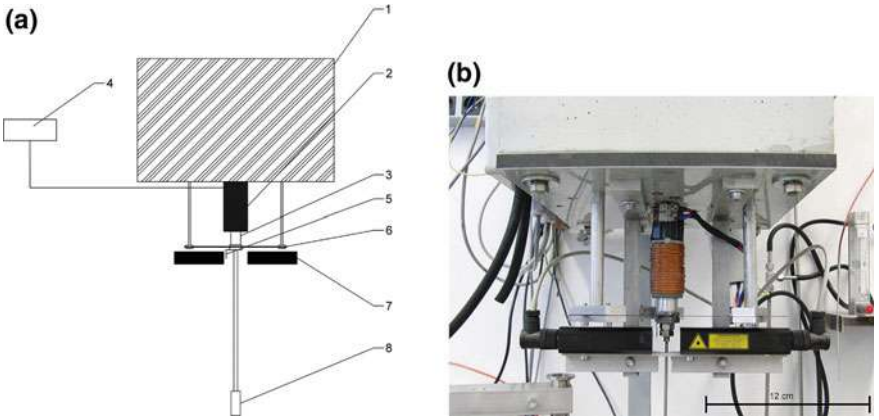

Fig. 3.16 Vibrating finger viscometer: **a** scheme of the unit, where (1) absorber, (2) field coil, (3) neodymium magnet, (4) microcontroller 12-bit ADC, (5) diaphragm, (6) spring and spring holder, (7) laser micrometer, (8) BN–ZrO_2 finger [18]; **b** appearance of the oscillating system [19]

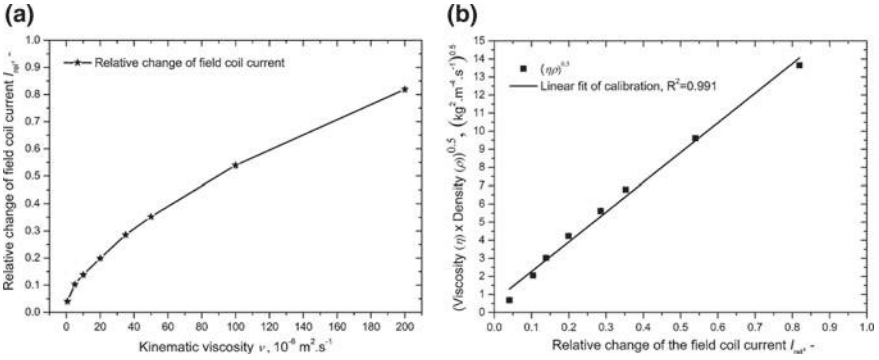

Fig. 3.17 Relative change of the field current as a function of the kinematic viscosity (**a**) and linear fit of the calibration as a function of the field coil current (**b**) [19]

head, touches the liquid the current in the field coil rumps-up in order to keep stable amplitude. For the measurement of viscosity, the vibrating finger is immersed into the liquid on 20 mm depth. The square root of the product of density and viscosity is a function of relative current change in this case:

$$\sqrt{\eta\rho} = I_{\text{rel}} \cdot b + a \tag{3.5}$$

In order to define the viscosity of the measurement a cell is calibrated at room temperature. Calibration is accomplished with the reference liquids of known viscosity (silicon oils) in the range of 0.7–200 mPa s. As a result, the calibration line is obtained (Fig. 3.17). As can be seen from (3.5), for the estimation of viscosity, the density of the liquid is required.

An essential aspect of a new cell development was the selection of the material for vibrating finger. The requirements to this material were as follows: easy machinability in order to create complex geometry (screw-thread), high-temperature corrosion resistance to withstand contact with liquid metals and alloying elements, relatively low cost. All these requirements were met in a boron nitride ceramic which was further used as a material for vibrating finger.

The new measurement cell was tested on the metals with vast reference data on their viscosity. The vibrating finger was immersed into liquid gold, silver and tin. Density data on these metals were taken from the previous study [20]. Viscosity values obtained by the newly developed unit are in a very good agreement with the literature values. A viscosity of the liquid gold measured with a vibrating finger viscometer was ~ 0% higher than previously reported in literature and decreased from 5.6 mPa s at 1100 °C (1373 K) to 4.0 mPa s at 1400 °C (1673 K). A viscosity of liquid silver was 10–20% lower than in available literature and decreased from 3.4 mPa s at 1000 °C (1273 K) to 2.3 mPa s 1400 °C (1673 K). Liquid tin showed viscosity ~20% lower than reported in literature and reducing from 1.3 mPa s at 600 °C (873 K) to 1.1 mPa s at 800 °C (1073 K). This research has proven the ability of new viscometer to measure the viscosity of low reactive metals at elevated temperatures.

After a successful measurement of noble metals' viscosity, the next step was to apply the vibrating finger viscometer for the study of the viscosity of the liquid steel alloys. Research cell was used to investigate the effect of nickel content on the viscosity of the Cr–Mn–Ni steel alloys in the temperatures range of 1500–1600 °C [18]. The measurements were accomplished without severe erosion of vibrating finger surface and geometry changes. As can be seen from Figs. 3.18 and 3.19, the viscosities of CrMnNi steels decrease with temperature and significantly reduce at 20% of Ni.

In order to investigate the effect of melts' viscosity on the atomization process, a series of phosphorus alloyed steels were prepared (Table 3.5). It is known from literature that phosphorus significantly reduces the viscosity of liquid iron and iron-based alloys [21]. Application of a vibrating finger viscometer has confirmed a decrease of viscosity due to additions of phosphorus. Increase of phosphorus content from 0.022 to 0.2% led to a reduction of viscosity from 5.0 mPa s to 3.2 mPa s measured at 1600 °C [8].

Atomization of the phosphorus alloyed steels showed a tremendous effect of viscosity on the size of the powder particles [22]. As it can be seen in Fig. 3.20, there is a linear dependence of the median particle size on the dynamic viscosity at 1600 °C. Decrease of viscosity of 36% (from 5.0 to 3.2 mPa s) led to reduction of d_{50} of 34% (from 39.5 to 26 μm).

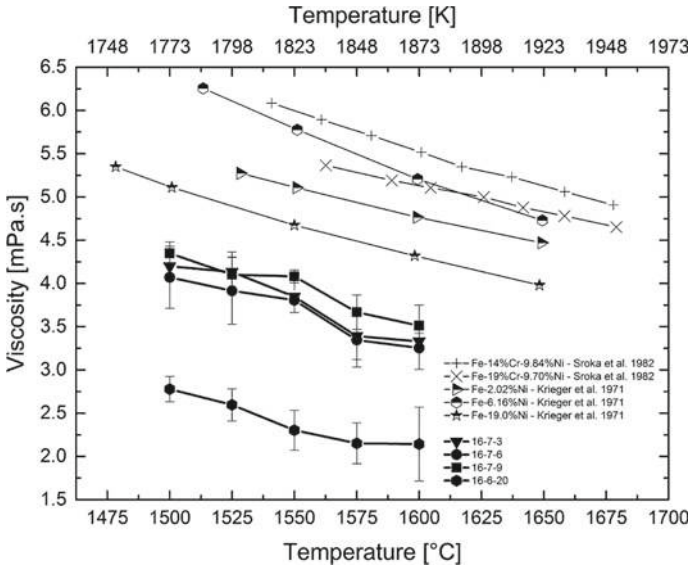

Fig. 3.18 Viscosity of the 16-7-3, 16-7-6, 16-7-9 and 16-7-20 alloys measured with the vibrating finger viscometer compared to previously reported values in the literature [18]

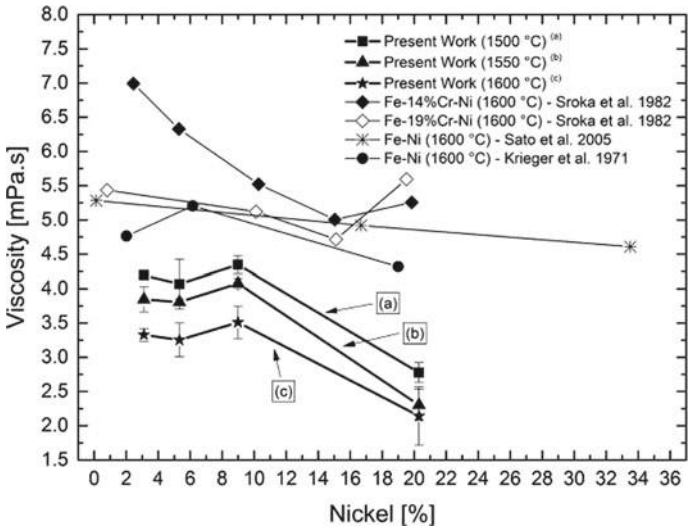

Fig. 3.19 Isothermal viscosity of Cr–Mn–Ni steel with varying nickel content and literature values [18]

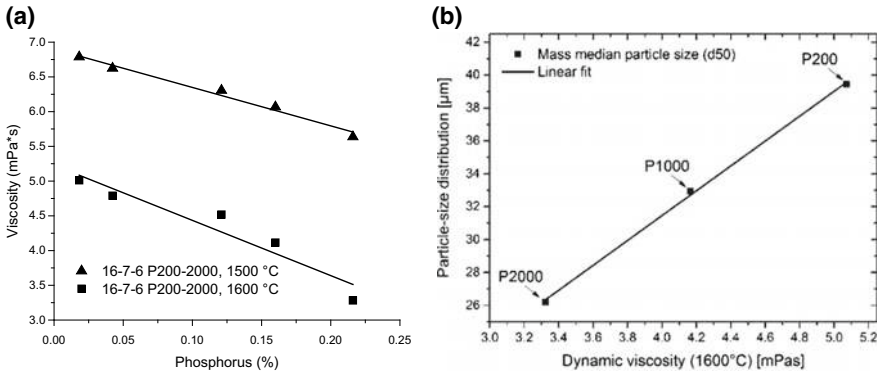

Fig. 3.20 Viscosity of 16-7-6 alloy as a function of phosphorus content measured at 1500 and 1600 °C based on [8] (**a**), and effect of viscosity on the median particle size d_{50} of atomized powder based on data from [8, 22] (**b**)

3.3 Density of Nitrogen Alloyed Steels

3.3.1 Development of Density Measurement Cell

One of the further targets was to develop a more precise density measurement cell based on the Archimedean principle. Why was the Archimedean principle selected to measure density? There are two features of the density measurement with the Archimedean principle to be selected:

1. High precision. The error of the density values reported in literature for liquid iron is less than 0.5% [23]
2. Low evaporation of sample and its alloying elements. The sample is usually measured in a ceramic crucible what means low surface to volume ratio.

There are several versions of the direct Archimedean principle methods to measure the density of liquids. In a classical single-sinker method one utilizes one body of a known volume which is immersed in the liquid. The body is suspended on a wire or attached to a thin rod. Presence of the rod has an almost negligible effect on the error of the measurement when single sinker method is applied for measurement of low surface tension liquid, e.g. water or oils. However, when the metals are measured, the effect of a surface tension on the rod has to be accounted for. Surface tension effect depends on the wetting angle between the liquid and the rod material and also on the capillary meniscus direction. These two factors are the primary source of errors for the estimation of liquid metals density with the use of the single-sinker method.

In order to overcome this effect of surface tension, a variety of modifications are proposed in literature [24]. They are based on the idea to use two bodies with different volume but the same rod diameter. When bodies are immersed, the effect of surface tension on their rods is supposed to be the same. However, the weight change

difference between the two different volumes indicates the density of the measured liquids (3.6). Therefore, the two-sinker method was selected for the measurement of the liquid iron alloys density:

$$\rho = \frac{(W_1 - W_0) - (w_1 - w_0)}{V_1 - V_2} \tag{3.6}$$

where W_1 is the weight of the big sinker immersed in liquid, W_0 is the weight of big sinker before immersion; w_1 is the weight of small sinker after immersion in liquid; w_0 is the weight of small sinker before immersion; V_1 is a volume of a big sinker, V_2 is a volume of a small sinker.

An additional measurement cell was added to existing MBP and vibrating finger viscometer facility in such a way that all three measurement units are utilizing the same induction furnace, positioning system and computer hardware. Scheme of the new unit is shown in the Fig. 3.21a. As it can be seen on the scheme, measurement of a density is accomplished via a high-precision balance (1) with the sinker assembly attached to its bottom hook. The assembly consists of molybdenum rod (2) connected to the ceramic rod with the sinker at the end (5). Additional weight (3) can be loaded on the assembly to keep it in vertical direction. The furnace has an extra thermocouple which measures temperature near the melt surface (10). The thermal field in the crucible was checked by immersion of a shielded thermocouple in the molten Ni and also in solid Mo. It was estimated that temperature in the melt was 8–10 K lower than the one measured by the side thermocouple. Therefore, side thermocouple is used as a sensor of melt temperature during experiments.

The procedure of measurement consists of:

(1) Heating of the sample to a target temperature with the rate of 20–30 K per minute
(2) 30 min holding time in order to get thermal equilibrium
(3) Measurement of sinker weight on 2–3 mm above the melt
(4) Immersion of sinker into the melt on 1 mm below the target level
(5) Subtraction of the sinker on the target level and measuring the weight change for 5 min
(6) Repetition of steps 4–5 two more times
(7) Measuring of sinker weight above the melt
(8) Withdrawing of sinker and repetition of steps 3–7 with the second sinker.

Step 4 was added after the preliminary test in liquid lead that showed significant improvement of accuracy due to reducing of a surface tension effect on the ceramic rod (Fig. 3.21b). All the sinkers used in this measurement cell before experiments were immersed into deoxidized water in order to estimate their volume (volume difference of pairs) at room temperature.

Copper, silver, and tin metals were selected for the first application of the measurement cell. The materials were melted in ZrO_2 crucibles (yttria-stabilized) and measured with ZrO_2 (MgO-stabilised) sinkers. As can be seen in the Fig. 3.26a, density of copper measured by Archimedean principle decreased from 8.06 g/cm^3 at

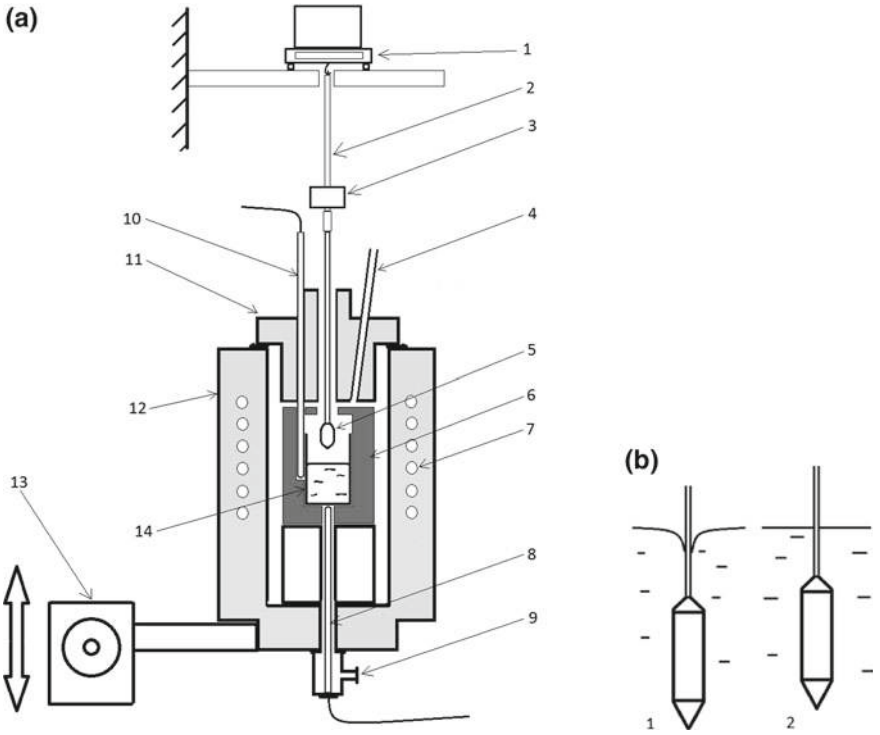

Fig. 3.21 **a** Density measurement cell. 1 Mettler-Toledo XS105 balance placed on a fixed platform; 2 molybdenum rod; 3 extra load (Cu); 4 top input of gas (argon); 5 ceramic sinker; 6 graphite heating crucible; 7 inductor coil; 8 bottom thermocouple (type B); 9 bottom gas input (argon); 10 side thermocouple (tape B); 11 ceramic cover of the reaction chamber; 12 ceramic furnace; 13 electric drive for vertical positioning; 14 graphite crucible [25]. **b** Shape of the capillary meniscus when sinker is immersed on 1 mm below the target level (1) and capillary meniscus when sinker is returned to target level (2)

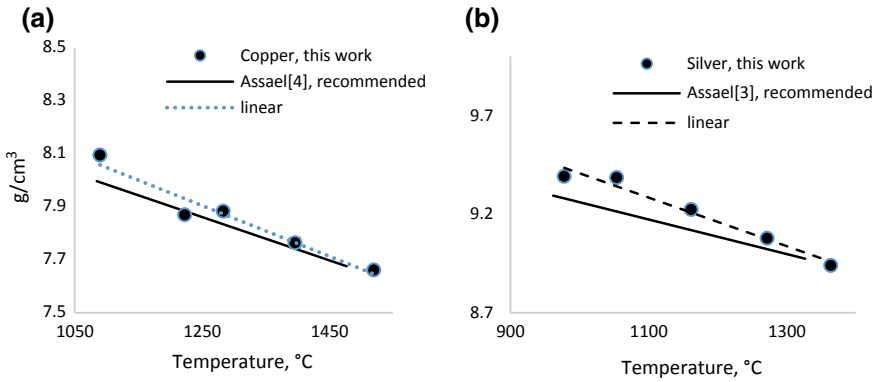

Fig. 3.22 Density of the copper (**a**) and silver (**b**) measured with the Archimedean principle with two sinkers method, based on [25]

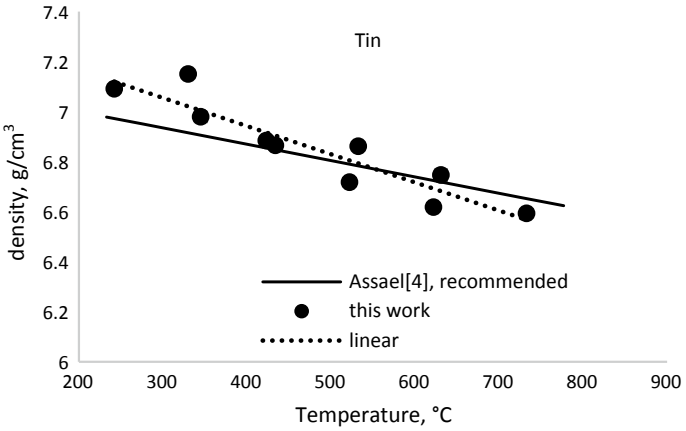

Fig. 3.23 Density of tin measured with the Archimedean principle with two sinkers method, based on [25]

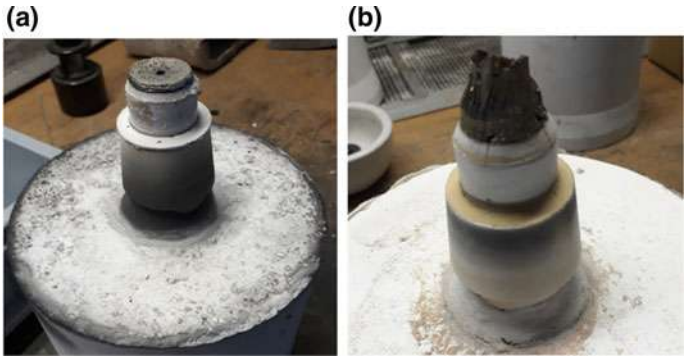

Fig. 3.24 Frozen metal formed on the face of tundish nozzle (crown) after atomization. **a** Crown is almost absent. **b** Severe crown formation [28]

1090 °C to 7.65 g/cm^3 at 1520 °C. Measured density deviates not more than 1% from values recommended in literature [26]. Density of silver had slightly higher deviation from recommended values [27] (Fig. 3.22b). Measured density decreased from 9.44 g/cm^3 at 978 °C to 8.94 g/cm^3 at 1364 °C. As for liquid tin, obtained density (Fig. 3.23) deviated up to 3% from recommended values [26]. Possible source of the error in the measurement of tin was oxidation of the surface level at temperatures below 700 °C.

In general, the measurement cell showed a relatively good accuracy and is considered for further study of iron-based alloys. It was decided to test a two-sinker method on the investigation of the density of steel alloys 15NC10.15 and 19NC15.15.

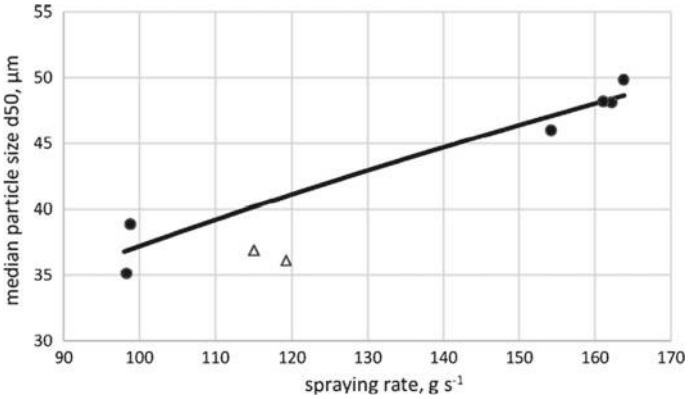

Fig. 3.25 Effect of spraying rate and temperature on the median particle size. Bullet atomized at 1600 °C, Triangle atomized at 1650 °C, square root trend line is built for all experiments at 1600 °C [28]

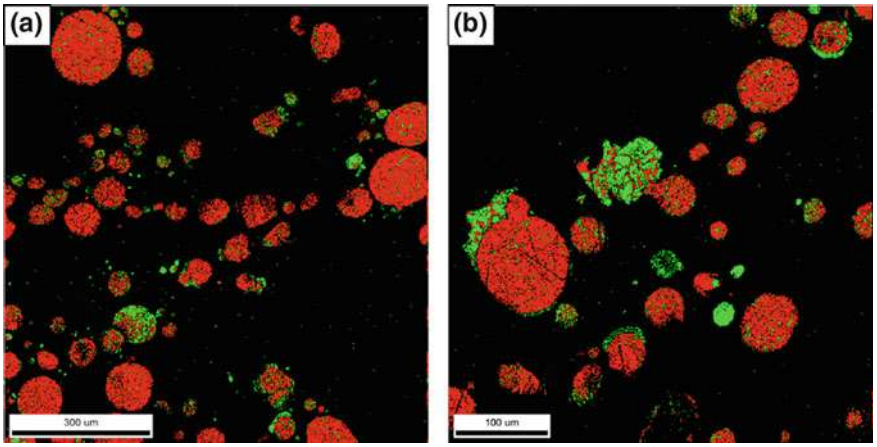

Fig. 3.26 EBSD analysis results for 19NC15.15+V with 2384 ppm N; **a** overviewand **b** higher magnification. Red colour represents the austenite phase and green color ferrite phase [28]

3.3.2 Atomization of Nitrogen Alloyed Steels

Along the duration of the CRC 799 inew steels 15NC10.15 and 19NC15.15 (Table 3.7) were developed. Exceptional tensile strength features of these steels are provided by high nitrogen content. At the same no extensive information on the effect of nitrogen alloying of the melt on the atomization process was found in the literature. Therefore, it was decided to conduct a series of atomization of the new nitrogen-alloyed steels [28]. In this study two parameters were selected as variables—nitrogen content and the temperature of the atomized melt. In order to

Table 3.7 Chemical composition of the nitrogen alloyed steels, modified after [28]

	C	Si	Cr	Mn	Ni	Al	Mo	V	N	O_{tot}	S	P
	%								ppm			
15NC10.15	0.151	0.427	15.5	2.97	2.91	0.0043	0.048	0.082	1089	45	67	203
19NC15.15	0.156	0.434	19.0	3.09	4.14	0.0089	0.059	0.085	1554	68	78	194
19NC15.15V	0.159	0.504	18.9	2.82	4.24	0.0132	0.046	0.620	3187	24	90	89

broaden the range of soluble nitrogen content in the steel 19NC15.15 it was alloyed with 0.65% of vanadium and was named as 19NC15.15+V. Atomizations were also accomplished at 1600 and 1650 °C for steels 15NC10.15 and 19NC15.15.

The amount of dissolved nitrogen in the liquid alloy was provided by adjusting argon/nitrogen ratio in the atmosphere in the upper vessel of VIGA-1B. A sampling at 1550 °C was done before atomization was launched. Unfortunately, not all samplings were successful. However, with the exception of 19NC30.15+V results showed relatively low nitrogen loss directly during atomization—in a range of 80–130 ppm. As for 19NC15.15+V, the significant difference between the sample and the powder nitrogen composition could be explained with the sampling procedure described in reference [28].

Series of atomization with variable nitrogen content did not reveal an apparent effect on the median particle size d_{50}. At the same time, another factor showed a strong influence on particles size. During the atomizations a frozen crown was formed on the face of the tundish nozzle (Fig. 3.24). The size of this crown was a defining factor for the metal flow rate. During big crown formation, the metal flow rate was reduced what led to lower spraying rate (higher gas/metal ratio). It is known that in industrial practice the gas/metal ratio is the main parameter to control powder size [11]. The results of these experiments were in very good agreement with the typical square root dependence of d_{50} from gas/metal ratio (see Fig. 3.25).

Series of atomization conducted at 1650 °C showed a significant shift of the value d_{50} below the square root trendline of 1600 °C, thus, illustrating the effect of temperature on refining the size of the particles. These results are in a good agreement with the existing literature on this topic [29].

The samples of two powders with maximum and minimum nitrogen content were analyzed with the use of magnetic saturation method. The results showed that powder with 765 ppm on *N* had 54% of ferrite, while sample with 2384 ppm *N* had only 17% of ferrite phase. Further analysis with electron backscatter diffraction of SEM confirmed a prevailing of austenite phase in high *N*-containing alloy (Figs. 3.26 and 3.27). Furthermore, particles smaller than 20 μm had more ferrite phase than bigger ones ($20 < d < 200$ μm). This indicated control of both cooling rate and nitrogen upon the austenite stabilization.

3.4 Analysis of Gas Atomization Process

This research was dedicated to the production of the inert gas atomized powders with the defined properties for further application in the TRIP-Matrix-Composites. Therefore, a commercial inert gas atomization facility supplied by ALD Vacuum Technologies was applied.

The main targets were:

- To measure and analyse the atomization process
- To study of new nozzles' geometries and systems

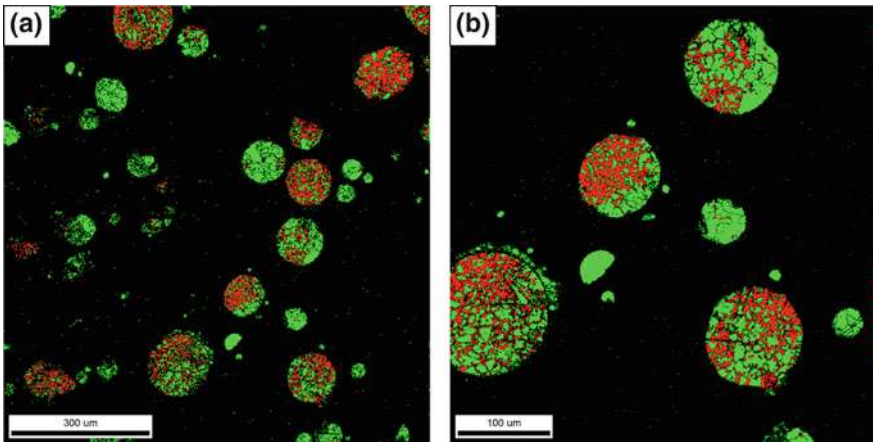

Fig. 3.27 EBSD analysis results for 19NC15.15+V with 765 ppm N_2; **a** overview and **b** higher magnification. Red color represents the austenite phase and green color ferrite phase [28]

- Targeted influence on the atomization process to produce steel powders of predefined size.

In order to affect the process of atomization it is necessary to accurately study the process of metal spraying. With this regard two special measurement units were developed for the 2-dimensional in situ measurement of temperature and velocity of the fluid particles within the gas atomization process.

3.4.1 Temperatures of the Particles

For measurement of the particle surface temperature a 2-color thermographic camera unit was developed [30]. The setup consists of two commercial CCD-cameras with installed dielectric optical filters, optical beam splitter and two lenses as object lenses. The components were selected with the requirements for being operational in the selected filter wavelengths. The maximal spectral emissive power of the studied liquid metal droplets at 1873 K is expected to be close to a wavelength of 1.5 μm. CCD camera sensors have their peak sensitivity typically at 0.5 μm. Their sensitivity at 0.9 μm is only a tenth of the maximum value. Therefore, the combined effect is that the recorded signal, i.e. intensity times sensitivity is low. In order to handle this shortcoming longer exposure times are used. This means that not the surface temperature of individual droplets is recorded, but a temporal average of the droplets that cross the area imaged onto each pixel. The cameras have a resolution of 1600 × 1200 pixels of 4.4 μm pixel size. Maximum frame rate is 16 fps. Images were obtained in an 8-bit greyscale. The optical dielectric bandpass filters have central transmission wavelengths at $\Lambda_1 = (850 \pm 8)$ nm and $\Lambda_2 = (900 \pm 8)$ nm. The set-up

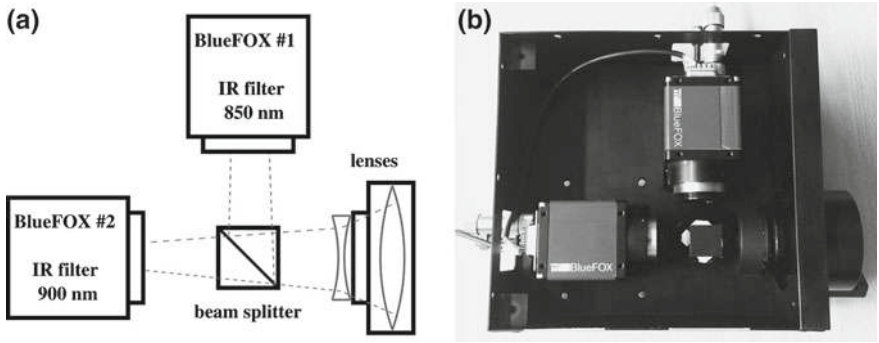

Fig. 3.28 Scheme (**a**) and picture (**b**) of the two-color pyrometer [14]

of the two-color pyrometer is shown in Fig. 3.28. The image was focused with the objective "Rollei-HTF Distagon 2.8/35". The images were focused onto the CCD sensors through the beam splitter cube. It splitted the optical path for the two camera sensors.

3.4.2 Image Processing

Two-color pyrometer was calibrated using a high-temperature furnace and a sample of silicon carbide in a temperature range of 1273–1873 K. The temperature of the sample was measured with a type B thermocouple assuring ± 1.5 K absolute measurement error. After calibration a particular correction term was obtained.

The newly developed two-color pyrometer was applied for the measurement of the metal stream temperature distribution at atomization in the VIGA-1B unit described previously in Fig. 3.13. The liquid steel (16-7-6 alloy) was heated ca. 200 K over its liquidus line to 1873 K. When the target temperature was reached, the atomization was launched. Figure 3.29 shows the results of measurements of the time-averaged temperature of the surface of the droplets. Due to the small depth of the field features of the camera, the pictures represent cross-sections of the spraying cone in the first half-second after the metal spraying initiation. The 0 mm point in the figure refers to the line of sight, which was 40 mm below the ceramic nozzle face. At 0.0 s the gas jet was not launched and only the metal stream is visible. At 0.1 s the disintegration of the metal flow began due to the gas stream. After 0.3 s the cone of sprayed metal was formed and later remained relatively stable. The primary breakup point was situated about 20 mm below the line of sight. Below that level a hollow cone of atomized melt with the length of approximately 50 mm was formed. At lower levels the hollow cone disintegrated on ligaments and droplets. Temperature iso-lines indicate that between 60 and 80 mm below the line of sight (nozzle metal) material was cooled down to its liquidus line. It corresponds to 100–120 mm distance from the nozzle face. This

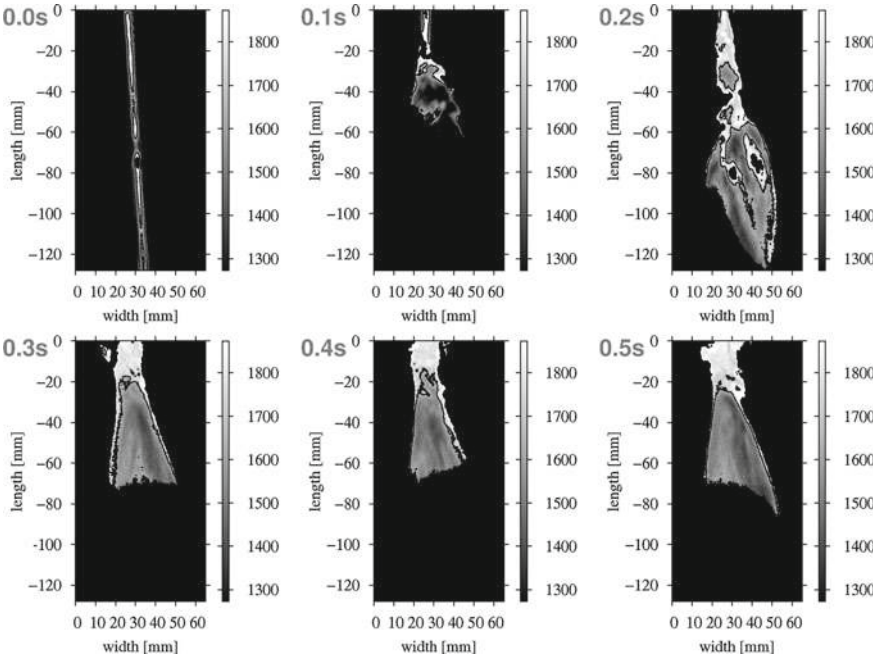

Fig. 3.29 Contour maps of the two-dimensional temperature measurement (in K) of the melt atomization. The quantity in the upper right corner of each temperature distribution is the image acquisition time t_{imag}. The black line within the region of the spray denotes the isoline of the liquidus temperature of 1673 K. The purple background means all temperatures are smaller than 1273 K which are out of the measurement range of the pyrometer, [14]

distance is about 30 times the diameter of the nozzle and is in a good agreement with literature data [31].

3.4.3 Velocity of the Particles

For the measurement of the velocity of the particles during metal atomization a special Particle Image Velocimetry (PIV) was applied (Fig. 3.30) [30]. The PIV measurement method is a non-contact optical method for measuring particle velocities in a 2D observation area within a particle flow. This area is defined by a thin light sheet generated by the passage of a laser pulse through a cylindrical lens. Two pulse laser cavities emit two laser pulses with an adjustable temporal separation. The pulse duration is on the order of 5 ns. The scattered light of the illuminated particles is picked up by a double-frame PIV camera arranged perpendicular to the light cross-section. Due to the time interval, the local positions of the particles differ in the double images. Special PIV evaluation software detects these positional differences

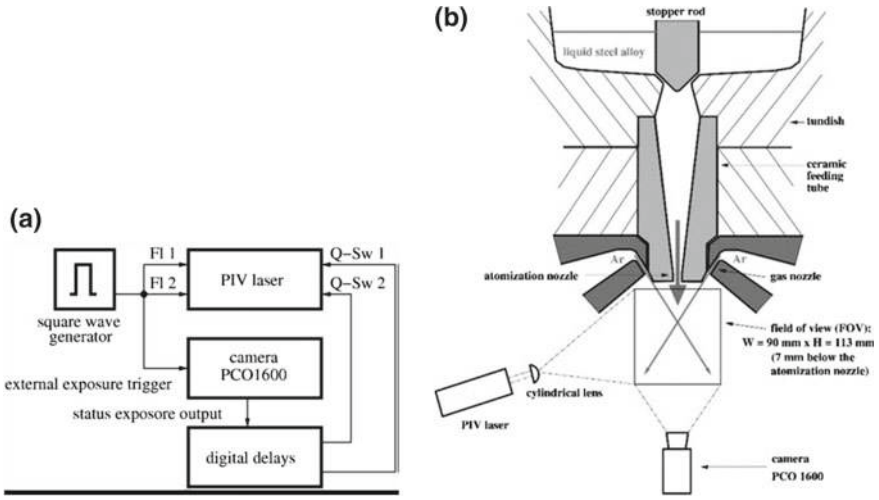

Fig. 3.30 **a** Block-diagram of the applied measurement apparatus. Square wave generator triggers the measurement with the frequency of 10 Hz. First, the flash-lamps Fl1 and Fl2 are triggered which pump the laser medium with energy. Simultaneously starts the double-images capturing with the PIV camera PCO 1600. In this case, digital delay units send control signals to the Q-Sw 1 and Q-Sw 2 Q-switches, whereby the laser pulses are triggered. The time of the 2nd double image is set in-camera. **b** Scheme of the atomization area of the VIGA 1B together with the position and size of the observed area (FOV) [30]

using correlation algorithms within the small windows in the image area, which defines a uniform grid structure. From the position difference at the correlation maximum and the time interval, a particle velocity vector is then calculated and assigned to the respective window center point. The result is a 2D velocity distribution in the observation area. PIV measurements in steel atomizers differ from those in continuous flows due to other boundary conditions.

Usually tracer particles are supplied to the fluids to be examined, which emit scattered radiation when passing the laser light section detected by the camera. Through this controlled particle addition (seeding), the number density of the determined velocity vectors can be significantly increased that aim to measure the flow velocity of the gas. In the present case of steel atomization, the aim is to truly measure the velocity of ligaments and droplets that constitute the particles. The use of a narrow band filter, whose wavelength coincides with that of the PIV laser, effectively blocks the thermal radiation of the melt.

Due to its large particle sizes, the melt in the vicinity of the ceramic nozzle scatters light strongly which leads to over-exposure of adjacent pixels on the camera sensor (blooming effect) and images with overexposed areas. Therefore, the correlation evaluation of the double images gives the wrong velocity data in this region.

Based on numerical simulations [32], it is known that gas velocities in the range of 400–500 m/s occur near the atomizer nozzle. The particle velocities in the axial range were calculated to be up to 250 m/s. The measurement of such high speeds

requires a correspondingly small time interval between the double pulses of the laser in the order of 2–3 μs. The entire measuring system must be triggered exactly in time in order to minimize the measuring error component of the time interval.

Measurements of the particle velocities were conducted for atomization of two steels: X5CrNi18-10 and X3CrNiMo13-4 in VIGA 1B unit. Both steel samples were atomized at the same conditions. Atomization was initiated at ca. 200 K superheating above the liquidus line at 1600 °C. Evolution in time of the measured particles velocities in the first 0.5 s after atomization launch is seen in the Figs. 3.31 and 3.32. The plots show a section through atomization cone. It can be seen that after 60 mm below the ceramic nozzle the metal stream breaks up and forms a hollow cone confirming the results published in [14]. The high speeds in the upper third of the observation window are due to the blooming effect. In the area of the interaction of the melt and atomizing gas, the measured particle velocities range between 120 and 210 m/s. The white dashed line indicates the area where the solidification temperatures are reached. The particle velocities of both melts in the solidification area are approximately 120 m/s. Obtained velocities are in a good quantitative agreement with numerically determined data, e.g. as [33]. Comparison of the averaged particles' velocities of two steels revealed that in case of X3CrNiMo13-4 the velocities were smaller than for X5CrNi18-10.

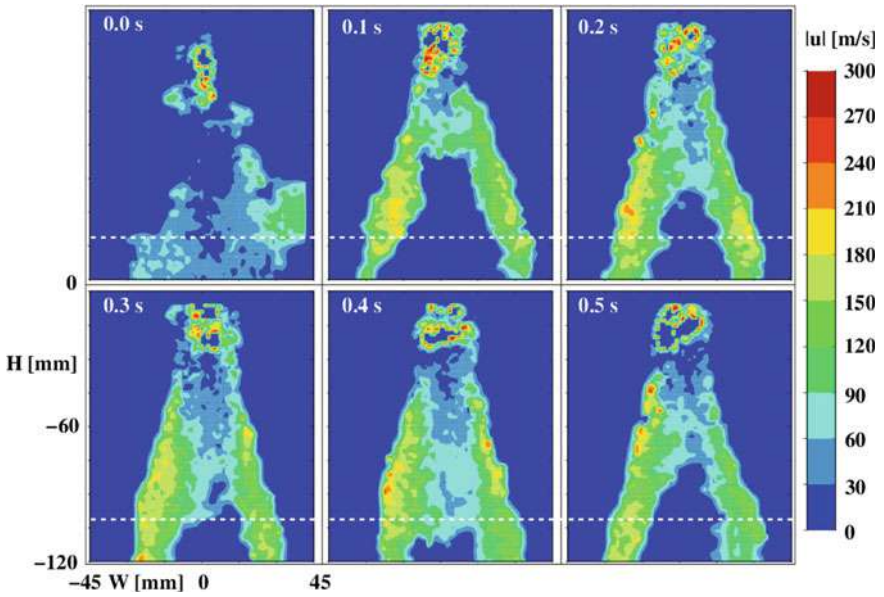

Fig. 3.31 Particle velocities for atomization of X5CrNi18-10 steel [30]

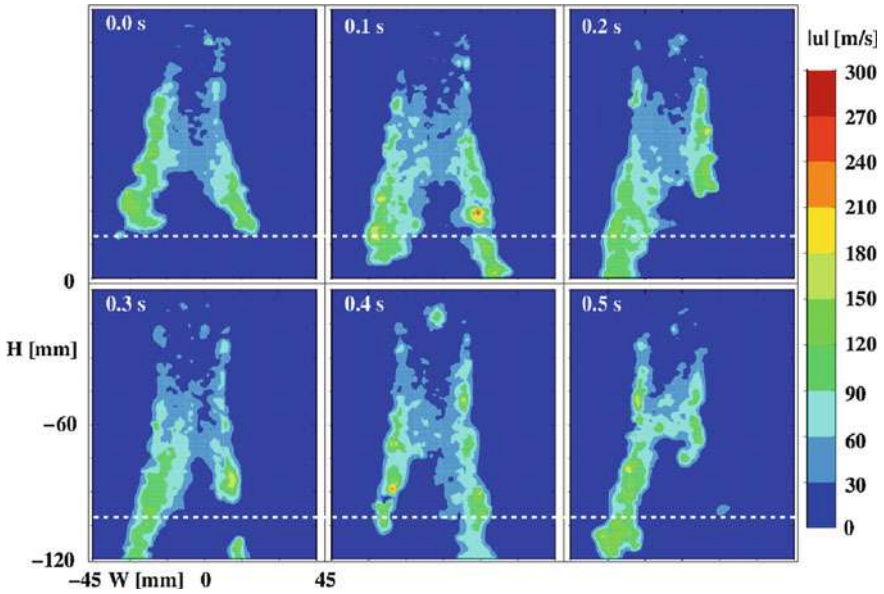

Fig. 3.32 Particle velocities for atomization of X3CrNiMo13-4 steel [30]

3.4.4 New Geometry and a Set-Up for an Inert Gas Atomization

Based on the results obtained in the previous chapters it became clear that there are three fundamental problems in the existing inert gas atomization techniques. The first problem is the very thick melt stream coming out of the nozzle. This is necessary to avoid freezing of the nozzle [34]. The result shows that the atomizing inert gas first breaks the stream into larger ligaments and sheets that have to be broken up in further steps downstream of the nozzle. The second problem is extremely low temperature of the gas when it contacts with the melt. The argon has expanded from an initial temperature around or slightly above room temperature to a velocity higher than Mach 1 up to 3 depending on the particular geometry. The result shows that the gas has a temperature around −50 °C for Mach 1 and down to −150 °C for higher Mach numbers. In principle, the high velocity of the gas is necessary for atomization but when it is that cold, it is counterproductive. This is the reason for the very high superheat of the melt needed for the VIGA set-up (200 K). Finally, the break-up of a thick stream in the centre of the flow with a surrounding gas can be changed. A thin layer of melt on the inner wall of a high-velocity nozzle for the gas is the closest the melt can be exposed to the gas. This is only possible if the gas is hot enough otherwise the nozzle would freeze. This rationale led to the development of a new set-up which has been patented [35]. The idea has been implemented first for the atomization of tin as a proof of principle. Figure 3.33a shows schematically

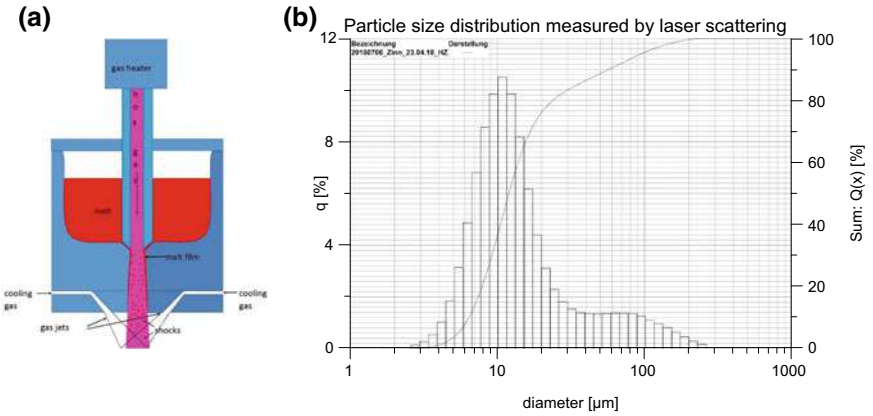

Fig. 3.33 Schematic set-up of the new atomization technique (**a**) and particle size distribution resulting for the atomization of tin using the new technique (**b**)

the tin atomization set-up. Figure 3.33b shows the resulting particle size distribution measured by laser scattering. The peak of the distribution centers at 10 μm for the first experiments. This factor is 2–3 lower than the VIGA results. Of course, the one result is for tin, and the other is for steel. However, when comparing with literature results for tin using similar set-ups as the VIGA the factor 3 is still valid [35].

3.5 Conclusions

The present work is focused on the investigations of inert gas atomization and the effects of thermophysical properties of liquid steel alloys' atomization process. Several new research units capable of measuring thermophysical properties of TRIP/TWIP steel melts as well as gas atomization were successfully developed, such as: maximum bubble pressure unit, patented vibrating finger viscometer, density measurement cell based on Archimedean principle, two-colour pyrometer, particle-image-velocimetry unit. The project allowed to gain new data on the surface tension, viscosity and density of the newly developed TRIP/TWIP alloys. Moreover, results regarding the effects of microalloying on the surface tension and viscosity of the steel were obtained. The primary research and practical results of the project development were:

- The surface tension of the TRIP/TWIP steel can be considerably reduced by microalloying with sulphur and selenium;
- reduction of a surface tension reduces the median particle size of the gas-atomized powders;
- The viscosity of the investigated TRIP/TWIP steel can be reduced with phosphorus;

- The viscosity directly affects the median particle size of the atomized powder;
- Nitrogen alloying does not significantly affect the inert gas atomization process in terms of particle sizes, however, powders phase composition is affected;
- Nitrogen leads to an increase of austenite phase fraction in ready powder particles;
- Temperature of atomization can be an effective measure to affect powder size;
- Measurements delivered data on particles temperature and velocity upon inert-gas atomization.

In general, besides delivering new thermophysical data on liquid alloys and metals, the primary outcome of the research is the confirmation of the successful control of the atomization process by modifying thermophysical properties of the atomized liquid.

Acknowledgements Authors would like to express sincere thanks to the former and current colleagues of the TP A2 and A3 who contributed to development of the CRC 799: Prof. Piotr-Roman Scheller, Dr. Andreas Jahn, Dr. Tobias Dubberstein, Clemens Cirmse, Peter Neuhold, and others. This work was funded by the Deutsche Forschungsgemeinschaft (DFG, German Research Foundation)—Projektnummer: 54473466-SFB 799.

References

1. K.J. Mysels, Colloids Surf. **43**, 241 (1990)
2. K.J. Mysels, Langmuir **2**, 428 (1986)
3. T. Dubberstein, M. Hötzel, R. Hagemann, P. Heller, P.R. Scheller, Steel Res. Int. **82**, 1122 (2011)
4. T. Dubberstein, P.R. Scheller, in *Scientific Reports on Resource Issues* (TU Bergakademie Freiberg, Freiberg, 2011), p. 7
5. T. Dubberstein, H.-P. Heller, P.R. Scheller, in *Ninth International Conference on "Molten Slags, Fluxes and Salts (Molten12)"* (Beijing, China, 2012), p. 10
6. T. Dubberstein, H.-P. Heller, Adv. Eng. Mater. **15**, 583 (2013)
7. T. Dubberstein, H.-P. Heller, J. Klostermann, R. Schwarze, J. Brillo, J. Mater. Sci. **50**, 7227 (2015)
8. T. Dubberstein, Beiträge zu den thermophysikalischen Eigenschaften flüssiger Metallschmelzen, Ph.D. Thesis, TU Bergakademie Freiberg, 2015
9. K. Ogino, K. Nogi, O. Yamase, ISIJ Int. **23**, 234 (1983)
10. B.J. Keene, Int. Mater. Rev. **33**, 1 (1988)
11. J. J. Dunkley, in *Powder Metal Technologies and Applications* (ASM International, 1998), p. 2762
12. J. J. Dunkley, in *Advances in Powder Metallurgy* (Elsevier, 2013), pp. 3–18
13. T. Dubberstein, H.-P. Heller, Steel Res. Int. **84**, 845 (2013)
14. C. Kirmse, H. Chaves, J. Therm. Spray Technol. **24**, 690 (2015)
15. Y. Su, Z. Li, K.C. Mills, J. Mater. Sci. **40**, 2201 (2005)
16. A. Jahn, K.-P. Steinhoff, T. Dubberstein, P. Franke, M. Weider, S. Wolf, A. Kovalev, A. Glage, A. Weiß, W. Schärfl, K. Eigenfeld, L. Krüger, P.R. Scheller, Steel Res. Int. **85**, 477 (2014)
17. T. Dubberstein, M. Schürmann, H.-P. Heller, H. Chaves, DE102014015301 (25 February 2016)
18. T. Dubberstein, H.-P. Heller, O. Fabrichnaya, C.G. Aneziris, O. Volkova, Steel Res. Int. **87**, 1024 (2016)
19. T. Dubberstein, M. Schürmann, H. Chaves, H.-P. Heller, C. G. Aneziris, Int. J. Thermophys. **37** (2016)

20. T. Dubberstein, H.-P. Heller, High Temp.-High Press. **44**, 393 (2015)
21. A.A. Romanov, V.V. Kochegarov, Phys. Metalle Und Metallkunde (Физика Металлов И Металловедение) **18**, 876 (1964)
22. T. Dubberstein, H.P. Heller, Adv. Mater. Res. **875–877**, 1265 (2014)
23. M.J. Assael, K. Kakosimos, R.M. Banish, J. Brillo, I. Egry, R. Brooks, P.N. Quested, K.C. Mills, A. Nagashima, Y. Sato, W.A. Wakeham, J. Phys. Chem. Ref. Data **35**, 285 (2006)
24. K.-C. Chou, J.-H. Hu, MTB **22**, 27 (1991)
25. I. Korobeinikov, D. Chebykin, X. Yu, S. Seetharaman, O. Volkova, Arch. Mater. Sci. Eng. **92**, 28 (2018)
26. M. J. Assael, A. E. Kalyva, K. D. Antoniadis, R. Michael Banish, I. Egry, J. Wu, E. Kaschnitz, W. A. Wakeham, J. Phys. Chem. Ref. Data **39**, 033105 (2010)
27. M.J. Assael, A.E. Kalyva, K.D. Antoniadis, R.M. Banish, I. Egry, J. Wu, E. Kaschnitz, W.A. Wakeham, High Temp. High Press. **41**, 161 (2012)
28. I. Korobeinikov, A. Perminov, H.-P. Heller, and O. Volkova, Adv. Eng. Mater. (2018)
29. D. M. Goudar, V. C. Srivastava, and G. B. Rudrakshi, EJ **21**, 155 (2017)
30. C. Kirmse, H. Chaves, Steel Res. Int. **87**, 1295 (2016)
31. R. Gjesing, J. Hattel, U. Fritsching, Eng. Appl. Comput. Fluid Mech. **3**, 471 (2009)
32. R. Kaiser, C. Li, S. Yang, D. Lee, Adv. Powder Technol. **29**, 623 (2018)
33. N. Zeoli, H. Tabbara, S. Gu, Appl. Phys. A **108**, 783 (2012)
34. K. Bauckhage, D. Bergmann, U. Fritsching, H. Lohner, P. Schreckenberg, Chem. Ing. Tech. 10 (2001)
35. H. Chaves, C. Kirmse, H. P. Heller, T. Dubberstein, DE 10 2015107 876A1 (2016)

Chapter 4
Production of Ceramic Steel Composite Castings Through Infiltration

Paul Rähmer, Claudia Dommaschk and Gotthard Wolf

Abstract TRIP-matrix composites unite the outstanding properties of austenitic-martensitic cast steels with those of ceramics. To manufacture them via infiltration by steel melt, basic investigations are needed. Therefore, the following aspects were studied: the influence of sodium silicate bonded sand molds on solidification of high alloyed TRIP-steels, chemical reactions between steel and molding sand and the positive impact of sulfur and phosphorus on the infiltration quality. Composite materials made of steel and ceramics, in particular, melt-broken zircon corundum, have comparatively high wear resistance. The wear behavior of the composites is characterized by a ring-block test rig. In order to generate a stable bond between the steel and the ceramic phase, the ceramics were coated with titanium oxide prior to infiltration. During infiltration of the coated ceramics, spinel compounds are formed which reduce expansion-related cracks in the boundary layer.

4.1 Introduction

A combination of different materials enables a targeted combination of material advantages while reducing lagging. Composite materials made of metals and oxides show high innovative potential .

The materials produced primarily by powder metallurgical (PM) processes offer a wide range of applications. Due to the high manufacturing costs of PM processes however, the production of composite materials using suitable casting processes is an important alternative. A combination of the properties of newly developed TRIP/TWIP alloys, which have a high deformation potential and also a high energy

P. Rähmer
Albert Hoffmann GmbH, Bergrather Straße 66–70, 52249, Eschweiler, Germany
e-mail: p.raehmer@albert-hoffmann.de

C. Dommaschk (✉) · G. Wolf
Foundry Institute, Technische Universität Bergakademie Freiberg, Bernhard-von-Cotta-Str. 4, 09599, Freiberg, Germany
e-mail: Claudia.Dommaschk@gi.tu-freiberg.de

H. Biermann and C. G. Aneziris (eds.), *Austenitic TRIP/TWIP Steels and Steel-Zirconia Composites*, Springer Series in Materials Science 298,
https://doi.org/10.1007/978-3-030-42603-3_4

absorption capacity, with a wear-resistant ceramic enables the production of fracture-resistant, wear-resistant components [1].

For the production of the MMCs basic investigations are necessary and different ways for the production of these are pointed out.

4.2 Thermal and Chemical Interactions Between Casted High Alloyed TRIP-Steel and Molding Systems

For the infiltration of macro porous ZrO_2 ceramic filter by liquid TRIP-steel melt a special mold, shown in Fig. 4.1, was developed [2, 3]. The depicted mold consists of an infiltration area in the middle of the mold with a height of 100 mm and a diameter of 50 mm. Floating of the ceramics foams into the feeder is prevented by quartz rods and a filter located underneath. The feeder is equipped with an outlet to ensure uniform metallostatic pressure and the bottom outlet allows more melt to flow through the infiltration area. The solidification time has a high impact on the infiltration quality of the TRIP-matrix materials and is influenced particularly by the molding material. Therefore, the solidification times of three different types of molding sands were investigated. In addition, the modification of the steel composition near the molding material was discussed. As molding sand for the ester hardened sodium silicate bounded mold, H32 (silica sand), chromite sand and Cerabeads 650 (synthetic mullite) were used. Because of the high density, the chromite sand has a binder content of only 2 mass%, while the other molding sands are bound with 3.5 mass% binder. The temperature was measured in the middle of the infiltration area by Pt-Rh/Pt-thermocouples [2, 3].

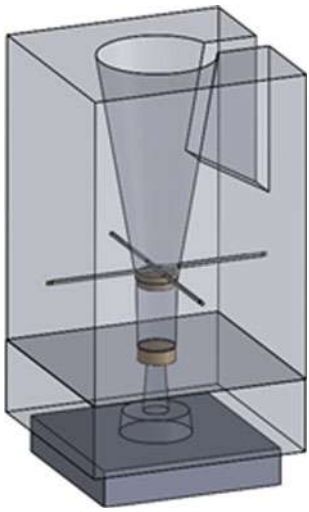

Fig. 4.1 Top pouring infiltration mold with floating preventing ceramic foams and quartz rods

4.2.1 Solidification Time Depending on the Molding Sand

The different molding sands have a strong effect on the cooling of the casting, and thus also on the solidification time of the steel. As shown in Fig. 4.2 the castings solidify faster in molds containing chromite sand than silica sand or Cerabeads. These results can be used to achieve a maximum solidification time, and thus to give the infiltration of the ceramics as much time as possible. Furthermore, the solidification can be specifically controlled by the use of the various molding sands, so that feeders or chills could be saved.

The different cooling times can mainly be explained by the different thermal conductivities and specific heat capacity. The thermal conductivity of Cerabeads is the lowest. Up to a temperature of 625 °C, chromite sand has a higher thermal conductivity and higher specific heat than silica sand, hence the amount of heat dissipated in this range is significantly greater and the castings tend to solidify faster [2, 4].

With the choice of molding sands the solidification time of the TRIP steel can be controlled and modified. Chromite sand has a cooling effect, while Cerabeads are insulating and therefore, they are best suited for the infiltration process [2, 3].

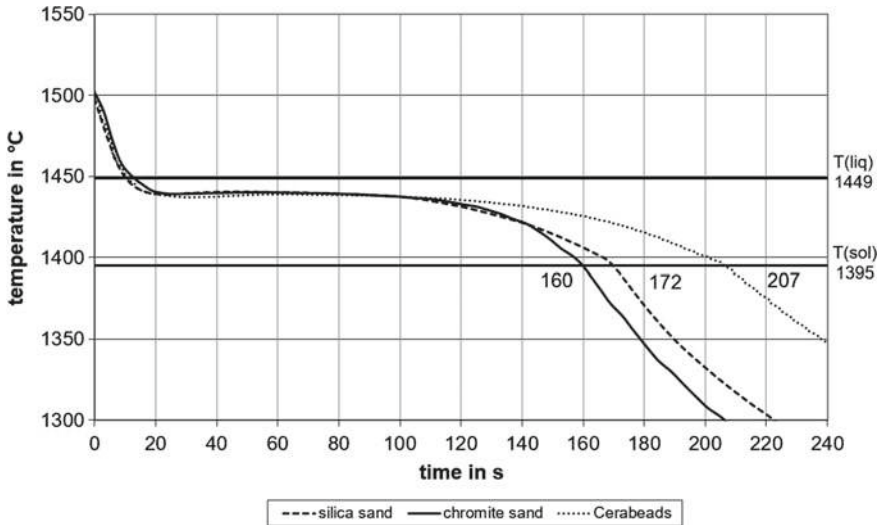

Fig. 4.2 Cooling curves of cast X3CrMnNi 16-7-6 TRIP-steel cylinders containing liquidus and solidus temperature depending on molding systems. Adapted from Weider [3]

4.2.2 Chemical Interactions Between Steel and Mold

The composition of the used steel is given in Table 4.1. To investigate the chemical interactions, samples were taken from the different thermally loaded layers of the molding material and were wet-chemically analyzed. The results are shown in Table 4.2. In addition, the bound and unbound molding materials were also examined without thermal loading. Locally, the exchange of elements is mainly restricted to the sintering zone, which is in direct contact with the melt. The organic components contained in the binder, e.g. the ester, are responsible for an increase of the carbon content in the melt. The chemical interactions can be measured in the molding sand and the casted steel. The exchange of the elements depends on the composition of the molding sand and their thermal behavior. Particularly noteworthy is the reactive element manganese through the combination of high vapor pressure and oxygen affinity [5]. This results in a strong degradation of acid refractory materials, so that especially the silica sand reacts with the manganese of the melt.

It can be concluded that all basic mold materials tend to accumulate alloying elements in the sintered layer. Cerabeads appear to form a very dense sintered layer, as there were found low levels of chromium and iron. Silica sand is relatively strongly enriched with MnO in the sintered layer, which only influences the casting composition locally at the surface [2].

4.3 Influence of the Ceramic Preheating Temperature and Phosphorus as Alloying Element on the Infiltration Quality

To determine the influence of the preheating temperature and the porosity of the ceramics, the top pouring infiltration was arranged according to the test described above. The casting temperature of the inductive melted steel, according to Table 4.1, was constant at 1600 °C. The ceramic preforms consisting of piled filters were preheated in an electric furnace to temperatures around 200, 600, 1000 and 1400 °C. To study the basic effects with molten steel and the general mechanism of the infiltration process commercial pouring filters where used, manufactured by Drache GmbH, Germany, with a porosity of 10 ppi. The quantification of the infiltration quality was done by measuring the infiltratable cavity thickness inside of the ceramics and by relating the infiltrated fraction of these cavities to the investigated area of the casting.

Table 4.1 Chemical composition of the used high-alloyed steel in mass% [3]

	C	Si	Mn	Cr	Ni	Fe
X3CrMnNi 16-7-3	0.035	0.89	7.21	16.36	3.09	Bal.
X3CrMnNi 16-7-6	0.05	1.06	7.10	16.20	5.94	Bal.

Table 4.2 Chemical composition of the molding sand before (without binder) and after thermal loading (sodium silicate bonded) in mass% [3]

Type and location of the samples		C	SiO_2	MnO	Cr_2O_3	Fe_2O_3	Na_2O	Al_2O_3	Others
Silica sand	Basic material	0.038	>99.0	<0.1	<0.1	<0.1	0.01	<0.1	
	Sintered layer	0.046	88.2	14.0	2.1	0.2	0.41	<0.1	
	Thermal affected	0.047	>99.0	<0.1	<0.1	<0.1	0.41	<0.1	
	Thermal unaffected	0.190	>99.0	<0.1	<0.1	<0.1	0.42	<0.1	
Chromite sand	Basic material	0.021	<0.1	0.1	30.6	26.2	0.014	15.5	<27.6
	Sintered layer	0.024	2.2	3.6	30.8	25.4	0.19	15.4	<22.4
	Thermal affected	0.035	0.1	0.15	30.6	26.0	0.22	15.6	<27.3
	Thermal unaffected	0.115	0.1	0.1	30.5	26.0	0.23	15.3	<27.6
Cerabeads	Basic material	0.038	35.8	<0.1	<0.1	1.1	0.49	61.7	
	Sintered layer	0.044	34.4	<0.1	1.9	2.0	0.78	60.8	
	Thermal affected	0.060	36.7	<0.1	<0.1	1.2	0.90	61.1	
	Thermal unaffected	0.158	36.3	<0.1	<0.1	1.2	0.92	61.5	

According to Dubberstein and Heller [6], the dynamic viscosity can be reduced by increasing the phosphorus content in the melt [6]. Therefore, the phosphorus contents in the steel melt were increased up to 0.2 mass% [7].

The effect of the preheating temperature on the infiltration of 10 ppi ceramic filter with a cast steel X3CrMnNi 16-7-6 is shown in Fig. 4.3. Due to the fact, that the melt cools down while flowing through the ceramic, the infiltration quality generally decreases with increasing depth of infiltration. The infiltratable cavity thickness is primarily dependent on the sample position, and thus on the flow length within the filter. A significant influence can only be detected in the middle section of the sample at a preheating temperature of 1400 °C. In the case of the proportion of infiltrated cavities, in addition to the dependence on the sample position, a dependence on the preheating temperature can also be determined, which is best visible in the lower areas. When these lower areas are underheated due to the low temperature of the melt or not efficient preheating of the ceramic filter, the melt solidifies faster, and the infiltration of the small cavities was impossible. As a result, the tests were performed with an additional cavity in the lower part of the mold, yielding a more uniform infiltration quality [3, 7].

The effect of the phosphorus content in the melt on the infiltration quality is shown in Fig. 4.4. By adding phosphorus, it is possible to infiltrate the 10 ppi filters preheated to 1000 °C nearly independent of the sample area. The best results concerning to the cavity thickness as well as the fraction of the infiltrated cavities were achieved by a phosphorus content of 0.2 mass% [3, 7].

To conclude, the infiltration quality depends primarily on the phosphorus content of the melt and thus on the viscosity and the melt flow through the filter package.

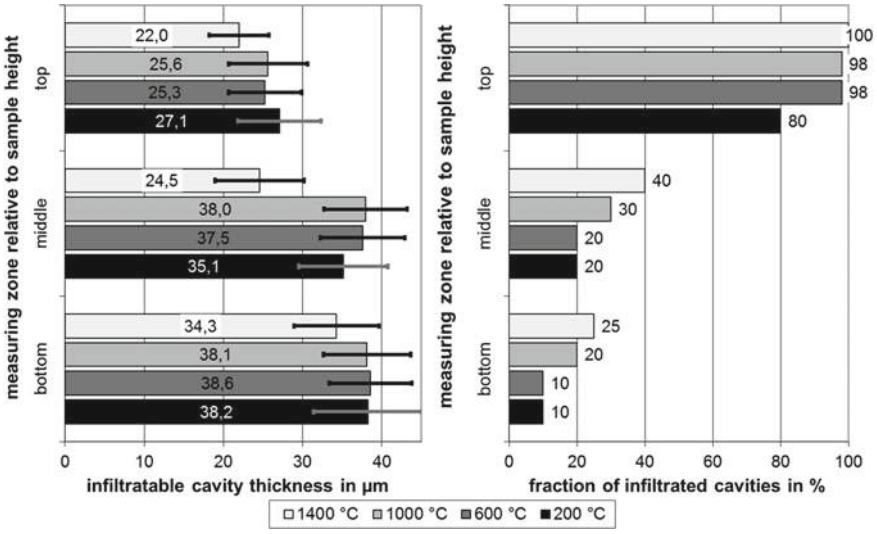

Fig. 4.3 Effect of the preheating temperature on the infiltration quality (cast steel X3CrMnNi 16-7-6 and 10 ppi filter). Adapted from Weider [3]

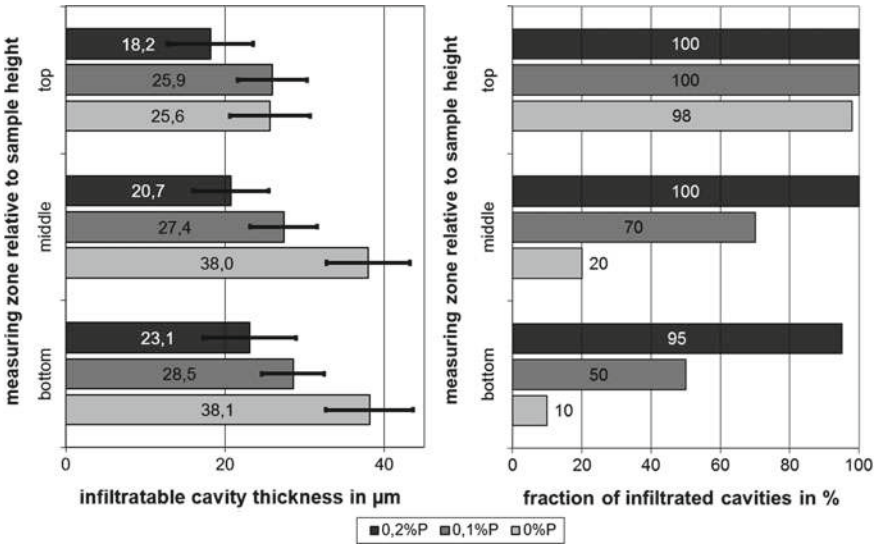

Fig. 4.4 Effect of phosphorus on the infiltration quality (cast steel X3CrMnNi 16-7-6 and 10 ppi filter). Adapted from Weider [3]

The influence of the preheating temperature of the ceramic filter before casting is less important in comparison to the location of the filter. In order to ensure a better infiltration quality, it is advisable to have an additional cavity under the filter package to preheat the ceramics by the additional melt flowing through the filters [3, 7].

4.4 Wear Properties of ZrO_2-Based Metal-Matrix-Composites

Metals can be reinforced with hard particles to increase the wear resistance of casings. For example, wear resistant parts are often made of white cast iron with a high content of carbide building elements, hard particles precipitating during solidification and heat treatment. If the hardness and wear resistance of the composites increases, the toughness often decreases. Therefore metastable austenitic-martensitic steels were chosen as matrix material, which demonstrates a TRIP-effect and transforms into α´-martensite by applying a load. As a consequence, the core of the castings is comparatively tough compared to the transformed wear area [8, 9].

To ensure good bonding of the steel to the ceramic, it is advisable to influence the thermophysical properties of the liquid melt. In addition to the contact angle and viscosity, the surface tension of the liquid melt can be reduced and the ability to infiltrate small pores in the porous ceramic structures can be increased. The flowability of CrMnNi steels can be increased by up to 0.18% of phosphorus content, so that

porous structures are infiltrated without any negative influence on the mechanical properties of the steel [7]. Furthermore, the contact angle between ceramic and melt can be reduced by adding titanium on the ceramic surface [10]. Dubberstein et al. reported in [11] about the influence of sulfur on the contact angle. Accordingly, the contact angle decreases from 102° at a sulfur content of 137 ppm to 92° at a sulfur content of 696 ppm.

4.4.1 Three-Body Abrasive Test

The characterization of the abrasive wear properties was carried out at a block/ring-testing station. The block/ring-testing station allows a variety of sample sizes, abrasive materials and metal pairings at different speeds and contact pressures. The results of the tribological test are a system parameter [12]. The most important advantage to other wear testing techniques is the variable sample size, so that the tests are also possible with MMCs with infiltrated hard particles in the range from 5 mm to 10 mm. The castings, needed for producing the wear samples, were manufactured as described in chapter 4.2. A 3.4 mass% magnesia partially stabilized zirconia foam structure with a porosity of 30 ppi was infiltrated. As matrix material metastable austenitic-martensitic X3CrMnNi 16-7-3 and 16-7-6 steels were chosen. The steel is poured into the infiltration mold at a casting temperature of 1600 °C. After solidification and cooling, the casting is machined and samples are taken out from the center of the infiltration area to investigate the wear properties. The samples had the dimensions 65 × 25 × 20 mm^3 with a 5 mm 45° bevel. A schematic illustration of the block/ring-testing station can be seen in Fig. 4.5 [9].

Abrasive particles can be dispersed in front of the sample for three-body abrasion. In these tests silica sand with a grain size of 0.1–0.5 mm flow out constantly in front of the chamfered edge to ensure new sand grains for each rotation. The sample was pressed onto the NiHard 4 ring with a load of 0.5 MPa, whereby the ring with a

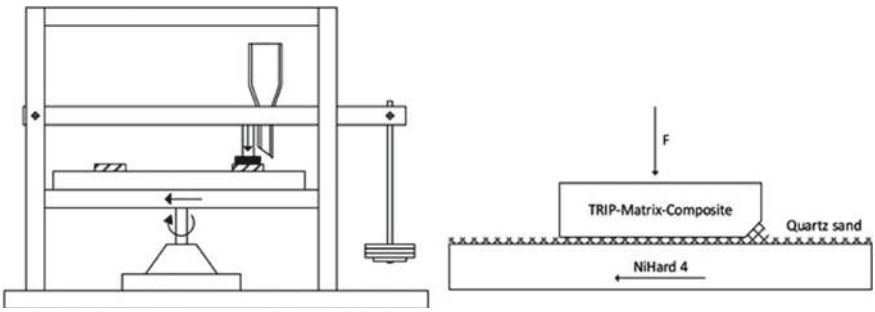

Fig. 4.5 Schematic illustration of the block/ring wear test [8]

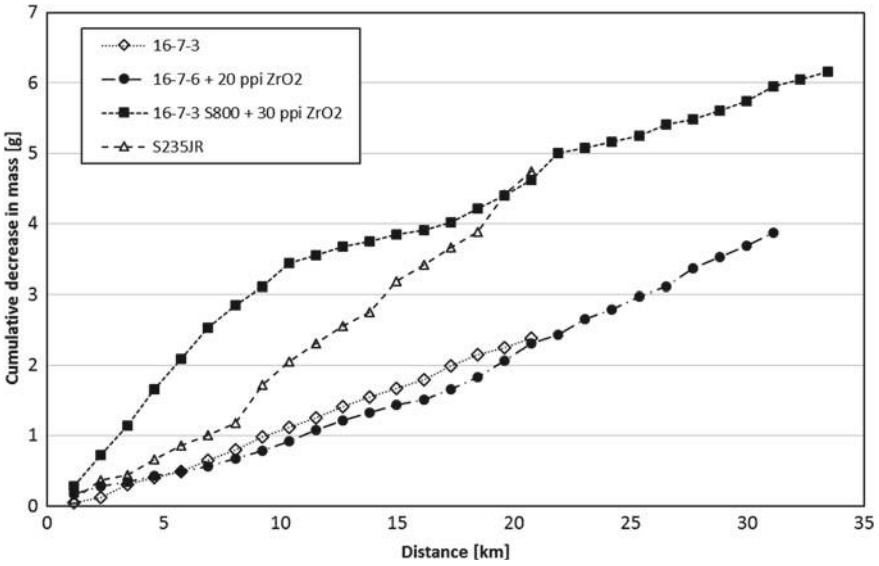

Fig. 4.6 Cumulative decrease in mass versus distance

circumference of 1.153 m was rotated with 26 min^{-1}. After 1000 rounds, the mass of the sample was measured and the wear test continued for at least 15 km [8, 9].

Figure 4.6 shows the decrease in mass of the wear samples over the distance on the block/ring-testing station. After an uneven loss of mass during the begin of the measurement, it stabilizes with increasing mileage. At the first 10 km, the 16-7-3-ZrO_2 sample demonstrates higher wear in comparison to the other samples. After that, it has decreased strongly and stabilized at 22 km. The pure TRIP steel has a significantly lower wear rate compared to construction steel. In order to evaluate the results better, the increase in wear is related to the distance. However, only the areas after the wear has evened out are considered. The results are shown in Table 4.3. The designations S800, S1000, P1800 and P2000 given therein describe the respective sulfur and phosphorus content in ppm.

Due to the lower M_s-temperature of the steel 16-7-3 compared to the steel 16-7-6, even smaller local stresses lead to martensitic transformation and thus to better wear behavior. The wear also increases with a fineness of the foam ceramics and with the sulfur as well as with the phosphorus content of the samples. The better infiltration tendency of sulfur-alloyed steels cannot compensate for the tendency of increasing wear known from the literature [9]. The finer foam ceramics have thin struts as well as a high microporosity due to the manufacturing process. This means that the ceramics have little resistance to abrasive wear, which is associated with breaking out of the metal matrix.

Table 4.3 Average wear in mass loss per distance and its standard deviation. Adapted from Acker [9]

Material	Mass loss per distance (mg/km)	Standard deviation (mg/km)
16-7-3	116	31
16-7-6	134	55
S235JR	241	64
16-7-3 S800 + 30 ppi ZrO_2	103	35
16-7-3 P1800 + 60 ppi ZrO_2	207	72
16-7-3 P2000 + 60 ppi ZrO_2	263	114
16-7-6 S1000	318	99
16-7-6 + 20 ppi ZrO_2	139	42
16-7-6 + 30 ppi ZrO_2	223	78

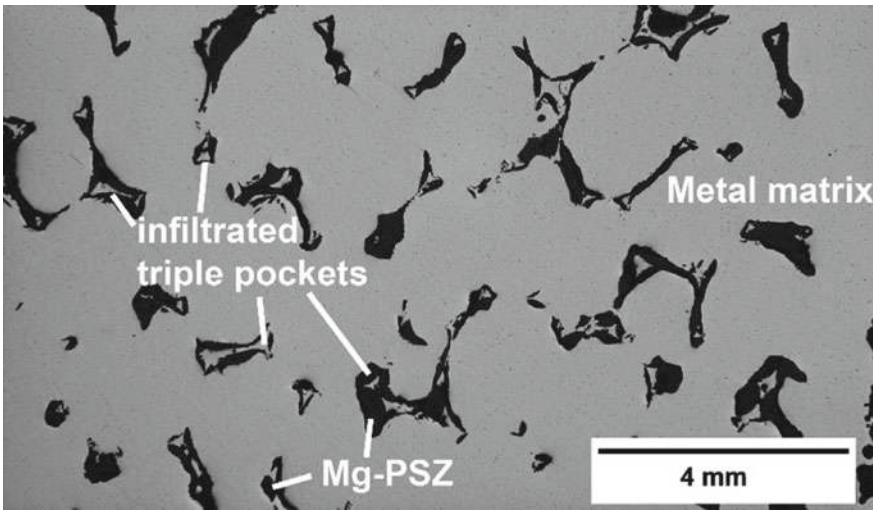

Fig. 4.7 Optical micrograph of a MMC containing cast steel X3CrMnNi 16-7-3 steel, alloyed with 800 ppm sulfur, and 30 ppi Mg-PSZ-foam ceramic [8]

4.4.2 Microscopy of the MMC

After casting, the samples were cut out of the middle part of the infiltration area at a distance of approx. 20 mm from the wall. Besides an optical microscope evaluation (Olympus BX51M), a scanning electron microscope investigation was carried out (ZEISS LEO 1530) with 20 kV in the backscattered contrast mode.

Figure 4.7 shows a micrograph of a 30 ppi Mg-PSZ foam and X3CrMnNi 16-7-3 alloyed with 800 ppi sulfur. Macroscopically no shrinkage cavities are visible. From a sulfur content of 500 ppm, the surface of the melt is covered with sulfur and thus

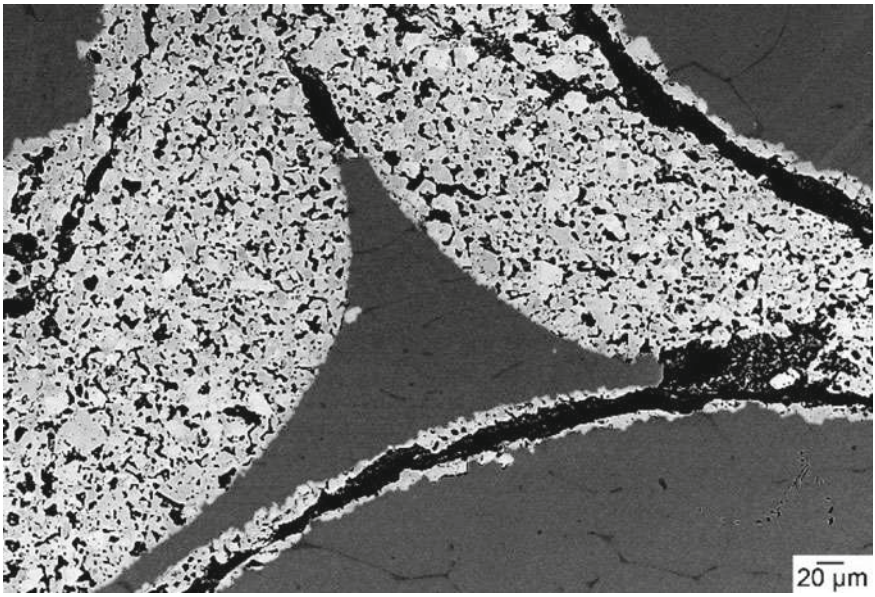

Fig. 4.8 SEM image of a 30 ppi Mg-PSZ foam infiltrated by cast X3CrMnNi 16-7-3 steel with cracks in the ceramic structure [9]

the surface tension of the melt is determined, so that the triple pockets could be filled [13].

In a closer SEM investigation, as displayed in Fig. 4.8, the good quality of the interface bonding is visible on a microscopic level. Due to the porosity-related low strength of the ceramic, the cracks do not run along with the interface, but within the ceramic. The different coefficients of expansion of steel and ceramic and the good interface bonding are leading to a stress gradient in the ceramic and the interface, which ultimately leads to cracks in the porous ceramic foams [14]. The tendency to crack formation is promoted by the infiltration of foam structures, since ceramic struts of different widths allow the melt to cool locally at different rates, which is associated with an increase in stress differences.

4.5 Infiltration of Loose Ceramic Particles with Steel and Their Wear Behavior

The MMC containing TRIP-steel and foam ceramics described in the previous chapter have no significant influence on the wear resistance. The expected phase transformation in the Mg-PSZ ceramic foam cannot be observed, because the force transmission of the deforming steel matrix is not sufficient. As a consequence the effect of closing micro cracks due to the transformation of the ceramic does not

occur in the present case [3]. In addition to the infiltration of the ceramic foams, the infiltration of loose ceramic particles has proven to be a practical way of producing wear-loaded cast parts with local ceramic reinforcement. Basic tests were carried out with the mold shown in Fig. 4.1. Special attention was paid to the wear resistance of the MMC and the interface between steel and ceramic. In order to transfer the knowledge gained to practice, a new possibility was developed to produce locally reinforced MMC in gravity casting. For this purpose, the lower density of the ceramics was exploited by rinsing the hard particles in a targeted manner.

4.5.1 Static Infiltration of Loose Ceramic Particles

Similar to the infiltration of ceramic foams, loose ceramic bulks were infiltrated. As matrix material, a high alloyed metastable austenitic-martensitic X3CrMnNi 16-7-3 was chosen. The composition is shown in Table 4.4. Due to its low M_s-Temperature of 61 °C, the chosen steel needs only low triggering stresses to transform from austenite to martensite [15]. As reference material, NiHard 4 in its cast and heat treated state was investigated. The composition is also displayed in Table 4.4.

As reinforcing material three hard particles, displayed in Table 4.5, were infiltrated. The aluminum oxide spheres have a particle size of 6.4 mm (Mühlmeier Mahltechnik, Germany). The white fused mullite (WFM) and the fused zirconia mullite (ZrM) (Imerys Fused Minerals, Germany) have a particle size between 4 and 12 mm. The WFM shows a uniform Al_2O_3-rich mullite structure with approx. 80% Al_2O_3 and 20% SiO_2 containing only minor SiO_2-rich areas. The ZrM consists of a mullite structure with incorporated ZrO_2-grains. All three ceramics exhibit lower thermal expansion coefficients between 5.0 and 6.4 10^{-6} K^{-1} compared to high alloyed stainless steels with a range of 16–18 $\times$ 10^{-6} K^{-1} [16].

According to their higher insulation capacity according to silica sand, CeraBeads 650 (Hüttenes-Albertus, Germany) were used as molding sand [4]. Sodium silicate binder is well known to minimalize the chemical reactions between the steel and the

Table 4.4 Chemical composition of the used TRIP-steels and the reference material. Adapted from Acker [9]

Alloy	C	Si	Cr	Mn	Ni	Mo	P	S	Fe
	(mass%)								
X3CrMnNi 16-7-3 ZrM	0.045	0.84	15.9	6.8	3.4	0.042	<0.003	0.009	Bal.
X3CrMnNi 16-7-3 WFM	0.045	0.85	15.7	6.7	3.4	0.034	<0.003	0.006	Bal.
X3CrMnNi 16-7-3 Al_2O_3	0.054	0.88	15.7	6.7	3.3	0.037	<0.003	0.007	Bal.
NiHard 4 heat treated	3.26	1.37	10.2	0.6	5.7	0.180	0.015	0.07	Bal.

Table 4.5 Composition of the infiltrated hard particles. Adapted from Acker [9]

Ceramic	Size	Al_2O_3	SiO_2	Fe_2O_3	CaO	MgO	Na_2O	K_2O	TiO_2	$ZrO_2 + HfO_2$
	(mm)	(mass%)								
Al_2O_3-spheres	6.4	99.5	0.1	<0.1	<0.1	0.2	<0.1	0.01		
WFM	4–7	76.0	23.5	0.05	0.02		0.2		0.02	
ZrM	5–12	45.7	17.8	0.1	0.1		0.1		0.1	36.0

molding sand and is therefore used. The steel was melt in a 30 kg open induction furnace. Directly before casting the preheated ceramics up to 1400 °C were filled into the mold. In order to prevent floating of the ceramics a 10 ppi casting filter (Drache, Germany) was placed on the ceramic heap and secured against floating with glass rods (Fig. 4.1). To ensure a minimum of heat loss, the melt was poured with a temperature of 1600 °C directly from the induction furnace into the mold.

After casting and cooling microscope investigation and three-body-abrasive tests were carried out.

4.5.1.1 Microscopy

All samples were completely infiltrated, depicted in Fig. 4.9. There was no macroscopic porosity and because of the directional solidification from the lower area to the upper one, there were no local cold runs visible.

At higher magnification, shown in Fig. 4.10, gaps of 10–20 μm can be seen for the Al_2O_3-steel composite. In the shown section no bonding between the steel and the aluminum oxide spheres is visible. The gaps result in breaking out of the spheres during machining. With the help of the SEM examination, it was possible to prove that oxides from the corundum side are on the steel surface and chromium, iron and manganese are located on the ceramic side. It can be therefore assumed that wetting has taken place and that the bond has broken as a result of solidification and cooling. The two materials move away from each other as a result of shrinkage. The cracks are caused by the stresses generated by the different thermal expansion coefficients.

Both mullites show a better interface connection. Slag phases were formed in the mullites. The white fused mullite formed a spessartite phase with a composition of 34% MnO, 40% SiO_2 and 22% Al_2O_3 and a resulting melting phase of 1195 °C. In zirconium mullite, the spessartite-like phase formed had a composition of 26% Al_2O_3, 37% SiO_2, 30% MnO and 2% NaO with a melting point below 1300 °C [17, 18]. The comparatively low melting point of the slags buffers the stresses arising during cooling down to their solidification temperature.

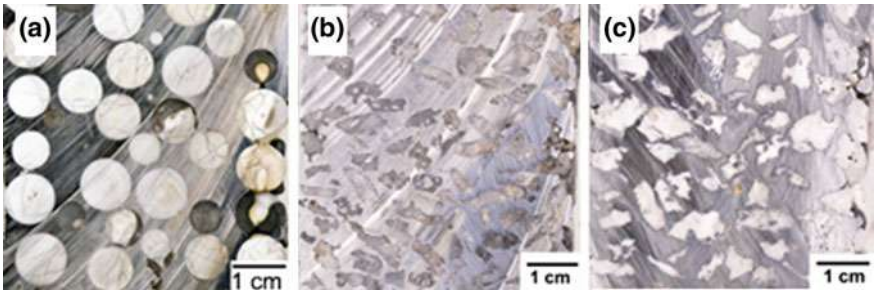

Fig. 4.9 Sectional views of the MMC, **a** Al_2O_3-spheres, **b** WFM, **c** ZrM

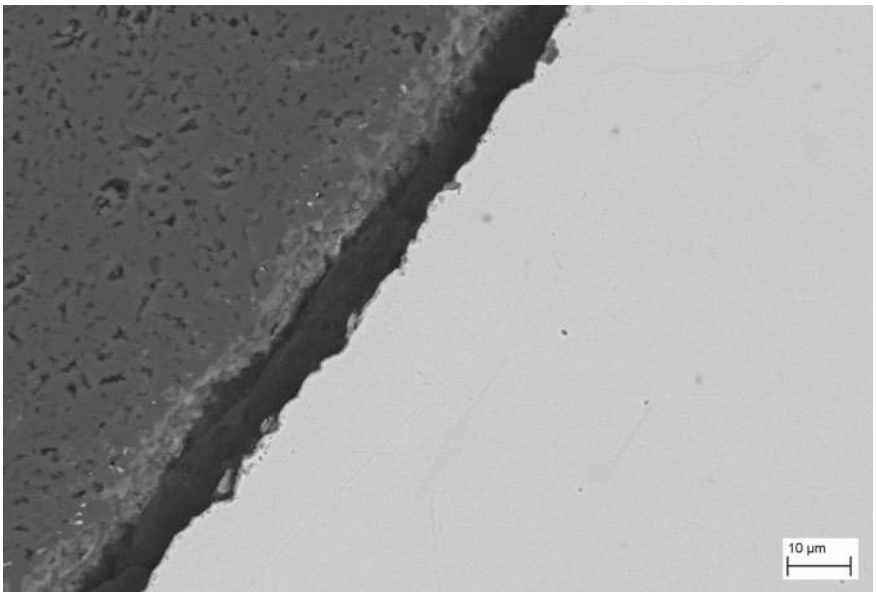

Fig. 4.10 SEM image of a MMC consisting of 9.6 mm Al_2O_3 spheres and X3CrMnNi 16-7-3 with the cooling crack between both materials

The irregular grain shapes creates a frictional connection between the matrix and the reinforcing phases. In addition, there was a different shrinkage in different directions of the ceramics because of the irregular particle shapes. The molten steel could image even small gussets on the ceramic side. Therefore, cracks in the boundary layer caused by cooling were unavoidable.

4.5.1.2 Wear Behavior

The wear behavior of the samples was investigated at a block/ring-station, as described above. The results are shown in Fig. 4.11. When comparing the wear rate as a decrease in mass per distance, the zirconia mullite based MMC demonstrates a wear reduction down to 93 mg km^{-1} and white fused mullite based MMC of 64 mg km^{-1}. Due to the breaking out of the corundum spheres, the wear value of the Al_2O_3-steel composite was not evaluated.

Generally, the mullite-based composites show better wear rates compared to NiHard4 and the cast X3CrMnNi 16-7-3 steel. The amount of α'-martensite in the investigated TRIP-steel is increasing up to 97% at the loaded surface [8]. The effect of the near-surface martensitic transformation and the associated increase in hardness is intensified by the addition of ceramics, which are form-fittingly embedded in the matrix.

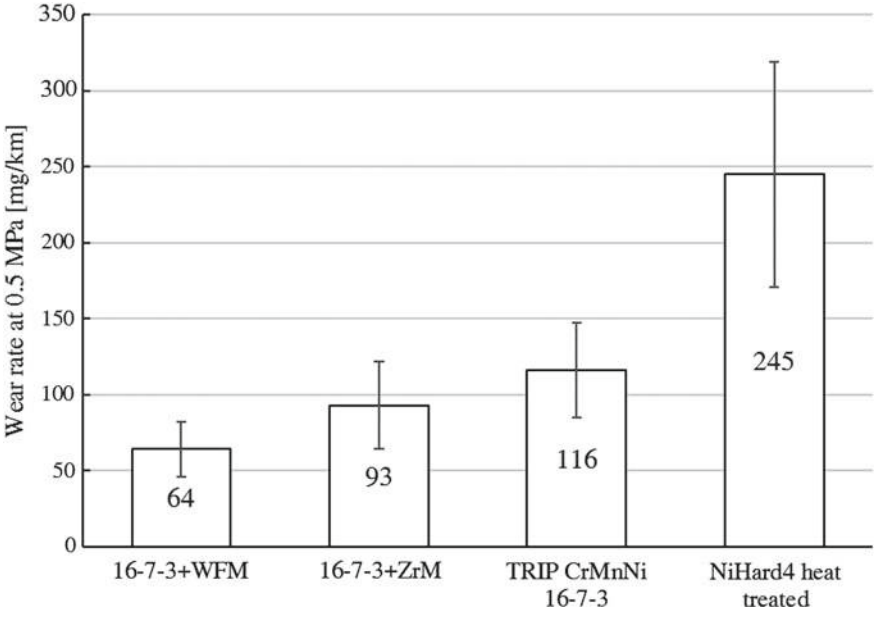

Fig. 4.11 Wear rate as a decrease in mass per distance

4.5.1.3 Interfacial Optimization by Coating with Titanium Oxide

Titanium is known as an alloying element because it is soluble in steels and also as an oxide in Al_2O_3. The absorption of titanium into the ceramic surface creates a layer that can serve as a bonding layer between metal and ceramic [17]. Especially on aluminum oxide, titanium melts can lead to an improvement of the interfacial bonding through the formation of titanium oxides and (Ti, $Al)_2O_3$ phases as well as intermetallic phases [18]. With this background, the interest was to improve the interface between steel and ceramics by the formation of aluminum titanate with the aim of crack reduction. Aluminum titanate is a high temperature phase which decomposes without the presence of stabilizers such as Fe_2O_3 or Si_2O_3 into rutile and α-Al_2O_3 at a temperature below 1280 °C [19].

First, the corundum spheres and mullite particles were produced by pelletizing in aqueous suspension, consisting of 30% TiO_2 powder and water, by dipping, drying and subsequent sintering. After mixing the spheres for 180 s, they were separated from the slurry using a sieve and then dried in a drying furnace for 24 h at 60 °C. The subsequent firing process was carried out at 1050 °C, to prevent the formation of aluminum titanate, as it can form at temperatures of 1100 °C and above [20].

After steel infiltration, the titanium oxide coated materials had a peripheral zone, which can be seen in Fig. 4.12. During the infiltration process, a reaction took place between the titanium oxide and the aluminum oxide. The interface layer between steel and ceramic had a thickness of about 10 μm and yielded a better connection. The

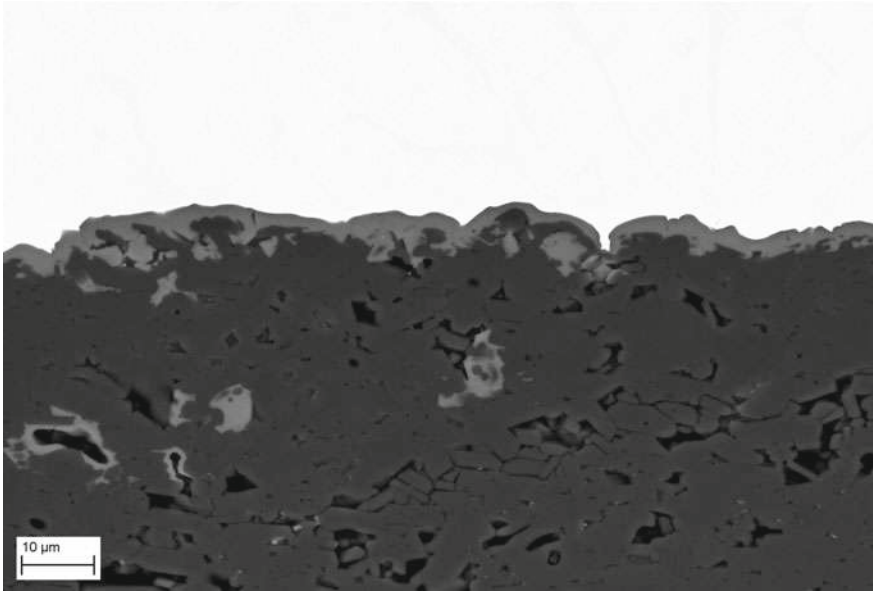

Fig. 4.12 SEM image of the interface between coated corundum spheres and X3CrMnNi 16-7-3

Table 4.6 Composition of the interface

	Al_2O_3	MnO	TiO_2	Cr_2O_3
	(mass%)			
Boundary layer	50	41	2	7
Incorporated spinel	52	38	6	4

EDX analysis of the interface, shown in Table 4.6, demonstrates, that a manganese-rich compound was formed with titanium oxides and aluminum oxide, which had a liquid phase fraction of up to 1100 °C and can therefore reduce stresses arising during cooling. The macroscopically visible discolorations consist of Al_2O_3 grains with incorporated spinel compound, which had a composition similar to the boundary layer. It can be assumed that the temporarily formed aluminum titanate has been transformed into manganese aluminate and manganese titanate by the presence of manganese.

4.5.2 Dynamic Infiltration of Loose Ceramic Particles

With the static infiltration method, it is difficult to produce industrial castings with a local ceramic reinforcement. In addition to static infiltration, where the ceramics

are infiltrated as bulk, the ceramics can also be infiltrated dynamically. This means that the ceramics are transported flow-induced through the melt to their destination. The large difference in density between steel and ceramics can consciously be used to rinse ceramics in the upper part of the casting.

Initially, a casting mold was developed, which makes only infiltration of ceramic particles possible, as it turned out that ceramic foams have no positive effect on the wear resistance. The gating system was deliberately designed generously, as the ceramics remove a large amount of heat from the melt despite preheating and this deficit has to be compensated by a larger melt mass.

The aim of the developed infiltration mold is to produce samples for the block/ring-testing station with a local ceramic reinforcement in the wear area, according to Fig. 4.13, with minimal resource expenditure. Between the wear sample and the spherical feeder is the flow zone in which various possibilities can be tested to stop the further buoyancy of the ceramics and to ensure a glistening distribution of these. A 5 mm thick ceramic filter has proven its worth as insert for the flow zone. A cell filter with a mesh width of 2 mm is used, as foam filters of this thickness possess not sufficient strength. The falling casting system was chosen, so that the preheated ceramics, which were filled in the sprue directly before casting, were carried along by the turbulences arising during the casting process. As can be seen in Fig. 4.14,

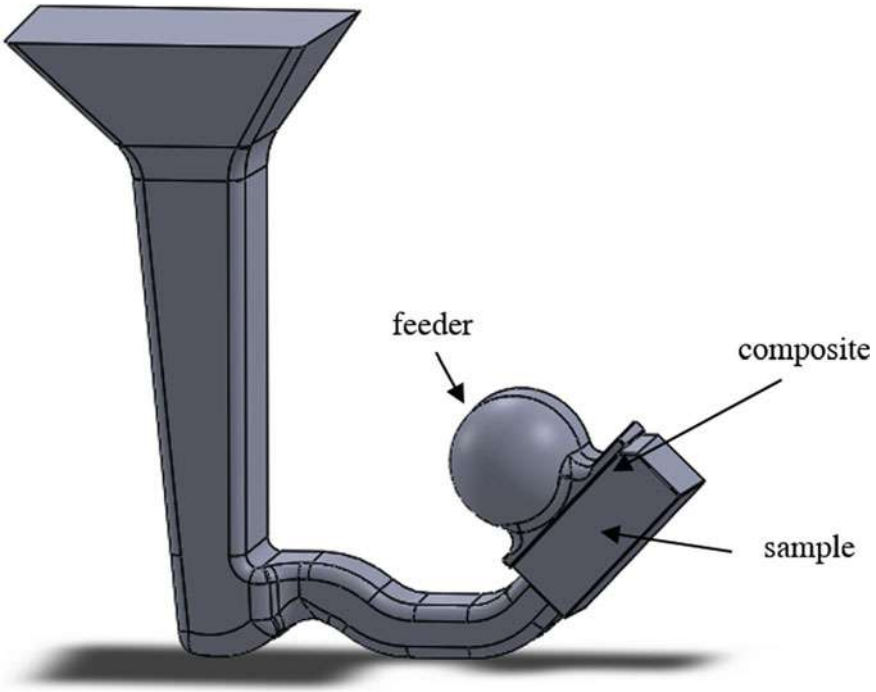

Fig. 4.13 CAD model of the infiltration casting with the wear sample below the spherical feeder

Fig. 4.14 Simulated static flow conditions in the lower area of the mold at the end of the casting process

Table 4.7 Chemical composition of the casted steels

Alloy	C	Si	Cr	Mn	Ni	Mo	Fe
	(mass%)						
X3CrMnNi 16-7-3	0.04	1.08	16.91	6.4	2.93	0.02	Bal.
Mn-Hard	1.47	0.643	0.34	13.58	0.11	0.004	Bal.

the pressurized casting system leads to high flow velocity in the gate, so that as few ceramic particles as possible accumulate on the molding material wall. Due to the 45° inclination of the test specimen, the ceramics were rinsed specifically against the filter. After cooling down and solidification, the casting was machined by removing the gating and the feeder system with the flow zone, so that the resulting wear sample can be used directly at the block/ring-testing station.

A TRIP steel X3CrMnNi 16-7-3 and a Hadfield steel (called Mn-Hard) were selected for the tests. The compositions are shown in Table 4.7. Melting took place in a 50 kg induction furnace. After deoxidizing with 0.05 mass% aluminum, the melt was poured into the mold at a pouring temperature of 1600 °C. Before casting, the zircon corundum particles were heated up to 1400 °C in a laboratory furnace. Above 1400 °C, a sintering process begins so that the particles cannot be preheated at higher temperatures. An infiltration of not preheated ceramics could not be carried out successfully, because a solidified steel shell immediately formed around the ceramics, which prevented the ceramics from flowing away as well as an infiltration of the particles. The composition of the particles (Imerys Fused Minerals, Germany) with a size between 1230 and 1765 µm is shown in Table 4.8.

Table 4.8 Composition of the infiltrated zircon corundum particles

Al_2O_3	ZrO_2 + HfO_2	TiO_2	Fe_2O_3	Si-, Mg-, Ca-, Na-, K-Oxide
(mass%)				
55.0	41.0	3.0	0.1	0.9

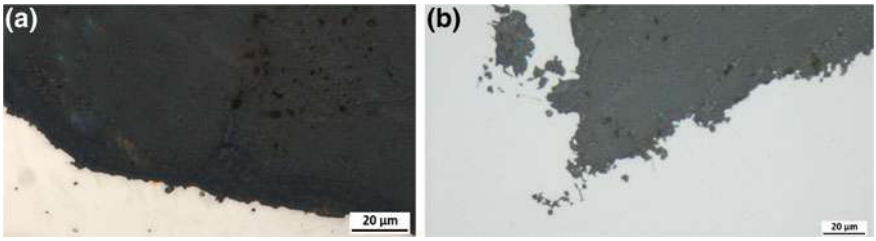

Fig. 4.15 Optical microscope images of infiltrated zirconia corundum with X3CrMnNi 16-7-3 (**a**) and Mn-Hard (**b**)

4.5.2.1 Microscopy

In order to assess the interface connection, microscopic examinations were carried out analogously to the previous chapters. On the one hand, images were taken with an optical microscope and on the other hand, pictures including line scan were performed with SEM. Figure 4.15 shows the bonds between the TiO_2 coated zirconia corundum and the two different types of steel. The ceramic has only a low porosity, which is important for good wear behavior. Both steels show a very good bond. By this kind of infiltration, whereby the ceramics are whirled by the melt, the liquid steel has sufficient time to heat the ceramics, so that a very good clinging takes place between steel and ceramics. The dynamical process is leading to an infiltration of small recesses in the ceramics. Due to the non-compact accumulations of the ceramics, local solidification between the ceramics and thus also the tensions in the boundary layer are reduced. It can be assumed that the steel can shrink onto the ceramic and thus the movement of the materials away from each other is prevented.

In order to analyze the composition of the boundary layer, examinations at a SEM with the aid of EDX are suitable. The line scan is useful to make statements about the change in concentration. The right area of Fig. 4.16 shows the steel, which is characterized by the high iron content. In the left area the ceramic is present, which consists of aluminum, zirconium and oxygen. The visible connecting layer has a thickness of approx. 7 µm. In comparison to the ceramics, the elements Mn, Ti and Zr are enriched in this area. The content of Al is below that in the ceramic. These facts coincide with the findings in Sect. 4.5.1.3. Complex manganese-rich mixing phases with a fluctuating Zr and Al content arise, which lead finally to a chemical bond between steel and ceramics.

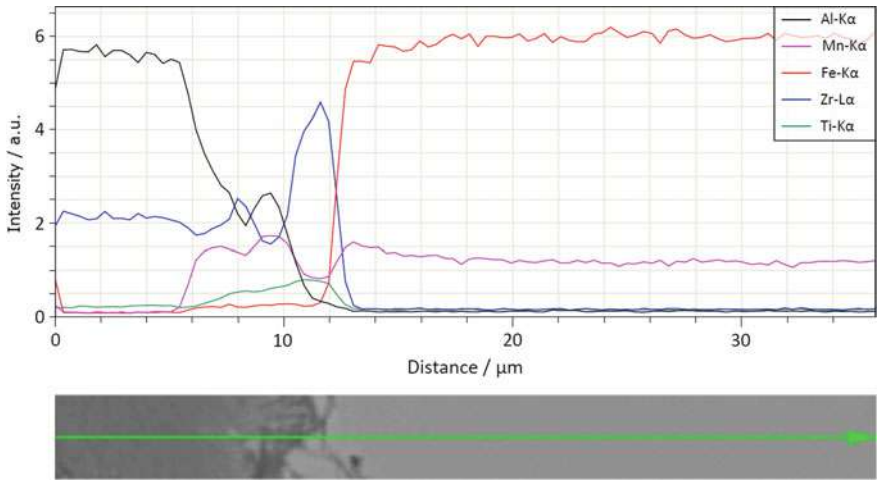

Fig. 4.16 EDX line scan of the boundary layer of TiO_2 coated zirconium corundum infiltrated by Mn-Hard steel

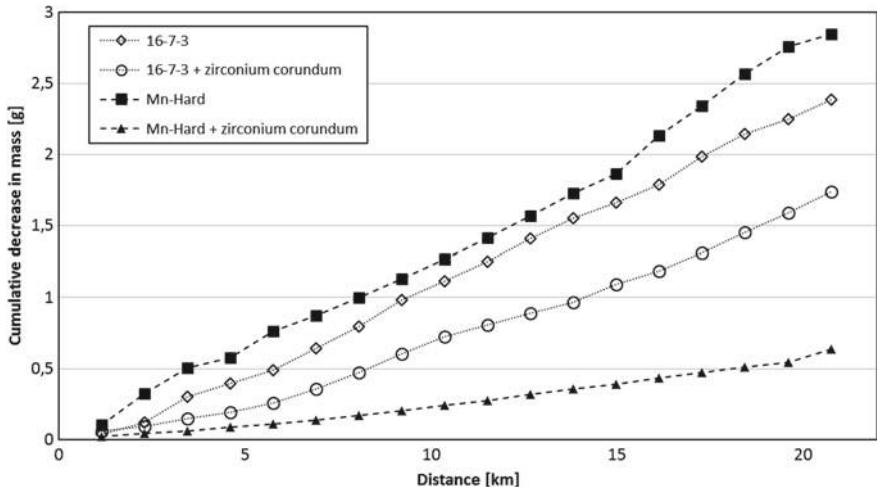

Fig. 4.17 Cumulative decrease in mass versus distance

4.5.2.2 Wear Behavior

The wear behavior of the samples was investigated at the block/ring-station. By optimizing the block/ring-testing station with a steadier supply of quartz sand, a more uniform wear behavior could be observed, which is reflected in straighter curves in Fig. 4.17. The investigations on the block/ring-testing station showed that the X3CrMnNi 16-7-3 steel behaves similarly in the point of abrasive wear behavior

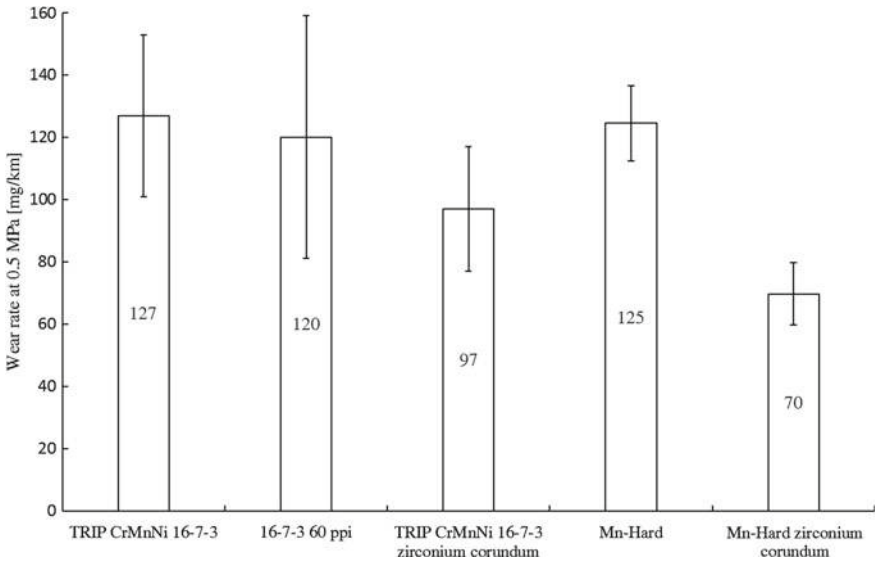

Fig. 4.18 Wear rate as a decrease in mass per distance

compared to the high manganese alloyed steel Mn-Hard. As can be seen in Fig. 4.18, the combination of Mn-Hard and zircon corundum shows the lowest abrasive wear. With a wear value of 70 mg/km, the MMC is significantly more wear resistant than the non-reinforced material. The low standard deviation of the wear value is reflected in the very good bonding and toughness of the zirconium corundum ceramic. These ceramics protrude from the metal matrix and do not break out in brittle layers. Investigations on a 3D microscope showed that the ceramics protrude up to 300 µm from the ablated metal matrix. The manufacturer's data show that the fine crystalline structure combined with the high proportion of tetragonal stabilized zirconium oxide produces a very pronounced self-sharpening effect during grinding. In addition to the self-sharpening effect of the ceramic, the good bonding between the steel and the ceramic has proven to be effective.

4.6 Conclusions

The manufacturing process of novel metal ceramic composite materials is described. First, basic investigations were carried out on the TRIP steel infiltration of ZrO_2 ceramic foams. Different mold materials were investigated and it turned out that Cerabeads have an insulating effect as mold material and that the chemical interactions were lowest. By adding 0.2% phosphorus, the infiltration quality of X3CrMnNi 16-7-6 melt can be significantly increased, while the melt temperature in this test arrangement has a lower effect. Furthermore, fine gussets in the ceramic foams can

be filled by the addition of sulfur. In order to characterize the wear behavior of the new composite materials, tests were carried out on the block/ring-testing station. The investigations revealed that MMCs with infiltrated ceramic foams show no advantage with regard to wear resistance. Rather, the MMCs with ceramic particles have the best wear properties. Particularly noteworthy is the composite of Mn-Hard steel with melt-broken zircon corundum. In addition to the positive effect on the boundary layer by coating the ceramics with TiO_2, the interlocking of the irregular particles leads to a reliable connection between ceramics and the steel. Based on these findings, a process was developed to produce a locally reinforced casting. The preheated ceramic particles were filled into the casting mold and then rinsed directly with the molten steel to the desired areas within the mold. The lower density of the ceramics is thus exploited in a targeted manner. This process significantly reduces the tendency to form cracks in the boundary layer between ceramic and steel. Since the ceramics are loose, the steel can shrink onto them. In the future, this process could be used to manufacture wear-resistant components, such as excavator teeth, etc. Figure 4.19 shows a section through the tip of a bucket tooth locally reinforced with ceramic particles, whereby the core of the tooth is free of ceramics and can therefore withstand the impacting stresses. The service life of such components can be extended because of the higher wear resistance, so that costs may be reduced.

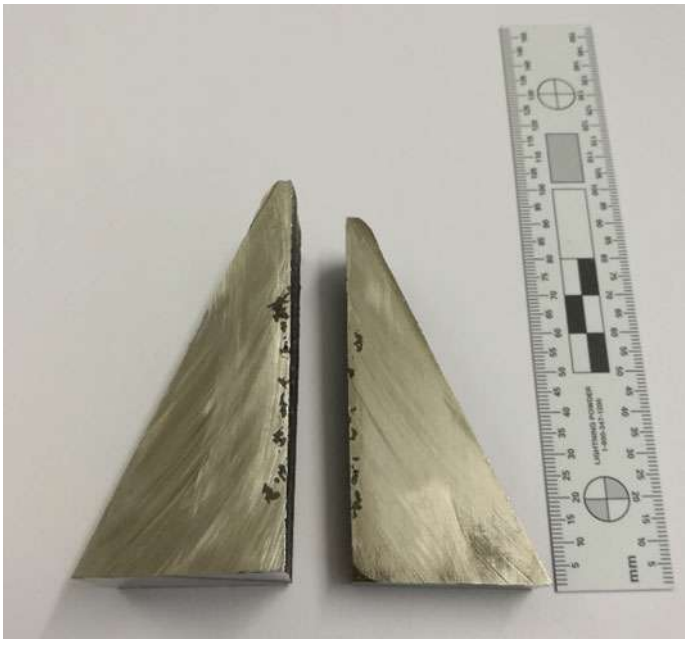

Fig. 4.19 Section through the tip of a bucket tooth locally reinforced with ceramics

Acknowledgements The authors gratefully acknowledge the financial support for this research by the Deutsche Forschungsgemeinschaft (DFG, German Research Foundation, Project number 54473466—CRC 799) and Prof. Dr.-Ing. Klaus Eigenfeld, Dr.-Ing. Marco Weider as well as Dr.-Ing. Richard Acker for the fundamental research in the field of steel casting infiltration by liquid melt in the subprojects A4, S1 and T4 of the collaborative research center (CRC799) "TRIP-Matrix-Composite".

References

1. A. Jahn, A. Kovalev, A. Weiβ, P.R. Scheller, S. Wolf, L. Krüger, S. Martin, U. Martin, Mechanical properties of high alloyed cast and rolled CrMnNi TRIP steels with varying Ni contents. ESOMAT **2009**, 05013 (2009). https://doi.org/10.1051/esomat/200905013
2. M. Weider, H. Polzin, K. Eigenfeld, W. Schärfl, Thermal interactions between casted high-alloyed TRIP steel and sodium silicate bonded moulding systems. Refract. World Forum **3**, 136 (2011)
3. M. Weider, Doctorate Thesis, TU Bergakademie Freiberg, 2015
4. W. Tilch, M. Martin, Properties and application of alternative moulding sands for the manufacture of light-weight-castings. Gießereiforschung **58**, 18 (2006)
5. F.D. Richardson, J.H.E. Jeffes, The thermodynamics of substances of interest in iron and steel making from 0 °C to 2400 °C: I-oxides. Iron Steel Inst. **160**, 160–261 (1948)
6. T. Dubberstein, H.-P. Heller, Effect of steel viscosity on metallurgical processing, in *6th International Congress on the Science and Technology of Steelmaking*, China Machine Press 2015
7. M. Weider, K. Eigenfeld, Steel Res. Int. **82**(9), 1064–1069 (2011). https://doi.org/10.1002/srin.201100071
8. R. Acker, S. Martin, K. Meltke, G. Wolf, Steel Res. Int. **87**(8), 1111–1117 (2016). https://doi.org/10.1002/srin.201500471
9. R. Acker, Doctorate Thesis, TU Bergakademie Freiberg, 2018
10. K. Lemster, T. Graule, J. Kuebler, Mater. Sci. Eng. A **1–2**, 385 (2005)
11. T. Dubberstein, H.-P. Heller, C. Wenzel, C.G. Aneziris, in *Proceedings of the 10th International Conference of Molten Slags, Fluxes and Salts* (Springer International Publishing, Basel, 2016), pp. 1371
12. A. Rosin, Doctorate Thesis, TU Bergakademie Freiberg, 2014
13. S. Seetharaman (ed.), *Fundamentals of Metallurgy* (Woodhead Publishing Limited, Cambridge, 2005)
14. V. Grethe, Doctorate Thesis, TU Clausthal, 1994
15. A. Kovalev, A. Jahn, A. Weiß, S. Wolf, P.R. Scheller, Steel Res. Int. **82**(9), 1101–1107 (2011). https://doi.org/10.1002/srin.201100065
16. W. Martienssen, H. Warlimont, *Handbook of condensed matter and materials data* (Springer, Heidelberg New York, 2005)
17. D. Wittig, A. Glauche, C.G. Aneziris, T. Minghetti, C. Schelle, T. Graule, J. Kuebler, Mater. Sci. Eng., A **488**, 580–585 (2008). https://doi.org/10.1016/j.msea.2007.11.065
18. L. Espié, B. Drevet, N. Eustathopoulous, Metall. Mater. Trans. A **25**, 599–605 (1994). https://doi.org/10.1007/BF02651601
19. C. Weigelt, C.G. Aneziris, D. Ehinger, R. Eckner, L. Krüger, C. Ullrich, D. Rafaja, J. Compos. Mater. **49**(28), 3567–3579 (2015)
20. J. Bossert, C. Ludwig, Materialwiss. Werkstofftech. **28**(5), 241–245 (1997)

Chapter 5
Ceramic Extrusion Technologies for Fine Grained TRIP Matrix Composite Materials

Christian Weigelt, Marie Oppelt and Christos G. Aneziris

Abstract Metal-Matrix-Composites (MMCs) based on steel with certain ceramic additions offer a wide range of applications in automotive, construction, and mechanical engineering. These MMCs combine the specific properties of steels such as their room temperature deformation behavior with the advantageous hard but brittle ceramic reinforcements which makes them favorable in crash-absorbing or strengthening components. However, common technologies such as casting or infiltration of ceramic preforms by metal melts suffer from the differences between metal and ceramic material characteristics involved during material processing and from geometrical restrictions. The adaption of the ceramics-derived extrusion technology at ambient temperature on materials established in the powder metallurgy (PM) enables an efficient manufacturing process of advanced fine-grained materials with particularly cellular (lightweight) structures as well as bulk specimens. Using powder raw materials enables a wide range of material combinations between TRIP/TWIP steels and various ceramic components considering the pronounced material characteristics of the composite. Knowing the influence of the raw materials, the processing parameters for shaping and the indispensable thermal processing transforming the formed powders into a solid material is crucial for proper manufacturing of MMCs with tailored characteristics. The joining process for these components extends the applicability of the investigated PM-MMCs.

5.1 Introduction

Composite materials based on metal and ceramic have been investigated for several years. The principle of combining different materials in order to achieve a new type of material that associates the specific properties of each component, proposes not only improvements of existing products, but also the creation of new materials

C. Weigelt (✉) · M. Oppelt · C. G. Aneziris
Institute of Ceramic, Glass and Construction Materials, Technische Universität Bergakademie Freiberg, Agricolastr. 17, 09599 Freiberg, Germany
e-mail: christian.weigelt@ikgb.tu-freiberg.de

H. Biermann and C. G. Aneziris (eds.), *Austenitic TRIP/TWIP Steels and Steel-Zirconia Composites*, Springer Series in Materials Science 298,
https://doi.org/10.1007/978-3-030-42603-3_5

and fields of application. Metal-matrix composites gained in popularity, since they provide a large variety of tailored characteristics, especially due their deformation behavior. Such materials enable various applications in the mobility or engineering sector due to their mechanical properties under static and dynamic loading at ambient temperatures. Further benefits as compared with conventional materials may be achieved by their thermal-, corrosion-, and wear-related properties. MMCs composed of a steel showing a transformation induced plasticity (TRIP) effect offer a matrix material with outstanding ductility, high strength, and reasonably high capacity for absorption of mechanical energy. These properties originate from the strain-induced martensitic phase transformation from austenite to α'-martensite under mechanical loading. Additionally, the phase transformation can be overlapped by a twinning induced plasticity (TWIP) effect, which further improves the deformability and strain hardening of such steels. The deformation mechanisms are governed by the austenite stability and by the stacking fault energy γ_{SF} (SFE) that depend on the chemical composition of the alloy and on the temperature applied during deformation [1–3]. The material concept covered by the CRC799 is focused on high-alloyed stainless CrMnNi-steels. The SFE determining the dominant deformation mechanism can be estimated by various empirical equations. The presence of austenite and martensite can be predicted from the chemical composition by using the proportions and individual weighting factors for each element of the alloy [4]. The nickel equivalent [Ni_{eq}, (5.1)] is calculated from the austenite promoting elements (e.g. Ni, C, Mn), while the chrome equivalent [Cr_{eq}, (5.2)] considers the ferrite stabilizing character of elements such as Cr, Ti, and Si. Apparently, the alloy composition is of great importance for the phase composition and their ability to undergo the desired deformation mechanisms.

$$\begin{aligned} Ni_{eq} = {} & \text{wt\%Ni} + 30 \times \text{wt\%C} + 18 \times \text{wt\%N} + 0.5 \times \text{wt\%Mn} \\ & + 0.3 \times \text{wt\%Co} + 0.2 \times \text{wt\%Cu} - 0.2 \times \text{wt\%Al} \end{aligned} \tag{5.1}$$

$$\begin{aligned} Cr_{eq} = {} & \text{wt\%Cr} + \text{wt\%Mo} + 4 \times \text{wt\%Ti} + 4 \times \text{wt\%Al} + 1.5 \times \text{wt\%Si} \\ & + 0.9 \times \text{wt\%Nb} + 0.5 \times \text{wt\%W} + 0.9 \times \text{wt\%Ta} + 1.5 \times \text{wt\%V} \end{aligned} \tag{5.2}$$

Zirconia (ZrO_2) ceramics offer enhanced mechanical properties at ambient temperature due to its polymorphism. The polymorphism is associated with the appearance of room temperature stable monoclinic (m-ZrO_2, space group $P2_1/c$) and high temperature stable tetragonal/cubic (t-ZrO_2, space group $P4_2/nmc$, and c-ZrO_2, space group Fm-3 m, respectively) crystal structures at ambient pressure. The martensitic phase transformation from the tetragonal to the highly distorted monoclinic modification during cooling below 1170 °C occurs simultaneously with a volume expansion of roughly 3% and which generates stress in the surrounding material resulting in cracking and failure of pure zirconia components. By the addition of stabilizing agents, such as MgO (forming magnesia partially stabilized zirconia—Mg-PSZ), the high temperature ZrO_2-modifications can be metastably retained at ambient temperature. These polymorphs are capable to undergo a delayed tetragonal to monoclinic phase

transformation, providing the well-known stress-assisted transformation-toughening mechanism and which results in the specific characteristics of commercial zirconia applications. The distinctive phase transformation triggered by external loading cannot only improve the mechanical properties of ceramics but also reinforce metal-matrix materials.

MMCs based on a TRIP/TWIP steel-matrix with certain ceramic additions have been in focus of several investigations. However, common technologies suffer from the different material characteristics involved during processing. Numerous MMCs have been investigated in the past using a variety of manufacturing processes such as stir casting [5], squeeze casting [6], spray forming [7], infiltration of ceramic preforms [8, 9] or powder manufacturing [10–14]. However, these conventional techniques cannot produce cellular structures with a wall thickness on the micron scale, since they are restricted to bulk structures or components. Therefore, powder metallurgy is of great interest in the development of new materials and their processing technologies. The adaption of the ceramics-derived extrusion (also referred to as plastic processing) technology at ambient temperatures on mixtures of steel and ceramic powder raw materials enables an efficient manufacturing of advanced fine-grained materials with particularly cellular (lightweight) structures as well as bulk fabrics. Thus, these materials are applicable in certain applications, such as crash-absorber, engineering or structural components, and damping elements. Figure 5.1 illustrates the latitude of the plastic enabling honeycomb structures with various cell geometries and cell densities (indicated as channels per square inch—cpsi) at cell widths of 250–450 μm and relative densities of 0.3–0.4.

The extrusion process is widely known in the production of ceramic materials covering, among others: tiles, rods, and thermocouple protection tubes. This process was initially applied to natural plastic raw materials (clay) and later adapted to non-plastic raw materials. In the latter case, solid powders are transferred into a room-temperature plastic paste by admixing organic additives and solvents (usually

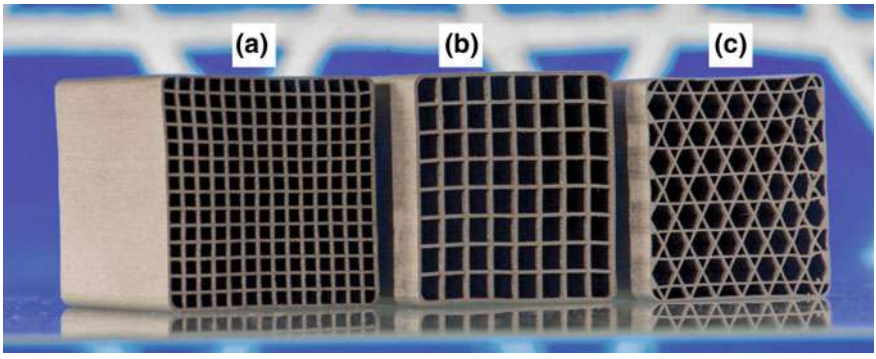

Fig. 5.1 Variants of cellular structures manufactured with the ceramics-derived extrusion process at room temperature: honeycombs with 196 cpsi (**a**), 64 cpsi (**b**) and with the 172 cpsi Kagome lattice structure (**c**), all variants with outer dimension 25 × 25 mm^2

water). Then, the paste can be easily shaped by forcing it through a rigid die with the geometry of the component to be produced. The thermal treatment comprising drying, removal of organic additives (debinding) at moderate temperatures and the sintering transfers the materials into their final state (see Fig. 5.2). Previous investigations on alumina [15] materials successfully demonstrated the efficient processing of honeycomb structures, and therefore, the processing has been selected as the most suitable method for forming metal-ceramic composite structures in the frame of the present study. Beyond, the ceramics-derived processing involves the cost- and material-efficient near-net shaping at ambient temperatures and the processing of any steel/ceramic ratio. However, the pressureless sintering implies higher remaining porosities and pronounced interactions between the metal and ceramic components as compared to MMCs prepared by pressure-assisted consolidation methods such as hot-pressing (HP) [11] or spark plasma sintering (SPS) [10].

Composite materials based on austenitic stainless steel with particulate reinforcement prepared via cold extrusion are in focus of the present work. The correlation of the initial materials, the processing and the resulting properties of the materials are presented. A very important part of this work deals with chemical and microstructural interactions between the components steel and the reinforcing ceramic particles during sintering. Hereto, no studies on magnesia partially stabilized zirconia in conjunction with high manganese steels have been reported.

The addition of ceramic particles to a ductile matrix increases the strength, but lowers the material's deformability by inducing typical damage events like debonding, particle fracture or crack coalescence even at moderate fractions of ceramic particles. Thus, improving the interface bonding between the metal matrix and the zirconia particles is of major importance. Wittig et al. [8] reported the pressureless infiltration of zirconia preforms with a CastX38CrMoV5-1 (AISI H11) steel by adding 20 wt% elemental titanium. Previous investigations revealed similar results with alumina preforms [16]. The high diffusibility of Ti, the formation of TiO_x interlayers, and the improved wetting behavior promote sufficient infiltration and the formation of reliable interface boundaries. Titanium is also used as an active component in the brazing of zirconia/zirconia or zirconia/alloy joints [17, 18]. Beyond

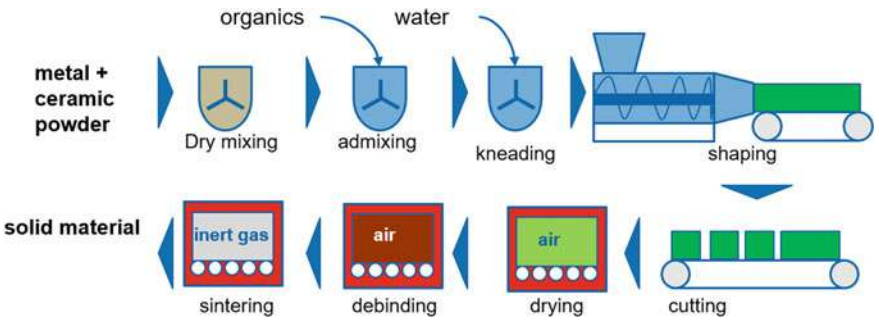

Fig. 5.2 Scheme of the plastic processing route

this, titanium is known for its partial stabilization efficiency in zirconia ceramics by sintering in inert gas atmosphere [19, 20]. Variants of steel and magnesia partially stabilized zirconia were admixed with minor fractions of titanium in order to improve the interface formation during sintering in the frame of this work. The influence of the active interface agent on the mechanical properties has been tested by quasistatic compression tests. The microstructure and the phase compositions were investigated in order to correlate the mechanical response with the desired phase transformations of TRIP steel and zirconia.

Nevertheless the aspiration of improving the mechanical behavior, especially the increase of the specific energy absorption (SEA) capacity, leads to intensive investigations of the raw materials, the selection of materials, the adaption of process parameters and finally to the knowledge of the processing-characteristic-knowledge of a branch of composite materials. Not only the well-known zirconia reinforcing particles but also the introduction of alternative ceramics led to significant improvements of the material properties. In general, the steel/zirconia interface shows destabilization due to the diffusion of Mg out of the particles and the formation of precipitations at the metal/ceramic interface as a result of indispensable thermal treatment at temperatures inappropriate for zirconia sintering. These ZrO_2 particles with high amounts of non-transformable monoclinic zirconia are loosely embedded in the metal matrix. Thus, the ability of the reinforcing phase transformation is restricted to the low remaining amount of tetragonal/cubic zirconia. The alloying elements of TRIP/TWIP steels are also prone to diffusional interchange which boosts the interface formation but also the shift of the steel composition. But the interfacial reactions can also improve the material characteristics when exploiting alternative reinforcing ceramics. By replacing zirconia with aluminium titanate (Al_2TiO_5) a new family of MMCs with advanced mechanical properties under compressive and under tensile deformation is generated.

Furthermore an important issue in this work was the joining of MMCs using a ceramic-derived technology. Bulk specimens from the pure CrMnNi steel, and MMC variants reinforced with 5 or 10 vol% magnesia partially stabilized zirconia were used as joint partners. The samples were prepared via the ceramics-derived extrusion technology and different material combinations were joined in their dry green state using an aqueous paste to form the bonding. The mechanical testing comprised quasistatic tensile deformation tests of the base materials and of the sinter-joint variants at room temperature. The microstructural analyses revealed considerable differences between the ceramic joining process and the conventional welding of steel materials which is beneficial in future practical applications [21, 22].

5.2 Experimental Details

5.2.1 *Plastic Processing of Steel/Zirconia Composite Materials*

Numerous experiments have been performed in order to evaluate proper material compositions, processing parameter and thermal treatment conditions. The initial plastic pastes based on the extrusion of alumina honeycombs [15] as listed in Table 5.1 are prepared with a standardized grade steel powder of type AISI 304 (German grade 1.4301) [23–25]. Various powder types were used in the frame of the present study due to the intense research on the alloying concept and the related mechanical characteristics (cf. Table 5.1). The steel variants and their chemical compositions are summarized in Table 5.2. All steel powder variants (TLS, Germany) were manufactured via the gas atomization process which resulted in the formation of mainly spherical shape particles with some satellite particles and a few imperfections (see exemplary Fig. 5.3). Three variants of magnesia partially stabilized zirconia were used in the frame of the present study. Their compositions are given in Table 5.3.

Table 5.1 Composition of the initial mixtures, in wt% [23]

Material	Raw materials		Recipes		
	Type	Supplier	0Z	5Z	10Z
Austenitic steel	AISI 304 d_{50} = 45 µm	TLS, Germany	95.50	91.84	88.17
ZrO_2 with 3.5 wt% MgO	PMG3.5 d_{50} = 2 µm	Unitech, UK	–	3.66	7.32
Plasticizer flour	HW FGB	Kampffmeyer, Germany	2.60	2.60	2.58
Tenside	Denk mit	Henkel, Germany	0.40	0.40	0.43
Dispersant	Castament FS 60	Degussa, Germany	0.15	0.15	0.15
Plasticizer methyl cellulose	HPMC 874	Aqualon, Germany	1.35	1.35	1.35
Water	Deionized	–	4.5	4.8	5.0

Table 5.2 Chemical composition of steel powder variants, in wt%

Type	Fe + Others	Cr	Mn	Ni	C	Si
PMX2CrMnNi18-1-8A	Bal.	18.1	1.4	8.3	0.02	0.4
PMX2CrMnNi18-1-8B	Bal.	18.3	1.4	8.1	0.02	0.3
PMX1CrMnNi18-1-9	Bal.	18.4	1.1	9.3	0.01	0.7
PMX5CrMnNi18-1-8	Bal.	17.5	1.3	8.4	0.05	0.4
PMX5CrMnNi17-7-3	Bal.	16.7	7.1	3.4	0.05	0.9

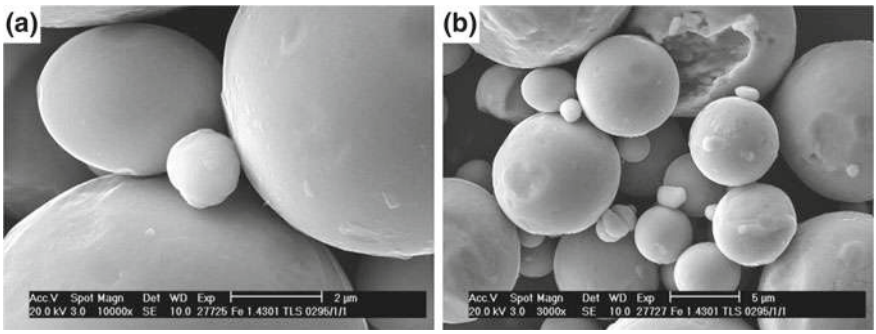

Fig. 5.3 SEM image of the as-delivered spherical steel powder at different magnification (PMX2CrMnNi18-1-8B)

Table 5.3 Composition of the zirconia powder variants, in wt%

Type	Supplier	ZrO_2 + Others	MgO	SiO_2	Al_2O_3	TiO_2	HfO_2
PSZ1	Unitech, UK	Bal.	3.4	n.m.	0.7	0.2	0.8
PSZ2	Saint-Gobain, USA	Bal.	2.8	0.4	0.4	0.1	1.7
PSZ3	Saint-Gobain, USA	Bal.	3.4	2.4	0.6	0.1	1.7

Recipe 0Z consists of 100 vol% TRIP steel and recipes 5Z and 10Z are based on 95 or 90 vol% TRIP steel with 5 or 10 vol% zirconia, respectively. In a further step, the plasticizers and water have been added to the batch during mixing. Because of a piston extruder (ECT, Germany), honeycombs 25.5 mm × 25.5 mm with 164 channels (200 cpsi) and a wall thickness of 250 µm have been extruded. The applied pressure was between 10 and 11 MPa. After extrusion, cube-shaped samples (25.5 mm × 25.5 mm × 25.5 mm) have been cut before stepwise water-removal in an air-circulated dryer. After drying, the debinding process has been carried out at 350 °C for 90 min in air in the same aggregate. The binder-free samples have been placed in an alumina crucible and protected against O_2 contamination by a Ti casketing. The samples have then been sintered at 1350 °C for 2 h in an electrical furnace with high purity flushing Argon atmosphere.

Microstructure characterization was performed using scanning electron microscopy (SEM), energy dispersive X-ray analysis (EDS) and electron backscatter diffraction (EBSD). In addition, phase labeling was performed on sintered surfaces by X-ray diffraction (XRD) with Cu–Kα radiation. The relative phase content of zirconia was determined by the method described by Evans et al. [26]. The open porosity, the average pore radius and the pore size distribution of the sintered samples were measured by mercury porosimetry. The macroscopic structure of the honeycomb samples after deformation was examined by optical microscopy of metallographic sections. The mechanical in-plane testing of the sintered specimens was carried out under compressive loading in a 500 kN servohydraulic universal testing machine type MTS 880 with a displacement rate of 0.016 mm/s at ambient temperature.

Table 5.4 Composition of mixtures for Ti-activated interface formation, in vol% [27]

Recipe	0Z	10Z	10Z-1T	10Z-2T	10Z-3T
Stainless steel	100	90	89	88	87
Zirconia	0	10	10	10	10
Titanium	0	0	1	2	3

A gas-atomized high-purity >99.7% Titanium powder (TLS, Germany) with a mean diameter of 13 μm and a spherical particle shape was used in some tests as interface activation agent. The basic composition for MMC production was a mixture of 90 vol% steel (PMX5CrMnNi18-1-8) and 10 vol% zirconia (see Table 5.4). In MMC compositions with minor titanium fractions (1, 2, or 3 vol%) of the matrix material were replaced by Ti powder. Additionally, the pure steel specimens provide a reference material without any additions. Taking the interest of interface reactions and the mechanical properties into consideration, a bulk sample geometry was used, but prepared from a modified processing route.

5.2.2 *Composite Variants with Additions of Zirconia and/or Aluminium Titanate*

Further work was conducted on the development of alternative reinforcing mechanisms since the zirconia particles are prone to undergo the tetragonal to monoclinic phase transformation during thermal processing of the composite materials. Alumina and yttria are well established as reinforcing additions for steel-matrix composites [28, 29]. However, the alumina particles show no phase transformation and insignificantly interface formation. A new approach is the introduction of aluminium titanate as a reinforcing material which is a promising refractory material due to its excellent thermal properties but not prestigious for its mechanical properties.

Bulk specimens were prepared by the well-established ceramic-extrusion technology with an austenitic stainless steel of type PMX5CrMnNi17-7-3 (see Table 5.2) with a median diameter of 18.1 μm. The reference materials with the standard zirconia reinforcing powder were prepared from the commercially available Mg-PSZ of type PSZ2 (cf. Table 5.3). Aluminium titanate was synthesized from a stoichiometric mixture of high-purity 99.8 wt% alumina Martoxid MR70 (Martinswerk, Germany) and 98 wt% titania Hombikat N100 (Sachtleben, Germany) since proper batches are not commercially available. The addition of 6 mol% of a of high-purity grade (98%) MgO powder (neoLab, Germany) improved the thermal stability and protected the aluminium titanate from decomposition on cooling after reactive sintering. The mixture was pre-fired at 1400 °C in an oxidizing atmosphere in order to ensure high Al_2TiO_5 formation, and crushed after cooling to obtain powder fineness similar with the zirconia powder. The Al_2TiO_5 mean particle diameter was 4.2 μm and consisted of 95% aluminium titanate with minor residues of unreacted alumina and titania

Table 5.5 Composition of mixtures, in vol%

Recipe	0Z	5Z	10Z	5AT	10AT	2.5ZAT	5ZAT
Steel	100	95	90	95	90	95	90
Zirconia	0	5	10	0	0	2.5	5
Tialite	0	0	0	5	10	2.5	5

according to X-ray analysis. The basic composition 0Z refers to the pure steel material without any ceramic additions. The composite variants were prepared with solely zirconia (Z) or aluminium titanate (AT) or with balanced fractions of both (ZAT) at a total fraction of 5 or 10 vol% (see Table 5.5).

The plastic processing was similar to previous materials with certain modifications of the binder system and the water fraction necessary for shaping. The specimens were heated up to 450 °C in an oxidizing atmosphere, applying a heating gradient of 1 K/min and a dwell time of 30 min at maximum temperature to eliminate organics from the extrusion process. After cooling to room temperature (at a rate of 1 K/min), the specimens were reloaded into a second furnace with a graphite lining and graphite heating elements (Xerion, Germany). The sintering step was conducted in a flushing argon atmosphere using a heating rate of 5 K/min and a maximum temperature of 1350 °C and a dwell time of 2 h at the maximum temperature before cooling with a maximum cooling gradient of 5 K/min.

The fired specimens were processed to a cylindrical geometry (6 mm in diameter and height) for compressive loading tests, as well as to round tensile specimens with a gauge diameter of 5 mm and a gauge length of 30 mm according to DIN EN ISO 6892-1 for tensile loading tests. The tensile test series were performed with a 100 kN universal testing machine of type Zwick 1476. Compression tests utilised a 200 kN servo-hydraulic testing machine of type MTS 810. All tests were carried out at a quasistatic nominal strain rate of 0.001 s^{-1} at room temperature.

5.2.3 Innovative Joining of Powder Metallurgically Processed TRIP/TWIP Steel Materials

The manufacturing of a composite structure by extrusion is limited to a uniform cross section throughout its entire length, which limits later use. Thus, the availability of a reliable (mechanical) joining technique is a major task in the development of MMCs for commercial applications. Fundamental research was performed on the adaption of a ceramics-derived joining process by adding a slurry on the joining partners at room temperature with the subsequent thermal processing.

Pure steel specimens, the composite variants, and the joining paste were composed of the steel powder batch PMX5CrMnNi17-7-3 (see Table 5.2). The ceramic component was the commercially available magnesia partially stabilized zirconia of type PSZ2 (cf. Table 5.3) [22, 30]. The basic composition (0Z) corresponds to 100%

steel without any ceramic additions. Composite mixtures were prepared with fractions of 5 vol% (5Z) or 10 vol% (10Z) zirconia in their total solids composition. The powders were mixed for 90 min in their dry state before adding the organic binder system and water. Rods of 11 mm in diameter were extruded using a single-screw extruder of type LK III 2A (Linden, Germany) at ambient temperature. The water was removed stepwise in an air circulated dryer applying a maximum temperature of 110 °C. Dried samples of each composition were cut to a length of 50 mm and the surfaces to be joined were then polished with a rotary grinding machine to obtain a smooth surface.

The aqueous joining paste was prepared from pure metal powder and water with a ratio of 9:1 by weight. In addition, an organic binder system composed of 1.0 wt% KM2000 (Zschimmer & Schwarz, Germany), 0.6 wt% KM1001 (Zschimmer & Schwarz, Germany) and 2 wt% Optapix G1457 (Zschimmer & Schwarz, Germany) was necessary in order to ensure a sticky paste with well dispersed steel particles.

The joining paste was brushed on the polished end faces of the partners to be joined immediately before these specimens were manually assembled which led to some leaking of the paste and, thus, complete filling of the gap between both parts. The joined specimens were placed on the firing auxiliaries and handled without any rigid clamping during further processing. Then the samples were again dried stepwise in an air circulated dryer starting at 40 °C and increasing to a maximum temperature of 110 °C. Debinding and sintering was performed as shown before. The fired specimens were machined to round tensile loading test geometry with a gauge diameter of 4 mm and a gauge length of 25 mm according to DIN EN ISO 6892-1. The test series with 5–9 samples of each variant were performed at room temperature with a 50 kN universal tensile testing machine of type Tiratest 2850 (Germany) at a quasistatic nominal strain rate of 0.001 s^{-1}. Microstructural characterization was conducted using light optical microscopy and scanning electron microscopy (SEM, Philips XL30). Energy dispersive X-ray analysis (EDS, EDAX Inc., USA) complemented the microstructural study.

Hardness profiles were recorded using a LECO M400 micro hardness tester. Measurement of the profiles was carried out after Vickers procedure with HV0.3 (2.94 N, 10 s load duration) in a triple row with a total length of 6 mm and 100 μm increment. Furthermore, macro hardness was likewise measured on a conventional hardness testing device after Vickers with HV10 (98.04 N, 10 s load duration).

5.3 Results and Discussion

5.3.1 Characteristics of Materials Prepared via Plastic Processing

The many opportunities of geometries processed via the ceramics-derived extrusion technology are illustrated in Fig. 5.4. Lightweight honeycomb structures as well as

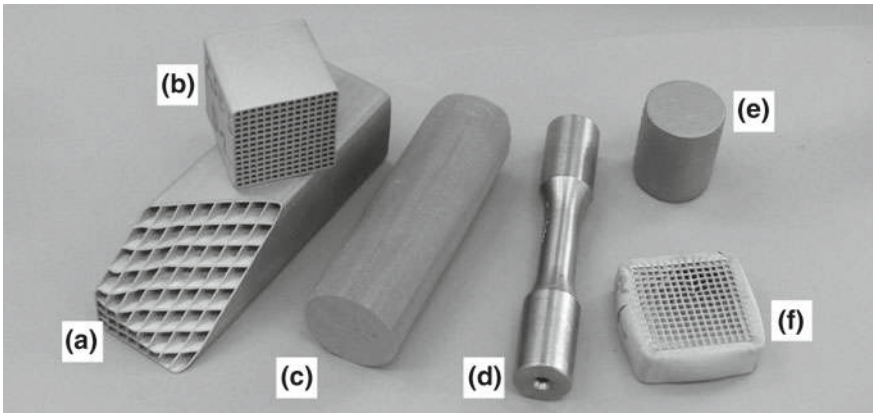

Fig. 5.4 Variations of sample geometries produced by the powder metallurgical route via extrusion: honeycomb structures with 64 cpsi (**a**) and 200 cpsi (**b**), green body rod (**c**) for fatigue specimens (**d**) and compressive test (**e**), 200 cpsi honeycomb at 50% compressive strain (**f**) [24]

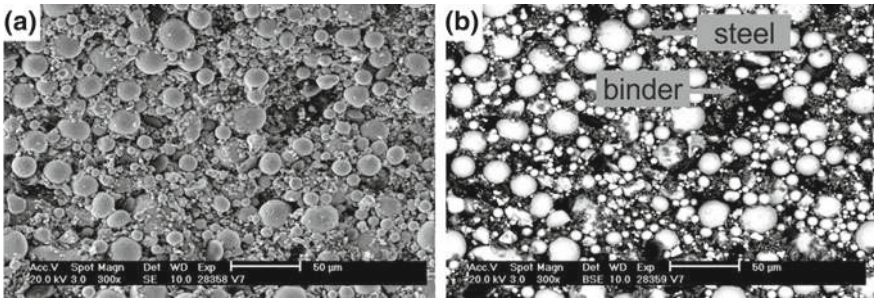

Fig. 5.5 SEM-image of a honeycomb structure (exemplary material variant without any ceramic additions) after drying with steel particles (bright) and polymer binder (dark) in secondary electron mode (**a**) and backscatter electron mode (**b**) [24]

bulk specimens can be processed with almost similar plastics pastes enabling a large variety of sample geometries. Thus, the mechanical testing, e.g. under compressive or under tensile loading tests, fatigue tests and ductility tests can be performed with respect to mutual applications.

Figure 5.5 illustrates the microstructure of the 100% steel sample without any ceramic additions after the extrusion process and their dry state. The spherical steel particles are surrounded uniformly by the organic additives. A certain porosity is derived from the particle size distribution of the metal powder and the removed water portion necessary for sound extrusion. The microstructure undergoes fundamental changes during thermal processing. The organic components, as being removed during debindering, cause not only porosity but also impurities (ash) and carbon residue from inappropriate settings. The pressureless sintering at temperatures slightly below the melting temperature of the metal initiates the final consolidation.

The carbon content is crucial for the mechanical characteristics of TRIP/TWIP steel-matrix materials since carbon crucially affects the deformation mechanism of the steel matrix. Furthermore, the presence of enhanced carbon fractions promotes the formation of carbides during sintering which are likely to decrease the strength and ductility of the material. Thus, the complete removal of the organic processing aids during thermal treatment is essential for the mechanical properties of powder metallurgically processed materials. The carbon fraction decreases by increasing the maximum temperature during debindering. However, the thermal binder removal at higher temperatures is limited due to the oxidation of the steel particles. These oxides are thermodynamically stable during sintering causing undesired inclusions even in the material without any further addition of ceramic particles. The binder removal for honeycomb structures is possible with heating rates up to 2 K/min. Faster heating results in cracks and incomplete binder removal in the center of test specimens. Figure 5.6 presents the microstructure of a typical sample fracture surface of the composite variant 5Z after sintering at 1350 °C. Here, a continuous steel matrix with well dispersed zirconia particles can be seen. The fine grained ceramic particles usually appear as agglomerates in the interstices of the coarser grained metal. According to EDS-analysis three different regions can be identified. First, the composition of the steel matrix which largely correlates with the chemical composition of the as-delivered material, and second, the ceramic regions with dominating zirconia content can be observed. Further on, particles that were not present in the starting materials and that were most likely formed during sintering are randomly spread throughout the whole material. They are characteristically composed of varying compositions of chromium, manganese, magnesium, aluminium and silicon and they are detectable among all materials processed via the plastic processing. They are particularly not exclusively present in the composite variants but also in pure steel samples.

Another aspect of the pressureless sintering is the thermally induced tetragonal to monoclinic phase transformation of the zirconia particles. Figure 5.7 presents the EBSD-phase analysis of zirconia agglomerates (dispersed in PMX1CrMnNi18-1-9) in the material variant 5Z after sintering, and after 20% compressive deformation [3].

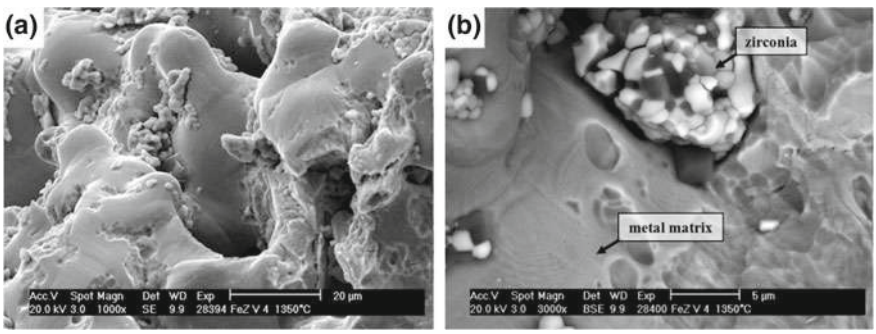

Fig. 5.6 SEM image of a typical fracture surface region of the composite material 5Z in the as-fired state at different magnifications [3]

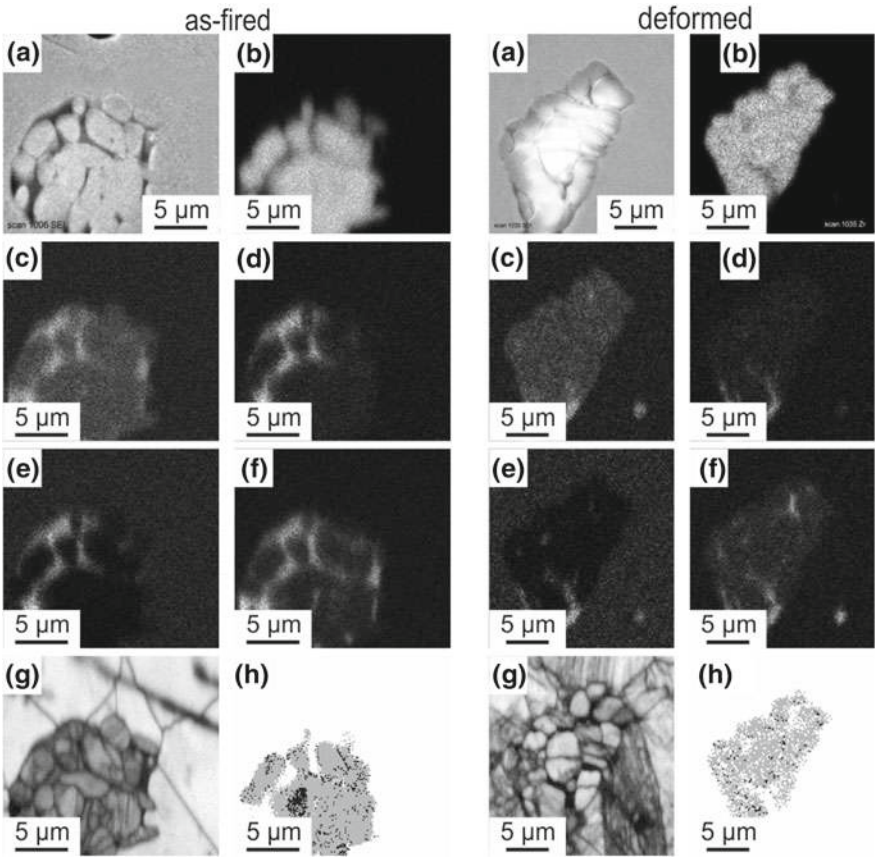

Fig. 5.7 Cross-section of zirconia agglomerates in the as sintered state A) and after 20% compressive strain B) with the composition 5Z: **a** SEI, **b** EDS Zr map, **c** EDS O map, **d** EDS Mg map, **e** EDS Mn map, **f** EDS Si map, **g** EBSD quality map, **h** EBSD phase map showing t/c-ZrO_2 (black), and m-ZrO_2 (gray) [3]

Both spots show zirconia agglomerates embedded in the steel matrix. The EDS maps clarify the edge between metal and ceramic phase enabling separated phase analysis. The EBSD image quality for zirconia particles is lower in comparison to steel in case of the as-fired specimen. After plastic deformation, both components appear with nearly the same validity due to distorting the crystal lattices during deformation. The dominating amount of non-metastable monoclinic phase after sintering is obvious. Nevertheless, the m-ZrO_2 quantity is increased after compressive deformation.

The interactions between the steel matrix and the zirconia particles were investigated in detail from model mixtures of the zirconia variants PSZ2 and PSZ3 with solely additions of the main alloying elements (Cr, Ni, Mn and Fe) [21]. The addition of Cr leads to several chemical reactions associated with a change of phase composition in zirconia matrix. Up to 18% of the steel mass are delivered as chromium, which

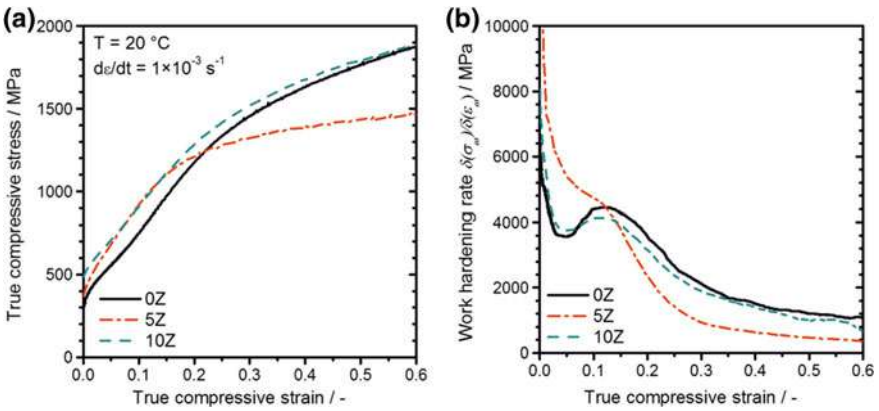

Fig. 5.8 Mechanical behavior of the compressed specimens indicating the reinforcing effect of Mg-PSZ on the compressive yield strength and on the work hardening: **a** flow stress curves, **b** work hardening rates [31]

reflects the importance of PSZ-Cr interactions in the present composite materials. Sintering magnesia partially stabilized zirconia at 1300–1400 °C causes pronounced changes in the phase composition with a minor fraction of tetragonal and/or cubic ZrO_2 after firing. Additions of Mn and Fe already start reacting with zirconia matrix when sintering at 1300 °C leading to either destabilization (Fe) or stabilization (Mn). Further heating to 1400 °C indicates the reaction of chromium with stabilizer magnesia to form magnesia chromite. Variations of the dwell time at maximum temperature have negligible effects on ZrO_2 phase composition. In contrast Ni has no significant influence on the sintering progress and phase composition of the fired zirconia.

Figure 5.8 depicts the stress-strain behavior of the materials under quasistatic compressive deformation. The composite materials showed higher stresses over a wide range of strain than the unreinforced material 0Z. The yield strength at 0.2% plastic compressive strain was ≈70 MPa higher for both MMC variants as compared with the pure steel specimens. The composites 10Z revealed a pronounced strengthening effect under quasistatic compressive loading up to a deformation degree of approximately 45%. In contrast, the strengthening effect of material 5Z was exhausted when exceeding 18% compressive strain. Comparing these results with values from SPS material prepared from similar materials indicates the dominating effect of the consolidation process [28]. The lower strengthening effect of the present specimens is due to higher porosity in the matrices, the larger austenite grain size, and the distinctive reactions at the steel/zirconia interfaces. Because of damage initiation and propagation, the compression stress of composite materials dropped below the values measured for the pure steel specimen at higher strain levels. The characteristics of the matrix material mainly controlled the stress-strain level and the deformation behavior of all specimens tested. The matrix strain hardening was driven by the dislocation movement, by the accumulation of dislocations and by the strain-induced α'-martensite formation (TRIP effect) [28]. The work hardening rates, as shown in

Fig. 5.8, illustrate the strengthening effect of the ceramic particles in a certain range of strain followed by a decreasing work hardening rate at further deformation [31].

A similar material behavior was observed under quasistatic tensile loading (see Fig. 5.9). As expected, the pure steel specimens exhibited the highest tensile strength and fracture strain among all materials tested. The composite materials suffer from poor interfacial connections between the metal matrix and zirconia reinforcing particles. Therefore, the presence of ceramic dispersed within the ductile steel matrix lowers the material's deformability, inducing typical damage events like debonding, particle fracture or crack coalescence, which initiates MMC's failure at lower strain [10, 32, 33]. This effect is more pronounced under tension than under compression. The influence of the ceramic fractions on the MMCs' tensile yield strengths is negligibly small. Nevertheless, the composite variant 5Z shows a higher stress level than the pure steel at the expense of their ductility. As similar to compressive deformation the material 5Z fails at lower strain than specimens with 10 vol% zirconia which is most likely caused by larger pores and voids in the matrix material. The in situ tests revealed the kinetics of strain-induced α'-martensite during deformation. The 0Z specimens exhibited the highest overall percentage of strain-induced α'-martensite. The lower formation of strain-induced α'-martensite in the composite variants was in accordance with the less pronounced sigmoidal shape of their strain hardening response.

The strength of the steel/zirconia-interface is of great importance for the global mechanical behavior of the composite material. Adding small fractions of Ti is one opportunity for the initiation of reliably bonded ZrO_2 particles within the steel matrix. The particle size distribution of the initial solid powder mixtures demanded a large number of organic agents to allow adequate paste processing [24, 34]. Nevertheless, the debinding settings provide samples with carbon contents of $(0.05 \pm 0.01)\%$ and which corresponded to the concentration of the as-delivered steel powder (cf. Table 5.2). Hence, the formation of carbides during high-temperature processing was

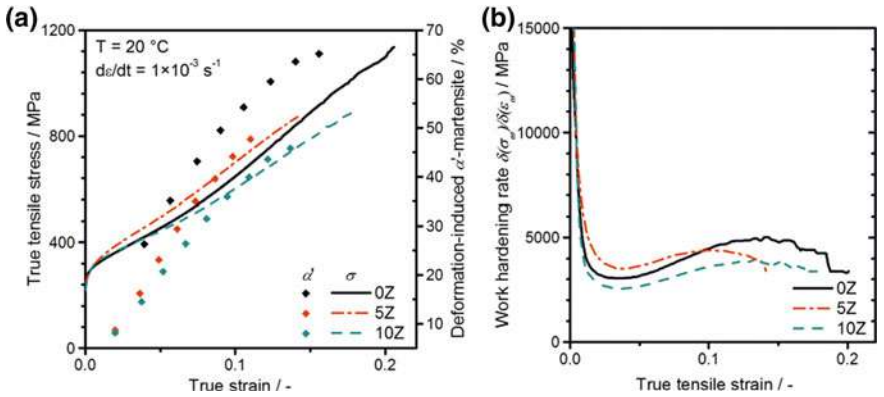

Fig. 5.9 Tensile properties of the TRIP steel and the composite variants showing the strengthening and embrittling effect of certain ceramic fractions: **a** flow stress curves, **b** work hardening rates [31]

unlikely to occur. The sintered specimens appeared with a glossy metallic surface indicating the absence of considerable metal oxidation during thermal processing. Shrinkage, bulk density and porosity of all material variants considered in the frame of interface modification experiments are summarized in Table 5.6. Only small differences between the pure steel and MMC material can be recognized. The shrinkage of specimens with additions of titanium is lower than in recipes 0Z/10Z but rises as a function of the Ti fraction. The calculated porosities declined from 10.7 to 4.6% by rising the titanium fraction from 1 to 3 vol% [27].

Figure 5.10 shows representative flow curves of the quasistatic compressive loading tests at room temperature. The presence of 10 vol% magnesia partially stabilized zirconia particles lead to a significant increase of the compressive stress level in a wide range of deformation. At 0.2% plastic strain the pure TRIP steel specimens show an engineering stress of 206 ± 8 MPa and a sigmoidal stress-strain curve on further deformation that could be related to the martensitic phase transformation. In comparison, the 10Z composite material is characterized by a similar behavior with higher yield strength of 249 ± 4 MPa and advanced mechanical response at moderate strain (up to 100 MPa higher stress level than 0Z). However, the strengthening effect of material 10Z was exhausted when exceeding $\varepsilon_{true} = 0.5$ and the stress level of the composite material dropped below the specimens without any ceramic additions (0Z). The essential material characteristics of 0Z and 10Z specimens were similar to

Table 5.6 Properties of the as-fired specimens [27]

Recipe	SS	10Z	10Z-1T	10Z-2T	10Z-3T
Shrinkage (%)	11.2 ± 0.5	11.4 ± 0.2	10.3 ± 0.3	10.6 ± 0.3	10.8 ± 0.4
Bulk density (g/cm^3)	7.01 ± 0.02	6.79 ± 0.03	6.77 ± 0.04	7.06 ± 0.04	7.16 ± 0.01

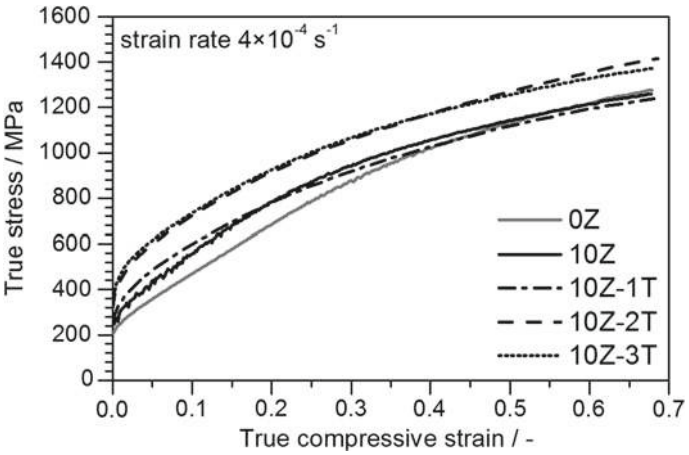

Fig. 5.10 Compression stress versus strain of the steel and the composite variants illustrating the effect of titanium [27]

composite materials reported by Martin et al. [28]. The higher level of mechanical response could be assumed to origin from less than 2% porosity as the samples were prepared by spark plasma sintering. The influence of titanium on the mechanical properties differs in a wide range. In general the presence of Ti results in an increase of the yield strength: 260 ± 21 MPa (1 vol% Ti), 327 ± 3 MPa (2 vol% Ti) and 345 ± 4 MPa (3 vol% Ti). Specimens with 1% Ti exhibited higher true stresses in a certain range of strain in comparison to pure TRIP steel specimens and 10Z composite material. However, the points of intersection can be observed at a true strain of approx. 0.2 and 0.4, respectively. The mechanical properties of composite materials with 2 and 3 vol% titanium are almost equal.

5.3.2 *Effect of Zirconia and Aluminium Titanate on the Mechanical Properties of Composite Materials*

As already mentioned, the conventional pressureless sintering process facilitates chemical reactions, segregations, and the formation of δ-ferrite in the unreinforced TRIP steel specimens and in the composite variants during firing [35] (Table 5.7). Thus, the ferromagnetic volume fraction in the as-fired state strongly depends on the material's composition and particularly on the presence of primary aluminium titanate in the material variants. The highly dense metal matrix exhibited several pores and precipitations that were characterized by high concentrations of Mn, Mg, and Si as measured by EDS. It was assumed that these precipitations originated from the refractory material used in the gas atomization process. In general, the steel grains exhibited segregations at grain boundaries with enhanced concentrations of Cr and lower concentrations of Ni, forming δ-ferrite. The pronounced transformation of the highly metastable steel from austenite to martensite on the specimens' surfaces is a result of mechanical polishing. The ferromagnetic phases δ-ferrite and α'-martensite were confirmed by magnetic balance measurements. The presence of carbides was negligible. The characteristic microstructure of composite specimens with zirconia is shown in Fig. 5.11. The ceramic particles are randomly dispersed and widely embedded in the surrounding steel matrix. Delamination and broken-out particles indicate the loose bonding at the metal/ceramic and ceramic/ceramic interfaces. This is most likely a consequence of the firing temperature of the composite material, which was considerably below the normal sintering temperature of such zirconia ceramics (>1600 °C).

Table 5.7 Physical characteristics of the material variants

Recipe	0Z	5Z	10Z	5AT	10AT
Shrinkage (%)	15.9 ± 0.1	16.4 ± 0.1	15.9 ± 0.1	15.2 ± 0.2	12.5 ± 0.1
Bulk density (g/cm^3)	0.1 ± 0.1	0.1 ± 0.0	0.4 ± 0.3	0.4 ± 0.4	14.1 ± 0.7
Porosity (%)	7.54 ± 0.05	7.34 ± 0.04	7.25 ± 0.05	7.26 ± 0.05	6.39 ± 0.12

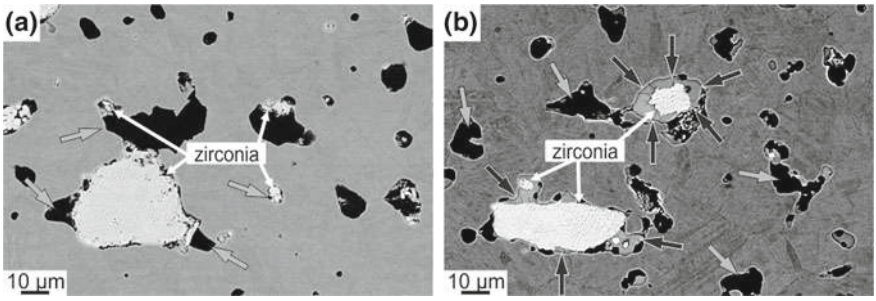

Fig. 5.11 Microstructure of MMC specimens with combinations of zirconia and aluminium titanate in their as-fired state showing the particular inclusion of zirconia particles by aluminium titanate/spinel (light grey arrows) and a solid solution of Zr–Ti–O also containing Mn (dark grey arrows): **a** 2.5ZAT, **b** 5ZAT [36]

The in situ tests revealed the kinetics of strain-induced α'-martensite during deformation. The S100 specimens exhibited the highest overall percentage of strain-induced α'-martensite at rupture (see Fig. 5.12). The lower formation of strain-induced α'-martensite in the composite variants 5Z/2.5ZAT was in accordance with the less pronounced sigmoidal shape of their strain hardening response. The reduction of the austenite stabilizing alloying element Mn was caused by its evaporation, diffusion and the formation of phases containing Mn at the metal/ceramic interfaces like $(Mg, Mn)Si_2O_4$ and/or $(Mn, Mg)(Al, Ti, Cr)_2O_4$, and led to a distinct shift of the initial metallic phase composition. This mechanism is more pronounced in MMCs

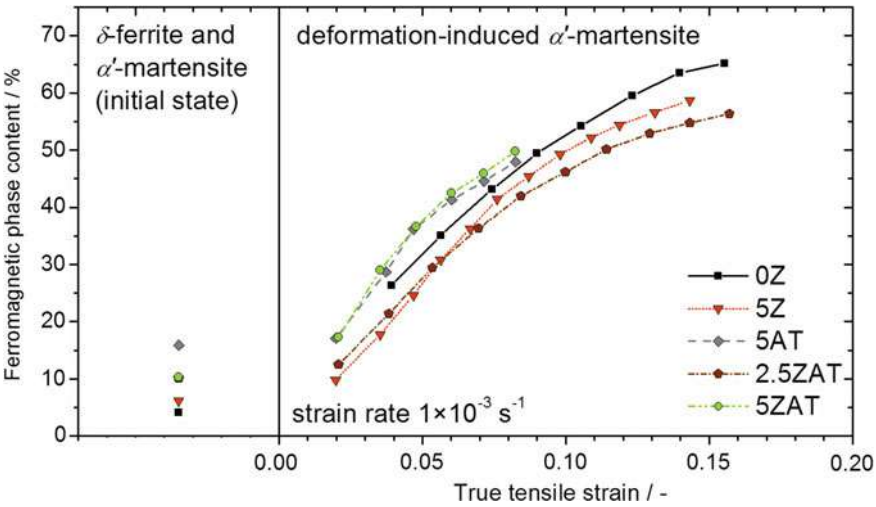

Fig. 5.12 Evolution of the ferromagnetic phase fraction under tensile deformation at room temperature, normalized by the metal fraction in the material [36]

with aluminium titanate as compared with steel/zirconia mixtures. Hence, the composites of types 5AT and 5ZAT reveal a higher α'-martensite content and formation rate at the beginning of plastic deformation. Then, the constrained matrix of the work hardened austenitic/martensitic steel suffers from the lack of strain relaxation, which promotes crack initiation and propagation [36].

The microstructure of the specimens after tensile deformation tests was analyzed in order to explain the mechanical behavior as well as the characteristic failure mode of the material and is shown in Fig. 5.13. The small strengthening effect of zirconia in the MMCs is a result of the loose embedding of the Mg-PSZ particles, of the irregular formation of silicates as an intermediate layer between steel/zirconia and zirconia/zirconia particles and of the lack of pronounced metastable ZrO_2 phase regions. The zirconia agglomerates are broadly crushed and fissured after tensile deformation; considerable delamination occurred at the steel/ceramic interface, which indicates loose interface boundaries [37, 38]. Thus, sufficient load transfer from the steel matrix can be assumed. Still, the sintering temperature of the composite material was well below the regular sintering temperature of Mg-PSZ, thus the clustered particles are expected to fail at lower stresses as compared with the commercially available bulk material. Since the majority of the zirconia particles exhibited the non-transformable monoclinic crystal structure already after sintering, the probability of the desirable tetragonal to monoclinic phase transformation is low. However, a large amount of voids in the ceramic sections, caused by broken-out particles, hampered a detailed and representative phase analysis of the material.

It is obvious that the zirconia particles with a silicate intermediate layer and these silicate structures remained reliably bonded in the matrix material, whereas a large amount of zirconia particles was broken out after specimen preparation. The tensile deformed microstructure of MMCs with 5 vol% initial aluminium titanate powder is characterized by the spinel particles that maintained their pronounced interface bonding to the steel matrix despite the extended multiple-crack formation in the interior of the ceramic particles. In contrast, debonding was the dominant damage initiation mechanism in previous TRIP steel/Mg-PSZ composites [11, 38, 39]. The intact particle/matrix interfaces indicate a higher shear strength at the interface than

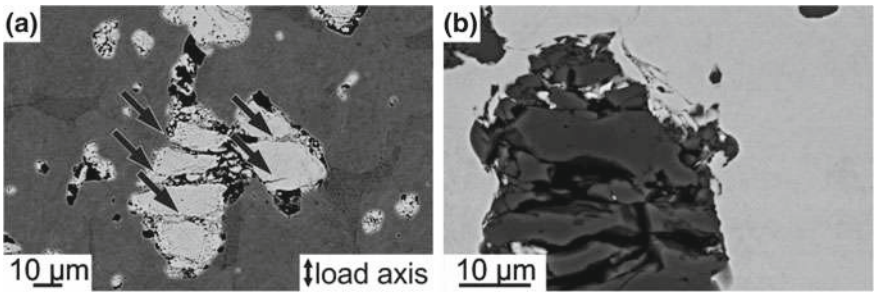

Fig. 5.13 SEM image of the composite materials at fracture strain showing broadly crushed ceramic particles and isolated cracks in the surrounding steel matrix: **a** 5Z, **b** 5AT [36]

the particle fracture strength which is a further indication for the improved interface-related performance of the MMCs with initial Al_2TiO_5 [37, 40]. Still, some of the small-grained spinel particles were nearly intact and exhibited neither cracking nor debonding. Although these composites underwent internal damage by crack initiation and the ceramic particles show no phase transformation or decomposition as compared with composite materials comprising metastable zirconia particles [3, 28], the addition of aluminium titanate results in a higher strain-induced α'-martensite formation and these MMCs sustain a higher stress level than the pure matrix material. The microstructure of the composite materials with concurrent additions of Mg-PSZ and aluminium titanate largely complied with the observations on 5Z and 5AT and the specific features for each type of ceramic particles. Here, the zirconia particles were subject to intense cracking but less to debonding due to the formation of the Ti-enriched spinel interlayer between the ZrO_2 particles and the steel matrix. The mutual interference of the zirconia particles and the initial aluminium titanate particles was apparently more pronounced in the MMCs with the higher ceramic volume fraction due to the coincidental distribution of these particles within the steel matrix [36].

The stress-strain curves of the TRIP steel alloy and the MMCs determined under compressive and tensile loading at a quasistatic strain rate of 0.001 s^{-1} at ambient temperature are displayed in Figs. 5.14 and 5.15. The stress level of the TRIP-matrix composites under compressive loading is significantly higher than the pure steel material considering a certain range of plastic deformation. As a consequence of damage initiation and propagation, the compression stress of material 10AT firstly dropped at approximately 11% engineering strain below the values measured for the pure steel specimen. Finally, catastrophic failure with sample fragmentation was induced achieving 45% strain. The strengthening effect of 5 vol% Mg-PSZ was

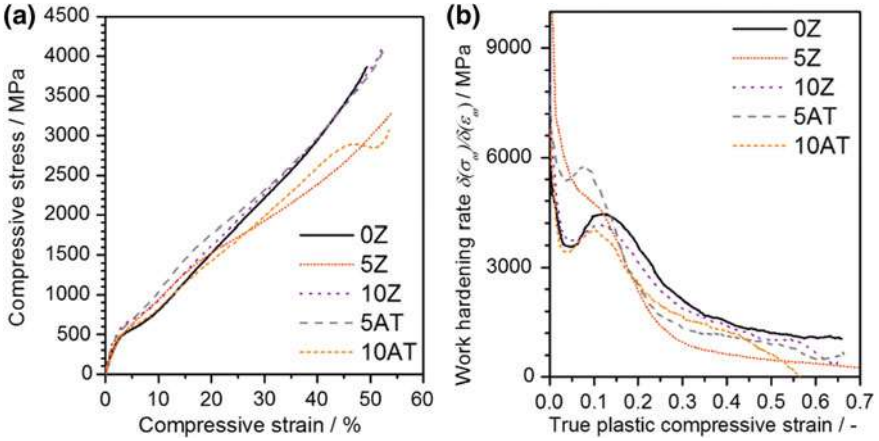

Fig. 5.14 Mechanical behavior of the specimens tested under quasistatic compression: **a** engineering stress-strain curves and **b** work hardening rates versus plastic compressive strain [35]

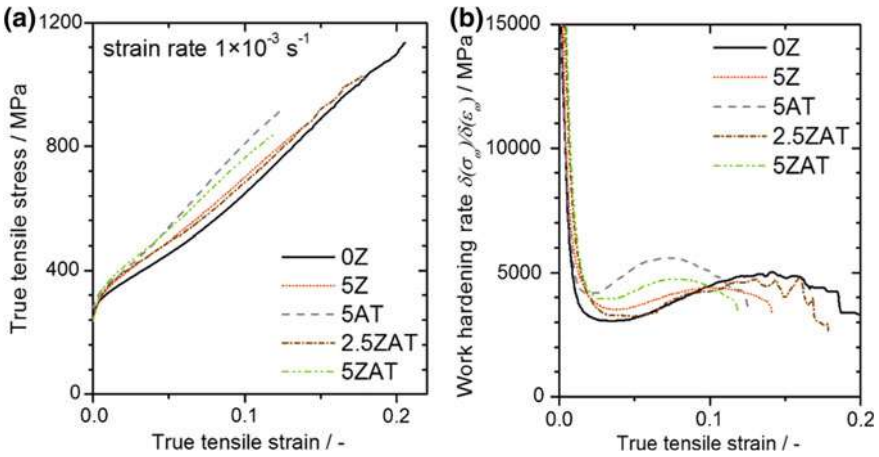

Fig. 5.15 Tensile deformation behavior of the material variants showing the strengthening and strain-depressing effect of certain ceramic fractions: **a** flow stress curves, **b** work hardening rates [36]

Table 5.8 Properties of the fired base materials without joining [30]

	0Z	5Z	10Z
Shrinkage (%)	16.0 ± 0.2	16.5 ± 0.1	15.9 ± 0.2
Total porosity (%)	4.1 ± 1.4	4.4 ± 0.6	4.5 ± 0.5
Bulk density (g/cm^3)	7.46 ± 0.11	7.34 ± 0.04	7.24 ± 0.04

exhausted when exceeding 18% compressive strain. However, the strain range with enhanced compressive stress compared with the pure TRIP steel was extended for the MMCs comprising 5 vol% Al_2TiO_5 and 10 vol% Mg-PSZ up to approximately 45% deformation. All composite materials exhibited higher yield strengths than the variant without any ceramic additions. The work hardening rates also illustrate the strengthening effect of the ceramic particles in a certain range of strain followed by a decreasing work hardening rate on further deformation [35].

5.3.3 Joining of Zirconia Reinforced MMCs

The base materials for joining experiments show similar macrostructure and microstructure as compared with the standard bulk materials previously reported. The determination of the physical characteristics (shrinkage, porosity and density) of the fired specimens revealed similar properties among all base materials (see Table 5.8) regardless the ratio of zirconia particles dispersed within the steel matrix. The residual porosity of approximately 4–5% is caused by the particle size of the

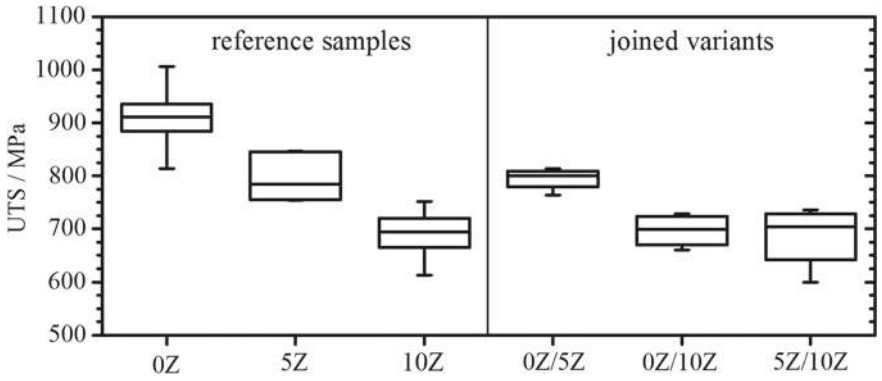

Fig. 5.16 Ultimate tensile strength of the materials tested under a quasistatic tensile loading at a rate of 0.001 s^{-1} at room temperature, featuring the minima, maxima and the 25%-, 50%-, and 75%-percentiles [22]

raw materials, the presence of the binder system during extrusion, and the applied pressureless sintering. The fired specimens appeared with a glossy metallic surface indicating the absence of considerable metal oxidation during thermal processing.

The results of tensile tests are given in Fig. 5.16. As expected, the composite materials had a lower ultimate tensile strength (UTS) and fracture strain as compared with the pure steel specimens. The decline of UTS by increasing the zirconia volume fraction results from the partial replacement of the ductile matrix material by brittle ceramic particles and which facilitates crack initiation and propagation.

Since the surface preparation is of major interest in joining processes, the sample preparation and material derived variations have to be taken into consideration. Nevertheless all surfaces to be joined appeared smooth with some transverse stress marks from the rotating grinding wheel indicating the definitive inclusion of the steel particles in the binder matrix in their dry green state. Break-off of particles and spalling on the edges of the samples was not observed. The addition of 5 or 10 vol% Mg-PSZ did not significantly affect the properties of the surface to be joined, since the ceramic particles were well dispersed and reliably fixed in the composite variants with their metal/binder matrix. The average roughness value R_a of the machined joining surface of the material variants (21.7 µm—0Z; 20.2 µm—5Z; 18.1 µm—10Z) marginally deviates among all materials tested and, thus, a preparation-driven impact on the material characteristics is not to be expected [22, 30].

The location of the joints could easily be assigned in the as-fired state due to some leaked paste from the joining process. The microstructure of the material combinations 0Z/10Z and 5Z/10Z is shown in Fig. 5.17. The base materials show a homogeneous microstructure with some pores and inclusions (all), and a good dispersion of the ceramic particles at a certain degree of agglomeration (5Z and 10Z). The smaller sized zirconia particles tended to form coarse-grained agglomerates in the interstices of the steel particles during manufacturing, which is more pronounced in the specimen with 10 vol% zirconia.

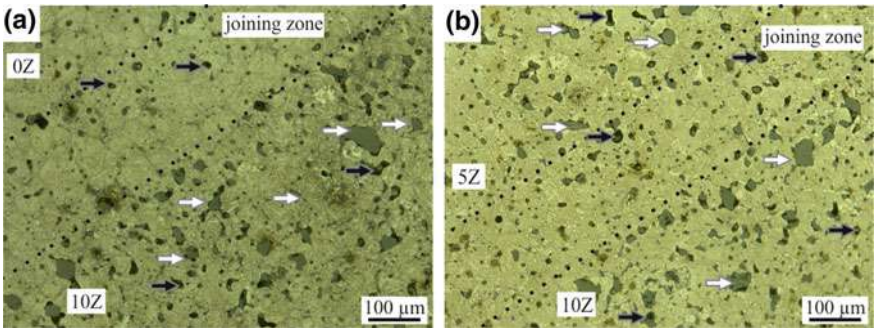

Fig. 5.17 Micrograph of sinter-joint variants: **a** 0Z/10Z, **b** 5Z/10Z; black arrows: pores and nonmetallic inclusions, white arrows: zirconia particles [22]

The formation of distinctive sections, e.g. heat-affected zone and welding seam as known from fusion welding, was neither detected by light optical microscopy nor scanning electron microscopy in the present sinter-joint samples. The joining interface is characterized by a smooth transitional area at a thickness of roughly 100–400 µm. The measurement of the width is only feasible in the material combination 5Z/10Z due to an enlarged zirconia-free intersection between the base materials (see Fig. 5.17b). Contaminations and nonmetallic inclusion are present in all material variants since the pressureless sintering promotes the formation of silicates and spinels at the steel/zirconia interface and even in the pure steel material [3, 41]. Firing the pure joining paste under equivalent thermal conditions results in the formation of a microstructure (e.g. grain size, porosity, and precipitations) similar to the fired 0Z base material [22].

The micro hardness profiles of the joint variants transverse to the joining zone were examined. The microstructure and the elemental distribution of the material combination 0Z/10Z is shown in Fig. 5.18. Both components (0Z and 10Z) are characterized by a similar microstructure with randomly dispersed pores and nonmetallic inclusions. The location of the joining zone could clearly be allocated by taking the presence of the zirconia particles and the concentration of Fe and Zr (using EDS) into consideration. The presence and concentration of Si is not a function of the zirconia volume fraction, since Si was incorporated as a contamination of the initial steel as well as of the zirconia powder (cf. Tables 5.2 and 5.3). The investigation of samples with material combinations 0Z/5Z and 5Z/10Z revealed similar results, however the smaller the difference in zirconia volume fractions between both joining partners, the more difficult was the localization and identification of the joining zone [22].

All joined material combinations failed at lower UTS and strain than the stronger component. The failure of all sinter-joint material combinations was initiated within the base material containing the higher volume fraction of Mg-PSZ particles. As pressureless sintering of the powder metallurgical processed composites involves thermal treatment for several hours at high temperature interactions between all components affect the microstructure and the material properties. Both the alloying elements of

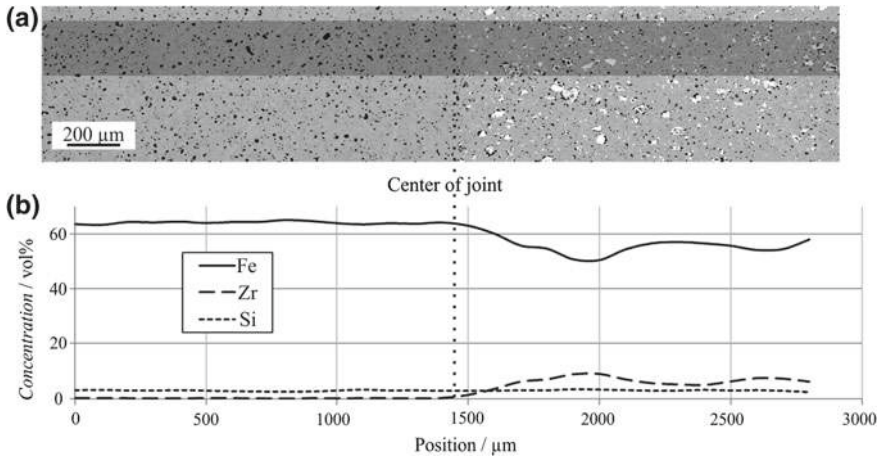

Fig. 5.18 Microstructure of combination 0Z/10Z after firing: **a** SEM image: dark grey: steel, light grey: zirconia; black: pores and nonmetallic inclusions, **b** transversal EDS line scan of the joint section showing the concentrations of Fe, Zr, and Si including the highlighted area (measuring field size 200 µm × 200 µm, step size 100 µm) [22]

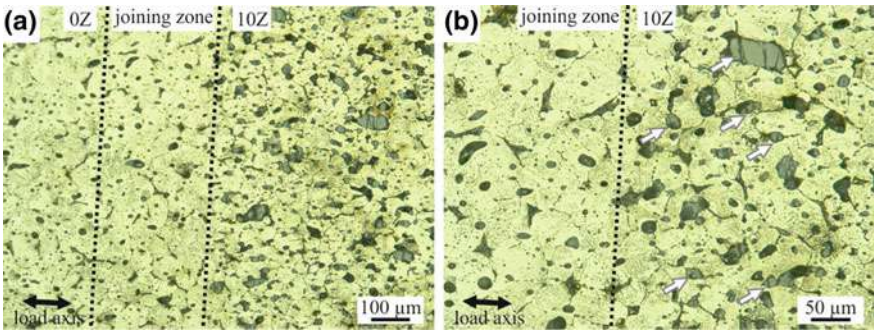

Fig. 5.19 Micrograph of the material combination 0Z/10Z after 20% tensile deformation showing particle fracture in large zirconia particles (indicated by white arrows), rare debonding at the metal/ceramic interface, and the well-preserved joining zone [22]

TRIP steel and the stabilizing agent of the zirconia reinforcing particles (Mg) are prone to diffusional interchange [21]. However, the composite material suffers from poor interfacial bonding, which is apparently more pronounced under tensile than under compressive loading. Thus, the reinforcing particles or agglomerates debond in an early state of deformation and micro crack formation initiates MMC's failure at lower strain than the pure steel material. Also the pronounced multiple crack formation within the coarse zirconia agglomerates could be observed as shown in Fig. 5.19 [35]. In contrast, the sinter-joint appeared almost intact and the boundary surface between the joining zone and the base materials indicated no detachment [22].

5.4 Conclusions

The ceramics-derived extrusion technology has been successfully applied on the manufacturing of metallic matrix composites. The combination of austenitic stainless TRIP/TWIP steel matrix variants with certain ceramic additions at metal volume fractions $\geq$90% is feasible. Mixing solid powders with an aqueous organic binder system enables the shaping of bulk and cellular lightweight structures at room temperature. The particle size and shape of the starting powders, the metal/ceramic-ratio, and the binder system crucially affect the shaping process and the microstructure of the shaped specimens. Generally, the ceramic particles were homogeneously dispersed within the metal matrix with a certain degree of agglomeration. To improve the particle dispersion, the size distribution of the metal and the ceramic component should be narrow and compliant to avoid clustering of fine reinforcing particles in the interstices of the metal matrix. Set proper drying parameters (temperature, heating rate) prevents the material from detrimental crack formation and damage of the materials. The subsequent thermal processing comprising the binder removal (debindering) and the consolidation (sintering) transfers the material into its final state. Pressureless sintering of the powder metallurgically processed materials requires temperatures slightly below the metal melting temperature with maximum temperatures of 1300–1400 °C and distinct dwell time of 1–2 h. The thermally induced diffusional interchange of the alloying elements of the steel and the ceramic fractions led to mutual alterations of the components. The crystal structure of zirconia in the MMCs was predominantly monoclinic due to diffusion of Mg out of the particles and the formation of spinel and/or silicate precipitations at the steel/zirconia interface during firing. Thus, the desired tetragonal to monoclinic transformation of the zirconia particles during mechanical testing is hampered.

The reinforcing mechanism of ceramic particles dispersed in TRIP/TWIP steel matrices enables composite materials with superior mechanical properties in a certain range of deformation. The stress-strain and deformation behavior of the materials were mainly controlled by dislocation hardening and α'-martensite phase formation in the steel matrix further affected by the reinforcing mechanisms of the ceramic particles. Finally, all composite materials failed at a lower strain than the unreinforced matrix material by internal damage after cracks have initiated in the steel matrix surrounding the ceramic particles and which is more pronounced under compressive deformation than under tensile loading. Advanced properties of the composite variants have been observed in terms of higher compressive stresses as well as an improved energy absorption capability. The desired martensitic phase transformation was proven in both, the matrix material and the zirconia particles with pronounced phase evolution in an early stage of deformation. Upon exceeding a critical strain the materials without ceramic additions benefit from the lack of non-plastic particles leading to higher strength at equivalent deformation. The addition of 1–2 vol% titanium improves the densification of the matrix material and the firm incorporation of zirconia particles into steel matrix. The formation of a Ti–Zr–O solid solution was observed at the metal/ceramic interface that promotes reliable interface boundary.

Aluminium titanate was identified as a proper reinforcing material for TRIP/TWIP composite materials in the frame of the present study. The diffusional interchange of the alloying elements of the steel and the aluminium titanate particles led to the decomposition of the aluminium titanate and the formation of a dense (Mn, Mg)(Al, Ti, Cr)$_2$O$_4$ spinel structure during firing. The intergranular bonding strength and the toughness of the metal/ceramic interfaces seem to be higher than in composites with loosely embedded zirconia particles. The composite materials with aluminium titanate offered a significant strengthening effect and a distinctive strain hardening under quasistatic compressive and tensile loading as compared with the matrix material. The void-free interface between the steel and the spinel structures of the initial microstructure offered optimal conditions for the load transfer; the intergranular bonding strength and the toughness of the metal/ceramic interfaces are assumed to be higher than in composites with zirconia particles. The combination of Mg-PSZ and Al_2TiO_5 further improved the stress level of the MMCs during deformation.

An innovative technique for joining metal-matrix composite materials with minor fractions of zirconia reinforcing particles was studied. The bulk specimens were prepared with the powder metallurgical processing route via extrusion of plastic pastes at room temperature. Various combinations of the base materials with 0, 5 or 10 vol% zirconia were joined by applying an aqueous high-solids paste on the surfaces to be joined in their dry green state at room temperature. The preparation of the surfaces before joining comprised cutting and rotary grinding with low mechanical and thermal impact on the base materials. During consecutive thermal processing the material's consolidation and the generation of the joint took place simultaneously. Thus, the formation of a consistent metal-matrix composite material and the formation of high bonding strength were initiated. Microstructural analysis revealed a homogeneous structure without inhomogeneities within the metal matrix nor segregation of the ceramic particles. Since the sintering and joining proceeded simultaneously the formation of a heat-affected influence zone as known from metal joints prepared by brazing or welding did not occur. The hardness of the pure steel specimens, the composite materials and the joining zone was measured in terms of Vickers's indention method. Since the fired specimens showed certain porosity and precipitations, the addition of zirconia particles showed no excessive hardening in the composite materials. Also, the formation of the joining zone had a negligible effect on the micro hardness. Mechanical tests under quasistatic tension at room temperature revealed similar strength of the joint variants as compared with the base materials. Strength and plasticity decreased as soon as ceramic particles were present in the base materials. Therefore, the deformation behavior of the joint variants is closely related to the mechanical properties of the base materials. In general the failure is initiated within the joining partner with the higher zirconia volume fraction without fracture at the bonding interface. The sinter joining technology is applicable for a wide range of material combinations and geometries. Efforts to improve the mechanical properties of joint materials demand improved base materials, since the materials are prone to fail beyond the joint.

Acknowledgements The authors gratefully acknowledge the financial support of the Deutsche Forschungsgemeinschaft (DFG, German Research Foundation) for funding the research project A5 and transfer project T1 within the frame of the Collaborative Research Center 799—TRIP-Matrix-Composites—project number 54473466. Additionally, the authors thank all technical employees and students who were involved in processing, machining, and analyzing the materials.

References

1. S. Martin, S. Wolf, U. Martin, L. Krüger, Solid St. Phenom. **172–174**, 172 (2011)
2. H. Biermann, J. Solarek, A. Weidner, Steel Res. Int. **83**, 512 (2012)
3. C. Weigelt, C.G. Aneziris, H. Berek, D. Ehinger, U. Martin, Adv. Eng. Mater. **14**, 53 (2012)
4. A. Weiß, H. Gutte, M. Radke, P.R. Scheller, Patent No. WO 002008009722A1 (24.08.2008)
5. M. Hajizamani, H. Baharvandi, Adv. Mater. Ph. Chem. **1**, 5 (2011)
6. E.G. Okafor, V.S. Aigbodion, Tribol. Ind. **32**, 31 (2010)
7. K. Kaur, O.P. Pandey, J. Alloys Compd. **503**, 410 (2010)
8. D. Wittig, A. Glauche, C.G. Aneziris, T. Minghetti, C. Schelle, T. Graule, J. Kuebler, Mater. Sci. Eng., A **488**, 6 (2008)
9. L.M. Peng, J.W. Cao, K. Noda, K.S. Han, Mater. Sci. Eng., A **374**, 9 (2004)
10. Y. Guo, Y. Zhou, X. Duan, D. Li, T. Lei, J. Mat, Sci. Technol. **19**, 137 (2003)
11. A. Glage, C. Weigelt, J. Räthel, H. Biermann, Int. J. Fatigue **65**, 9 (2014)
12. S. Decker, L. Krüger, S. Richter, S. Martin, U. Martin, Steel Res. Int. **83**, 521 (2012)
13. Y. Guo, Y. Zhou, X. Duan, D. Li, T. Lei, Ceram. Int. **30**, 6 (2004)
14. S.S. Panda, A. Upadhyaya, D. Agrawal, J. Mater. Sci. **42**, 966 (2007)
15. C.G. Aneziris, W. Schärfl, B. Ullrich, J. Europ. Ceram. Soc. **27**, 3191 (2007)
16. K. Lemster, T. Graule, J. Kuebler, Mater. Sci. Eng., A **393**, 229 (2005)
17. D. Sciti, A. Bellosi, L. Esposito, J. Europ. Ceram. Soc. **21**, 8 (2001)
18. W.B. Hanson, K.I. Ironside, J.A. Fernie, Acta Mater. **48**, 4 (2000)
19. C. Lin, D. Gan, P. Shen, J. Am. Cer. Soc. **71**, 6 (1988)
20. R.F. Domagala, S.R. Lyon, R. Ruh, J. Am. Cer. Soc. **56**, 584 (1973)
21. C. Weigelt, S. Giersberg, C. Wenzel, C.G. Aneziris, Adv. Eng. Mater. **12**, 486 (2010)
22. C. Weigelt, H. Berek, C.G. Aneziris, R. Eckner, L. Krüger, Mater. Sci. Forum **825–826**, 498 (2015)
23. C.G. Aneziris, W. Schärfl, H. Biermann, U. Martin, Int. J. Appl. Ceram. Technol. **6**, 727 (2009)
24. C. Weigelt, C.G. Aneziris, A. Yanina, S. Guk, Steel Res. Int. **82**, 1080 (2011)
25. H. Biermann, U. Martin, C.G. Aneziris, A. Kolbe, A. Müller, W. Schärfl, M. Herrmann, Adv. Eng. Mater. **11**, 1000 (2009)
26. P.A. Evans, R. Stevens, J. Binner, Br. Ceram. Trans. **83**, 39 (1984)
27. C. Weigelt, H. Berek, C.G. Aneziris, S. Wolf, R. Eckner, L. Krüger, Ceram. Int. **41**, 2328 (2015)
28. S. Martin, S. Richter, S. Decker, U. Martin, L. Krüger, D. Rafaja, Steel Res. Int. **82**, 1133 (2011)
29. M.P. Phaniraj, D.K. Kim, J.H. Shim, Y.W. Cho, Acta Mater. **57**, 9 (2009)
30. C. Weigelt, E. Jahn, H. Berek, C.G. Aneziris, R. Eckner, L. Krüger, Adv. Eng. Mater. **17**, 1357 (2015)
31. C. Weigelt, C.G. Aneziris, R. Eckner, L. Krüger, in *Proceeding of the World PM2016 Congress and Exhibition*, The European Powder Metallurgy Association, Hamburg, Germany, 9–13 Oct 2016
32. W. Zhang, J. Xie, C. Wang, Mater. Sci. Eng., A **382**, 387 (2004)
33. S. Noh, A. Kimura, T.K. Kim, Fusion Eng. Des. **89**, 1746 (2014)
34. Z. Chen, K. Ikeda, T. Murakami, T. Takeda, J. Am. Cer. Soc. **83**, 1081 (2000)
35. C. Weigelt, C.G. Aneziris, D. Ehinger, R. Eckner, L. Krüger, C. Ullrich, D. Rafaja, J. Compos. Mater. **49**, 3567 (2015)

36. C. Weigelt, G. Schmidt, C.G. Aneziris, R. Eckner, D. Ehinger, L. Krüger, C. Ullrich, D. Rafaja, J. Alloys Compd. **695**, 9 (2017)
37. N. Chawla, Y.-L. Shen, Adv. Eng. Mater. **3**, 357 (2001)
38. R. Eckner, M. Krampf, C. Segel, L. Krüger, Mech. Compos. Mater. **51**, 707 (2016)
39. M. Droste, H. Biermann, Mater. Sci. Forum **825–826**, 176 (2015)
40. S. Prüger, L. Mehlhorn, U. Mühlich, M. Kuna, Adv. Eng. Mater. **15**, 542 (2013)
41. H. Berek, A. Yanina, C. Weigelt, C.G. Aneziris, Steel Res. Int. **82**, 1094 (2011)

Chapter 6
Understanding of Processing, Microstructure and Property Correlations During Different Sintering Treatments of TRIP-Matrix-Composites

Sergey Guk, Rudolf Kawalla and Ulrich Prahl

Abstract This chapter presents scientifically robust results on the sintering behavior of transformation-induced plasticity (TRIP)-matrix composites based on different consolidation processes, such as conventional sintering, resistance sintering and hot pressing. The correlation of the processing parameters to the adjusted properties, such as the density, porosity, grain size, phase composition and mechanical properties is discussed. The theoretical modeling, including validation with experiments, enabled us to describe, understand and quantitatively optimize the sintering process.

6.1 Introduction

Powder metallurgy (PM) is an attractive production route for conventional metal matrix composites (MMCs) because it offers a wide range of reinforcing particle size amounts and distributions in the matrix material. The additional advantages of PM processes are that the grain growth is lower than that from the ingot metallurgy route, and the reaction between the matrix and reinforcing particles can be minimized by using solid-phase sintering processes. This route is most commonly used in the case of composite materials with steel or other high-performance materials as a matrix that cannot be produced by means of the conventional ingot metallurgy route due to the high processing temperatures, different melting points or different densities of the composite components. Conventional PM production normally consists of three steps: blending the metal and ceramic powders, compacting and sintering. In some cases, a sizing step follows the sintering step. During the processing, such when the blending and compacting of the powder particles and pores inside the green compact are adjusted, consolidation processes, such as conventional or conductive sintering, hot pressing (HP) or hot isostatic pressing (HIP), complete the final compaction of the composite material. They differ in the type of heating that occurs (radiative or

S. Guk (✉) · R. Kawalla · U. Prahl
Institute for Metal Forming, Technische Universität Bergakademie Freiberg,
Bernhard-von-Cotta-Str., 09599 Freiberg, Germany
e-mail: sergey.guk@imf.tu-freiberg.de

H. Biermann and C. G. Aneziris (eds.), *Austenitic TRIP/TWIP Steels and Steel-Zirconia Composites*, Springer Series in Materials Science 298,
https://doi.org/10.1007/978-3-030-42603-3_6

conductive heating) and whether additional consolidation acceleration occurs due to the presence an external compressive load (conductive sintering, HP and HIP).

In the past, the described advantages of PM instigated many investigations into MMCs that dealt with the optimization of the sintering processes. In several studies, conventionally sintered composite materials, such as functionally gradient materials (FGMs), that were based on stainless steel with a ceramic component, namely, ZrO_2, were investigated [1–4]. The results showed significant residual stresses in the consolidated composite material that resulted in a high concentration of microcracks after the completion of all manufacturing steps. These stresses can be attributed to a difference in the thermal expansion coefficients between the ceramic and steel and the volume expansion during phase transformation. However, an optimal selection of sintering conditions that considers the layer structure leads to good interface quality. For example, a 4-layer FGM extruded in the form of a tube, consisting of a 316L steel matrix and yttrium partially stabilized ZrO_2 (PSZ), was produced after sintering at 1350 °C for 1.5 h with a good layer interface quality [5]. The good interface formation in composite materials is based on a chemical reaction at the phase interface, which can cause destabilization of the tetragonal(t) phase of ZrO_2 [6]. A variation of the sintering atmosphere showed that while nitrogen positively influenced the mechanical properties of the sintered composite materials, good corrosion properties were achieved by sintering in a vacuum or hydrogen [7].

The consolidation of powders by conductive sintering can be based on different technologies, such as spark plasma sintering (SPS), pulsed electric current sintering (PECS), pulse discharge sintering (PDS), plasma activated sintering (PAS), and field activated sintering technique (FAST). The resistance sintering used in this research is characterized by a direct conversion of electrical energy into heat in the sintered material by applying an electrical voltage to the sample. In [8], a sintering progress was investigated on chromium powder ПХ1М in the temperature range from 1300 to 1500 °C and for sintering times that reached 5 min. The results showed that at the beginning of the isothermal holding time, the effect of the electric current dominated, after which small pores were distributed in the microstructure. The increasing holding time at constant temperature caused low coagulation and enlargement of the pores as well as an increase in the microscopic stresses, which was explained by the action of Laplace forces. Similar investigations of iron powder showed that the densification of a sample to 95% of its relative density when it had dimensions of ∅12.8 mm × 3.6 mm was possible by heating at 600 K/s to a sintering temperature of 800 °C and with a sintering time of 6 min [9]. The tests were carried out with a relatively low voltage of 3–10 V and with high current values above 10 kA. The authors indicated that fast densification of the material occurred during the heating phase since at this time, the elevated resistance caused a high Joule heating effect. Furthermore, a theoretical prediction of the influence of the composition of the conductive and nonconductive phases on the physical-mechanical properties of the composite materials was carried out [10]. Theoretical modeling that included experimental validation showed that the limit of percolation (the limiting value of the conductor content at which the conductivity becomes zero) depends on the ratio of the particle sizes of the conducting and the insulating phases. As long as the particle size of the

conducting phase decreases compared to that of the insulating phase, the percolation limit decreases (conductivity can also be achieved with a small content of the conducting phase). In other cases, the percolation limit increases (a small content of the insulating phase leads to the composite material becoming insulating).

Many investigations and broad experience from industrial practice have proven that an externally applied pressure accelerates the sintering process of a porous body. The influence of the pressure on the sintering kinetics at different pressures and temperatures results from the different deformation mechanisms in the porous sintered material, which have been described in detail in Geguzin [11]. The advantages of processes that apply pressure include the manufacturing of dense materials with lower sintering temperatures and shorter sintering times than those of conventional sintering processes; this results in sintered parts with an increased strength that quite often do not require sintering aids. While a substantial amount of knowledge has already been gained regarding the HP of ceramics, metals and cermets, there are only a few papers regarding HP of steel-ZrO_2 composites. For example, the properties of a ZrO_2(2Y)/transformation-induced plasticity (TRIP)-steel composite produced by HP were investigated depending on the value of applied stress [12]. The powder mixtures were subjected to HP at 1250 °C at 20 MPa for 30 min. The results indicated that the tensile strength and the modulus of elasticity of the composite material decreased under static loading with increasing ZrO_2 content up to 35 vol% due to weak bonding at the ZrO_2–ZrO_2 and ZrO_2-TRIP steel phase interfaces. The dynamic yield strength of the composite was greater than that of the static composite due to the induced martensite transformation, which provided improved plasticity and overall formability. The effect of the ZrO_2 content on the tensile strength of the composite material at the beginning of dynamic deformation was not evident. The rheological stresses increased with increasing ZrO_2 content and deformation in the ZrO_2(2Y)/TRIP-steel composites. Nevertheless, the formability and dynamic strength of the composites decreased with decreasing ZrO_2 content. Furthermore, manufacturing of FGMs based on tetragonal zirconia polycrystal (TZP) and stainless steel or Ni in the form of SUS304-TZP or Ni-TZP, respectively, could be achieved by HP at 1250 °C for 1 h in a nitrogen atmosphere with 5 K/min heating and cooling rates [13–15]. Finite element modeling of the process indicated that the coefficient of thermal expansion of the composite components was a decisive factor in the production of FGMs free of residual stresses and cracks caused by cooling. Thus, Ni-TZP composites were demonstrated to have better thermal insulating properties than SUS304-TZP.

The postdensification of sintered parts can be achieved by HIP. Unfortunately, there are no data available in the literature about the postdensification of TRIP steel-ZrO_2 composites, while sufficient information is available on the HIP behavior of stainless steel powders. The HIP investigations showed that the relative density of AISI 316L samples was more influenced by the HIP temperature than they were by the HIP pressure. The maximum density of 97% was achieved by HIP at 1250 °C and 120 MPa [16]. Furthermore, the compression behavior of AISI 304 steel-based components at various manufacturing parameters was investigated in [17], whereby the manufacturing route consisted of compacting by selective laser sintering (SLS) with

simultaneous cold isostatic pressing (CIP) in the range between 300 and 600 MPa and then sintering in the temperature range between 1250 and 1350 °C for 1 h under a vacuum of 10^{-3} Pa. Finally, the components were hot isostatically pressed at 1200 °C at 120 MPa for 1 h. The component manufactured at the maximum CIP pressure and sintering temperature achieved a maximum density of 97% after HIP.

The aim of the present work is the investigation of the densification behavior and final mechanical properties of TRIP-matrix composites depending on the different fabrication processes.

6.2 Materials and Methods

Both stainless steel and PSZ powders were used for the investigations. The gas-atomized steel powder was purchased commercially as grade AISI 304 stainless steel (grade 1.4301 stainless steel). Three batches were available, and each was used for one of the three consolidation routes. The batches differed slightly in chemical composition and the resulting delta ferrite fraction (Table 6.1). The particle size varied minimally from batch to batch and was in the range of approximately $d_{10} = 10\ \mu m$, $d_{50} = 25\ \mu m$ and $d_{90} = 45\ \mu m$.

The solidus temperatures of the stainless steel powder batches calculated with the help of the FactSage® program based on the present chemical analysis were 1426 °C (conventional sintering), 1361 °C (resistance sintering) and 1405 °C (HP).

ZrO_2 powder was used for the investigations in the partially stabilized ZrO_2 (PSZ) form. MgO was applied as a stabilizer. The chemical composition of the powder is shown in Table 6.2. The ceramic particles had an angular shape with a approximate particle size in the range of $d_{10} = 0.2\ \mu m$, $d_{50} = 3\ \mu m$ and $d_{90} = 22\ \mu m$. The phases were distributed among the monoclinic (m), t and cubic (c) phases at nearly equal amounts of 35:32:33%.

The fabrication of MMCs was carried out by conventional and resistant sintering as well as by HP with partial application of the HIP process. The preparation of the powder mixture for all consolidation routes was carried out either by blending for conventional sintering and HP with partial application of the HIP process or by mechanical alloying of the powder mixtures for resistance sintering. Before blending, the volume fraction of ZrO_2 was adjusted from 0 to 30 vol%. The inorganic powder mixture was then blended by means of ZrO_2 balls stabilized with yttrium for approximately 30 min in a ball mill. Especially for the conventional sintering process, approximately 2.5 mass% of organic binder was added.

The powder mixture was prepared for resistance sintering using a mechanical alloying technique in a vibrating mill with high energy output (attritor) [18]. The grinding duration was approximately 90 s for each 250 g of the initial powder mixture. At the end of the process, the powder mixture was fabricated with an activated surface.

Compacting the green bodies for conventional sintering was carried out by extrusion of the prepared powder mixture. Extruded rods 20 mm in diameter were fabricated using a single-screw extruder with a vacuum chamber in combination with

Table 6.1 Chemical composition of the AISI 304 stainless steel powder for the respective consolidation route, wt%

Consolidation route	C	Mn	Si	S	Cr	Ni	Mo	Ti	Nb	N	δ-ferrite
Conventional sintering	0.01	0.9	0.2	0.007	17.5	10	0.03	0.004	0.007	0.04	7
Resistance sintering	0.08	0.8	0.8	0.014	21.3	11.9	–	–	–	0.25	9
Hot pressing	0.03	1.4	0.3	0.006	16.7	8.5	0.3	0.007	0.035	0.126	18

Table 6.2 Chemical composition of ZrO_2 powder, wt%

ZrO_2	Y_2O_3	SiO_2	Al_2O_3	HfO_2	CaO	MgO	TiO_2	K_2O	Na_2O	BaO	Fe_2O_3
96.3	–	0.4	–	–	0.6	2.8	0.13	–	0.1	–	0.13

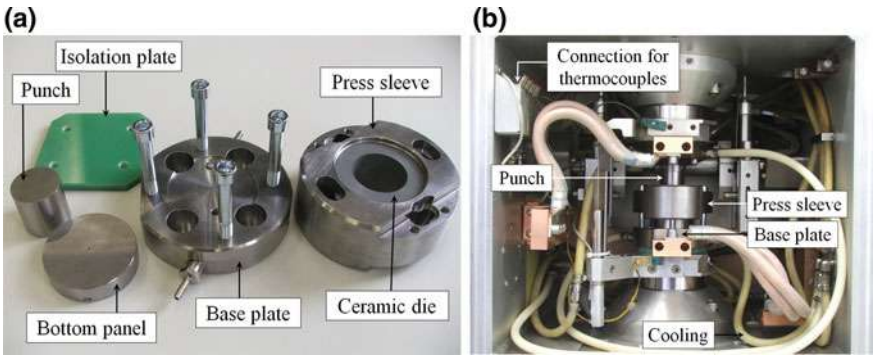

Fig. 6.1 Parts of the tool for resistance sintering (**a**) and their locations in the test chamber of the GLEEBLE HDS-V40 (**b**)

a kneading machine. After the extrusion process, the green compacts were cut into segments of the required length. Afterwards, the water added to the powder mixture before kneading was removed by an air dryer. The relative density of the extruded green bodies was approximately 60%. The subsequent removal of the organic binder occurred in the air at 350 °C for a duration of 5 h. The heating took place up to 100 °C at a rate of 2 K/min and at a rate of 0.2 K/min above 100 °C. The cooling took place at the same rates.

Conventional sintering was performed on extruded and debindered green compacts in an Astro 1100-60100-M1 model refractory metal hot-zone laboratory furnace (Thermal Technology LLC_{TM}). The accuracy of the temperature measurement was ±4 K over the applied temperature range. According to the furnace manufacturer, the typical temperature homogeneity of the furnace at 1700 °C is ±3 K for 35% and ±6 K for 50% of the furnace chamber volume. The sintering process took place in argon and nitrogen atmospheres (class 5.0) as well as in a vacuum of 10^{-6} mbar. The heating rate was approximately 5 K/min, while the cooling rate was approximately 10 K/min.

A multifunctional GLEEBLE HDS-V40 simulation system (Dynamic Systems Inc.) was used for the resistance sintering. The parts of the specially designed tool for resistance sintering in the GLEEBLE are shown in Fig. 6.1 and consisted of water-cooled base plates, a bottom panel, a ceramic die (Si_3N_4) with conical inward and outward design features, and a steel press sleeve to reinforce the ceramic die and a punch. To reduce the heat dissipation from the face of the sample in the front through the bottom panel, additional plates of carbon-fiber-reinforced carbon (with a thermal conductivity of 3 Wm^{-1} K^{-1} and specific electrical resistance of 26 μΩ)

were interposed for thermal insulation. Furthermore, a higher electrical conductivity than that of steel was achieved by using punches fabricated from a material based on a molybdenum alloy with the addition of Ti and Zr. The base plates had current connections but were electrically insulated from the other parts of the GLEEBLE by isolation plates. The powder mixture to be sintered filled the ceramic die before resistance sintering, where the mass of the powder mixture to be sintered was always 250 g. The dimensions of the sintered samples were ∅50 mm × 18 mm. The ceramic die and tool surfaces were lubricated by hexagonal boron nitride spray before each test to improve the removal of the sintered sample from the tool after the process. To avoid welding the powder mixture to the bottom panel and the punch as well as carburization of the sample by the carbon-fiber-reinforced carbon plates, a tantalum foil was placed in those areas. After closing the ceramic die with the punch and applying a critical presintering pressure of approximately 50 MPa, the resistance sintering was carried out according to a specified temperature-time cycle with an almost constant sintering pressure of approximately 20 MPa. The temperature of the sample during the sintering process was continuously controlled and adjusted with the help of a thermocouple that was located in the bottom panel and carbon-fiber-reinforced carbon plate so that the heating rate was approximately 50 K/min. Another thermocouple was used for the temperature measurement of the punch and was placed near its working surface. The sample resistance controlled the sintering temperature depending on the ZrO_2 content, the presintering pressure and the sintering pressure as well as the temperature profile. In the course of the resistance sintering tests, the voltage and current values were measured and recorded with an accuracy of ±0.01 V and ±1 A using an ALMEMO 2690-8 measuring instrument. The peak values of the voltage and current were approximately 4 V and 6 kA, respectively. Based on the determined values, the electrical resistance of the samples R was calculated according to the following equation:

$$R = I/U, \tag{6.1}$$

where I is an electrical current and U is an electrical voltage.

After the tests, the samples were cooled in the sintering tool before they were removed.

Preliminary tests that directly hot pressed the powder mixtures in the molds (at 1250 °C for 2 h at 30 MPa) resulted in destruction of the graphite molds as a result of the penetration of the mixture into the mold gaps and its interaction with the mold material. For this reason, two methods of mixture precompaction into billets were tested: die cold pressing (CP) of the powder mixture and CIP followed by short-term presintering in a hydrogen atmosphere (Table 6.3). Significant advantages of the first method include the simplicity of the process, high productivity and possibility of mechanization. However, a significant heterogeneity of the billets in terms of the density and inability to produce parts with a complex shape did not allow us to consider this as a universal method. The second method overcomes the disadvantages of the die CP step, but the size inaccuracy of fabricated green compacts and their high surface roughness require the application of additional labor-intensive machining. To

Table 6.3 HP consolidation routes

Method	Steps and their processing parameters			
1st	**CP** $P = 60$ MPa		**HP** $T = 1100$, 1200, 1250, 1275 °C $t = 1$ h $P = 30$ MPa	–
2nd	**CIP** $P = 350$ MPa	**Presintering** $T = 1100$ °C $t = 1$ h H_2 atmosphere		**Post-HIP** $T = 1225$ °C $t = 1$ h $P = 100$ MPa

avoid the appearance of cracks and stratifications in the billets after CIP, the addition of short-term sintering in a hydrogen atmosphere was carried out, and a relative density of approximately 85% was achieved.

The dimensions of the HP samples were ∅80 mm × 20 mm. To remove the residual porosity in the specimens after HP, HIP in an ABRA press apparatus (ABRA Fluid AG) was added and its impact on the microstructure and property evolution was investigated.

The density of the sintered samples was determined in accordance with DIN EN 623-2. The samples for metallographic analysis and mechanical testing were cut from the machined sintered workpieces. Tensile tests were carried out on an AG-100kNG universal testing machine at room temperature according to DIN EN ISO 6892-1 on cylindrical specimens with dimensions of ∅4 mm × 20 mm. The impact toughness of the 55 mm × 10 mm × 10 mm samples with a V-shaped stress concentration was tested on a RKP450 impact testing machine at room temperature according to DIN EN ISO 148-1. In all cases, samples were obtained in the axial direction for conventionally sintered samples and in the transverse direction for the resistance sintered or hot-pressed samples. The hardness HV10 was determined according to DIN EN ISO 6507-1 on a ZHU250 instrument. The microstructure and fracture surface analysis of the tested samples were carried out by light and scanning electron microscopy. A quantitative evaluation of the micrographs was conducted to determine the pore shape factor f according to Equation:

$$f = 4\pi A / C^2, \tag{6.2}$$

where A is a grain surface area and C is a circumference of a grain.

The size of the pores and grains was determined with the help of the image processing program Archive4Images. The phase analysis of the ceramics after different consolidation routes was conducted with X-ray diffraction (URD 6 X-ray diffractometer) with an accelerating voltage of 40 kV and current of 30 mA; energy-dispersive X-ray spectroscopy was also conducted.

Based on the experimental results, it was possible to model the sintering behavior with kinetics calculations equations [19] as follows:

$$\rho_{\mathrm{rel}}(t, \vartheta, Z) = \left(1 + z_1 \cdot Z + z_2 \cdot Z^2\right) \cdot (\rho_{\min} + (\rho_{\max} - \rho_{\min})) \cdot \left(1 - \mathrm{e}^{-\left(\frac{t}{T(\vartheta)}\right)^q}\right) \tag{6.3}$$

where ρ_{rel} is a relative density, t is a time, ϑ is a temperature, Z is a ZrO_2 content, z_1 and z_1 are constants to be determined from the available data. Furthermore,

$$T(\vartheta) = \frac{q}{k} \cdot \mathrm{e}^{\frac{Q}{R \cdot (\vartheta - \vartheta_B)}} \tag{6.4}$$

Here, parameters occurring in the equation, such as the Avrami exponent and activation energy, were determined using experimental results and the mathematical-numerical method of nonlinear least square approximation. It was assumed that heating did not have a significant influence on the sintering process, i.e. the assumption of isothermal conditions was used. The modeling approach was sufficient to allow interpolation of the measured values after their successful validation for the purpose of design of optimum technological parameters and thus find an understanding of the changes taking place in the material.

6.3 Results

6.3.1 Conventional Sintering

The results from the investigations showed that the development of the microstructure and pore morphology in the undoped steel matrix (ceramic free) was significantly influenced by the sintering temperature [20, 21]. Particle rearrangement processes took place at a temperature of 1300 °C, which was reflected in the local growth of the pore area (Fig. 6.2). The temperature increase led to the growth of sinter bridges between particles and the associated increase in relative density. This effect is based on the small pores combining with large pores to reduce the surface energy (Ostwald ripening). The final stage of the sintering process was characterized by morphological changes. This involved pore rearrangement due to the ongoing Ostwald ripening phenomenon, including the effect of enclosed gases, as well as the nearly doubled the austenite grain growth. Finally, only closed pores that were isolated from each other were present. The sintering carried out at 1430 °C indicated that the shape of the sample began to change, and this limit was noted.

To achieve advantageous mechanical properties, the favorable sintered microstructure should have, on the one hand, the highest possible value of the shape factor in combination with the lowest possible value of the pore area. On the other hand, minimal grain coarsening should occur. This combination of favorable microstructure properties was achieved at a sintering temperature of 1390 °C.

For the case of a steel matrix doped with ceramic constituents, the sintering behavior was analyzed based on measurements of the electrical resistance of the

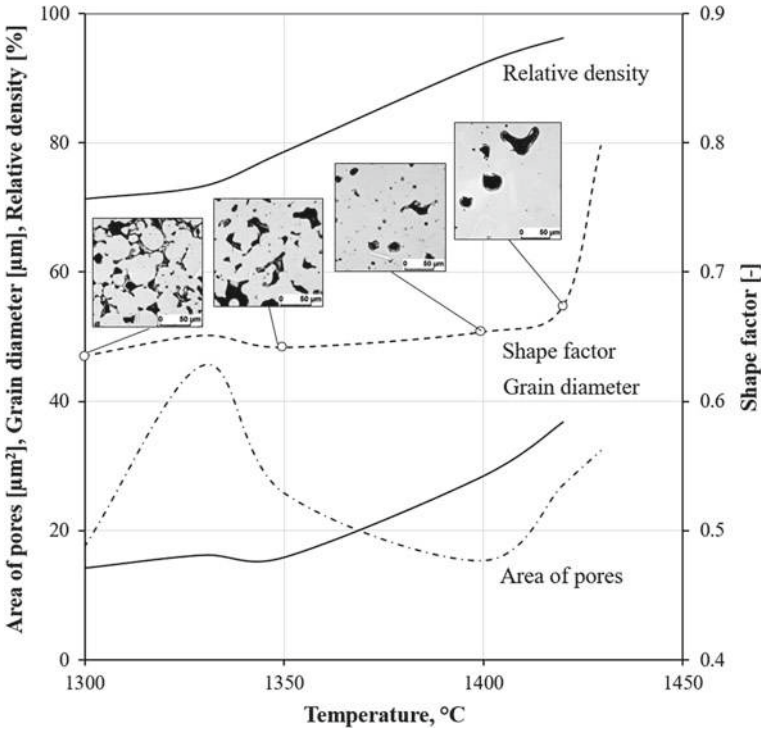

Fig. 6.2 Development of the microstructure and pore morphology in the undoped steel matrix with increasing sintering temperature for a sintering time of 2 h

specimen. Figure 6.3 presents exemplary results for the composite with 5% ZrO_2. The results show that the electrical resistance trend can be divided into three zones for this specimen [22]. In the first zone, the contact between the powder particles was substantially responsible for the electrical resistance of the specimen. The contact area of the powder particles increased during the sintering process, which was reflected in the significant decrease in the electrical resistance. Furthermore, in the first zone, a local region that experienced a resistance increase can be clearly seen in the continuously decreasing electrical resistance near the temperature of 730 °C, where the δ-ferrite phase was dissolved in the austenitic steel matrix according to the phase transformation diagram. Austenitic steel has a specific resistance up to 7 times greater than that of ferritic steel, which caused an increase in the electrical resistance of the composite material. In the second zone, the rate at which the electrical resistance decreased was noticeably reduced. Finally, in the third zone, the resistance passed into the range of pure material resistance. After the sintering process completed and while the specimen cooled, the resistance was slightly reduced due to its temperature dependence.

The scanning electron microscopy (SEM) images, including the chemical element distribution across the interface of the steel matrix doped with ZrO_2, showed that there

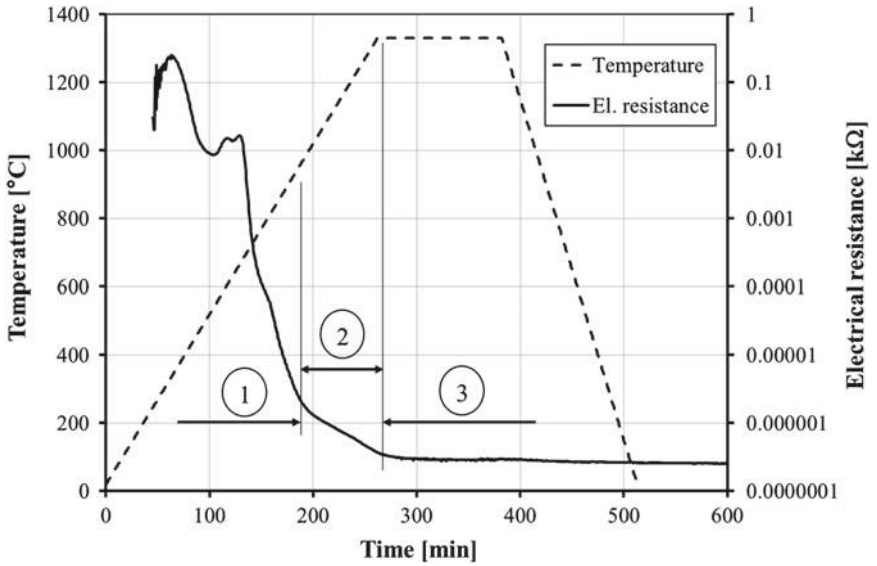

Fig. 6.3 Electrical resistance of the composite material with 5% ZrO_2 during conventional sintering

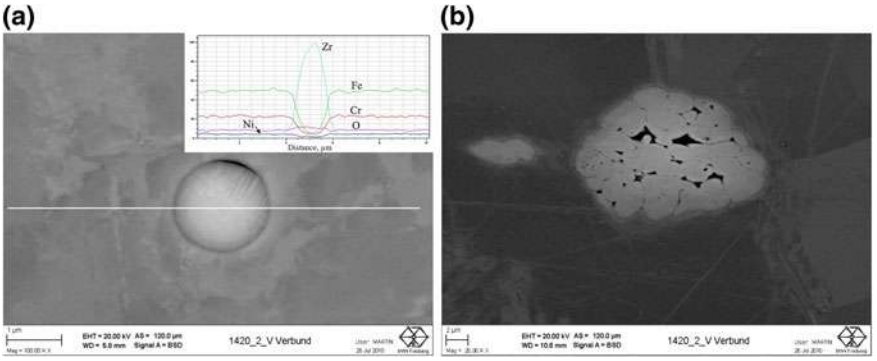

Fig. 6.4 Bonding between the ceramic and steel matrix for a composite with 2.5% ZrO_2 sintered at 1420 °C for 2 h for a single ceramic particle (**a**) and a ceramic agglomerate (**b**)

was a good bond between the ceramic particles and the matrix after sintering, while individual particles in the ceramic agglomerates were poorly sintered together due to the sintering temperature being too low for ceramic constituents (Fig. 6.4). The agglomerate formation of the ceramic particles in the cavities of the steel matrix was caused by a significant size difference between the steel and ZrO_2 powder particles. Furthermore, an increase in the sintering temperature of up to 1430 °C led to the formation of undesired Al–Mn–Mg-rich areas within the ceramic phase due to diffusion processes through the steel-ceramic interface [23].

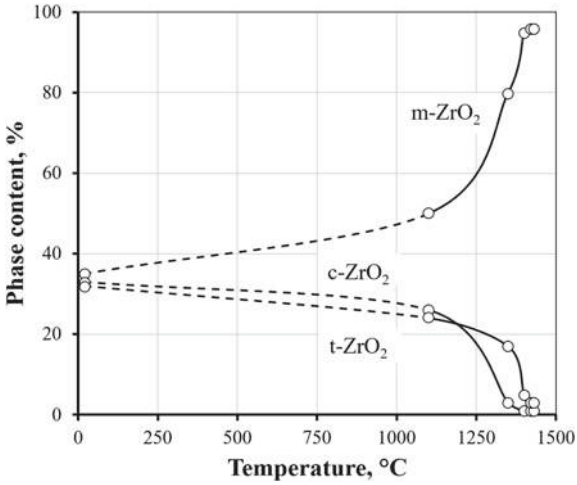

Fig. 6.5 Influence of the sintering temperature on the phase composition of ZrO_2 for the composite material with 5% ZrO_2 sintered in vacuum

The variation of the sintering atmosphere indicated that sintering under vacuum achieved a higher material density than that upon sintering in argon or nitrogen atmospheres. This resulted from practically no gas molecules being present in the pores, which facilitated the rapid shrinkage of the pores. After vacuum sintering, the material had fine pores with a high pore shape factor. However, the disadvantage of vacuum sintering lies in the evaporation of alloying elements from the steel matrix, such as C and Mn, which influenced the austenite stability, the characteristic temperatures of the martensite transformation (M_s, M_f) and finally the associated mechanical properties.

Furthermore, the negative influence of a high sintering temperature on the phase composition of the ceramic constituent was determined [24]. The exemplary results for the composite material with 5% ZrO_2 are shown in Fig. 6.5. It can be seen that increasing the sintering temperature led to an increased content of the undesired m ZrO_2 phase (m-ZrO_2) at the expense of the c (c-ZrO_2) and t (t-ZrO_2) phases, which were reduced.

The sintering of composite materials with varied ZrO_2 content showed that the density of the steel matrix doped with 2.5% ZrO_2 was similar to that of the undoped steel but with a slight deviation of up to 2% depending on temperature and time, while the material with 5% ZrO_2 had a density value similar to that for the composite with 10% ZrO_2. The increase in ZrO_2 content of up to 10% caused a density increase and associated microstructural developments in the composite materials. The ceramic particles became settled in cavities between the steel particles, which caused, among other things, a decrease in the porosity. An additional increase in the ZrO_2 content of up to 30% led to the formation of large ceramic particle agglomerates outside the cavities, which had an unfavorable effect on the densification process and thus on the density of the specimen (Fig. 6.4). Therefore, Fig. 6.6 shows the density of the undoped steel and composite materials with 10 and 30% ZrO_2 as a function of the sintering temperature and time. The steel matrix doped with 30% ZrO_2 had the lowest

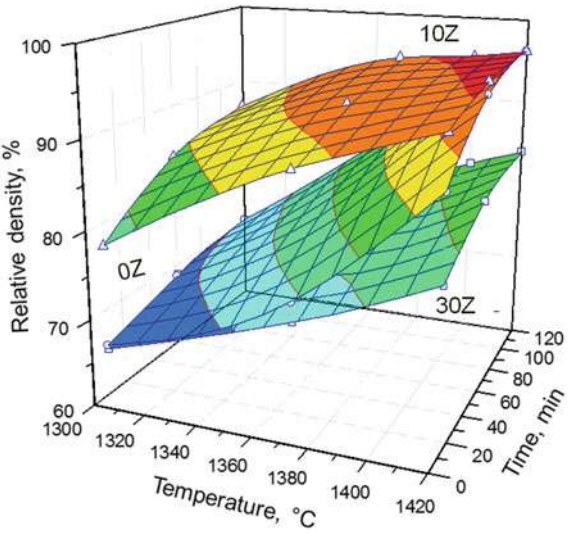

Fig. 6.6 The relative density of the vacuum-sintered steel (0Z) and composite materials with 10% (10Z) and 30% ZrO_2 (30Z) as a function of the sintering time and temperature

density values herein over the entire investigated time and temperature ranges. After sintering at 1300 °C, its density values were almost as high as those of the undoped steel, regardless of the sintering time. However, a further increase in temperature increased the density difference by up to approximately 13%. The maximum density was 85%. The relative density increase in the steel in the investigated temperature and time ranges was approximately 30%, while that of composite materials was a maximum of 20%. Among the materials investigated over the entire temperature and time ranges herein, the 5 and 10% ZrO_2 composites had the highest relative densities. Thus, the optimal sintering conditions from the point of view of the relative density were determined for the composite materials with a ceramic content of up to 10% ZrO_2. These optimal results were obtained at the temperature of 1420 °C and sintering times of 1–2 h. Under these circumstances, the composite materials with 5 and 10% ZrO_2 after sintering showed a maximum radial shrinkage of approximately 24% compared to that of approximately 18% for the undoped steel.

The results of subsequent modeling were able to show that the applied physical-empirical approach with regard to the ZrO_2 content (6.3) reflected the obtained experimental results sufficiently well (Fig. 6.7). Among the samples herein, the maximum density was observed for a composite with approximately 10–15% ZrO_2. As expected, the density increased with increasing sintering temperature. Figure 6.7b provides an example of how the relative density was influenced by the sintering time for a sintering temperature of 1420 °C and for ZrO_2 contents up to 30%. It is obvious that the ZrO_2 content caused a relative density decrease that reached approximately 13%.

The good validation agreement between the experimental results and the modeling values made it possible to quantify the densification rate of composite materials by a derivation of (6.3) over time. Figure 6.8 shows an exemplary of the densification

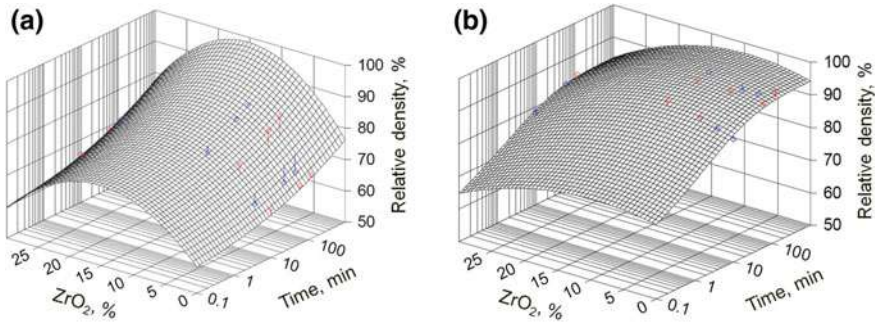

Fig. 6.7 Modeling results for the relative density development in relation to the ZrO_2 content and the sintering time at sintering temperatures of 1300 °C (**a**) and 1420 °C (**b**). The experimental results are marked with dots

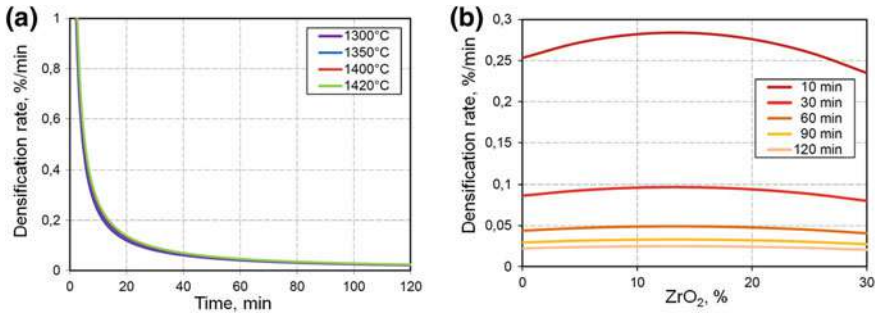

Fig. 6.8 Densification rate of the composite material with 5% ZrO_2 as a function of the sintering temperature and time (**a**) and the ZrO_2 content at the sintering temperature of 1420 °C (**b**)

rate for a composite material with 5% ZrO_2 as a function of the sintering temperature and time. Figure 6.8a shows, for example, that the densification rate at the beginning of sintering rapidly decreased from very high values to rates below 0.1%/min within a few minutes, while the dependence on temperature was comparatively very low. The sintering process was thus almost completed after a sintering time of 2 h, and it was confirmed that an optimum was achieved with regard to both the advantageous material properties and fabrication effort.

It can also be seen that the densification rate in the investigated temperature range showed a low dependency on the ZrO_2 content (Fig. 6.8b). The composite material with approximately 15% ZrO_2 content had the maximum densification rate among the samples herein at the experimentally realized shortest sintering time of 10 min, while the material with 30% ZrO_2 showed the lowest densification rate at the same time. Furthermore, the results indicate that the densification rate at sintering times of approximately 1 h and above is practically independent of the ZrO_2 content.

Figure 6.9 shows the mechanical properties of the sintered composites as a function of the relative density and ceramic phase content. It is obvious that while the

tensile strength was linearly dependent on the relative density (Fig. 6.9a), the dependence of the total elongation had an exponential relationship (Fig. 6.9b). The increasing in the ceramic content tended to contribute to an increase in the tensile strength, while its large values presented a decrease in the tensile strength due to the increasing tendency of the ceramic to form agglomerates.

The investigation of the fracture surfaces of the undoped tensile specimens revealed that two fracture phenomena occurred depending on the sintering temperature: a prevalent intergranular failure at 1330 and 1350 °C (Fig. 6.10a) and a ductile fracture with a characteristic void structure at 1400 °C (Fig. 6.10b). The microscopic relief of the fracture surfaces in the investigated temperature range essentially depended on the porosity, which was adjusted by the sintering temperature and sintering time. Residual pores and nonmetallic inclusions in the SiO_2 and MnO are also visible on the fracture surface since crack propagation through these areas was facilitated.

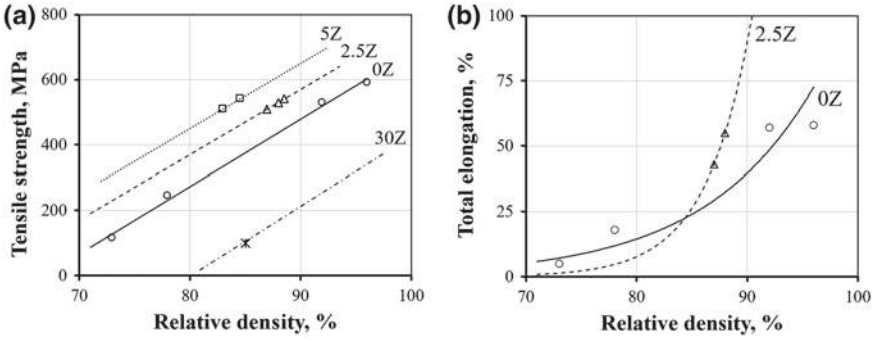

Fig. 6.9 Tensile strength (**a**) and total elongation development (**b**) for steel (0Z) and composite materials (from 2.5 to 30Z) after conventional sintering under vacuum

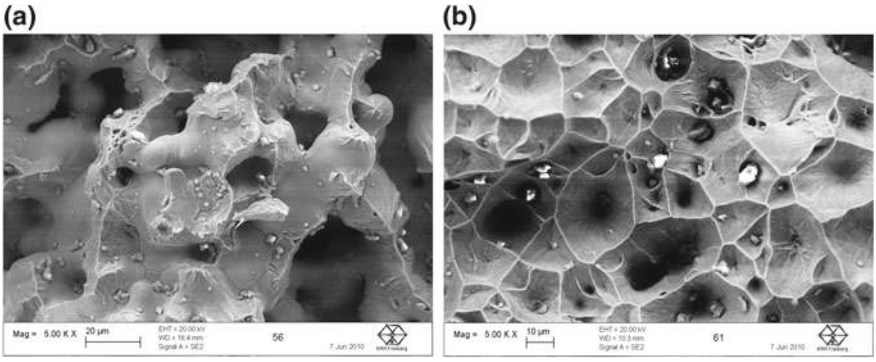

Fig. 6.10 The fracture surfaces for steel samples sintered under vacuum for 2 h at sintering temperatures of 1350 °C (**a**) and 1400 °C (**b**)

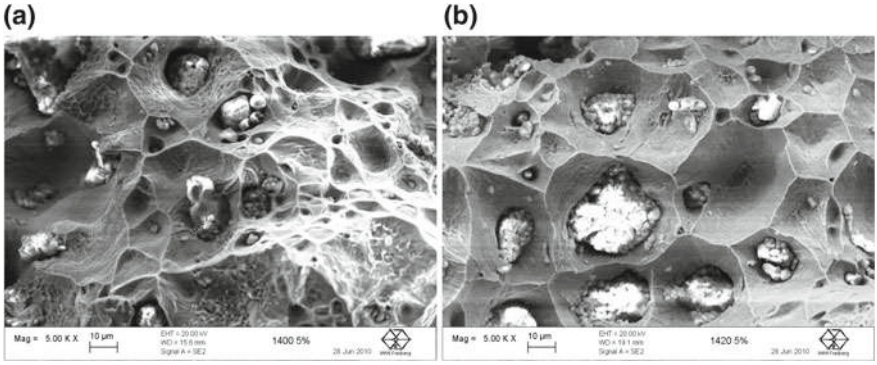

Fig. 6.11 The fracture surfaces for a composite material with 5% ZrO_2 sintered under vacuum for 2 h at sintering temperatures of 1400 °C (**a**) and 1420 °C (**b**)

The SEM images of the fracture surfaces of the composite material with 5% ZrO_2 show a similar failure behavior to that the an undoped steel matrix (Fig. 6.11). Here, single embedded ceramic particles and agglomerates are visible in the austenitic matrix. Pores can be seen in the area between the two phases. In addition, there are visible ZrO_2 particles on the fracture surface, like nonmetallic inclusions and pores, that represent the most favorable places for crack initiation and propagation.

The fracture behavior of MMCs with up to 5% ZrO_2 after tensile loading was influenced by the relative density and associated strength and ductility. Thus, the MMCs with up to 7% residual porosity showed ductile fracture behavior, which was caused by the void formation mechanism and the coalescence of the micropores. The fracture occurred along the grain boundaries near the residual pores in the steel matrix or near the ZrO_2 particles in the MMCs. This effect can be explained by the inhomogeneous distribution of the stress and strain fields due to the mechanical loading of the porous material. The stresses were more likely to be located in the interface region between the grain boundary and the pore than elsewhere since the radius there was minimal. As the sintering temperature increased and the sintering time increased, the material densified to a certain extent while the porosity was eliminated. In the final stage of the sintering process, when only closed pores were present in the microstructure, the intracrystalline pores were formed. The disadvantage of intracrystalline pores is that they can be reduced neither in number nor in size due to the low activation energy for volume diffusion. The advantage is that the intracrystalline pores can be spherical, and spherical pores have a lower stress concentration than that of other shapes, and thus they had a decreased tendency to form notches.

6.3.2 Resistance Sintering

Figure 6.12 shows the temperature and force trends during a stroke-controlled sintering process of the TRIP-matrix composite with 5% ZrO_2. The process consisted of three stages [25]. In the first stage, there was a temporary increase in the force for a time up to approximately 400 s, where in the middle of the sample, the temperature increased to 950 °C. This force increase was due to the thermal expansion of the sample and tools. The immediately following second stage is characterized by a reduction in the force with a corresponding large specimen shrinkage and decrease in the porosity. Finally, in the third and final stage, the shrinkage slowed dramatically, which was reflected in the force stabilizing at a constant level. During the entire sintering process, the electrical resistance decreased almost continuously to a few mΩ.

Metallographic analysis for the center of a densely sintered composite material showed an average grain diameter of $d_{50} = 9.6\ \mu m$ (Fig. 6.13a). Such a fine-grained microstructure resulted from both the mechanical alloying technique and the short residence time at the sintering temperature, where the resistance sintering was dominant. In the high-magnification SEM images, good bonding of the ZrO_2 particles to the steel matrix can be seen in addition to individual residual pores on the phase interface (Fig. 6.13b). In contrast, the ceramic particles in the agglomerates demonstrated a poor local bonding quality.

However, the microstructure of sintered samples sectioned across their median showed sufficient inhomogeneities (Fig. 6.14). The highest obtained relative density of approximately 99% was reached in the middle of the sample at the side of the

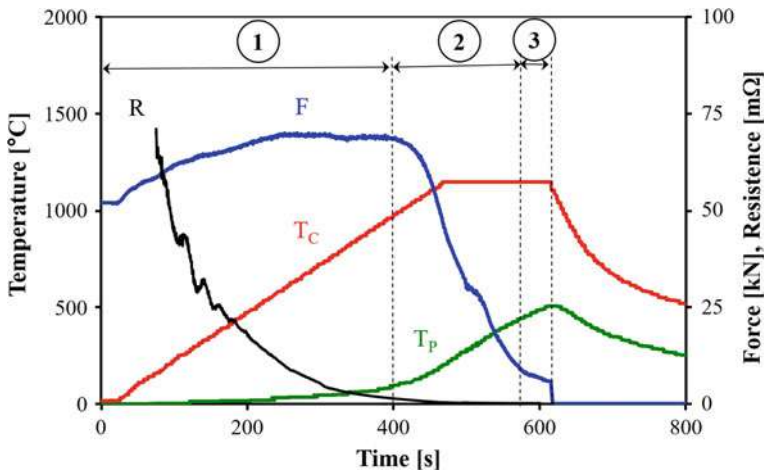

Fig. 6.12 Development of the electrical resistance R and the force F during a stroke-controlled resistance sintering process of the TRIP-matrix-composite with 5% ZrO_2 (T_C and T_P are the temperatures in the center of the sample and on the punch working surface, respectively)

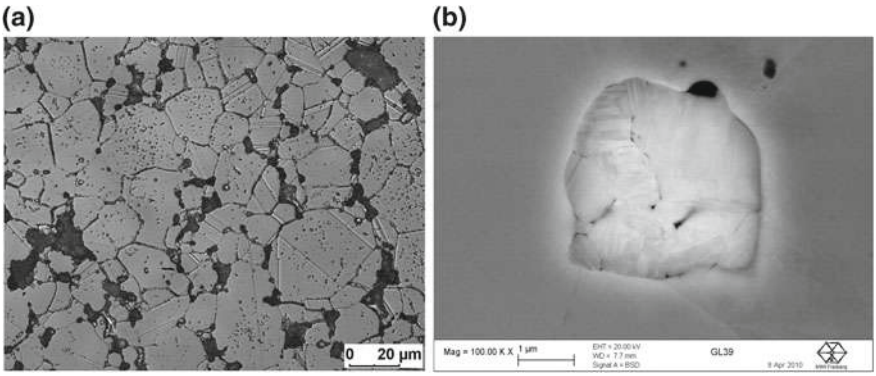

Fig. 6.13 Light microscopy image for a composite sample with 5% ZrO_2 sintered at 1100 °C for 11 min (**a**) and SEM image of the resulting bonding between ZrO_2 particles agglomerate and the steel matrix (**b**)

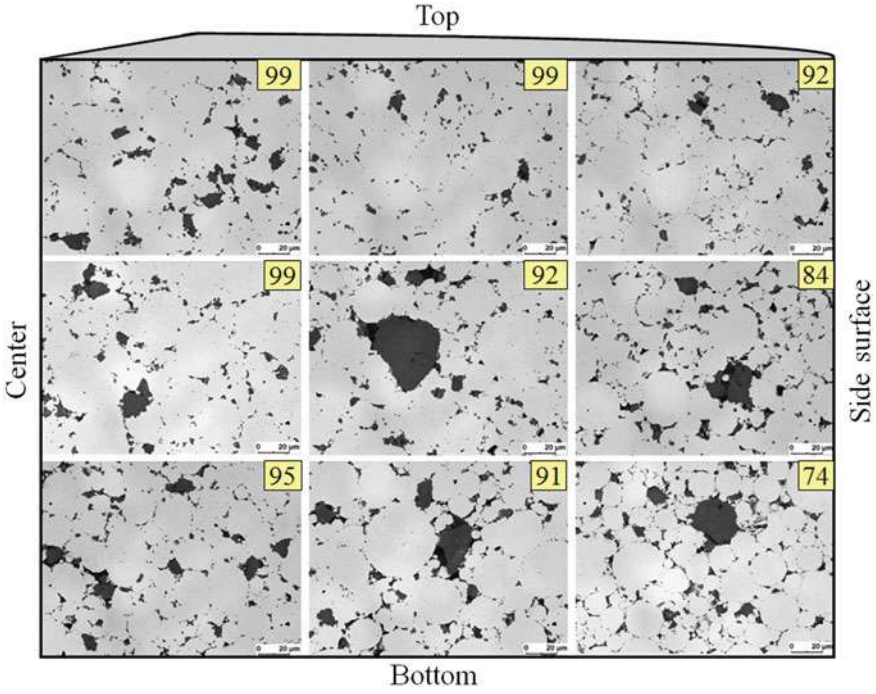

Fig. 6.14 Inhomogeneity of the sintered microstructure shown by a quarter cut of a 5% ZrO_2 composite sample. The numbers in the square represent the local relative density measured in %

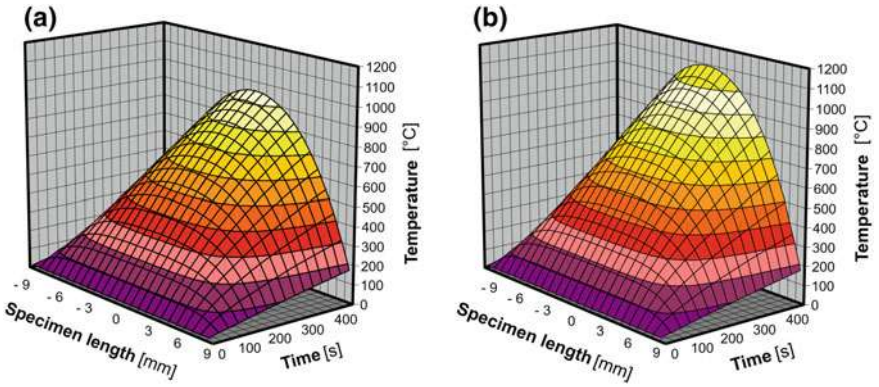

Fig. 6.15 Temperature evolution in a sintered sample with 5% (**a**) and 20% ZrO_2 (**b**) as a function of the sintering time for an electrical current value of 290 A

punch (top). These values then decreased in the direction of the side surface of the sample and the water-cooled bottom panel as a result of heat dissipation.

Since the microstructure evolution depended essentially on the temperature distribution in the sample, an analytically closed solution in the form of a Fourier series was searched for by mathematical means and solved numerically for the implemented sintering conditions with regard to the temperature profile [26]. The plot in Fig. 6.15a shows the distribution of the temperature field that arose in a sintered sample with increasing sintering time for an electrical current value of 290 A. The sintered material used here was a mixture of the steel powder with 5% ZrO_2 powder. This clearly shows that a temperature gradient of approximately 800 K between the side surface and the center of the sample accumulates after 400 s. When the ZrO_2 content increased to 20% and the same electrical current value was maintained, the heating process correspondingly increased due to the increased electrical resistance. This led to a temperature increase of 150 K in the center of the sample (Fig. 6.15b). At the same time, however, the temperature gradient increased, and the microstructure became even more inhomogeneous.

The evolution of the mechanical properties of the resistance sintered samples was similar to that of the conventionally sintered samples. Figure 6.16a shows the local macrohardness measured over the sample cross section as a function of the relevant relative density. The dependence represents a linear relationship. The increase in the nonconductive ZrO_2 phase content from 5 to 20% drastically influenced the conductive sintering process since the electrical current only flowed through the steel matrix. Thus, the individual ZrO_2 particles in the ceramic agglomerates were not attached to each other. This led to a decrease in the macrohardness. The tensile strengths calculated from the macrohardness values using the correction factor of 3.3 are shown in the plot in Fig. 6.16b. The small differences in the development of the mechanical properties for conventional and resistance sintered specimens were due, on the one hand, to the chemical composition of the initial powders and; on the

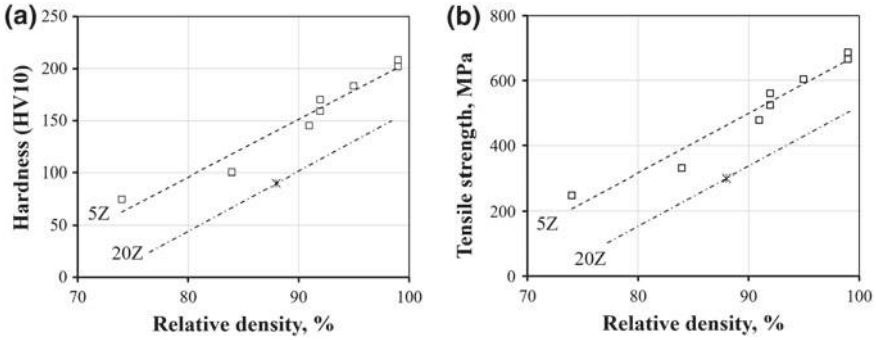

Fig. 6.16 Measured macrohardness (**a**) and calculated tensile strength (**b**) for composite materials with different ZrO_2 contents after resistance sintering under vacuum

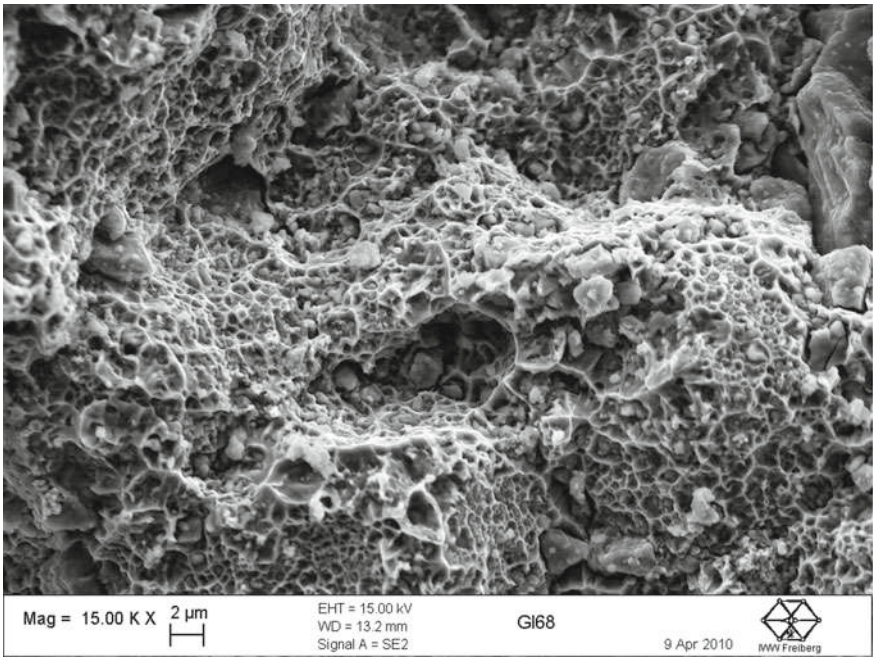

Fig. 6.17 Fracture surface of a composite sample with 5% ZrO_2 sintered at 1100 °C for 11 min

other hand, they were due to the different thickness of the surface oxide layer on the particles, which was influenced by the mechanical alloying technique since the particle size distribution of the powders was the same.

The fracture surface of a sintered sample with 5% ZrO_2 is shown in Fig. 6.17. The fine-grained void structure of the austenite with embedded ZrO_2 particles can be observed.

6.3.3 Hot Pressing

Figure 6.18 shows the microstructure of the composites with 5% and 10% ZrO_2 as a function of the HP temperature. According to the figure, the microstructure consists of austenite grains (light gray) with pronounced twins, PSZ (dark gray) and residual pores (black). A quantitative evaluation of the microstructure indicated that

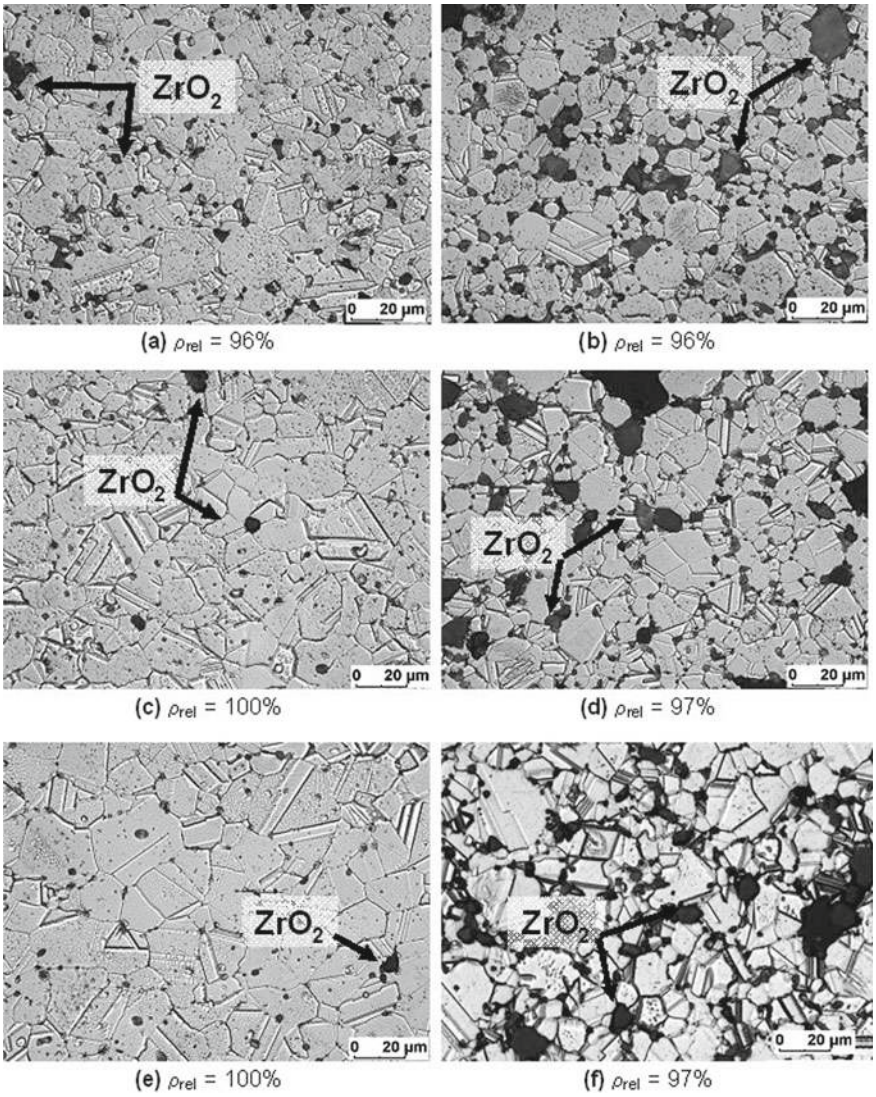

Fig. 6.18 **a**, **c**, **e** microstructure evolution of composites with 5% and **b**, **d**, **f** 10% ZrO_2 after HP by the 2nd method at (**a**, **b**) 1100 °C, (**c**, **d**) 1200 °C and (**e**, **f**) 1250 °C

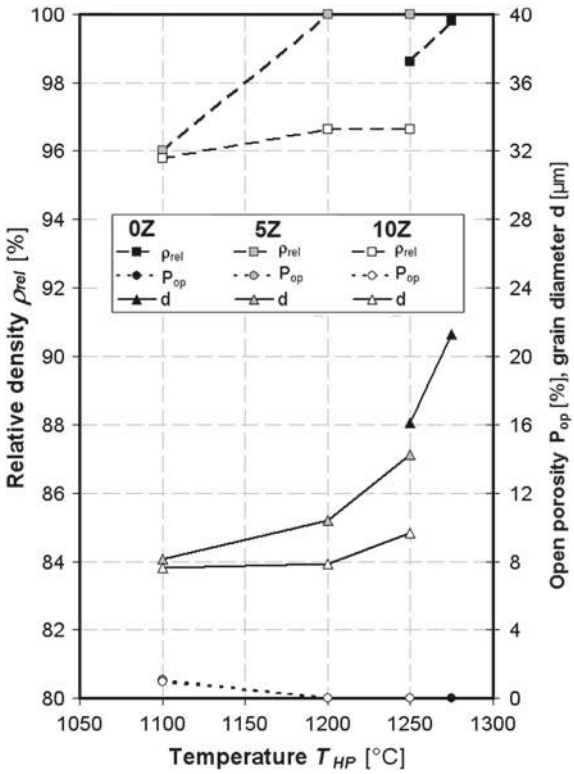

Fig. 6.19 Relative density, open porosity and average grain size produced by the 2nd precompaction method for fabricating composites as a function of the HP temperature

an increase in the HP temperature led to a decrease in the residual porosity and growth of austenitic grains (Fig. 6.19). For all investigated ceramic contents in the steel matrix, the absence of open pores in the samples was observed beginning at the HP temperature of 1200 °C. While the theoretical density of the undoped steel matrix was only achieved at 1275 °C, the addition of 5% ZrO_2 into the powder mixture had a positive effect on the reduction of the required HP temperature by 25 K. The presence of ceramic components in the mixture also had a significant effect on the reduction of the austenitic grain growth. For example, when 10% ZrO_2 was added, the size of the austenite grains at a HP temperature of 1250 °C was reduced by approximately half compared to that of the undoped steel matrix.

The investigations showed that the same HP conditions for composites with 5% ZrO_2 according to the 1st and 2nd precompaction methods to compress the powder mixture into billets without HIP had a different effect on the size of austenitic grains and final relative density of the finished part (Table 6.4). The presintering operation led to an increase in the relative density of the finished part at the expense of the austenite grain growth, which increased by approximately 25%.

To increase the relative density of the undoped steel samples pressed by the 2nd precompaction method at 1250 and 1275 °C to their theoretical value, they were subjected to a final HIP at 1225 °C at a pressure of 100 MPa. The results of the

Table 6.4 Relative density and average grain size of the composite with 5% ZrO_2, hot pressed at 1250 °C according to the 1st and 2nd precompaction methods that compact the powders without HIP

Method	ρ_{rel} (%)	d (μm)
1st	98.6	11.5
2nd	100	14.3

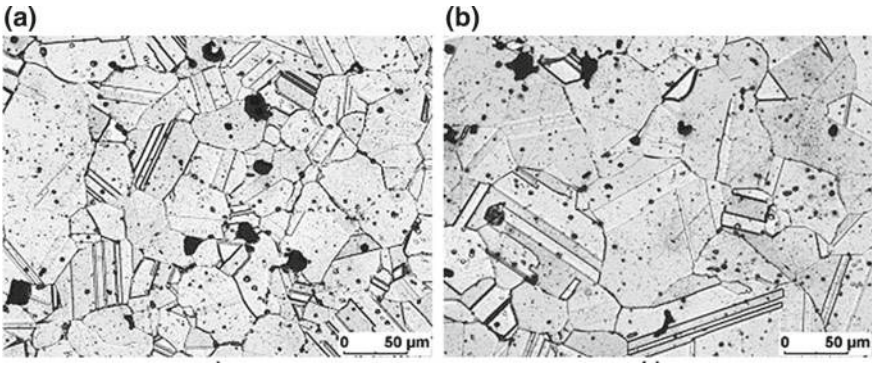

Fig. 6.20 Microstructure development after HP by the 2nd precompaction method at 1250 °C without (**a**) and with a final HIP operation at 1225 °C (**b**)

Table 6.5 Influence of the post-HIP operation on the relative density and the average grain diameter of the undoped steel powder mixture after HP by the 2nd HP precompaction method

HP temperature, °C	After HP		After post-HIP	
	ρ_{rel} (%)	d (μm)	ρ_{rel} (%)	d (μm)
1250	98.6	16.1	100	44.1
1275	99.8	21.3	100	48.3

microstructural analysis showed that as a result of an additional thermomechanical treatment, there was significant growth of the austenitic grains (Fig. 6.20). Despite the complete densification of the samples, the grain size more than doubled (Table 6.5). A similar effect was also observed in [27] on the same material.

The analysis of the mechanical properties of hot-pressed composites was based on the already observed linear dependence of the tensile strength and exponential dependence of the total elongation on the relative porosity of the material. As shown in Fig. 6.21, the extrapolation of the results into the area of low relative porosity correlated well with the previous results obtained by conventional and resistance sintering of the composites. The insignificant deviations are due to differences in the initial chemical composition of the powder mixture. A comparison of the mechanical properties of the composites with 5 and 10% ZrO_2 shows that a material with 10% ZrO_2 shows increased strength values and decreased total elongation.

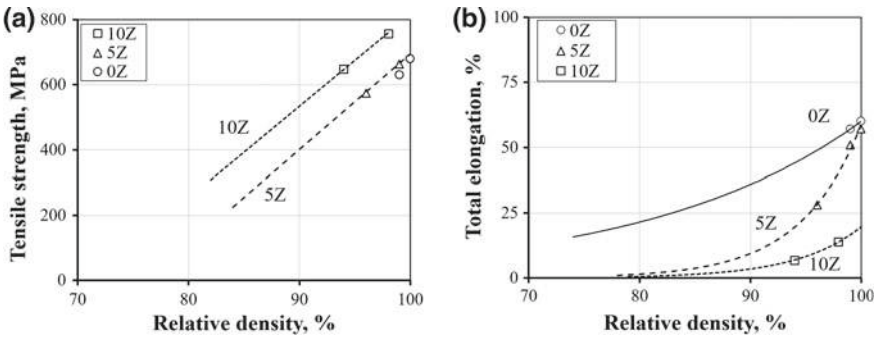

Fig. 6.21 Influence of the relative density of composites with 0% (0Z), 5% (5Z) and 10% ZrO_2 (10Z) on the tensile strength (**a**) and total elongation (**b**) after fabrication by HP according to the 2nd method of precompaction

The results of the tensile tests for samples with 5% ZrO_2 by the 1st method of precompaction of the powder mixture into billets indicated a total elongation that decreased by 3 times and an insignificant reduction in the strength; the tensile strength, in particular, was reduced by 1.4 times. The mechanical properties of the undoped steel specimens subjected to the final HIP operation showed that the additional technological step led to a reduction in the yield strength by more than 20% and tensile strength by 1.5 and 3% while increasing the total elongation by 6 and 18% in accordance with the HP temperature [28].

The results of the impact toughness measurements of the composites with 5% ZrO_2 showed an increase from 9 to 37 J in the investigated range of HP temperatures [29]. At the same time, the composite with 10% ZrO_2 remained brittle because its impact toughness values did not exceed 5 J. The results of the impact toughness measurement on the samples fabricated by the 1st precompaction method also showed lower values than that of the 2nd precompaction method over the whole investigated temperature range. For example, the impact toughness values of the composite with 5% ZrO_2 showed a decrease of nearly 4 times to 10 J in the case of the 1st method of precompaction.

Figure 6.22 shows the fracture surfaces of the hot-pressed samples after tensile testing. The precompaction of the powder mixture was carried out by the 2nd method at the HP temperatures of 1100 and 1250 °C. A common feature of the fracture surfaces for the composite with 5% ZrO_2 was the ductile nature of the failure with individual brittle ceramic particles. The higher HP temperature of 1250 °C enabled a high elongation of the sample and the production of inhomogeneous and deep dimples on the ductile fracture surface (Fig. 6.22c). The increase in ZrO_2 content led to a decrease in the fraction of ductile fracture over the entire investigated HP temperature range. In the fractures of the composite with 10% ZrO_2, finely dimpled and mixed failure areas along the phase boundaries corresponding to low ductility are observed (Fig. 6.22b, d).

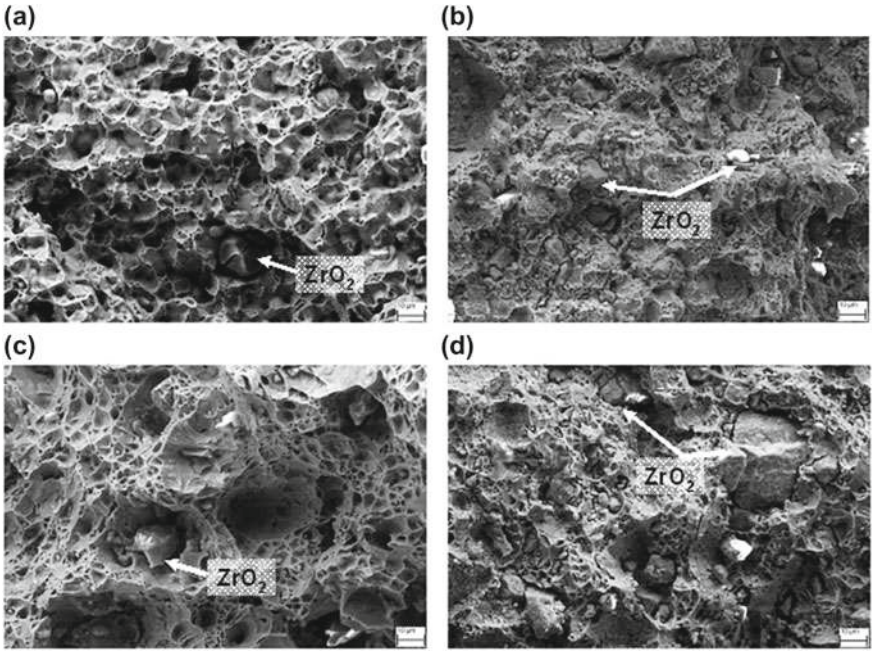

Fig. 6.22 Fracture surfaces of the hot-pressed composites with 5% ZrO_2 at (**a**) 1100 °C and (**c**) 1250 °C. Fracture surfaces of the composites with (**b** and **d**) 10% ZrO_2 hot pressed by the 2nd precompaction method

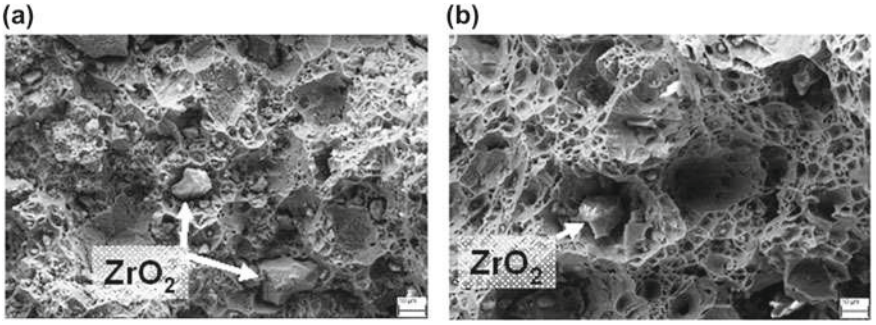

Fig. 6.23 Fracture surfaces of hot-pressed composite with 5% ZrO_2 by 1st (**a**) and 2nd precompaction methods (**b**)

A comparison of the fracture surfaces for the composite with 5% ZrO_2 after HP at 1250 °C showed that the samples precompacted by the 1st method (Fig. 6.23a) are characterized by a mixed failure mode and differ significantly from the ductile dimpled structure of the samples precompacted by the 2nd method (Fig. 6.23b).

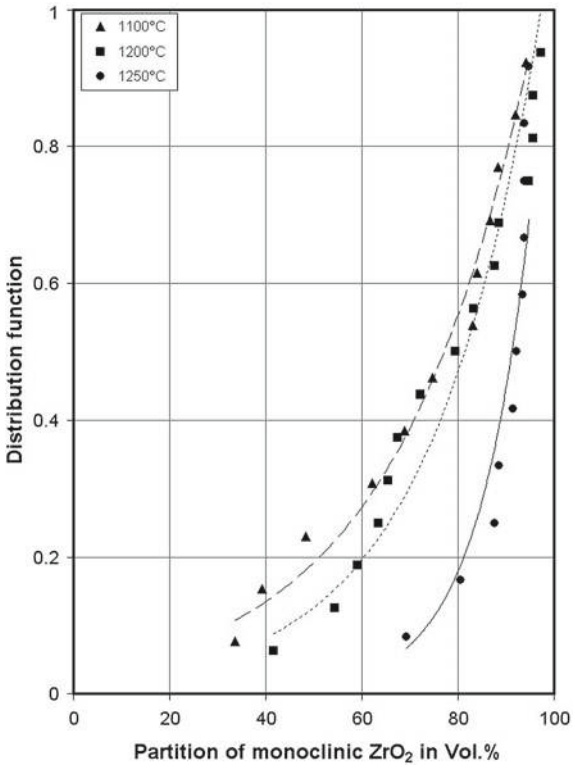

Fig. 6.24 Influence of the HP temperature (2nd precompaction method) on the amount of m-ZrO_2 in the composite with 10% ZrO_2

Figure 6.24 shows that the distribution of the m-ZrO_2 crystallographic phase in a composite with 10% ZrO_2 depended on the HP temperature. The results indicate that the distribution function of the ceramic particles that underwent transformation into the monoclinic phase had an exponential dependence [30]. The increase in the HP temperature led to the displacement of the 20% quantile toward an increase in the m-ZrO_2 content. A similar tendency in the slightly smoothed form is also observed for the 50% quantile, whose values increased from 79 to 92% with increasing HP temperature.

6.4 Conclusions

In this work, the densification behavior and final mechanical properties of TRIP-matrix composites were investigated. The composites were based on 1.4301 stainless steel powder, which was available in the form of three batches with slight differences in their chemical composition and contained up to 30% MgO-PSZ. The materials were fabricated using three different PM consolidation processes: conventional sintering, resistance sintering and HP. In the case of resistance sintering, a special tool

was designed and optimized to achieve low heat dissipation from the specimen. The microstructure evolution and material properties along each consolidation route were compared to each other. The experimental analysis of the densification kinetics was based on electrical resistance measurements and microstructure evaluation. It was shown that the chemical composition of the steel matrix had a significant influence on the optimum sintering temperature among the investigated sintering technologies.

Experimental investigations of resistance sintering have shown that increasing the presintering and sintering pressures and decreasing the heating rate result in an elevated density of the material. The sintering residence time for composites with a high ZrO_2 content should be extended compared to those with a low ZrO_2 content since the ZrO_2 content delays the consolidation process.

The investigations on HP showed an almost optimal production route, namely, by CIP, subsequent presintering at 1100 °C for 1 h and then HP. The HIP treatment has proven to be ineffective for the postcompaction of hot-pressed samples.

During conventional sintering, the dependence of the composite density on the sintering temperature and sintering time as well as on the ZrO_2 content was quantified by means of a physical-mathematical approach and experimentally supported modeling. It was shown that the densification rate in the investigated temperature range had a low dependency on the ZrO_2 content. The temperature distribution and evolution in the sintered material during resistance sintering was determined based on the physical-mathematical equations as a function of the electrical current value, the sample geometry and the ZrO_2 content. The modeling provided the basis for the densification kinetics and the local character in the composite specimen volume.

A fine austenite microstructure and higher density and tensile strength was achieved with the optimized HP route (2nd precompaction method) and presented a better combination of properties than those of conventional and resistance sintering. Furthermore, low sintering temperatures and short sintering times made the optimized process favorable. The optimally determined HP parameters are 1250 °C with a holding time of 30 min to 1 h and pressure of 30 MPa.

Furthermore, it was shown that the mechanical properties of the consolidated composites primarily depended on the relative density of the material and the ceramic content in the composite. Here, a linear correlation of the tensile strength and an exponential correlation of the total elongation with the relative density of the material was observed. There was no significant influence of the consolidation technique on these mechanical properties. The insignificant deviations could be explained by differences in the initial chemical composition of the powder mixture. With a particle content of approximately 10–30% ZrO_2, strength increases of up to approximately 40% were found. An increase in the tensile strength was accompanied by a decrease in the total elongation. The obtained dependences partially exceeded the mechanical properties of the particle-reinforced composites with a light metal matrix [31]. However, an increasing ZrO_2 content up to 20% caused early failure of the composite under tensile loading due to the formation of ceramic agglomerates with poor bonding to the ZrO_2 particles. Therefore, the best mechanical properties require sufficient

fineness of the ceramic particles (<10 μm) and a uniform distribution as well as good bonding into the steel matrix and low destabilization of the t-ZrO_2 crystallographic modification.

Finally, it was shown that the content of m-ZrO_2 increased with increasing sintering temperature. The increase in the impurities in the ceramic powder caused a greater initial destabilization of the metastable t-ZrO_2 crystallographic phase. In contrast, the influence of the PM consolidation processes investigated in this research on the m-ZrO_2 content had a secondary effect.

Acknowledgements The authors are grateful to the employees of the Institute for Metal Forming (*) and of the Fraunhofer Institute for Ceramic Technologies and Systems (**), who participated in the powder compaction processes: Dr.-Ing. Anna Yanina (*), Dr.-Ing. Werner Jungnickel (*), Dr.-Ing. Wolfhart Müller (*), Dr. rer. nat. habil. Mathias Herrmann (**) and Dipl.-Ing. Jan Räthel (**). Special thanks are addressed to Dr. rer. nat. Dr.-Ing. habil. Harry Berek for the SEM investigations. The authors gratefully acknowledge the German Research Foundation (DFG) for supporting the Collaborative Research Center TRIP-Matrix-Composites (Project number 54473466—CRC799 subproject A6).

References

1. E.C. Bain, The nature of martensite. Trans. Am. Inst. Min. Metall. Eng. **70**, 25–46 (1924)
2. S.P. Buyakova et al., Механическое поведение пористого диоксида циркония при активной деформации сжатием. Pisma v JETF **25**, 44–48 (1999)
3. A.G. Bratuhin et al., Высокопрочные коррозионно-стойкие стали современной авиации (MAI, Moscow, 2006)
4. Y.G. Jung, U. Paik, S.C. Choi, Influence of the particle size and phase type of zirconia on the fabrication an residual stress of zirconia/stainless steel 304 functionally gradient material. J. Mater. Sci. **34**, 5407–5416 (1999)
5. W. Zhang, J. Xie, C. Wang, Fabrication of multilayer 316L/PSZ gradient composite pipes by means of multi-billet extrusion. Mater. Sci. Eng. A **383**, 371–377 (2004)
6. M. Wildan, H.J. Edrees, A. Hendry, Ceramic matrix composites of zirconia reinforced with metal particles. Mater. Chem. Phys. **75**, 276–283 (2002)
7. J. Abenojar et al., Atmosphere influence in sintering process of stainless steels matrix composites reinforced with hard particles. Compos. Sci. technol. **63**, 69–79 (2003)
8. L.O. Andryschik et al., Влияние параметров спекания на структуру спеченного электроконтактным нагревом порошкового хрома. In: Порошковая металлургия (1989)
9. K. Feng et al., Rapid sintering of iron powders under action of electric field. Powder Metall. **48**, 203–204 (2005)
10. O.V. Konstantinova et al., Численное моделирование влияния соотношения размеров частиц проводящей и изолирующей фаз на проводимость композитов типа проводник-изолятор порошкового происхождения. Порошковая металлургия **1/2**, 31–40 (2005)
11. J.E. Geguzin, Physik des Sinterns Deutscher Verlag für Grundstoffindustrie, 1973
12. Y. Zhou et al., Effects of load mode on mechanical properties of ZrO_2(2Y)/TRIP steel composites. Trans. Nonferr. Met. Soc. China **13**, 1086–1091 (2003)
13. H.L. Yakel, Atom distributions in sigma phases. Acta Cryst. **39**, 20–28 (1983)

14. Y. Yamada et al., Effect of debonding at the phase interface on Young's modulus in sintered PSZ/stainless steels composites. Mater. Trans. JIM **35**, 814–820 (1994)
15. Y.-G. Jung, U.-G. Paik, Residual stress and thermal properties of zirconia/metal (nickel, stainless steel 304) functionally graded materials fabricated by hot pressing. J. Mater. Sci. **32**, 3841–3850 (1997)
16. L.Z. Liang et al., Characteristics of complicated AISI 316L automobile components manufactured by powder metallurgy. J. Mech. Sci. Technol. **23**, 1924–1931 (2009)
17. Z.L. Lu et al., Investigation into the densification of AISI 304 parts fabricated by hybrid powder metallurgy techniques. Indian J. Eng. Mater. Sci. **17**, 49–55 (2010)
18. C. Suryanarayana, E. Ivanov, V.V. Boldyrev, The science and technology of mechanical alloying. Mater. Sci. Eng. **304–306**, 151–158 (2001)
19. W. Müller, Temperaturverhältnisse und Reaktionskinetik beim Ziehen und Wärmebehandeln von Draht. Bd. B292 (TU Bergakademie Freiberg, 1998)
20. S. Guk, A. Yanina, R. Kawalla, Ch. Aneziris, W. Schärfl, Ch. Weigelt, Bewertung und Vorhersage von mechanischen Eigenschaften und Porosität von Metall-Keramik-Compositen mit Zirkoniumdioxid, in *Proceedings of the 2nd International Conference* "*Pavlovs lectures*" in Baikov Institute of Metallurgy and Materials Science (IMET) Moskau der russischen Akademie der Wissenschaft (RAN) 2–627. Oktober 2010, pp. 504–511
21. A. Yanina, S. Guk, R. Kawalla, Ch. Aneziris, W. Schärfl, Ch. Weigelt, Einfluss der Sinterparameter auf die Sinterkinetik und mechanische Eigenschaften von MMC, in *Proceedings of the 2nd International Conference "Pavlovs lectures"* in Baikov Institute of Metallurgy and Materials Science (IMET) Moskau der russischen Akademie der Wissenschaft (RAN) 26.–27. Oktober 2010, pp. 493–499
22. A. Yanina, S. Guk, W. Müller, R. Kawalla, Influence of sintering parameters on the mechanical properties of TRIP-matrix composite materials, in Book series *Materials and Material Engineering Applications*, Band 37, ed. by B. Wielage (Chemnitz, 2011), pp. 236–243, ISBN 978-3-00-032471-0
23. A. Yanina, S. Guk, W. Müller, R. Kawalla, Einfluss der Sinterparameter auf die mechanischen Eigenschaften von TRIP-Matrix-Composit-Werkstoffen, in Tagungsband zum 13. Werkstofftechnischen Kolloquium. ISBN 978-3-00-032471-0, Chemnitz 30.09.–1.10.2010, pp. 236–243
24. A. Yanina, S. Guk, Special features of sintering TRIP-matrix-composites based on steel and ceramic by conductive heating, Tagungsband der internationalen Konferenz Fortschrittliche Technologien zur Plastischen Deformation 21–26. September 2009, MISIS, Moskau, ISBN 9785-87623-278-6, pp. 151–152
25. A. Yanina, S. Guk, W. Müller, R. Kawalla, C. Weigelt, Herstellung und Weiterverarbeitung von TRIP-fähigen Partikelverbundwerkstoffen. Tagungsband der internationalen Konferenz MEFORM 2012 "Material technology and forging processes". ISBN 978-3-86012-434-5, Freiberg 28.03.–30.03.2012, pp. 216–231
26. S. Guk, A. Yanina, W. Müller, R. Kawalla, Mathematical-physical model of resistance sintering with current conducting electrode punches of steel ceramic composites. Mater. Sci. Eng. Technol. **41**(1), 33–38 (2010)
27. S. Irukuvarghula, H. Hassanin, C. Cayron, M.M. Attallah, D. Stewart, M. Preuss, Evolution of grain boundary network topology in 316L austenitic stainless steel during powder hot isostatic pressing. Acta Meterialia **133**, 269–281 (2017)
28. S. Guk, K. Pranke, W. Müller, A. Yanina, Development of high-strength TRIP-matrix-composite materials, in *Proceedings of the International Conference of production and processing of cladded materials and metal matrix composites MEFORM 2014*, ISBN 978-3-86012-481-9, Altenberg 26.03.–27.03.2014, Herausg.: ACATRAIN e.V., Verein für Weiterbildung an der TU Bergakademie Freiberg, Institut für Metallformung, pp. 149–159
29. A. Yanina, S. Guk, R. Kawalla, New TRIP-matrix-composite production, properties and softening behaviour during warm forming. Tagungsband der internationalen Konferenz "Neuere Entwicklungen in der Massivumformung". ISBN 978-3-88355-386-3, Fellbach/Stuttgart 17.05.–18.05.2011, pp. 271–281

30. S. Guk, A. Yanina, R. Kawalla, H. Berek, J. Räthel, Densification and properties of an Mg-PSZ reinforced TRIP-Matrix-Composite produced by hot pressing: Comparison with other powder metallurgy techniques, in *International Science and Technology Congress OMD-2014, Hrsg.*: MISIS, Moskau, ISBN: 978-5-905714-27-6, pp. 364–369
31. Manufacturer specifications: DWA Composite Specialties Inc., Chatsworth, Ca., USA and DACC Dural Aluminium Composites Corp., San Diego, Ca., USA

Chapter 7
Understanding of Processing, Microstructure and Property Correlations for Flat Rolling of Presintered TRIP-Matrix Composites

Sergey Guk, Rudolf Kawalla and Ulrich Prahl

Abstract Descriptions of material behavior during forming operations have become increasingly important in recent years due to the increasing use of simulation systems for understanding processing-microstructure-property correlations and regulating forming facilities. This information has become particularly important for composite materials, including metal matrix composites. This necessity poses new challenges in particular for testing technology, which significantly contributes to the analysis of material characteristics. The characteristic values of materials are prerequisites for the numerical design of manufacturing processes. This chapter presents an overview of the strategies currently available for describing material behavior during flat rolling; the materials investigated herein are presintered TRIP-matrix composites. In addition, the test procedures and methods necessary for determining material parameters are briefly listed and explained. Furthermore, this chapter presents both the classical test methods and equipment and their areas of application, which have been further developed in recent years.

7.1 Introduction

For the development, industrial production, and processing of materials, it is becoming increasingly necessary to describe and optimize the associated technologies as completely as possible with the help of models. Depending on the manufacturing conditions, the corresponding models can then be used to estimate important characteristics of the surface (scale), geometry, microstructure, texture, internal stresses, mechanical properties, and physical properties of materials. For the customer, the mechanical properties of construction materials, which—depending on the field of application—may be combined with the chemical or special physical properties of the semifinished product or component, are often in the foreground [1].

S. Guk (✉) · R. Kawalla · U. Prahl
Institute for Metal Forming, Technische Universität Bergakademie Freiberg,
Bernhard-von-Cotta-Str. 4, 09599 Freiberg, Germany
e-mail: sergey.guk@imf.tu-freiberg.de

H. Biermann and C. G. Aneziris (eds.), *Austenitic TRIP/TWIP Steels and Steel-Zirconia Composites*, Springer Series in Materials Science 298,
https://doi.org/10.1007/978-3-030-42603-3_7

The entirety of the material description often represents an almost insoluble task in its complexity. Rather, individual models are linked together on different bases and used depending on a particular specification as well as scientific and technical requirements [2].

From the process description perspective, material models for flow curves, formability and physical properties, such as thermal conductivity and heat capacity as a function of temperature, are required for the forming process, among other things [3, 4]. Such models enable the material flow in the forming zone to be described and the characteristic values for the load and design of forming facilities to be calculated in advance. For multistage forming processes, some models must include time as an influencing factor, especially for all diffusion-controlled processes during deformation pauses. The resulting structural changes must be incorporated into the description via metallurgical models, which contributes to better calculation results.

The product properties of components are ultimately determined by the microstructure conditions, which can be specifically influenced during fabrication and further processing using various forming operations. The interaction of forming and microstructural development is illustrated in Table 7.1. A continuous description of the material behavior according to the column "Technologically related parameters" is possible with several methods if the necessary forming parameters and the physical properties are known. Microstructural development can be determined through the simplest methods of regression, semiempirical or semiphysical equations or complex computational methods on a physical basis.

The relationships between the forming conditions and the microstructural development during the production of cold and hot strips from transformation-induced plasticity (TRIP)-matrix composites, which are highlighted in *italics* in Table 7.1, are described below. The remaining microstructural developments, such as grain growth or precipitation of the δ-ferrite phase, have either already been discussed in

Table 7.1 Interlocking interaction of forming and microstructural development in cold and hot forming processes

Process	Technological step	Technologically related parameters	Microstructural development
Cold forming	Forming	Distribution of forming parameters	*Strain hardening* *Formability* Material flow/texture
Hot forming	Heating	Heating curve Temperature profile	Grain growth *Dissolution of precipitates*
	Forming	Distribution of forming parameters Cooling curve Temperature profile	*Strain hardening* *Strain softening* *Formability* *Material flow*/texture Precipitation
	Cooling	Cooling curve Temperature profile	Phase transformation Precipitation

the Chap. 6 of this volume or are of minor relevance compared to the others in this context. The material used was a TRIP-matrix composite produced by the powder metallurgical route with different fractions of ceramic particles. In this chapter, the details of material data, sample preparation, and testing to characterize the material behavior during deformation under conditions similar to flat rolling at different temperatures are provided in Sect. 7.2. Section 7.3 presents the results of the experimental observations and corresponding discussions involving comparisons with the state of the art. Finally, the investigation is concluded in Sect. 7.4.

7.2 Materials and Methods

The investigated material is based on two components: a Mn-containing gas-atomized metastable high-alloyed TRIP-steel powder ($d_{10} = 8$ µm, $d_{50} = 23$ µm, $d_{90} = 45$ µm, and $\rho = 7.81$ g/cm^3). On the other hand, there is a powder of MgO partly stabilized ZrO_2, which was separated by means of wind sifting into four fractions with corresponding particle size distributions:

1. <10 µm ($d_{10} = 0.7$ µm, $d_{50} = 2.5$ µm and $d_{90} = 9.0$ µm);
2. 10–30 µm ($d_{10} = 12.5$ µm, $d_{50} = 20.7$ µm and $d_{90} = 29.1$ µm);
3. 30–50 µm ($d_{10} = 32.2$ µm, $d_{50} = 39.0$ µm and $d_{90} = 48.6$ µm) and
4. >50 µm ($d_{10} = 52.4$ µm, $d_{50} = 56.8$ µm and $d_{90} = 81.9$ µm).

The chemical composition of the steel and the ceramic powders are shown in Table 7.2. The proportions of the phases in ZrO_2 were distributed between monoclinic (m), tetragonal (t) and cubic (c) crystallographic modifications at approximately equal amounts of 35:32:33%. By varying the ceramic particle content between 0 and 30% during blending as well as varying the ceramic particle size distribution, different powder mixtures were obtained. These mixtures were cold precompressed into disc form with a diameter of 155 mm and a height of 36 mm at a uniaxial pressure of 90 MPa and finally hot-press sintered. The sintering was carried out under a Varigon (5% H_2 and 95% Ar) atmosphere at 1250 °C and 30 MPa for 30 min. Metallographic examinations clearly showed that the particle distribution in the steel matrix was nearly homogenous. Only small agglomerates of ceramic particles were found for the composites with 20 and 30% ZrO_2 (Fig. 7.1). The porosity measurements using

Table 7.2 Chemical compositions of the investigated powders (wt%)

Steel powder											
C	Cr	Mn	Ni	Si	N	S	Mo	Ti	Nb	Al	δ-Ferrite
0.03	16.4	6.3	6.3	0.9	0.06	0.008	0.02	0.003	0.021	0.10	16
ZrO_2 powder											
ZrO_2		SiO_2		HfO_2		CaO		MgO	TiO_2		Fe_2O_3
Bal.		0.41		1.74		0.15		2.82	0.13		0.13

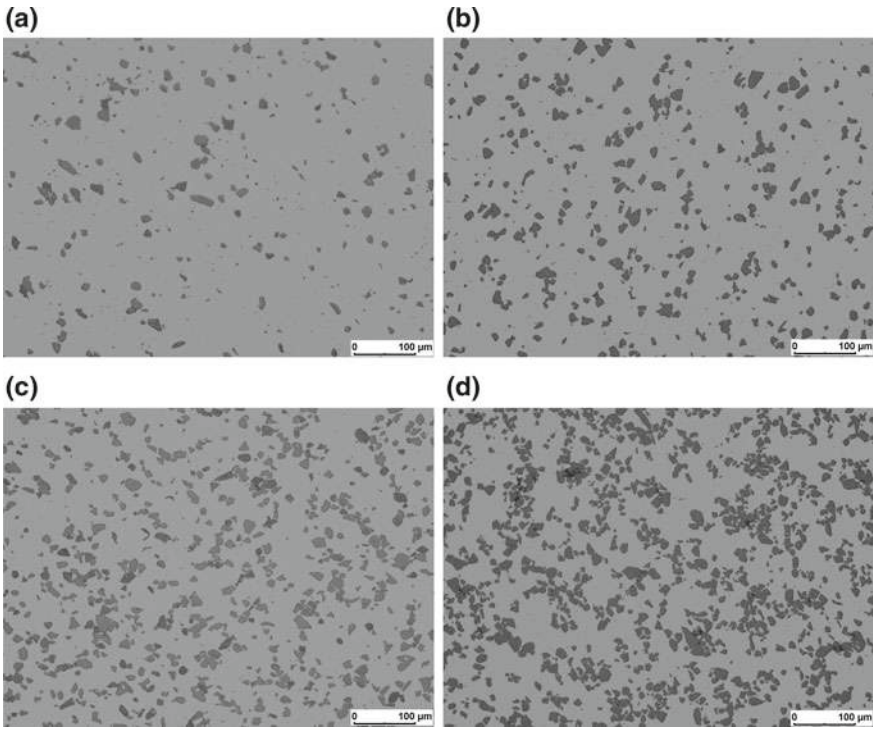

Fig. 7.1 Distribution of second-phase particles of ZrO_2 with particle sizes between 10 and 30 µm in the steel matrix: **a** 5%, **b** 10%, **c** 20%, **d** 30% ZrO_2 [5, 6]

the Archimedes method, conducted in accordance with DIN EN 623-2:1993, showed that nearly full density was achieved: the values of total porosity were at most 0.1%. The measured proportions of m-, t- and c-ZrO_2 after hot pressing were 60:7:33%.

The solution state of the steel matrix defined by the selected heating rates and temperatures was calculated for the investigated chemical composition using ChemSage, a computer program for calculating complex chemical equilibria, and SteelMap, a program specializing in calculations with steels. The calculation took place in a temperature interval between 200 and 1200 °C in 10 K steps. The calculated solution states are valid for the thermodynamic equilibrium and reflect the possible maximum values related to the experimental test conditions.

A completely new approach was chosen to determine the nonrecrystallization temperature. Usually, an attempt is made to determine the region of nonrecrystallization using a torsion machine [7, 8]. The machined samples are subjected to torsional stress and then evaluated. However, a decisive disadvantage lies in the sample geometry because the stress is not distributed homogeneously over the cross-section of the sample. Therefore, a MAXStrain® device in the multifunctional simulation system GLEEBLE HDS-V40 (Dynamic Systems Inc.) was applied to determine the nonrecrystallization temperature (Fig. 7.2). Due to the cube-shaped geometry of the

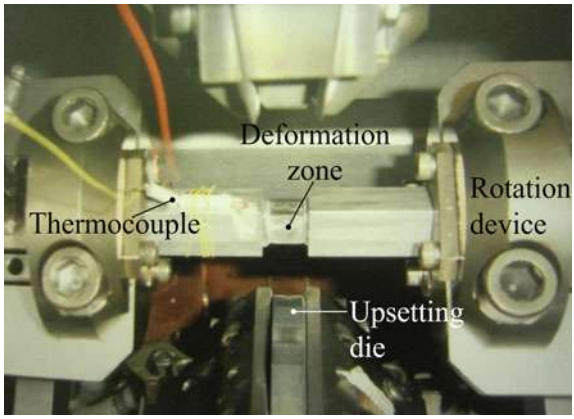

Fig. 7.2 Determination of the nonrecrystallization temperature using the MAXStrain® device

deformation zone in the MAXStrain® specimens, this influence is eliminated. An alternating deformation of the cube-shaped zone of the specimen with a strain value of 0.5 per deformation step is carried out by means of upsetting dies and a 90° rotation of the specimen after each deformation step. Twenty deformation steps were performed with a strain rate of 10 s^{-1} and a pause time of 8 s. Then, by recording the stress development during the reduction in deformation temperature from 1100 to 700 °C at 20 K decrements per deformation step, the region of nonrecrystallization due to strongly increasing stress levels can be determined.

To determine the strain hardening behavior of consolidated samples, compression tests were carried out at room temperature and in the range between 700 and 1200 °C with a 100 K step using the servo-hydraulic test system with a maximum force of 400 kN. The upsetting samples to be tested were taken from the hot-pressed discs in the axial direction. The specimen dimensions for the cylindrical compression tests were ∅10 mm × 18 mm. The test was carried out in accordance with DIN 50106:2016. The strain rates were 0.1, 1 and 10 s^{-1}. To reduce friction, the end faces of the cylindrical specimens were lubricated with oil (for tests under room temperature) or graphite solution (for tests under high temperatures). Flow curves were calculated based on the data obtained with friction and temperature adjustments [9]. These adjustments were based on the physical and tribological properties, such as density, heat capacity and friction coefficient, which were determined experimentally for all investigated composite material states.

To evaluate the kinetics of the α'-martensite evolution for the steel matrix under room temperature testing conditions, the ferromagnetic phase fraction of the samples with different contents of ZrO_2 particles were measured using magnetic balance testing (Metis Instruments and Equipment NV) and a previous calibration. The measuring principle is based on a magnetic induction method. In the investigated steel matrix, ferromagnetic phases, such as δ-ferrite and α'-martensite, can be found. At the beginning of each experiment (i.e., in the α'-martensite-free state), the amount of δ-ferrite was determined to extract these contents from the measurement values of the experiment, thereby determining the exact amount of α'-martensite.

The determination of the softening kinetics was carried out on the multifunctional simulation system GLEEBLE HDS-V40 by means of a cylinder compression test (dynamic softening) and a double compression test (static softening). In the double compression test, a specimen was deformed at a constant strain rate of 1 s^{-1} up to a strain of 0.4, unloaded and, after a variable isothermal holding time, was loaded again at the original strain rate up to the strain value above. Here, cylindrical samples with dimensions of ∅10 × 18 mm, which were taken from the hot-pressed disc axis direction, were heated to the deformation temperature at a heating rate of 3 K/s and held at this temperature for 1 min. The double compression tests were carried out at temperatures between 900 and 1100 °C. To minimize the influence of friction and heat of deformation on the flow stress and subsequently on the hardening and softening characteristics, all measured flow curves were subjected to a temperature and friction adjustment [9]. The flow curves were evaluated according to the offset method [10]. The modeling of the dynamic softening behavior was carried out with the help of reaction kinetic calculation equations [10–13] based on data from the experimentally generated flow curves. For strains over the critical value, dynamic recrystallization can take place. Otherwise, only dynamic recovery occurs. The part of the dynamic recovery is described by

$$\sigma_{\mathrm{DRV}}(\varepsilon) = u \cdot \sqrt[n_2]{1 - \exp(-r \cdot \varepsilon^{n_1})}. \tag{7.1}$$

The dynamic recrystallization degree is described by

$$\sigma_{\mathrm{DRX}}(\varepsilon) = a \cdot \dot{\varepsilon}^{c} \cdot \exp\left(\frac{\Theta_2}{R \cdot \Theta}\right). \tag{7.2}$$

The static recrystallization degree is described by

$$X_{\mathrm{stat}} = 1 - \exp\left(h_1 \cdot \left[\frac{t}{t_{0.5}}\right]^{h_2}\right). \tag{7.3}$$

To determine the cold formability of the composite materials under deformation conditions similar to flat rolling, transverse extrusion tests were carried out on the servo-hydraulic press with a maximum force of 400 kN at room temperature (Fig. 7.3a); these tests were repeated six times for each sample type. A simplified illustration of the transverse extrusion tool used is shown in Fig. 7.3b. Cylindrical specimens with dimensions of ∅10.65 mm × 19 mm were machined from the hot-pressed discs. Before inserting a specimen into the test tool, it was lubricated on all sides with hydraulic oil. The strain rate in all tests was 0.1 s^{-1}. The evaluation of the tests was carried out according to the methodology described in [14, 15].

The hot formability was characterized according to the methodology of [16] based on the hot flow curves measured under different temperatures and strain rates. The energy dissipation and an instability map were generated based on these experimental

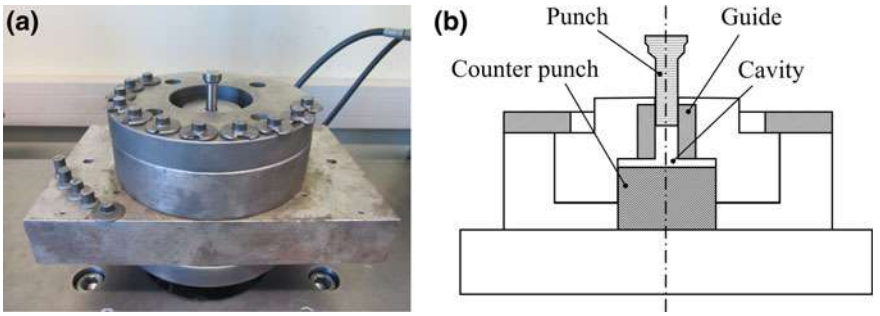

Fig. 7.3 Transverse extrusion tool: **a** photograph and **b** schematic drawing

results, and a process map was derived. The numerical analysis was carried out by means of a MATLAB® subroutine.

The hot rolling tests were carried out on a reversible stand with a dual roll mill, which has a maximum rolling force of 2.4 MN and a maximum rolling torque of 60 kN m. The rolls used had a diameter of 360 mm. The rolls were preheated to approximately 150 °C. The roll speed was chosen to be constant at 0.5 m/s. The samples were preheated in a furnace and purged with inert argon gas to prevent scale formation on the metallic surface. After rolling, the samples were cooled to room temperature in air.

Sheets, stuck rolling specimens and wedge rolling specimens were flat rolled. Stuck rolling specimens were only partially rolled products that—after removing the specimen from the roll gap—produce a largely realistic image of the deformation conditions directly in the roll gap. This technique made it possible to carry out extensive and complex investigations on the influence of the roll gap geometry on the extension and overall spread of material, the rolling force and torque, and the mean deformation resistance during hot rolling. Moreover, this technique helped clarify the material flow along the length of the contact arc as a function of the roll gap geometry. In contrast, the wedge rolling specimens represented initial semifinished products with a wedge-shaped longitudinal cross-section of 135 × 20 mm^2, which consequently undergo different strains over the specimen length during rolling with a constant roll gap. Thus, the evaluation of the rolling parameters, such as pass reduction, deformation temperature and strain rate, could be carried out with fewer initial samples. For mesoscopic characterization of the material flow, the initial specimens were marked with grid patterns (line spacing of 5.0 mm and a depth of approximately 0.3 mm) for forming strain analysis by means of the laser marking system Lasebox XS (Östling Marking Systems GmbH) on the surface and cross-sectional area [17, 18]. On the microscopic scale, densification processes and material flow were analyzed using light microscopy and scanning electron microscopy (SEM) on transverse and longitudinal sections from the different areas of the deformation zone. For this aim, the samples were cut, ground and polished. The degree of orientation of partially oriented linear structure elements AI and Ω_{12}, which characterize the

banding of the material, was measured in accordance with ASTM E 1268:94. These degrees of orientation were calculated with the following equations:

$$AI = \frac{\overline{N_{L\perp}}}{\overline{N_{L\parallel}}} \tag{7.4}$$

$$\Omega_{12} = \frac{\overline{N_{L\perp}} - \overline{N_{L\parallel}}}{\overline{N_{L\perp}} + 0.571 \cdot \overline{N_{L\parallel}}}, \tag{7.5}$$

where $\overline{N_{L\perp}}$ and $\overline{N_{L\parallel}}$ are the numbers of feature interceptions with test lines perpendicular to the deformation direction and in parallel direction, respectively. The degree of orientation Ω_{12} can vary from zero for a completely random distribution to one for a fully oriented material (banding microstructure).

7.3 Results

7.3.1 Heating and Dissolution of Precipitates

The investigations on the dissolution behavior of precipitates during heating of the steel matrix aimed to determine in advance the possible causes for influencing recrystallization and determine an optimum heating temperature for the composite material before forming from the perspective of the completely dissolved alloying elements. After heating to 900 °C and holding for 3 min, undissolved precipitates were determined in the steel matrix using the energy-dispersive X-ray spectroscopy (EDX) method; these precipitates essentially consisted of chromium (Fig. 7.4a). The precipitates have a size range from 70 to 300 nm [19].

Figure 7.4b shows the precipitation fraction as a function of the heating temperature. According to this figure, chromium carbonitrides are precipitated at 900 °C after

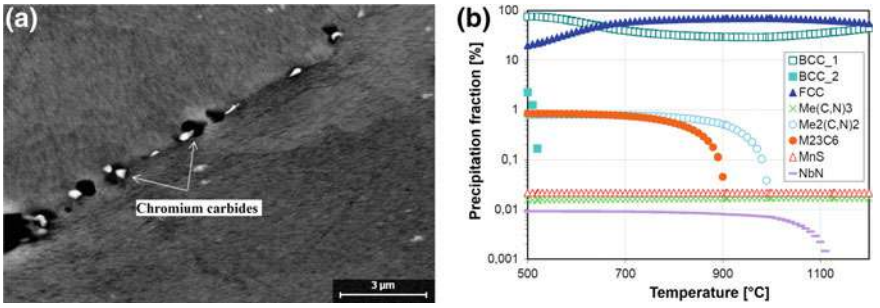

Fig. 7.4 **a** SEM image of the steel matrix with Cr carbides precipitated at the grain boundaries and **b** the calculated dissolution behavior of the precipitates of the investigated steel matrix

heating close to equilibrium; this finding has also been validated. The identification of the precipitates was carried out by means of EDX analysis. This analysis showed a high chromium content of 28%. The figure also shows that NbN precipitates in steel are resistant up to a temperature of 1120 °C and only then dissolve. For this reason, it was decided to set the heating temperature to 1100 °C to obtain a homogeneous matrix with dissolved chromium carbonitrides, inhibit normal grain growth, and prevent abnormal grain growth at the cost of retaining NbN precipitates, which were not dissolved at this temperature.

7.3.2 *Strain Hardening and Its Partitioning Between the Present Phases of the Composite*

To characterize the hardening behavior of the composite material during cold forming, interrupted compression tests were performed. The documentation of geometric changes of the specimen shape enabled the calculation of axial, tangential and hydrostatic stress components for the different material states [20]. The hydrostatic stress located close to the circumferential surface of the compression test sample is represented in Fig. 7.5a, which is exemplary of the composite material with a ZrO_2 particle distribution between 10 and 30 μm. The hydrostatic stress is illustrated, which is in fact negative. It is obvious that a significant change in the curve progression starts from 20% ZrO_2 content upwards. The further development of the model according to Pyshmintsev [21] allowed an exact prediction of the strain-induced $\gamma \rightarrow \alpha'$ phase transformation from the measured values of the axial strain and the calculated hydrostatic stress. The results showed very good agreement with the experimental values determined with the help of the magnetic balance [5]. Due to the small fraction of the t-ZrO_2 phase in the initial state of the composite after hot pressing, the $t \rightarrow m$ phase transformation was not taken into account. According to the general mixture

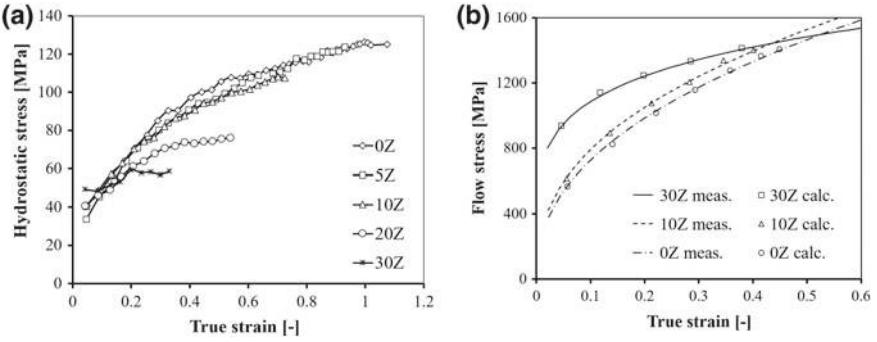

Fig. 7.5 **a** Variation in hydrostatic stress (negative) for different ZrO_2 contents and **b** a comparison between the predicted and the measured cold flow curves [5, 6]

rule by Tamura et al. [22], the flow stress of the composite was defined from the flow stresses of the single microstructural phases, such austenite γ, α'-martensite and ZrO_2, as well each phase volume fraction as

$$\sigma_{\text{mix.}}(\varepsilon_{\text{mix.}}) = f_{\gamma}(\varepsilon_{\text{mix.}}) \cdot \sigma_{\gamma}\left(\varepsilon_{\gamma}\right) + f_{\alpha'}(\varepsilon_{\text{mix.}}) \cdot \sigma_{\alpha'}(\varepsilon_{\alpha'}) + f_{ZrO_2} \cdot \sigma_{ZrO_2}\left(\varepsilon_{ZrO_2}\right) \tag{7.6}$$

under the condition that the sum of all phase volume fractions remains constant at any moment of the deformation

$$f_{\gamma}(\varepsilon_{\text{mix.}}) + f_{\alpha'}(\varepsilon_{\text{mix.}}) + f_{ZrO_2} = 1. \tag{7.7}$$

Assuming that the energy density has the same value for each single microstructural constituent and for the whole sample at every moment of the deformation (the so-called ISO-E hypothesis), the flow curves of the composites with different ceramic contents were calculated (Fig. 7.5b). The results showed very good accuracy between the calculated and measured datasets. The specific prediction accuracy of the correlation is 2%, 2% and 1% for the chosen ZrO_2 contents of 0%, 10% and 30%, respectively. Thus, a fast and accurate method was developed for predicting the strain hardening behavior of TRIP-matrix composites under cold deformation conditions [5].

To improve the convergence of calculation based on the mixture rule, the accuracy of the total strain estimates for the composite has to be increased. The mixture strain of the composite is determined by

$$\varepsilon_{\text{mix.}} = f_{\gamma} \cdot \varepsilon_{\gamma} + f_{\alpha'} \cdot \varepsilon_{\alpha'} + f_{ZrO_2} \cdot \varepsilon_{ZrO_2} \tag{7.8}$$

using the local strains and volume fractions of each phase.

Because the experimental determination of local phase strains is fraught with difficulties [23], the ISO-E method in inverse mode was used. Based on this approach, the relationship between the mixture strain of the composite and the local strain values of each phase was determined (Fig. 7.6). The figure shows that the curves for each phase component are nonlinear. The deformation of austenite in the low mixture strain range of the composite corresponds substantially to the composite strain. With a further increase in the mixture strain of the composite, the local deformation of austenite tends to have higher strain values than the composite. The local strains of martensite and ZrO_2 are significantly lower than the mixture strain of the composite.

Based on the calculations performed, a graphical working map was developed to predict the mixture strain of the composite according to the known ZrO_2 volume fractions and mixture stress. In Fig. 7.7, an example is illustrated and marked with arrows. For a composite with 10% ZrO_2 and a mixture stress of 900 MPa, a mixture strain of the composite $\varepsilon_{\text{mix.}} = 0.16$ is determined. On the lower left side, the known ZrO_2 content of 10% (0.1) is used, and the mixture stress gives the value of $\varepsilon_{ZrO2} = 0.03$. On the upper right side, the known mixture stress and the isoline for $\varepsilon_{ZrO2} = 0.03$ are used to find the strain $\varepsilon_{\text{mix.}} = 0.16$.

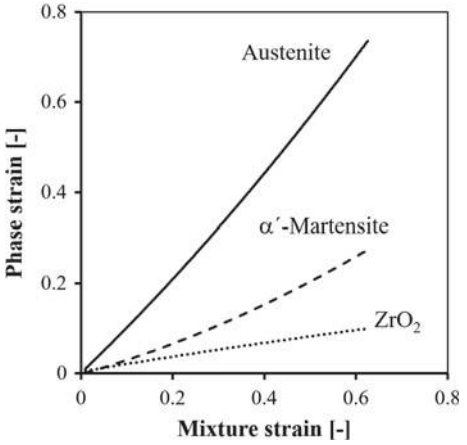

Fig. 7.6 Relationship between the mixture strain of the composite and the local strain values of each phase within the composite under cold forming conditions calculated with the ISO-E method [6]

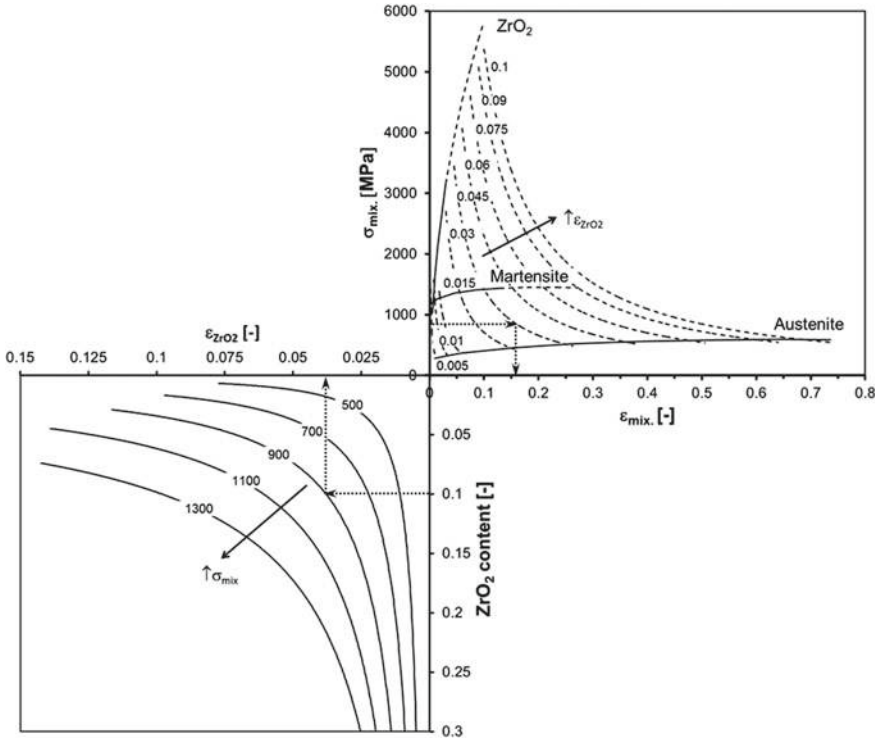

Fig. 7.7 Working map for strain dependence of the composite under cold forming conditions [6]

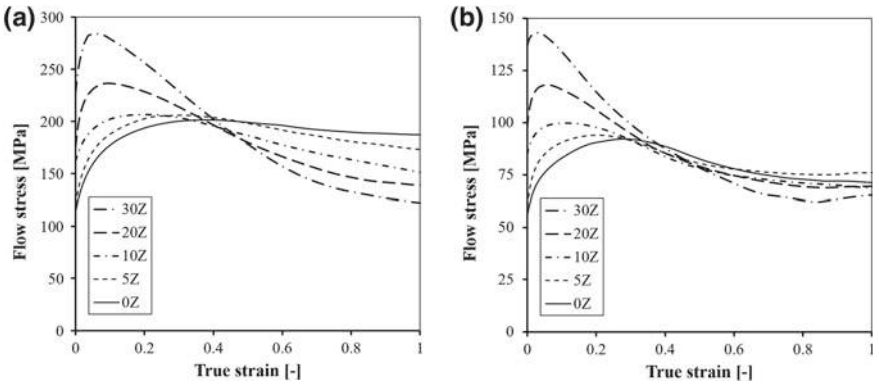

Fig. 7.8 Influence of the ZrO_2 content with a particle size less than 10 μm on the flow curve at a strain rate of 0.1 s^{-1} for **a** 900 °C and **b** 1100 °C

To separate the hot forming temperature region from the cold forming temperature region, investigations were carried out to determine the nonrecrystallization temperature. The results showed that the addition of ZrO_2 with the investigated contents and particle distributions had no significant effect on the nonrecrystallization temperature and that this temperature remained at approximately 900 °C. The result is not surprising given the large size of the ceramic particles (>1 μm) compared to the hardening phases (<0.01 μm) in precipitation hardening alloys of delayed recrystallization kinetics.

Under hot forming conditions, the flow stress was determined as a function of the ceramic content and the technological influencing variables, such as deformation temperature and strain rate. There is no strain-induced $\gamma \rightarrow \alpha'$ phase transformation in this temperature region. The ZrO_2 content had a considerable influence on the flow curves. Figure 7.8 shows the courses of two flow curves for composite materials with a ZrO_2-particle size less than 10 μm. This figure clearly shows that the hardening at the beginning of the hot deformation is much more pronounced in samples with a high ZrO_2 content than in samples with a lower ZrO_2 content. Specimens with a ZrO_2 content of 30% reach their maximum flow stress of 280 MPa at a strain of approximately 0.1. On the other hand, the undoped steel matrix exhibits a flow stress of 177 MPa at this strain value. Thus, the composite exhibits up to 58% higher flow stress at low strain values. However, this effect is not valid over the entire range of the flow curve. Therefore, from a strain over 0.25–0.4, the flow stress level of the undoped steel matrix is higher than that of the composite material. At a strain of 1.0, the undoped steel matrix has a flow stress of 185 MPa and the composite material has a flow stress of 120 MPa, which corresponds to a decrease of 35%. Thus, the ZrO_2 content has a clear influence on the hardening and softening behavior of the composites. The hypothesized reason for the different hardening behavior is that the ZrO_2 particles under hot deformation conditions only participate insubstantially in the deformation process (cf. Sect. 7.3.4). Therefore, the applied force must be distributed over a smaller volume. Consequently, the strain in the steel matrix is

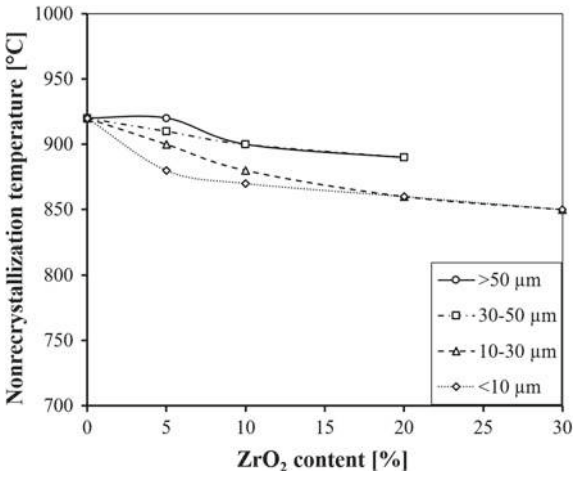

Fig. 7.9 Influence of the ZrO_2 content in the composite on its nonrecrystallization temperature

significantly higher than initially assumed. As a result, the strain rate ultimately increases, which leads to faster hardening of the composite material. The higher level of strengthening can also be explained by the deformation-induced $t \rightarrow m$ phase transformation of the ZrO_2. Due to this phase transformation, a hydrostatic stress condition occurs that enables higher strains in the matrix, which also leads to higher hardening. By enabling higher strains in the matrix, all samples from 0 to 30% ZrO_2 also achieve similar macroscopic strain values of approximately 1.

These findings show that the critical strain required for recrystallization beginning is achieved sooner than the macroscopic deformations suggest. This phenomenon is also confirmed by measurements to determine the nonrecrystallization temperature. As the compilation of determined values in Fig. 7.9 shows, the addition of ZrO_2 in the investigated contents and particle distributions slightly decreases the nonrecrystallization temperature. The results confirm the hypothesis. Therefore, the flow curves with increased ZrO_2 contents exhibit monotonic changes at lower strains. Furthermore, from this point of view, the load-bearing cross-section of the samples changes. The applied force is distributed only over the steel matrix, which ultimately results in a lower flow stress. Figure 7.8a can be used as an example of this behavior. According to this consideration, the load-bearing cross-section of the sample is reduced by the proportion of the ZrO_2 content. The undoped steel matrix achieves a flow stress in the steady-state range of approximately 185 MPa, and with the addition of 30% ZrO_2, the achievable flow stress also decreases by a similar percentage (35%) to 120 MPa. The same tendency can also be seen in Fig. 7.8b.

On the basis of the determined influence of the ZrO_2 content on the characteristics of the hot flow curves of the composite, a modification of the well-known Freiberg flow curve approach for homogeneous conventional materials was carried out so that the ZrO_2 content was taken into account. Since the influence of the strain rate is not important for the consideration of the dependence of the ZrO_2 content, this factor was not implemented in the calculation of the flow curves. The basic prerequisite

for the approximation of the hot flow curves was the Freiberg approach number 4 according to the form [9]

$$\sigma_{\text{mix.}} = A \cdot e^{m_1 \cdot T} \cdot \varepsilon^{m_2} \cdot e^{\frac{m_4}{\varepsilon}} \cdot (1+\varepsilon)^{m_5 \cdot T} \cdot e^{m_7} \tag{7.9}$$

To adapt the Freiberg approach to the deformation conditions of the composite materials, this approach was modified by adding four factors. At first, this is the ZrO_2 content Z. With increasing Z, the hardening of the composite material also increases; thus, the factor ε^{m_2} changes to $\varepsilon^{m_2 \cdot Z}$, and the factor $(1+\varepsilon)^{m_5 \cdot T}$ changes to $(1+\varepsilon)^{m_5 \cdot T \cdot Z}$. After reaching the critical strain for the beginning of recrystallization, the softening factor is also influenced and results in $e^{\frac{m_4}{\varepsilon} \cdot Z}$. Moreover, the Freiberg approach was extended by an e-function for a better approximation in the range of increased strains and by two exponential functions dependent on ε and Z, which take into account the increased strain hardening. This resulted in a modified Freiberg approach for hot deformation of composite materials, which is expressed as

$$\sigma_{\text{mix.}} = A \cdot e^{m_1 \cdot T} \cdot \varepsilon^{m_2} \cdot e^{\frac{m_4}{\varepsilon}} \cdot (1+\varepsilon)^{m_5 \cdot T} \cdot e^{m_7 \cdot \varepsilon} \cdot \varepsilon^{m_{11} \cdot Z} \cdot e^{m_{12} \cdot Z} \cdot (1+\varepsilon)^{m_{13} \cdot Z \cdot T} \tag{7.10}$$

Table 7.3 shows, for example, the coefficient and exponents determined for ZrO_2 particle sizes below 10 µm. Moreover, the modified Freiberg flow curve approach also provides a very high coefficient of determination and a small standard deviation for a ZrO_2 content of 0%.

Based on the modified Freiberg flow curve approach, the flow curves were then calculated using a combination of the ISO-E method and the mixture rule. Assuming that the energy density in the steel matrix and in the ZrO_2 particles is the same during the deformation of the composite material, the area integrals of the hot flow

Table 7.3 Parameters for the modified Freiberg flow curve approach for hot deformation of composites with particle sizes <10 µm (valid for temperatures between 900 and 1200 °C)

Parameter	Value	ZrO_2 content, %	Coefficient of determination	Standard deviation, MPa
A	4559.889	0	0.977	16.90
m_1	−0.002793			
m_2	0.285427	5	0.987	11.50
m_4	0.000837			
m_5	−0.001802	10	0.997	4.10
m_7	0.424686			
m_{11}	−0.187844	20	0.989	12.40
m_{12}	1.330402			
m_{13}	0.00485	30	0.987	15.10
		100	0.983	51.50

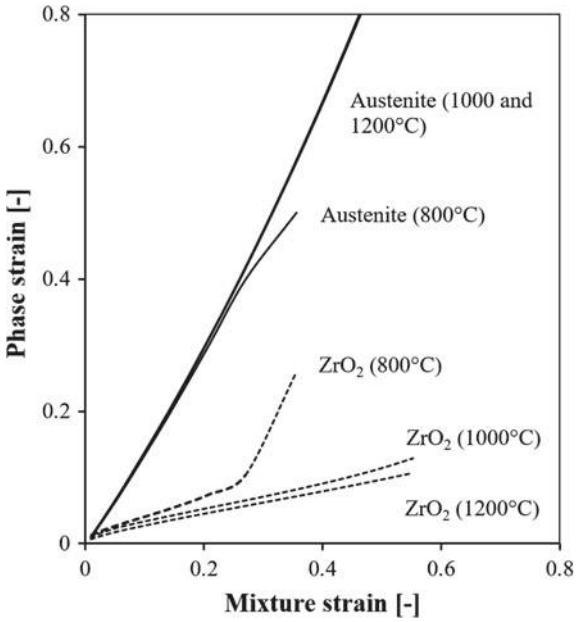

Fig. 7.10 Relationship between the mixture strain of the composite and the local strain values of each phase within the composite under hot deformation conditions calculated with the ISO-E method

curves of the steel and the ceramic can also be equated. The integration limits ε_1 and ε_2 are the strains here. By means of a previous determination of the equations for flow stress using the modified Freiberg approach, it was now possible to calculate the corresponding strain of ZrO_2 by specifying a strain for the steel matrix. The strain dependencies for the three selected temperatures are shown in Fig. 7.10. This figure clearly shows that the specification of the ISO-E method at low temperatures imposes very high strains on the ZrO_2. Even at higher temperatures and high steel matrix strains, the ZrO_2 achieves strains that are significantly higher than the strains from the compression tests. The flow stresses calculated using the mixture rule were compared with the measured values. This comparison shows that the calculated flow stresses exceed the actual flow stresses by up to 600%.

The reasons for the large deviations are diverse and can be justified by the mixture rule. For example, by equating the area below the flow curve (energy density), the ZrO_2 is forced to deform to an excessively high strain, or the steel matrix is not loaded to failure. This results from the fact that if a high strain is specified for the steel matrix, the integral also assumes very high values. However, these can only be equalized by means of high ZrO_2 strains.

This finding shows that the deformation in the high temperature range is not divided among the present phase components but nearly exclusively among the steel matrix. Thus, the assumption of an evenly distributed energy density regarding the deformation of steel and ceramics at high temperatures can be rejected.

Another approach would be to consider the composite as a viscous fluid with hard inclusions. The maximum stress the composite can withstand is the flow stress of

the steel matrix. As a result, the ZrO_2 particles cannot be subjected to higher stresses than the matrix. This aspect is completely ignored by the ISO-E method. For this consideration, only the volume fraction of the ZrO_2 is decisive for the development of the flow curve. Thus, a high ZrO_2 content corresponds to a low matrix content, which leads to a lower flow stress because the deformation is only localized in the matrix.

This approach is of course not suitable for very high ZrO_2 contents. As soon as the particles "touch" each other and form a kind of "skeleton" in the matrix, they can also absorb a portion of the applied stress, thereby contributing significantly to the hardening of the composite. On the other hand, a small fraction of ZrO_2 means a higher flow stress because more material is available to cope with the stress.

In conclusion, the presented modified Freiberg approach is the most advantageous variant with regard to the modeling of hot flow curves of composite materials. The ISO-E method does not provide any useful results due to errors caused by a principle calculation assumption.

7.3.3 Strain Softening

The dynamic softening behavior was analyzed on the basis of warm flow curves (cf. Fig. 7.8). All measured hot flow curves have a maximum value and then decrease continuously with increasing strain due to dynamic recovery and recrystallization processes. As the shape of the flow curves shows, dynamic recrystallization and dislocation hardening are the determining processes during hot deformation. One of the main reasons for this phenomenon is the low stacking fault energy of the face-centered cubic (FCC) crystal structure of the steel matrix [24].

The ZrO_2 particles represent barriers to dislocation movement in the hardening processes due to faster and higher hardening values. After exceeding the critical flow stress, the new grains form near the ZrO_2 particles due to the increased dislocation density in these locations. Compared to the undoped steel matrix, the addition of ZrO_2 to the composite material creates an additional grain boundary surface, which favors the formation of new grains. Therefore, the softening processes run faster in composite materials (cf. Fig. 7.8) [25].

Figure 7.11a shows exemplary results from modeling dynamic softening on the basis of reaction kinetic calculation equations. The model calculation shows that a largely complete dynamic recrystallization can only be achieved at higher strains of approximately 1.5. In contrast, the influence of temperature is less pronounced in the investigated area and causes faster dynamic softening only in the medium strain range with increasing temperature. This effect can be explained by thermal activation.

The static softening behavior was measured by means of double compression tests. In the entire investigated temperature and strain rate range, the composite material showed a sigmoidal softening process. As expected, static softening occurred faster with increasing strain rate and rising deformation temperature. The results indicated

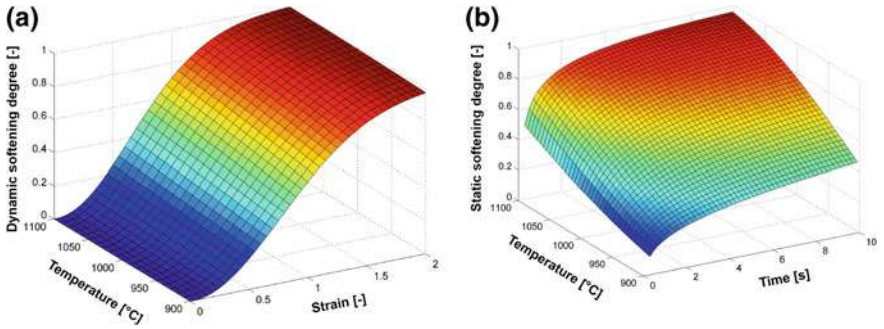

Fig. 7.11 **a** Dynamic and **b** static softening kinetics of composite material with 10% ZrO_2 as a function of deformation temperature, strain and pause time at a strain rate of 1 s^{-1}

that the ZrO_2 particles present in the composite material significantly accelerate the processes of static softening compared to the undoped steel matrix.

The investigations have contributed to the development of a model for static softening based on kinetic reaction equations. Figure 7.11 shows exemplary results from modeling the composite material with 10% ZrO_2 at a strain rate of 1 s^{-1}. An increase in temperature from 900 to 1100 °C at a constant pause time of 10 s led to a doubling of the static softening degree, resulting in a completely recrystallized microstructure.

7.3.4 Formability

Transverse extrusion tests were used to characterize the cold formability of the composite materials with different ZrO_2 contents. Figure 7.12a shows an example of the change in cold formability for the ceramic particle distribution of 10–30 µm, wherein the values are normalized to the formability of the undoped steel matrix. The results indicate that the normalized cold formability decreases nearly hyperbolically with increasing ZrO_2 content in the composite material. For ceramic phase contents below 20%, the normalized cold formability decreases by approximately 2.5% per 1% increase in ceramic content. This trend correlates well with the decreasing content of transformed α'-martensite and subsequently with the decreasing value of macroscopic residual compressive stresses generated in front of the crack tip, which increase the crack propagation velocity. The decreasing cold formability is visible in the changing appearance of the cracked flange area of the specimen after failure. Figure 7.12a shows that the increase in the ceramic content leads to an increasing number of small radial macrocracks, which developed under the effect of tangential tensile stresses starting from the specimen flange edge. Considering the fact that microcracks always occur at the largest microstructural inhomogeneities [26], which in this case is at the ZrO_2 particles, at high ceramic contents, there is always

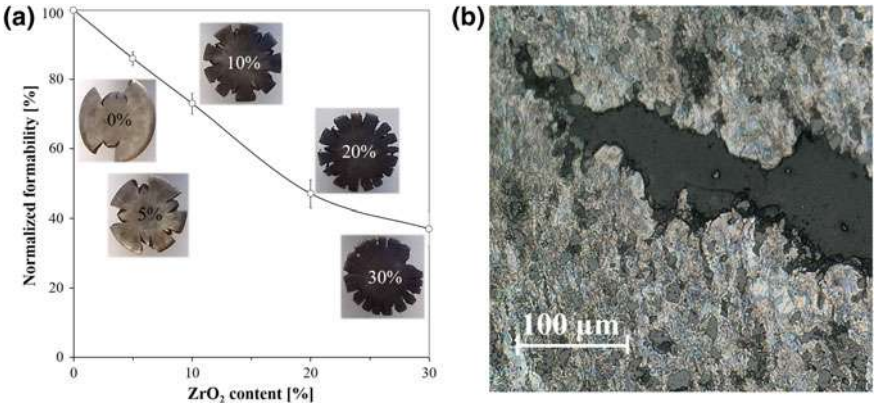

Fig. 7.12 **a** Development of the normalized cold formability with increasing ZrO_2 content determined by means of transverse extrusion tests with appearances of the cracked flange area of the specimen after failure. **b** Image of a macrocrack on the flange area of the specimen with 20% ZrO_2, in which the ZrO_2 particles are shown in light gray and the pores are shown in black

at least one large particle at the edge of the sample where the maximum tangential tensile stresses are acting during deformation. Due to the strain obstruction, stress concentrations occur at these points in the steel matrix in the vicinity of the ceramic particles. These stress concentrations lead to cracking in the steel matrix near the phase interfaces. Once local damage occurs, crack propagation initiates under the acting tangential tensile stress. Here, the free path length between ceramic particles determines the size of the damage zone in front of the growing crack, in which mainly the steel matrix fails at the phase interface (Fig. 7.12b). The positive phenomenon of the failure by means of delamination at the phase boundary is reflected in the decreasing crack propagation velocity in the steel matrix because the pores formed by the delamination locally increase the multiaxiality and slow the crack propagation, which occurs through local plastic deformation. The microcracks formed in this way quickly combine to form a larger macrocrack, the growth rate of which is ultimately determined by the hardness and toughness of the steel matrix. Figure 7.12b shows that the microcracks also grow outside the main crack path. There, energy is converted, which does not serve the propagation of the main crack. The results show that when the ZrO_2 content is 30%, more ceramic particles are located in the damage zone, thereby inhibiting the crack propagation velocity through the formation of secondary cracks and crack branching. With a constant ceramic content in the microstructure, the crack propagation velocity decreases with increasing particle size because the free path length between two ZrO_2 particles increases. Based on the investigations, it was possible to limit the maximum ZrO_2 content for cold rolling processes to 10% due to an increased risk of edge cracking.

The hot formability was characterized according to the methodology in [16] based on the measured hot flow curves. The resulting calculation of process maps made it

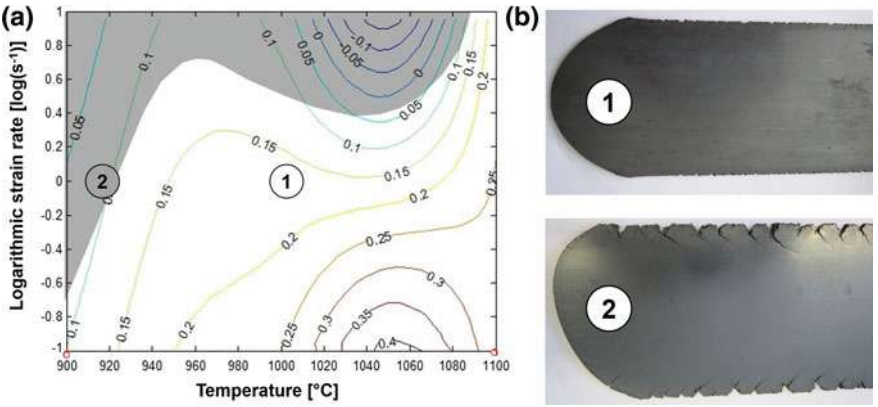

Fig. 7.13 **a** Process map for hot deformation conditions of composite with 10% ZrO_2 and strain of 0.3 and **b** the validation results after hot rolling

possible to determine the optimum process window from the point of view of failure-free deformation. Figure 7.13a shows an exemplary process map for the composite material with 10% ZrO_2 content for a strain of $\varepsilon = 0.3$ in the temperature interval of 900–1100 °C and the strain rate interval of 0.1–10 s^{-1}. The bright and gray areas of the map correspond to stable (fracture free) and unstable deformation, respectively. The values at the isolines reflect the efficiency of the dissipation process. One part of the energy used for deformation gets lost (for example, due to heating) and is not available for the dynamic recovery, the dynamic recrystallization, the closing of pores and so on. A comparison of the process maps and the experimental data of all investigated composites showed their dependence on the different deformation conditions. It was obvious that some combinations of strain rate, temperature and composite microstructure led to failure (gray areas of the maps; for example, position 2 in Fig. 7.13a). The technological combinations reflected the main role of ZrO_2 content and coarse particle fraction during the deformation process. However, it was deduced that at the lowest investigated deformation temperatures of 700 and 800 °C, failure is only slightly influenced by the increased ZrO_2 content. Here, an increased risk of failure already occurred in the course of strain hardening. The best hot deformation conditions for the investigated temperatures of 900 and 1100 °C are at a maximum strain rate of approximately 0.2 and 10 s^{-1}, respectively (cf. position 1 in Fig. 7.13a). It is obvious that the agglomerates lead to failure, and the increase in deformation temperature extends the interval of failure strains. Regarding the initial material condition, it was shown—analogous to cold deformation—that composite materials with finer ceramic particles are significantly more sensitive to material failure due to the reduced free path length between ceramic particles for the same ceramic content. Further investigations using light microscopy and SEM confirmed interfacial delamination as the cause of failure. The results showed that, from the point of view of thermomechanical treatment, only conventional rolling in the high

temperature range is suitable for achieving sufficient formability of the composite material [27].

7.3.5 *Material Flow During Rolling*

Investigations on the deformation behavior and the quantitative microstructure analysis showed that after a rolling reduction of approximately 30%, the porosity was eliminated in all composites. Furthermore, the results show that the number of pores is accompanied by an agglomeration affinity of the composite. It is important to mention that the composites with high rates of agglomerates have twice the number of pores than found in the initial state in the case of maximal deformation. This behavior can be explained with the help of a model, which is qualitatively shown in Fig. 7.14. There are large pores around single ZrO_2 agglomerates in the initial state, which are still present on the phase borders because of insufficient sintering results (Fig. 7.14a). As elaborated in [28], the larger particles of irregular shape produce a greater effect on the local curvature, especially at lower deformation. The angular component of the deformation tensor can be evaluated at the turning of phase and grain boundaries and has a higher influence on inhomogeneous deformation. The primarily common plasticization of the steel matrix is promoted, and the realignment of ZrO_2 particles is observed. This process is the initial phase of local plastic deformation, which can create local bonding between composite phases according to their form and structure. The local inhomogeneity of deformation promotes local flow stress. The initial large pores can split into many small pores (Fig. 7.14a) and move or align in the direction of local stress together with the grain boundaries, phase boundaries, and agglomerates. The changeable influence of the composite microstructure on the evolution of the number of pores confirms the reality of a qualitative model [27].

Furthermore, the results show that reorientation of single ZrO_2 particles with partial line formation depends on the agglomeration grade of the composite. This behavior applies to the less agglomerated composites and is related to single enclosed ZrO_2 particles or to the small line groups (clusters) consisting of 4–8 particles. Their arranged length is correlated to the austenite grain size during plasticization of the steel matrix (Fig. 7.14b). In contrast, a destruction of large agglomerates could not be revealed.

Regarding the material flow and the particle rearrangement resulting from deformation, metallographic investigations were carried out on sheets and on the compression, wedge rolling and stuck rolling specimens. The light microscopy images were examined based on quantitative metallographic parameters. Thus, the determined anisotropy index AI provides information on the homogeneous distribution of the particles. For the same strain value, no influence of particle size, deformation temperature or deformation zone geometry on AI was determined for the hot-compressed specimens. In contrast, investigations on the wedge rolling specimens showed that the particle distribution in the composite material becomes anisotropic with increasing

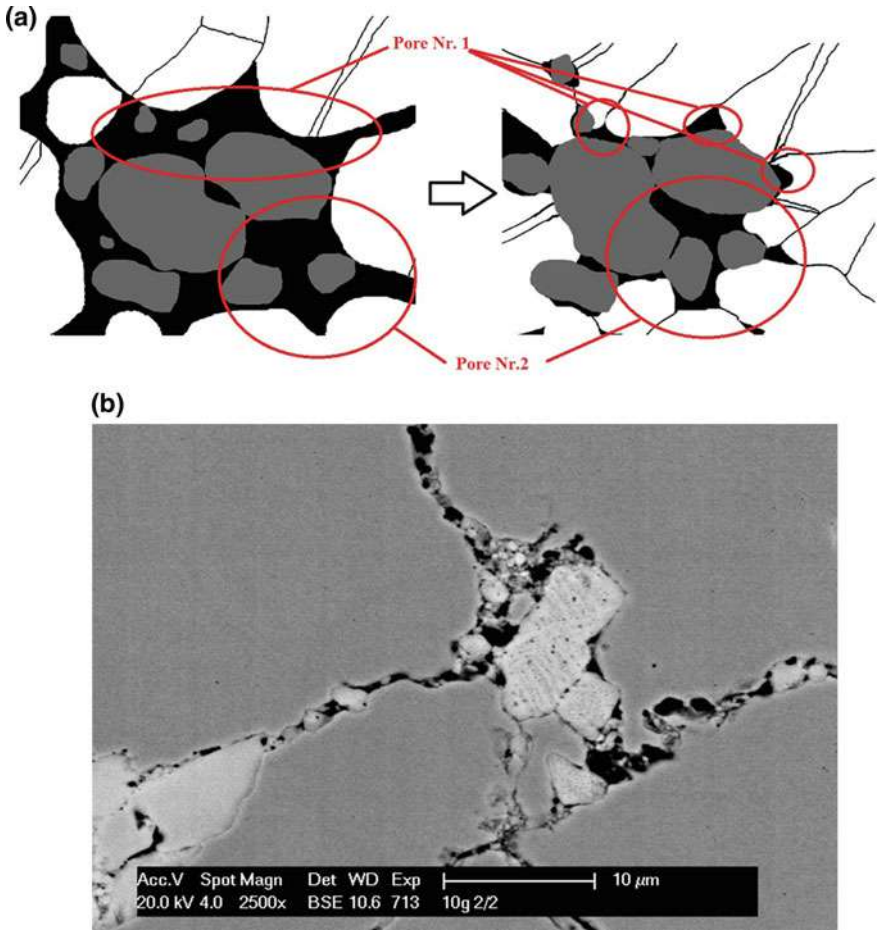

Fig. 7.14 **a** Qualitative model of the deformation behavior around a ZrO_2 agglomerate and **b** realignment of ZrO_2 particles [27]

strain. The corresponding increase in anisotropy depended primarily on the deformation temperature. A further characterization of the material flow during deformation with regard to a preferred direction of the particles is given by the degree of orientation Ω_{12}. This value also increased with increasing strain (Fig. 7.15a). This finding supported the conclusion that the ceramic particles move with the flowing steel matrix as a result of the deformation and align in the flow direction (cf. Sect. 7.3.2 and Fig. 7.15b) [29].

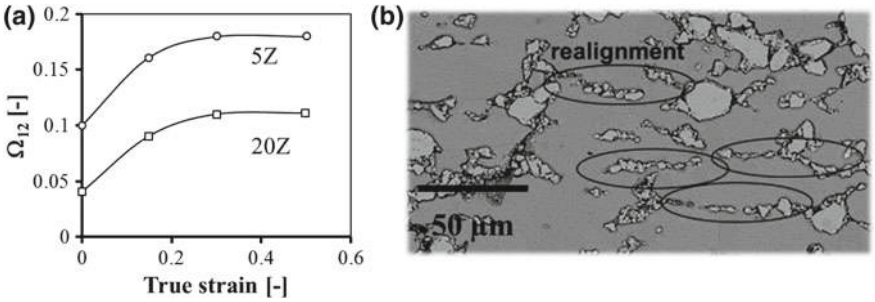

Fig. 7.15 **a** Development of the degree of orientation Ω_{12} of ZrO_2 particles with respect to the true strain for composites with 5 and 20% ZrO_2 and **b** the realignment (line) formation in the microstructure after hot rolling with a thickness reduction of 45% [27, 29]

7.4 Conclusions

Currently, models are increasingly being used to perform computer simulations of material manufacturing and further processing from semifinished products to finished parts and to predict the mechanical properties of the finished components. In this chapter, the deformation behavior of the TRIP-matrix composite under conditions similar to flat rolling in a wide temperature range was tested and analyzed using current test methods. The initial material was available in the presintered form with different ceramic contents between 0 and 30% and with closely spaced particle sizes between approximately 2 and 60 µm (classified by wind sifting) in the high-alloy austenitic steel matrix.

In the field of cold deformation, interrupted compression tests were carried out. The registration of geometrical changes in the specimen shape enabled the calculation of axial, tangential and hydrostatic stress components for different material states. These were implemented in the flow curve modeling. A comparison with the experimental results showed that the prediction accuracy is very good. In further calculations, it was possible to create a flow stress work map for materials with different compositions, where a prediction of local phase strain is possible from the measured macroscopic strain in the composite material.

In the field of hot deformation, technological parameters such as the deformation temperature and the strain rate showed effects on the flow stress level already known from conventional materials. The influence of the varying material condition at constant deformation conditions was expressed as follows. The increase in the ZrO_2 content at constant particle size generally leads to an increase in flow stress. The finer the ZrO_2 particles are, the greater the increase in flow stress. The deformation temperature has the primary influence and the strain rate has a secondary influence. Based on the determined influence of the ZrO_2 content on the characteristics of the hot flow curves of the composite material, the well-known Freiberg flow curve approach for homogeneous materials was modified so that the ZrO_2 content was taken into account. For a ZrO_2 content of 0–100%, this modified approach provided a very high

coefficient of determination and a small standard deviation. Based on the Freiberg flow curve approach, the flow curves were then modeled using a combination of the ISO-E method and the mixture rule. This method did not provide any useful results due to errors caused by a principle assumption that is applicable in the determination of cold flow curves but cannot be applied in the area of hot forming.

The analysis of the measured flow curves enabled the following interpretation of the dynamic hardening and softening processes. At temperatures up to 800 °C, softening occurs exclusively through recovery, whereby the flow curve does not pass through a maximum. Above this deformation temperature, dynamic recrystallization appears to be the dominant softening mechanism. The ZrO_2 content has the primary influence and the particle size has a secondary influence on the critical strain. The latter decreases with increasing ceramic content and finer particle size.

Transverse extrusion tests were used to characterize the cold formability of the composite materials with different ZrO_2 contents. The results indicated that the normalized cold formability decreased hyperbolically with increasing ZrO_2 content in the composite material. This trend correlated well with the decreasing fraction of transformed α'-martensite and subsequently with the decreasing value of the resulting macroscopic residual compressive stresses in front of the crack tip, which increased the crack propagation velocity. The results showed that if the ZrO_2 content was 30%, more ceramic particles were in the damage zone, thereby inhibiting the crack propagation velocity through secondary crack formation and crack splitting. With a constant ceramic content in the microstructure, the crack propagation velocity decreased with increasing particle size because the free path length between two ZrO_2 particles increased.

Based on the measured flow curves, the optimum process window was determined from the point of view of failure-free deformation by creating process maps in accordance with the methodology reported in [30]. It could be deduced that at the lowest investigated deformation temperatures of 700 and 800 °C, failure was only slightly influenced by the ZrO_2 content. Here, an increased risk of failure already occurred in the course of strengthening. With regard to the condition of the material, it can be seen that composite materials with finer ceramic particles at the same ceramic content were significantly more sensitive to material failure. Further investigations using light microscopy and SEM confirmed that interfacial delamination between phases was the cause of failure. Furthermore, the results showed that, from the point of view of thermomechanical treatment, only conventional rolling was suitable for achieving sufficient formability of the composite material in a wide temperature-strain rate window.

With regard to the material flow and the particle rearrangement caused by deformation, metallographic examinations of sheets and the upsetting, wedge rolling and stuck rolling specimens were carried out. These examination quantitatively verified that the ceramic particles move with the flowing matrix material as a result of the deformation and align in the direction of flow. An influence of the deformation temperature within a constant strain value could not be verified.

Acknowledgements The authors are grateful to the employees of the Fraunhofer Institute for Ceramic Technologies and Systems (*) and of the Institute for Metal Forming (**), who participated in the powder separation, presintering and rolling processes: Dr. rer. nat. habil. Mathias Herrmann (*), Dipl.-Ing. Jan Räthel (*), Dr.-Ing. Katja Pranke (**) and Dr.-Ing. Wolfhart Müller (**). Special thanks are addressed to Dr. Gizo Bokuchava from the Joint Institute for Nuclear Research, Dubna, Russia, for the execution of the neutron diffraction studies. The authors gratefully acknowledge the German Research Foundation (DFG) for supporting the Collaborative Research Center TRIP-Matrix-Composites (Project number 54473466—CRC799 subproject A6).

References

1. R. Kawalla, A. Nam, S. Guk, Technological methods to control the final properties of the rolled product. J. Chem. Tech. Metall. **50**(6), 606–612 (2015)
2. S. Guk, K. Pranke, R. Kawalla, Modeling of properties of sheet metal products from the TRIP-matrix-composite along the process chain. Postersession im Rahmen der 5. ICAFT/22. SFU Tagung vom 10. bis 11. November 2015 am Fraunhofer-Institut für Werkzeugmaschinen und Umformtechnik IWU in Chemnitz
3. F. Qayyum, S. Guk, M. Schmidtchen, R. Kawalla, U. Prahl, Modelling and understanding the deformation behaviour of TRIP steel at microstructural level using DAMASK. Konferenz MEFORM2019 "Simulationsbasierte Technologieentwicklung", Freiberg, den 20.–21.03.2019
4. A. Yanina, S. Guk, W. Müller, R. Kawalla, C. Weigelt, Herstellung und Weiterverarbeitung von TRIP-fähigen Partikelverbundwerkstoffen. Tagungsband der internationalen Konferenz MEFORM 2012 "Material technology and forging processes". ISBN 978-3-86012-434-5, Freiberg 28.03.–30.03.2012, pp. 216–231
5. S. Guk, K. Pranke, W. Müller, Flow curve modelling of an Mg-PSZ reinforced TRIP-matrix-composite. ISIJ Int. **54**(10), 2416–2420 (2014)
6. S. Guk, W. Müller, K. Pranke, R. Kawalla, Mechanical behaviour modelling of an Mg-stabilized zirconia reinforced TRIP-matrix-composite under cold working conditions. Mater. Sci. Appl. **5**, 812–822 (2014)
7. S. Solhjoo, R. Ebrahimi, Prediction of no-recrystallization temperature by simulation of multi-pass flow stress curves from single-pass curves. J. Mater. Sci. **45**, 5960–5966 (2010)
8. S. Vervynckt, K. Verbeken, P. Thibaux, Y. Houbaert, Evaluation of the austenite recrystallization by multideformation and double deformation tests. Steel Res. Int. **82**(4), 369–378 (2011)
9. T. Spittel, M. Spittel, Ferrous alloys (2009)
10. C. Biegus, Anwendung von Werkstoffmodellen auf das Entfestigungsverhalten und die Ferritkorngröße mikrolegierter Baustähle. Diss (1996)
11. F. Bubeck, *Charakterisierung und Modellierung der Gefügeentwicklung bei der Warmumformung von Kupferwerkstoffen* (Diss, TU Bergakademie Freiberg, 2007)
12. W. Müller, Temperaturverhältnisse und Reaktionskinetik beim Ziehen und Wärmebehandeln von Draht. Bd. B292. TU Bergakademie Freiberg (1998)
13. H.-P. Schmitz, Entfestigungsverhalten kohlenstoffarmer Stähle bei der Warmumformung im Ferritgebiet. Diss. Freiberger Forschungshefte B307, TU Bergakademie Freiberg (2000)
14. S. Guk, R. Kawalla, Prozessnahe Beurteilung der Umformbarkeit beim Kaltfließpressen. MassivUmformung (März 2017) pp. 64–68. ISSN 2366-5106
15. F. Qayyum, S. Guk, R. Kawalla, U. Prahl, Experimental investigations and multiscale modeling to study the effect of Sulphur content on formability of 16MnCr5 alloy steel. Steel Res. Int. (2018). https://doi.org/10.1002/srin.201800369
16. Y.V.R.K. Prasad, T. Seshacharyulu, Modelling of hot deformation for microstructural control. Int. Mater. Rev. **43**(6), 243–258 (2013)

17. S. Guk, D. Plotnikova, R. Kawalla, The effect of microstructural and geometric inhomogeneities induced by laser for forming strain analysis on sheet metal formability. Mater. Sci. Appl. **7**, 247–256 (2016)
18. S. Guk, M. Preiß, R. Kawalla, Metal formability interactions in laser marking for creating of grid patterns for forming strain analysis of high strength steels. Key Eng. Mater. **746**, 92–98 (2017)
19. S. Guk, K. Pranke, W. Müller, A. Yanina, Development of high-strength TRIP-matrix-composite materials, in *Proceedings of the International Conference of Production and Processing of Cladded Materials and Metal Matrix Composites MEFORM 2014*, ISBN 978–3-86012-481-9, Altenberg 26.03.–27.03.2014, Herausg.: ACATRAIN e.V., Verein für Weiterbildung an der TU Bergakademie Freiberg, Institut für Metallformung, pp. 149–159
20. M. Abdel-Rahman, M.N. El-Sheikh, Workability in forging of powder metallurgy compacts. J. Mater. Process. Technol. **54**, 97–102 (1995)
21. I. Pyshmintsev, M. Meyer, B. Cooman, R. Savray, V. Shveykin, M. Vermeulen, The influence of the stress state on the plasticity of transformation induced plasticity-aided steel. Metall. Mater. Trans. A **33**, 1659–1667 (2002)
22. I. Tamura, Y. Tomota, H. Ozawa, in *Proceedings of 3rd International Conference on Strength of Metals and Alloys* (Cambridge, England, 1973), p. 611
23. G.D. Bokuchava, Y.E. Gorshkova, V. Papushkin, S. Guk, R. Kawalla, Investigation of plastically deformed TRIP-composites by neutron diffraction and small-angle neutron scattering methods. Surf. Invest. X-ray, Synchr. Neutr. Tech. **12**(2), 227–232 (1995)
24. A. Yanina, S. Guk, W. Müller, R. Kawalla, C. Weigelt, Dynamic and static softening of sintered MgO-PSZ/TRIP-matrix composites with up to 10 vol-% ZrO_2. Steel Res. Int. **82**(9), 1158–1165 (2011)
25. A. Yanina, S. Guk, R. Kawalla, New TRIP-matrix-composite production, properties and softening behaviour during warm forming. Tagungsband der internationalen Konferenz "Neuere Entwicklungen in der Massivumformung". ISBN 978-3-88355-386-3, Fellbach/Stuttgart 17.05.–18.05.2011, pp. 271–281
26. M. Petrov, S. Guk, P. Petrov, J. Bast, Kraft- und Deformationscharakteristika beim Umformen eines Stahlblech-Verbundwerkstoffs. Lightweight Des. **5**(5), 50–57 (2012)
27. S. Guk, D. Milisova, K. Pranke, Influence of deformation conditions on the microstructure and formability of sintered Mg-PSZ reinforced TRIP-matrix-composites. Key Eng. Mater. **684**, 86–96 (2016). Advanced materials and processes of metalworking. ISBN-13: 978-3-03835-522-9
28. S.S. Gorelik, *Recrystallization in metals and alloys* (MIR Publishers, Moscow, 1981)
29. K. Pranke, S. Guk, Material flow in Mg-PSZ particle reinforced TRIP-matrix-composites due to hot-rolling. Key Eng. Mater. **684**, 97–103 (2016). Advanced materials and processes of metalworking. ISBN-13: 978-3-03835-522-9
30. Y. Prasad, S. Sasidhara, *Hot working guide: a compendium of processing maps* (ASM International, Materials Park, 1997)

Chapter 8
Powder Forging of Presintered TRIP-Matrix Composites

Markus Kirschner, Sergey Guk, Rudolf Kawalla and Ulrich Prahl

Abstract This chapter addresses bulk forming processes-especially powder forging-used to produce complex shaped components from presintered TRIP-matrix composites. Based on experimentally determined material and process parameters (e.g., shrinkage, Poisson's ratio, elastic modulus, oxidation behavior), extended process maps for compressible materials were presented. Subsequently, a characterization of the material flow as a function of the material conditions was reproduced via the visioplastic method and metallographic analysis, and then connections were drawn between the results and the extended process maps. The knowledge gained was used to develop a powder forging tool for a Gleeble HDS-V40, which was used to conduct model tests aiming to improve the component properties. The tool was equipped with compensating gaps to provide better compaction to the components. To find the optimal compaction for the solid material, different variants of compensating gaps were investigated. The components obtained through this approach were examined on the basis of their mechanical properties and microstructures. Furthermore, the deformation of graded components was analyzed in this study. In addition to the formation of a damage-tolerant interface and the shear strength of the different layers, special attention was paid to process-relevant parameters, such as the maximum deformation degree, the tool and specimen temperature and the pressure holding time.

M. Kirschner (✉) · S. Guk · R. Kawalla · U. Prahl
Institute for Metal Forming, Technische Universität Bergakademie Freiberg, Freiberg, Germany
e-mail: markus.kirschner@imf.tu-freiberg.de

S. Guk
e-mail: sergey.guk@imf.tu-freiberg.de

R. Kawalla
e-mail: rudolf.kawalla@imf.tu-freiberg.de

U. Prahl
e-mail: ulrich.prahl@imf.tu-freiberg.de

H. Biermann and C. G. Aneziris (eds.), *Austenitic TRIP/TWIP Steels and Steel-Zirconia Composites*, Springer Series in Materials Science 298,
https://doi.org/10.1007/978-3-030-42603-3_8

8.1 Introduction

The integration of various properties and functions in a component or in an assembly is constantly increasing to shorten product manufacturing times and enhance resource conservation. The required high functionality of materials often leads to chemical-physical requirements that cannot be met by a single material. In some cases, the use of high-performance materials can lead to compromises. Moreover, the range of properties of these innovative high-performance materials is often insufficient to cover all requirements, which is why composite materials are used to provide a combination of the desired properties.

Powder forging is a combination of sintering and precision forging technology that blends the advantages of sintering technology in terms of component design possibilities, good material utilization and narrow tolerances with the high strength of forged components [1–3]. Powder forging is used to turn pressed and sintered semifinished products into solid components with outstanding material properties for use in all types of applications [4, 5].

Therefore, the main task of powder forging is to achieve full density [6]. Based on the material flow that occurs, two process variants of powder forging exist [3, 7, 8, 9].

– "Hot repressing": Hot compression without significant material flow, which corresponds to uniaxial compression.
– "Upsetting" (also referred to as "flow forging" or "powder forging"): Hot forming process with significant material flow, wherein a preform with a simple shape is formed into a finished part with a more complicated shape.

The special advantage of powder forging over other compacting processes, such as hot isostatic pressing, lies in the combination of forging technology with the advantages of powder metallurgy. Here, the recrystallization to a finer grain structure and the texture, which is introduced into the component during the forging process, are decisive advantages over other processes. In addition, specimens with complex geometries that exhibit excellent mechanical properties can be produced in large quantities without or with very little further mechanical treatment.

Therefore, powder-forged components are used especially for high dynamic and vibration loads [10–12]. This approach can also produce graded components, which means that components can be manufactured with an inexpensive base material by using a second wear-resistant material for the highly stressed regions [1, 2, 13].

However, this capability is of little use in industry, as the final density of reinforced components and the distribution of the reinforcement phase after powder forging are difficult to control [14, 15]. Due to material flow and the forming process, reordering processes occur in the component that cannot yet be precisely defined. In addition, an additional phase, especially if it is a composite material of two different material classes, represents a barrier to compaction in a component during powder forging; thus, achieving a compact material becomes more difficult [16–18].

This work focuses on the development of basic principles for the production of compact components with different property profiles from a transformation-induced

plasticity (TRIP)-matrix composite. The main process used is powder forging in temperature ranges from 700 to 1100 °C, which follows the sintering process. The test specimens have a residual porosity and the forming process in the final stage is characterized as uniaxial deformation with and without lateral material flow. For this purpose, model compression tests are carried out on the forged specimens in a closed die in order to make a detailed statement on the rearrangement processes of ZrO_2 particles due to friction with contact surfaces, in which the local material flow during compaction is analyzed as a function of the geometry of the forming zone. The challenge here is to investigate the compaction process and the material flow during powder forging of homogeneously reinforced and graded materials. A further challenge is investigating the ability to generate a force-transmitting flat phase boundary via powder forging in the previously designed tool. The technological goal is to produce axially graded components during forming while retaining the graded structure when the material flow begins.

8.2 Materials and Methods

The investigated material is a composition of gas-atomized steel powder, which was austenitic in structure ($d_{10} = 12.4$ µm, $d_{50} = 25.9$ µm and $d_{90} = 46.6$ µm), and Mg-PSZ ceramic powder ($d_{10} = 0.2$ µm, $d_{50} = 4.3$ µm and $d_{90} = 30$ µm). The chemical compositions of both the metastable high alloyed TRIP steel (indicated as X3CrMnNi16-7-6) and the ZrO_2 ceramic are given in Table 8.1. The ceramic particle content was set to 0 vol% (0Z), 5 vol% (5Z), 10 vol% (10Z), 15 vol% (15Z), 20 vol% (20Z) and a graded layer structure. The structures of these five contents are shown in Fig. 8.1.

A binder (1.0 wt% Optapix PAF 35, Zschimmer & Schwarz, Burgstädt, Germany) is used to achieve a more homogeneous density distribution in powder pressing. This binder is added to the powder mixture of ZrO_2 and TRIP steel before powder pressing.

The powder pressing took place at room temperature in a one-sided coaxial press with a pressing force of 200–600 kN depending on the desired residual porosity; the specimens used in this process had a diameter of 10 mm and a height of 10 mm. The individual layers of the graded particle distribution have a height of 2 mm and are stacked individually, precompressed with a low force, and then pressed as a complete component. The subsequent debinding and sintering of the specimens after pressing took place in a furnace (Carbo-Lite/Gero HTK 8 MO/16-1). The debinding was completed before the actual sintering process started. This process took place at a heating rate of 300 K/h and a holding time of 1 h at 1100 °C, followed by a cooling rate of 600 K/h under vacuum (10^{-6} mbar) until reaching room temperature.

For the tests, cylindrical specimens with a height of 10 mm and a diameter of 10 mm were produced. Forming was carried out in a Gleeble HDS-V40 rolling simulator from DSI Europe GmbH (path-controlled) at appropriate temperatures, press forces and deformation degrees. For the desired compression of the specimens, the following three silicon nitride dies, shown in Fig. 8.2, with corresponding tungsten

Table 8.1 Nominal chemical compositions of the TRIP steel powder and Mg-PSZ powder

TRIP steel	Fe	C	Cr	Ni	Mn	Si	N	Al	S	Mo	Ti
[wt%]	bal.	0.03	16.3	6.6	7.2	1.0	0.09	0.04	<0.01	<0.01	<0.01
MgO-PSZ	ZrO_2		HfO_2	MgO		SiO_2	Al_2O_3	CaO		TiO_2	Y_2O_3
[wt%]	bal.		1.85	3.25		0.1	1.58	0.06		0.13	0.13

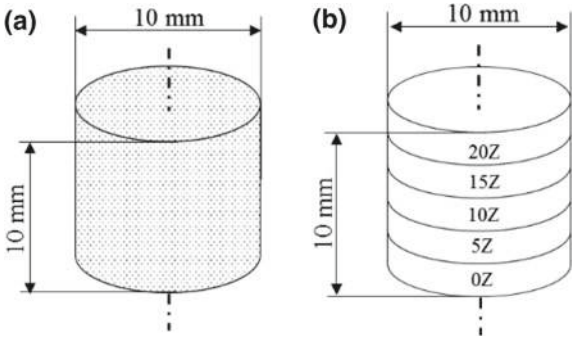

Fig. 8.1 Investigated specimens with **a** homogeneous particle distribution and **b** graded particle distribution

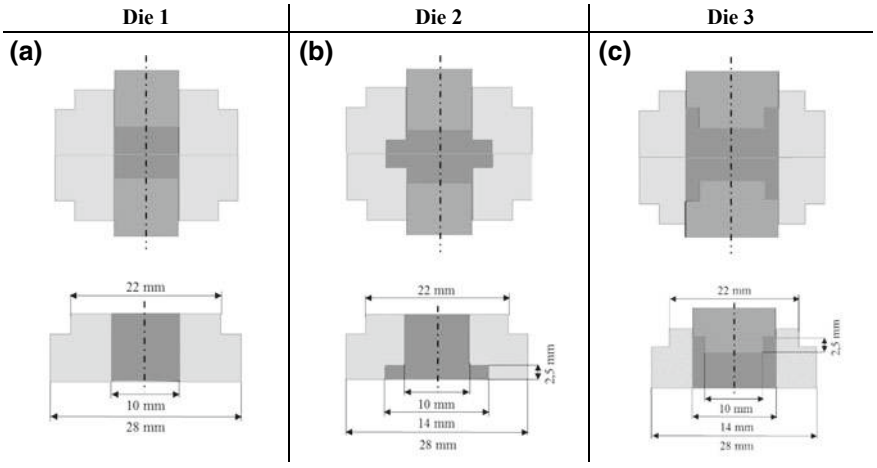

Fig. 8.2 Different die shapes for the investigation of the material flow: **a** Die 1: without a compensating gap; **b** Die 2: with lateral compensating gaps; and **c** Die 3: with upward compensating gaps

carbide punches were available for forming, in which the specimen was conductively heated prior to forming.

Boron nitride was used as a lubricant to reduce friction between the die and the material because carburization may occur during powder forging due to the high temperatures. To avoid this phenomenon, graphite was not used as a lubricant.

The density was determined by means of a hydrostatic balance at room temperature. For this purpose, the specimens were placed in distilled water in a water bath under vacuum for four hours. A magnetic stirrer at the bottom of the water tank prevented the formation of bubbles and kept the water moving. The mass was then determined in distilled water and in air by hydrostatic weighing.

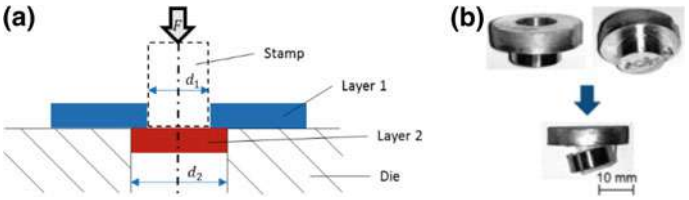

Fig. 8.3 Illustration of the **a** adhesion test and **b** the specimens before and after each test

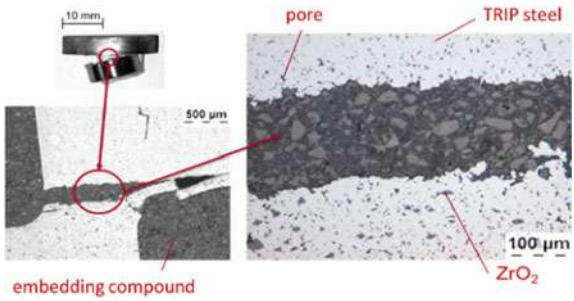

Fig. 8.4 Cross-section through the failure point in an adhesion test specimen

During the adhesion test, the two layers of the graded layer structure of the specimens were generated and the adhesion of the two layers was measured, as shown in Fig. 8.3. The pull-off forces of the individual composite layers were tested in accordance with DIN EN ISO 4624 in an AG-100 testing machine (Hegewald & Peschke, Siebenlehen, Germany). To check whether the phase boundary of the individual layers was also tested, a cross-section was made through the failure point. The results show that the crack did run exactly as desired through the phase boundary of the two structures, as shown in Fig. 8.4.

8.3 Results

To realize this production path, the process-dependent parameters were first examined to limit the process window for the model tests. The focus was on the shrinkage, the density-dependent Poisson's ratio, the density-dependent elastic modulus and the oxidation behavior of the material and on the creation of process maps. Subsequently, model tests were carried out with particular attention to the maximum possible compaction as a function of shear strain, elongation and temperature and to the phase boundary connection between ceramic and steel, which will enable the production of a compact material with complete particle bonding in the matrix. The mechanical properties were then determined from these specimens. Finally, the graded layer structures were investigated following the same approach, and the material properties of the graded layer structures were compared to those of the homogeneous material.

In the following sections, the results of the individual investigations are presented. Note that the analysis takes place in the Cartesian coordinate system and with the different ZrO_2 contents being represented as percentages.

8.3.1 Determination of Material- and Process-Dependent Parameters

Various process parameters were analyzed and evaluated to determine the optimum forging conditions. These parameters include the shrinkage, the density-dependent Poisson's ratio, the elastic modulus/density relationship, and the oxidation behavior of the specimens and process maps. The shrinkage of the components was investigated to calculate the dimensions of the components after sintering and forging, which was necessary for the calculation of the dimensions of the final part and the die dimensions. To consider the density-dependent Poisson's ratio, it is necessary to know the ratio of the horizontal to vertical material load direction when the pore density falls below 10%. The relationship between the density and the elastic modulus was used to determine the start of deformation or plastic flow under external loads. The oxidation behavior was analyzed to investigate the time of transfer between the furnace and the die. Process maps were used to calculate the process window of the different composite states.

8.3.2 Determination of Shrinkage

For the investigation of the specimens after sintering, the shrinkage behavior of the individual ZrO_2 contents was measured with a caliper; the results are shown in Fig. 8.5. The density of the specimens after sintering was 7.1 $\frac{g}{cm^3}$.

The results show that the shrinkage percentage of the sintered specimens reduces considerably with increasing ZrO_2 content. The smallest value of 0.4% can be seen with 20Z, whereas the highest value is 2.2% with 0Z. The specimens with an increasing ZrO_2 content show a decrease in shrinkage. The graded specimen with the value

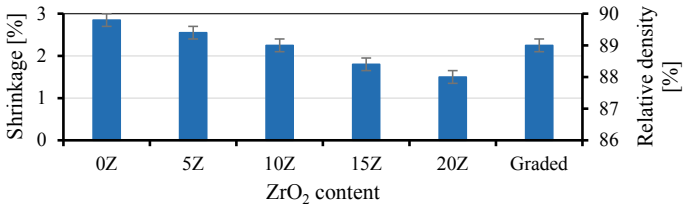

Fig. 8.5 Determination of shrinkage after sintering and powder forging

of 0.7% lies between the specimen with 20Z and the specimen with 15Z. The results also show that there is a considerable difference in shrinkage between the specimen with 0Z and the specimen with 20Z. This difference is important because the shrinkage of the TRIP steel is 2.2%, whereas the shrinkage of ZrO_2 is approximately 0% because the material does not sinter together and is only present as particles in the matrix. Therefore, the shrinkage values of the specimens with a ZrO_2 content are between the shrinkage values of the pure materials. This finding also shows that with increasing ZrO_2 content, the shrinkage of the specimens moves from that of the TRIP steel to that of the ZrO_2 in this particular case.

If these data are compared with shrinkage data from other metal matrix composites (MMCs), it is noticeable that the shrinkage of the TRIP-matrix composite is greater the shrinkage data of other MMCs. For copper matrix composites with a SiC reinforcement phase, the shrinkage is 0.3% [19, 20]. However, note that these specimens had a reinforcement phase content of 70%. A shrinkage of 0.75% was observed in aluminum MMCs, wherein the reinforcement phase was only 0.5% [21, 22]. Thus, the TRIP-matrix composites exhibit greater shrinkage than other particle-reinforced MMCs. However, compared to pure iron steel specimens without particle reinforcement, the specimens in this study exhibit significantly less shrinkage. The high shrinkage in this previous study occurred because a shrinkage of 2.5–3% can be observed in iron powder [23].

Observations show that, similar to the homogenous specimens, the graded specimens exhibit isotropic shrinkage.

The reduction in shrinkage with increasing particle content in the specimens can be explained by the particles themselves. Due to the number of particles in the sintered specimens, there is no specimen shrinkage during sintering because only the matrix material is sintered. The ceramic particles are simply present in the matrix without interacting with the matrix or with each other. The more matrix there is in a specimen, the more the specimen can shrink during sintering. Conversely, this phenomenon means that the more reinforcing particles there are in the matrix (i.e., more of the matrix is replaced), the less the specimen can shrink, as the ceramic particles prevent this shrinkage. This phenomenon can be seen in Fig. 8.5, as the shrinkage of the specimens decreases with increasing ZrO_2 content. The linear expansion coefficient of the matrix is $18.3 \times 10^{-6}\ K^{-1}$, whereas that of ZrO_2 particle is $10.5 \times 10^{-6}\ K^{-1}$.

With regard to shrinkage behavior, there are different approaches that describe the so-called shrinkage parameter. In Fig. 8.6, different shrinkage models are compared to the measured shrinkage of the TRIP-matrix composites. This figure clearly shows that the model according to Coble [24] comes closest to the shrinkage of the TRIP-matrix composite. The value from the Skorokhod model [25] after 60 min of sintering time comes close to the value of the composite, even if the value is an overestimation, whereas the Tikkanen Mäkipirtti model [26] does not show any similarity with the measured value. Note that in the Coble model, the porosity at a certain time works in conjunction with various other material constants, whereas the Skorokhod model and the Tikkanen Mäkipirtti model try to solve the problem via density differences and sample volume differences, respectively.

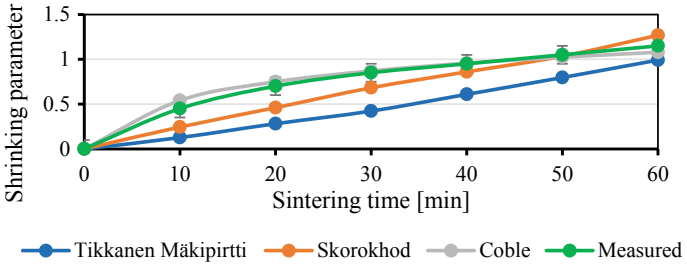

Fig. 8.6 A comparison of different shrinkage models with the measured parameters under the following conditions: 5% ZrO_2 and a residual porosity of 10%

However, in all equations there is no approach for a second material in the equation, which strongly influences the shrinkage parameter due to a different shrinkage. Therefore, the following equation was established on this basis for composite materials:

$$v_s = (-0.13Z + 0.15) \cdot \sqrt{t} \tag{8.1}$$

where Z is the volume content of the second material and t is the sintering time. The equation used here is similar to the equation according to Coble because both equations are based on the specimen porosity and the sintering time. However, this equation further discusses the properties of composites, since the amount of the second phase in the matrix is also taken into account. Thus, a coefficient of determination of 0.98 can be achieved.

8.3.3 Poisson's Ratio as a Function of Density

The Poisson's ratio was determined by compression tests, which were carried out on a Bähr MDS 830 testing system. The Poisson's ratio was determined in accordance with the literature [27]. The specimen was lubricated with boron nitride, and the strain was 0.5 at room temperature.

Figure 8.7 shows that the Poisson's ratio decreases with increasing residual porosity. This finding can also be found in the literature [27]. The reason for this phenomenon is the compression of the material during the compression test with increased residual porosity. The results also show that apart from some fluctuations in the results within the fault tolerance, there are no deviations from the theoretically determined Poisson's ratio. The minor deviations are due to measurement uncertainties.

When considering the dependence of the Poisson's ratio on the density, it is noticeable that the Poisson's ratio increases with increasing density, as shown in Fig. 8.8. This trend corresponds to the general state of the art [27–29]. Furthermore,

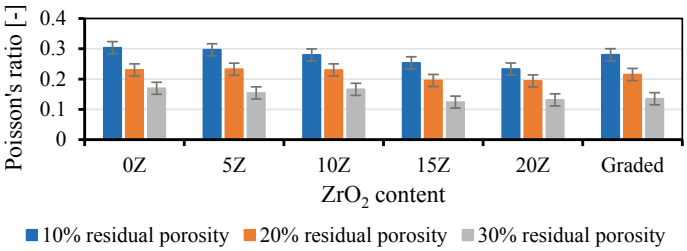

Fig. 8.7 Change in Poisson's ratio under different residual porosities

Fig. 8.8 Dependence of Poisson's ratio on density

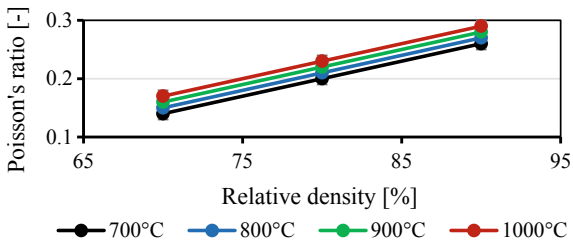

the results show that with increasing density, the Poisson's ratio changes slightly. This trend can be described using the following equation:

$$\vartheta_\rho = (0.6 \cdot \rho_0) + T \cdot 10^{-4} - a \tag{8.2}$$

where ρ_0 is the relative density, T is the working temperature in [°C] and a is a material constant. In this case, a is approximated to a value of 0.35. The equation is an extension equation according to Kuhn and Downey [30]. The equation was extended by the temperature term and a material constant. Nevertheless, the relative density plays a more decisive role in the equation than the temperature. This equation has a determination coefficient of 0.99 with the empirically determined data.

This phenomenon mainly occurs due to the relationship between the elastic modulus, shear modulus and the Poisson's ratio. Due to the heating of the material, the elastic modulus and shear modulus are reduced. As the shear modulus is doubled in the Poisson's ratio formula, the Poisson's ratio increases at higher temperatures.

For upsetting, the ratio of the material flow perpendicular to the pressing direction to that in the pressing direction can be described with a density-dependent Poisson's ratio [8, 30, 31, 32], as shown in Fig. 8.9 for the material here. The figure clearly shows that with increasing ZrO_2 content the density-dependent Poisson's ratio decreases. This phenomenon means that with increasing ZrO_2 content, the ratio of material flow perpendicular to the pressing direction to that in the pressing direction decreases. Moreover, this behavior can be explained by the ZrO_2 particles, which oppose the material flow. For this reason, the ratio of material flow in the pressing direction to that in the pressing direction also decreases.

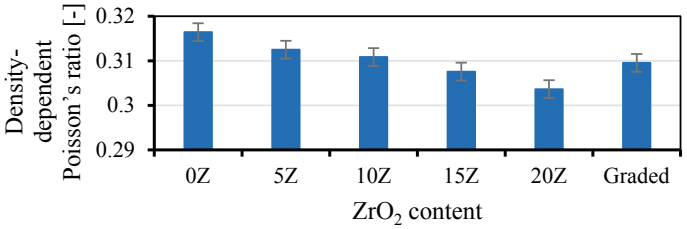

Fig. 8.9 Density-dependent Poisson's ratio with different ZrO_2 contents at a residual porosity of 10%

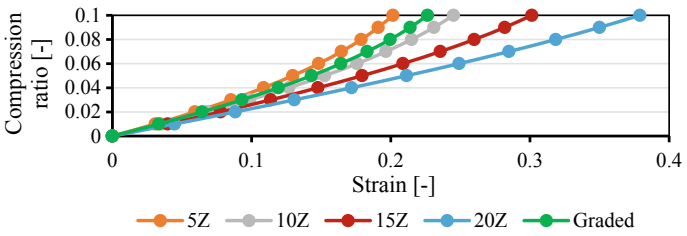

Fig. 8.10 Compression ratio as a function of strain over the Poisson's ratio determined at different ZrO_2 contents

Figure 8.10 shows the dependence of the compression ratio as a function of strain over the Poisson's ratio determined at different ZrO_2 contents, which was previous described for iron powder in the literature [33, 34].

In a composite, this relationship can be described using the following equation:

$$\phi_\rho = \left(25Z^2 - 13.95Z + b\right) \cdot \varphi^2 + 0.2\varphi \tag{8.3}$$

where φ is the strain and b is a material constant of the reinforcement content. In this case, b is approximated to a value of 1.9. This equation was derived from the empirical data to calculate the compression ratio of a composite with a corresponding strain. For this reason, the volume content of the reinforcement phase and the strain are also included in the equation. This equation has a determination coefficient of 0.98 with the empirically determined data.

A comparison of the data with those found in the literature shows that the values for iron powder are slightly higher than those for the TRIP-matrix composite, whereas the values for aluminum MMCs are clearly higher than those for the TRIP-matrix composite. However, note that the reinforcement phase in aluminum MMC is significantly higher at 70% [21]. The same trend (i.e., the values are higher than those for the TRIP-matrix composite) applies to magnesium MMCs that have a reinforcement phase of SiC, wherein the proportion of the reinforcement phase is approximately 30% [35]. Thus, it can be stated that the iron powder comes closest to the values of the TRIP-matrix composite.

8.3.4 Relationship Between Young's Modulus and Density

To determine the axial component of the Young's modulus, the formula of Pavlov et al. [27] was used, which makes it possible to determine the modulus of elasticity through compression tests, which were carried out on a Bähr MDS 830 testing system.

Figure 8.11 clearly shows that the modulus of elasticity increases with increasing ZrO_2 content. Moreover, the modulus of elasticity decreases with increasing residual porosity. This finding is particularly evident at ZrO_2 contents of 15 and 20%. Although the values are almost identical for ZrO_2 contents of 0 and 5%, an increase in the modulus of elasticity can already be seen in the specimen with 10%. The results also clearly show that the specimens with a graded layer structure have a modulus of elasticity between the elastic moduli of the specimens with 10 and 15% ZrO_2. In addition, it can be clearly seen that the measured values of the modulus of elasticity are the same as the values calculated according to the Tsai–Halpin mixing rule [36].

In this composite, the modulus of elasticity can be described using the following equation:

$$E = 90Z + 170\rho_0 \tag{8.4}$$

For simplification, an equation has been derived from the empirical data that agrees with the mixing rule according to Tsai–Halpin. The reinforcing phase and the relative density are included. Here, the relative density plays a larger role than the second phase. This equation has a determination coefficient of 0.95.

Figure 8.12 shows the relationship between the elastic modulus and density. This figure clearly shows that the modulus of elasticity decreases with increasing temperature. Furthermore, the modulus of elasticity increases with increasing density, as described in the literature [37, 38].

The decrease in the modulus of elasticity at elevated temperatures can be described by the temperature dependence of the bonding conditions. Due to the decreasing bonding forces in the matrix, the material flows more quickly. This explains the drop in the modulus of elasticity at elevated temperatures [38]. This change can be described by the following equation:

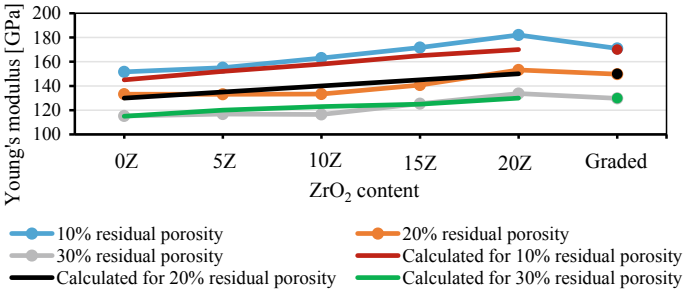

Fig. 8.11 Change in the modulus of elasticity with different residual porosities

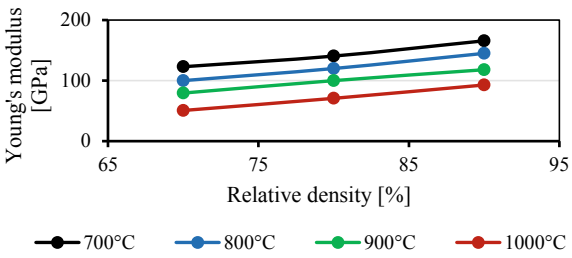

Fig. 8.12 Dependence of the modulus of elasticity on the density of the material with 5Z

$$E = 214\rho_0 - 0.0002T^2 - 0.1T \tag{8.5}$$

This equation was derived from the empirical data for calculating the Young's modulus of a composite at a certain temperature and relative density. For this reason, the density of the specimen and the temperature are also included in the equation. Moreover, the relative density plays a more decisive role in the equation than the temperature. This equation has a determination coefficient of 0.99 with the experimentally determined data.

8.3.5 Oxidation Behavior

For the experimental determination of the scale layer and the associated oxidized specimens were annealed at 1000 °C for 1 h in an inert gas atmosphere and subsequently oxidized in air at intervals of 0, 10, 30 and 60 s. These time periods reflect the transfer times from the furnace to the die in the industry. The oxidation states were then frozen and microsections were made. In addition, calculations of the scale thickness were carried out. This approach was done to simulate the process in industry, where powder forging is usually carried out directly from the sintering furnace. The tests were carried out on compact specimens and porous specimens with a relative density of 80%.

The compact material in Fig. 8.13 shows an average oxide layer of approximately 22 µm. In addition, the scale thickness calculations clearly show that there is a slight difference in the scale thickness of the specimens with 0 and 5% ZrO_2 and that of the specimens with 10 and 20% ZrO_2. In addition, the results show that there is no difference between the sampling times of 0 and 10 s. The first difference observed in the scale thickness of the specimens occurred at a sampling time of 30 s. Here, it can be seen that the specimens with a high ZrO_2 content have a thicker scale than the specimens with a smaller ZrO_2 content. This phenomenon becomes clearer with a sampling time of 60 s.

The porous material in Fig. 8.14 shows an average oxide layer of approximately 66 µm. In addition, the calculations of scale thickness show that there are clear differences between the specimens with 0% ZrO_2, the specimens with ZrO_2 contents of 5, 10, 20% and the graded structure because the latter are already higher than the

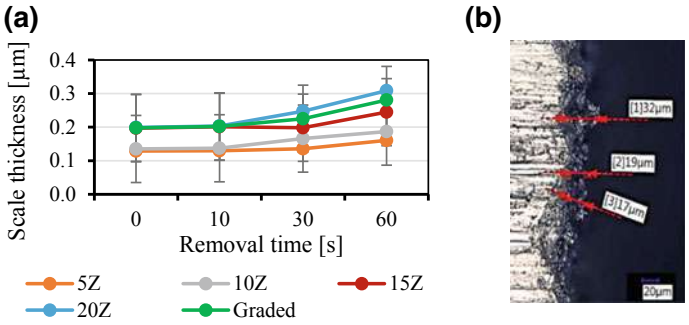

Fig. 8.13 Oxidation behavior of compact material: **a** scale thickness and **b** micrograph

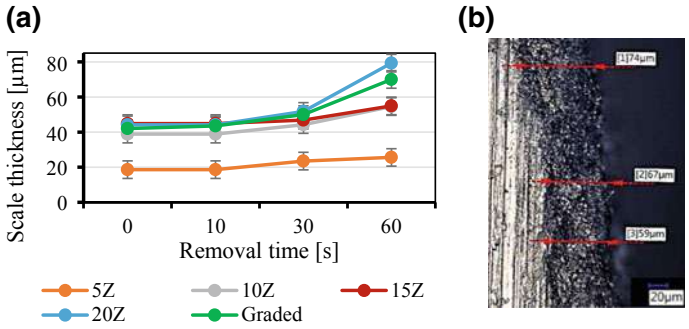

Fig. 8.14 Oxidation behavior of porous material: **a** scale thickness and **b** micrograph

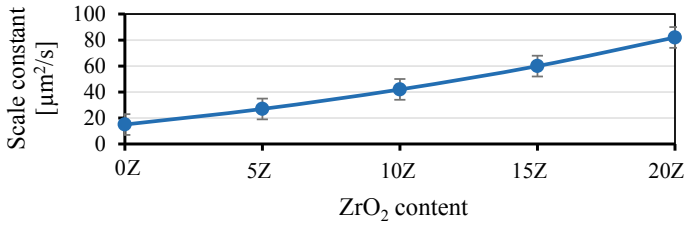

Fig. 8.15 Scale constant as a function of ZrO_2 content at 1000 °C

pure steel at the beginning of oxidation. In addition, there is no difference in specimen oxidation between the removal times of 0 and 10 s; the first notable difference occurred at a sampling time of 30 s. This phenomenon becomes clearer at a sampling time of 60 s. Here, it can be clearly seen that the specimens with ZrO_2 have a larger scale thickness than the specimens without ZrO_2.

This finding means that the different ZrO_2 contents have different scale constants (K_m), as shown in Fig. 8.15; these constants were calculated with the Wagnerian

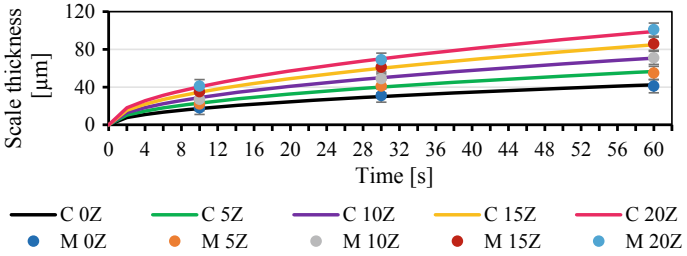

Fig. 8.16 Measured scale thickness at 1000 °C with different ZrO_2 contents (C—calculated and M—measured data)

Fig. 8.17 Temperature dependence of the scale constants

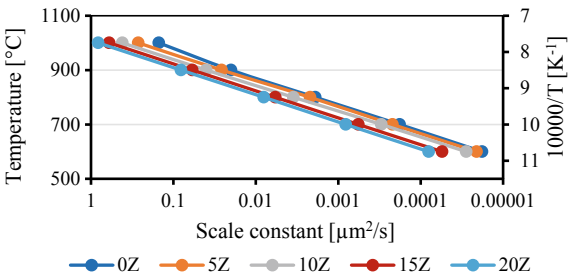

scale theory (parabolic scale growth). The scale constant shown here corresponds to that in the literature [39, 40]. This figure clearly shows that the scale constant increases with increasing ZrO_2 content.

With this scale constant, it is possible to calculate the scale thickness of the individual ZrO_2 contents, as shown in Fig. 8.16. This figure clearly show that with increasing time, the scale layer increases significantly, as reported in the literature [40]. Moreover, with increasing ZrO_2 content, the scale thickness increases. In addition, the simulated values correspond to the measured scale thicknesses.

The results also show that the scale constant is temperature dependent, as previously described in the literature [39, 40]. Figure 8.17 shows that the scale constant behaves linearly at all ZrO_2 contents. In addition, as the ZrO_2 content increases, the curve of the scale constant moves farther away from that of the TRIP steel without ZrO_2.

The oxidation behavior of the specimens generally shows that the scale thickness increases with increasing ZrO_2 content; this phenomenon occurs because the closed surface structure is broken up by the ZrO_2 particles on the surface. This broken structure has more points of attack for oxidation than a closed body. However, note that the porosity of each specimen on the surface is the same as that in the core. The same applies to the values of the porous specimens. Compared to a closed surface, this irregular, porous surface provides a larger area of attack for oxidation. In addition, there is a time factor. Because the porosity increases the area of attack, the more

time there is to oxidize the porous surface, the higher the scale thickness, as shown in Fig. 8.15.

For the same reason, each ZrO_2 content has its own scale constant, which increases with increasing ZrO_2 content in the specimen. The different scale thicknesses can easily be explained by the different scale constants and the different temperature dependencies.

It should therefore be noted that the optimum time for introducing the semifinished products from the sintering furnace into the forging tool is up to 10 s. As previously mentioned, there are no significant deviations in oxidation from a removal time of 0 s in either the nonporous or porous material. Due to the rapid and large formation of oxide layers, it is not advisable to allow for insertion times longer than 10 s.

8.3.6 Process Map Extension for Compressible and Graded Materials

Prasad et al. [41] developed a process map that is helpful in characterizing formability, optimizing the hot forming process and controlling the microstructure of the materials. The only disadvantage is that this process can only be used for incompressible materials. For this reason, this procedure is not applicable to compressible materials such as those used in powder metallurgy. However, in order to create process maps for powder metallurgical production processes that assume a porous initial state, important adjustments must be made. However, powder metallurgical materials can be produced as both homogeneous materials and graded materials. Hence, some adjustments must be made to the compressible material model for the creation of process maps. These modifications include adjustments of the friction due to the different material compositions between the specimen foot and the specimen head and adjustments to the specimen diameter due to the different bulges in the individual layers, which result from differences in composition, stresses, and residual porosity in the individual layers.

Powder forging was simulated on specimens with different ZrO_2 contents and different residual porosities. Therefore, the temperature range 700–1050 °C was investigated. The following conclusions can be drawn from Fig. 8.18.

For TRIP steel, it can be observed that the energy dissipation, starting from a residual porosity of 30% up to a residual porosity of 10%, creates new isolines and strongly shifts the existing isolines. Moreover, the solid material contains considerably fewer isolines than the specimens with residual porosity. In addition, the power dissipation of the compact material is significantly higher (between 15 and 40%) than the power dissipation in the specimens with residual porosity (between 5 and 20%). Furthermore, the only range that does not permit forming is between the forming speeds of 10 and 1 s^{-1} at all temperatures. In addition, component failure occurs at forming speeds of 10^{-1} s^{-1} and 0.1–0.01 s^{-1} in a temperature range of 750–800 and

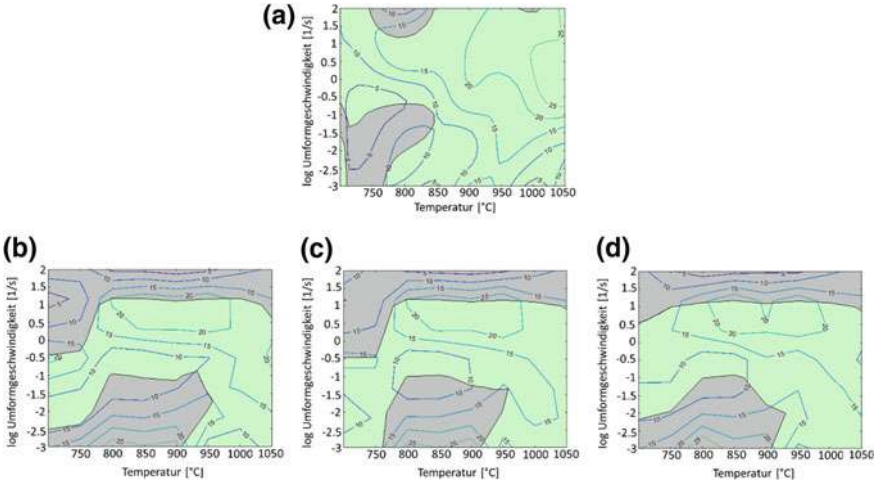

Fig. 8.18 Process maps with 10 vol% ZrO_2: **a** a solid specimen and specimens with residual porosities of **b** 10%, **c** 20% and **d** 30%

900–950 °C. In addition, as the residual porosity increases, the proportion of area where deformation can occur without failure increases.

The unstable area in the upper left corner of all process maps is due to the forming speed. At high forming speeds, the material has no time to absorb the resulting high stresses and subsequently flow. This phenomenon leads to cracking under further external loads. At higher temperatures, the yield strength of the material decreases to such an extent that, despite the rapid deformation, there is greater material flow.

The differences in power dissipation can be explained by the compaction process. Instead of converting energy of the forming process into another form, such as heat, the energy is used to compact the specimen. Therefore, the power dissipation also increases with decreasing residual porosity until reaching a maximum value in the solid material. Detailed and further information can be found in the literature [42].

8.4 Model Experiments on Powder Forging

For the simulation of powder forging and for the verification of the previously obtained data, model experiments of powder forging are presented. Powder forging using the visioplastic method was carried out to investigate the dependence of the shear strain percentage on the compression ratio and the associated mechanical properties. To check the theoretical pore closing behavior during powder forging, metallographic images were examined in various forming stages. In addition, this method was used to investigate the phase angle and boundary between ceramic and steel in order to determine whether the reinforcing particles are firmly embedded

in the matrix and contribute to the mechanical strength. In addition, the relationship between strain and temperature was analyzed to determine the minimum strain required for complete compaction and the temperatures at which optimum and rapid compaction occurs. At the end of powder forging, relative densities of 99.9% were achieved.

8.4.1 Visioplastic Method

The visioplastic method was used to determine the material flow and the associated compaction. For this purpose, cylindrical specimens with a diameter of 10 mm were separated along the sagittal plane and a grid was applied to the inside with a laser (Lasonall XS25, Östling, Solingen, Germany), as shown in Fig. 8.19. The grid mesh was 1 mm, and the depth of the grid was 0.1 mm.

The specimens were recombined. The specimens were compacted in a Gleeble HDS-V40 (Dynamic Systems Inc., Weissenhorn, Germany) (path-controlled) rolling simulator at appropriate temperatures and pressure and in dies 1–3. The temperature was set to 1000 °C, and the strain rate was set to 1 s^{-1}. After forming, the specimen halves were separated from each other again and the grid distortion was measured. Subsequently, with the help of the AutoGrid system (Vialux, Chemnitz, Germany), the major and minor strains were determined.

When considering the residual porosity as a variable parameter, the results show that the strain decreases with increasing residual porosity, as shown in Fig. 8.20. However, the deformed area increases with increasing residual porosity.

This finding can be explained by the increasing compression of the compressible material with increasing residual porosity: with higher residual porosity, there is more volume in the specimen that must first be compacted. This phenomenon leads to very early deformation and to distortion of the applied grid. In contrast, with a low residual porosity (i.e., a small pore volume), the deformation of the component only occurs later because the component exerts a counterforce against the deformation; thus, lower degrees of deformation occur in the samples with low residual porosity. This assertion is confirmed by considering the effective strain. Here, the results show that with increasing residual porosity, the degree of effective strain decreases slightly, whereas the deformed area exhibits a relatively strong increase. This behavior is also

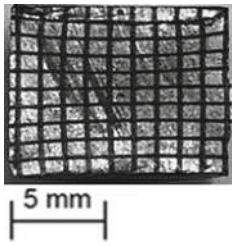

Fig. 8.19 Half of a specimen used for visioplastic analysis after grid preparation

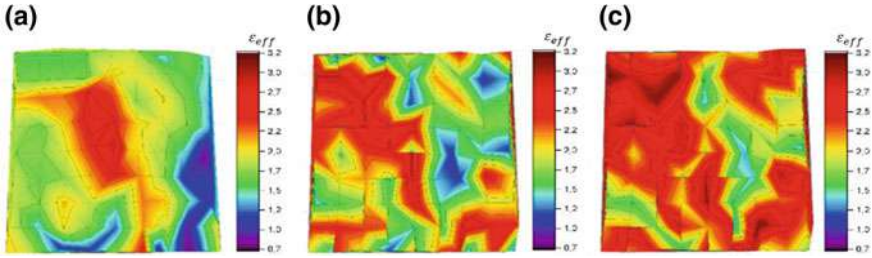

Fig. 8.20 Comparison of effective strain with different residual porosities: **a** 10% residual porosity, **b** 20% residual porosity, and **c** 30% residual porosity

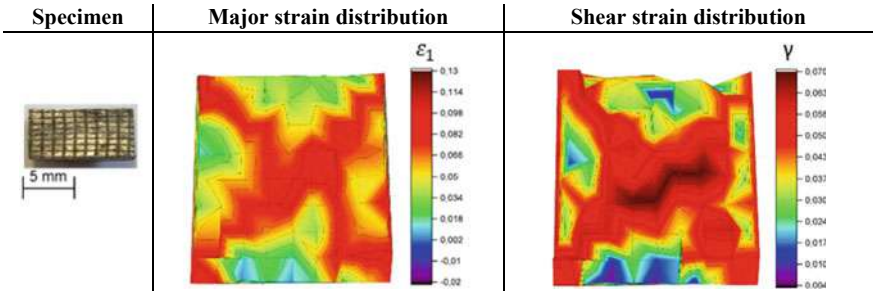

Fig. 8.21 Major strain and shear strain for the specimens in die 1

attributed to the compression of the residual pore volumes in the specimens with increasing residual porosity.

If the different dies (dies 1–3) with their different arrangements of compensating gaps are regarded as variable parameters, then the following information can be determined:

The results show that the major strain is found mainly at the outer corners and in the center of the specimen, as shown in Fig. 8.21. In addition, the specimen shear strain in die 1 is lower than that in the dies, and this shear strain only occurs at the outer corners and in the center of the specimen.

This result reflects the general representation of a forging cross. The creation of the forging cross can be explained simply by Schmid's shear stress law. This phenomenon occurs because the greatest shear stress in a body is at a 45° angle to the main stress axis. For this reason, the largest plastic deformation in the matrix occurs at a 45° angle from the corners of the specimen, which results in a forging cross in a real specimen. Because there are no compensating gaps in die 1 and the material is only compressed and compacted, a significant shearing of the component occurs. The typical bulging of the specimen during the formation of the forging cross is prevented by the die. The very slight shear strain is due to compression and the associated material flow during compression.

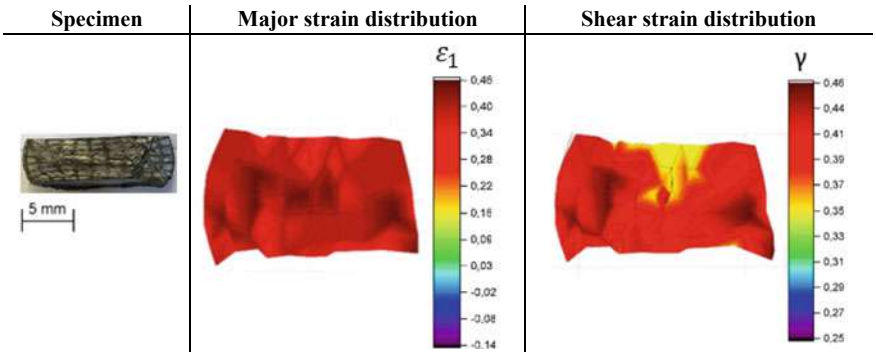

Fig. 8.22 Major strain and shear strain for the specimens in die 2

With die 2, the major strain is highest and can be found nearly exclusively at the level of the compensating gap. The material that has not flowed into the compensating gap shows nearly no deformation compared to the rest of the specimen, as shown in Fig. 8.22. A shear strain analysis shows that the specimen shear strain in die 2 is higher than that in the other two dies. Moreover, the highest shear strain is found in the area of a compensating gap, whereas there is approximately no shear strain in the area without a compensating gap.

This finding must be explained in terms of the material flow into the compensating gap during forming. When the material flows into the compensating gap, the specimen is subjected to a large shear, which results in a large deformation of the specimen and a very high major strain distribution. This phenomenon is verified by the proportion of shear strain in the specimen, which can also only be found in the area of the compensating gap. Due to this shear and the material flow, a forging cross is not formed. However, a high shear strain rate results in a strong compression of the specimen, as is the case in theory.

The specimen strain in die 3 is between that in dies 1 and 2. In addition, the largest major strain can also be seen at the outer edges and in the center of the specimen. With this die, the proportion of shear strain is concentrated primarily on the center and on the tips of the outer edges, whereas in other areas, there is approximately no shear strain, as shown in Fig. 8.23. Detailed and further information can be found in the literature [43].

On the one hand, this behavior can be traced back to the forging cross, which forms in the center of a body during compression. The high shear rates at the outer corners of the specimens are due to the shear of the specimen material with the punch, as the material flowed into the compensating gap at the desired points. However, note that the shear strain experienced by the material in this way is substantially lower than the shear strain produced by the structure of die 2. Thus, the density of the test specimens from die 3 is also lower than that of the test specimens from die 2.

If the relative density is now compared with respect to the selected die and the ZrO_2 content, it can be seen that the highest relative density was achieved with the dies

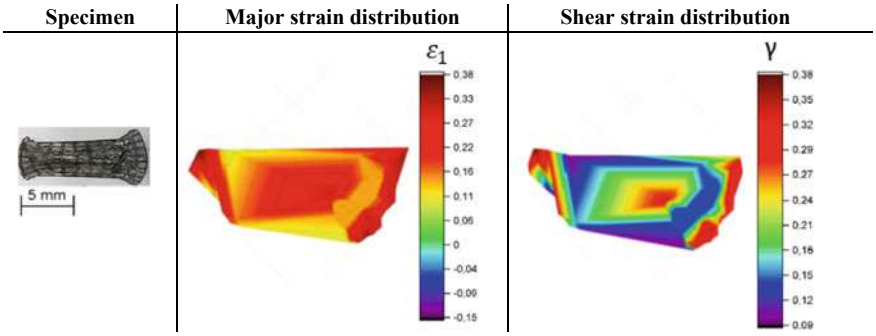

Fig. 8.23 Major strain and shear strain for the specimens in die 3

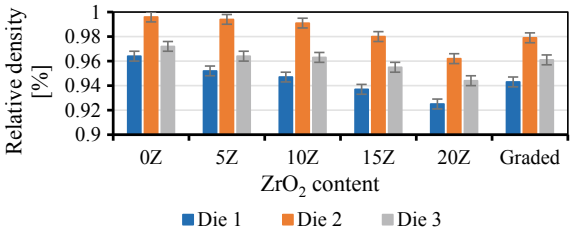

Fig. 8.24 Comparison of relative densities with different dies and ZrO_2 contents

with compensating gaps. In addition, as the ZrO_2 content increases in the specimens, the relative density of the final components decreases, as shown in Fig. 8.24. The change in theoretical density with increased ZrO_2 content was taken into account.

The large difference in the maximum relative densities achieved can be explained by the dies and the associated forming conditions. With pure compression without transverse flow, die 1 represents pure repressing. The state of the art is in agreement that with pure repressing only, relative densities up to a maximum of 95–96% are possible [1, 12, 44, 45, 46, 47, 48]. Therefore, the values measured here are in a very high range with respect to the achieved densities. Dies 2 and 3 have compensating gaps and should achieve a relative density of 100% due to the transverse flow of the material. This relative density was nearly achieved in some of the specimens in die 2. However, for die 3, the relative density of 100% was not reached due to the high stress on the matrix in the shear zone. Due to this stress, new pores and cracks occur within the specimen, as shown in Fig. 8.25. For this reason, complete compaction of the material is not possible in die 3.

The decreasing final density of the specimens with increasing ZrO_2 content is due to the increasing hydrostatic stresses in the matrix of the material, which increase due to the increasing number of reinforcing particles. These hydrostatic stresses oppose the yield stress, thereby inhibiting the material flow. However, shear strain and the associated material flow are the main mechanisms for the compression of compressible bodies. Thus, a compression of the specimens with a high ZrO_2 content is not exactly given, as with specimens with a low ZrO_2 content.

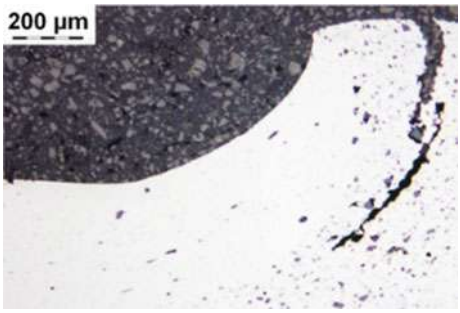

Fig. 8.25 New pores and cracks that appear during forming in die 3

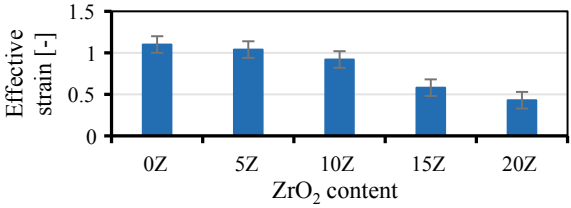

Fig. 8.26 Effective strain at different ZrO_2 contents in die 2

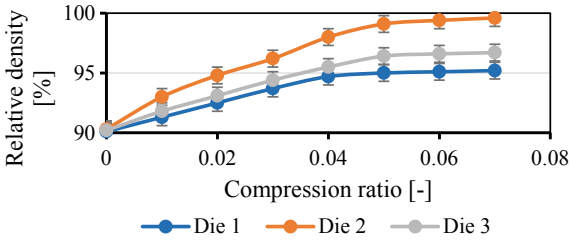

Fig. 8.27 Relationship between compression ratio and relative density for a specimen with a residual porosity of 10% and 5Z

An examination of the effective strain with variable ZrO_2 contents from die 2 shows that with increasing ZrO_2 content, the effective strain decreases strongly, as shown in Fig. 8.26. In addition, the deformed surface remains nearly constant.

These findings lead to the conclusion that as the ZrO_2 content increases in the samples, the hydrostatic stresses in the sample volumes increase due to the particle reinforcement and thus a material flow is inhibited. Thus, the force required for the same degree of deformation is increased accordingly. Hence, the particle amplification represents an obstacle for the material flow and generates a hydrostatic stress field that counteracts the stress field of the flowing material and brings a portion of the material to a standstill, which makes a postcompaction of the compressible material into the compact state more difficult or impossible.

Note that the presence of compensating gaps and a high effective strain lead to a high relative density and that the arrangement of the compensating gaps plays an essential role in the compaction, as shown in Fig. 8.27. The results clearly show

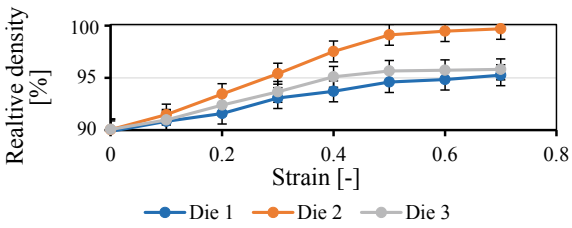

Fig. 8.28 Influence of the strain on the density during powder forging with the different dies at a working temperature of 1000 °C and 5Z

that dies 2 and 3 achieve a higher relative density than die 1 at the same degree of compression.

Thus, the arrangement of the compensating gaps plays a decisive role. The arrangement of the compensating gap must ensure that the greatest possible shear strain is generated in the component and that the greatest possible material flow is achieved. This influence of the compensating gap arrangement is demonstrated by the fact that the compaction in die 2 is greater than that in die 3, although both have compensating gaps.

The relationship between strain and temperature is investigated to find the minimum strain required for complete compaction and at which temperatures optimum and rapid compaction occurs.

To find the die with the best compression properties, the individual relative densities of the specimens were compared with the matrices depending on the strain. Figure 8.28 shows the influence of the strain on the relative density in labor tests with the different dies.

In addition, the results show that from a strain of 0.5, no significant compaction of the specimen occurs. Overall, the maximum achievable density is highest for die 2 at 99.8%, followed by die 3 at 96.3%, and finally by die 1 at 94.6%; note that die 1 was designed without a compensating gap and represents a pure postcompaction. The case of die 1 represents the worst compaction to solid material. From this finding, it can be deduced that the matrices with compensating gaps have a higher density than the matrices without compensating gaps. Thus, a higher density is achieved if transverse flow or shear strain occurs in the material.

The increase in density in die 3 is weaker than that in die 2, which is due to the arrangement of the compensating gap and the associated different shear deformation. In die 2, the material shears the specimen by a transverse extrusion process, whereas in die 3, there is a pure upsetting first and then shearing at the punch edges. According to the state of the art, the decisive factor for compaction is the hydrostatic stress component; however, for optimum full compaction, a certain mixture of hydrostatic stress component and shear strain is more suitable. Based on the available data, it can be assumed that the shear strain must correspond to the hydrostatic stress to achieve full compaction and that the shear strain should not begin subsequently as with die 2. Therefore, the arrangement of the compensating gaps in the die plays a decisive role in compaction.

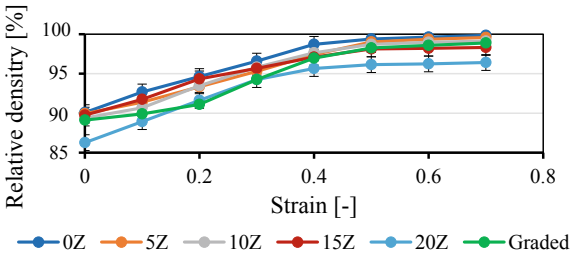

Fig. 8.29 Influence of the strain on the density in die 2

Figure 8.29 shows the influence of the different ZrO_2 contents and the strain on the density during powder forging with die 2. Note that the possible compaction decreases with increasing ZrO_2 contents. However, a higher density can be achieved overall with die 2 (i.e., with compensating gaps) than with die 1. In addition, from a strain of 0.5, no significant compaction of the specimen takes place. The increase in density from a strain of 0.5 is greater in die 2 than in die 1. In the case of specimens with a ZrO_2 content of 15 and 20%, the compaction is even less. Additionally, this phenomenon can be traced back to some measuring tolerances in the determination of the density. A maximum density of 99.8% can be achieved with a ZrO_2 content of 5%.

The differences in compaction between the individual ZrO_2 contents are due to particle reinforcement. With increasing ZrO_2 content in the specimens, the initial density of the specimens decreases. As previously stated, the stress field emanating from the reinforcing particles works against the hydrostatic stress component required for compaction. Since the ZrO_2 cluster formation additionally reinforces the stress fields, the material flow and the subsequent compaction nearly comes to a standstill. The reason that a higher compaction is still possible with these high ZrO_2 contents in die 2 lies in the previously described compensating gaps and the breakage of particle clusters due to shear strain. These phenomena allow material flow and compaction. However, from a ZrO_2 content of 20%, the stress field of the particles seems to be so large that even the shear strain is not sufficient to overcome it.

Furthermore, the specimens do not undergo significant compaction after a strain of 0.5. This finding could be explained by the fact that the material has already undergone full shear deformation in the compensating gaps; thus, a sharp increase in density has already occurred. Therefore, the specimen is now compressed and compacted only by postcompaction and no longer by shear strain. This compression only has a slow increase in relative density, which explains the slow increase in density from a strain of 0.5. Detailed an further information can be found in the literature [49].

8.4.2 Metallographic Examination

To examine the microstructure, metallographic microsections were carried out at each strain and the microstructure was analyzed. The images were taken at the forging cross of the specimens from die 2, as shown in Fig. 8.30. In this case, the specimen contains only 5Z. The residues on the specimens originate from V2A etching.

The metallographic examination (Fig. 8.31) shows the microstructure and some artifacts of the V2A etching, which are marked here as gray areas. Moreover, it is clearly visible that at a strain of 0, the individual grains of the TRIP matrix and the reinforcing particles are still visible. With increasing strain, the holes are compressed and stretched, as described in the literature [27, 50], until a large pore becomes many finely distributed pores. These pores are compressed and distributed by the beginning material flow, as observed in the microstructure of the specimen with a strain of 0.3. Moreover, the microstructure of the specimen with a strain of 0.3 is finer than the individual powder particles in the microstructure with a strain of 0. This phenomenon becomes very clear at a strain of 0.5. The results show that the material recrystallizes during powder forging. However, this recrystallization process is not accelerated or excited by the reinforcing particles since these particles are above a particle volume fraction-to-particle size ratio of 0.2 μm^{-1}; therefore, according to some authors, the particles do not support recrystallization [35, 51]. The grain size at the beginning of powder forging, measured via laser granulometry, was 37 μm, whereas the grain size after powder forging was only 19 μm, which confirms recrystallization.

For the analysis of the surfaces of the individual layers of the graded layer structure after forming, metallographic images of the surfaces of the individual phases were made according to different strains. These images were taken because these areas

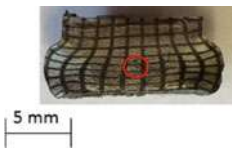

Fig. 8.30 Illustration where the microstructure of the specimens from die 2 were recorded

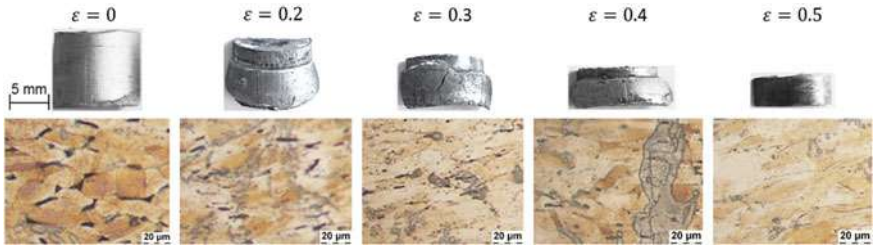

Fig. 8.31 Microstructure at the corresponding strain at the center of the specimen

that are most susceptible to interference (i.e., weak spots) in graded layer structures. These locations are particularly susceptible to interference due to the different stress fields in the individual layers. To fully utilize the mechanical properties of these components, a good connection of the individual phases is very important.

At the interface of the individual layers of the graded layer structure, no special features in the sense of defects can be recognized; however, the different ZrO_2 content is clearly recognizable, which distinguishes the layers from each other. Figure 8.32 also shows the bulging structure in the graded specimen at a strain of 0.4. This bulging structure deviates from the symmetric barrel-shaped bulge of homogeneous specimens. This deviation was taken into account when calculating the process maps of compressible graded materials; this phenomenon was mathematically described in that section.

8.4.3 Formation of the Interfaces of Phases

For the analysis of the ceramic/steel interfaces, metallographic images were taken both in the shear zone (Fig. 8.33) and in the forging cross (Fig. 8.34) of a specimen from die 2 after powder forging at 1000 °C.

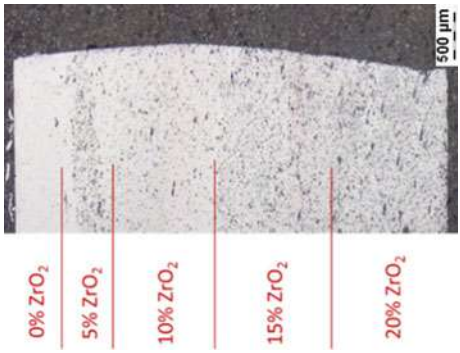

Fig. 8.32 Micrograph through the different layers of a graded specimen

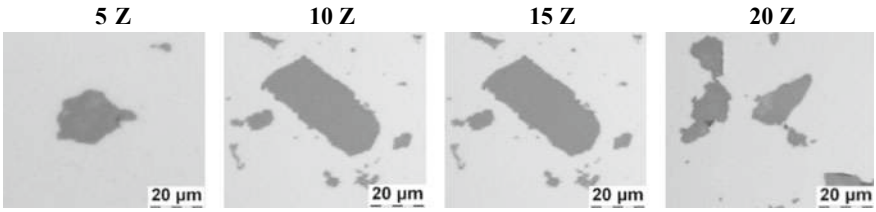

Fig. 8.33 Ceramic/steel interface in the shear zone with corresponding ZrO_2 contents

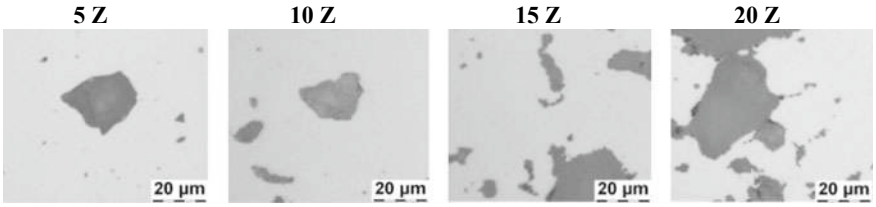

Fig. 8.34 Ceramic/steel interface in the forging cross with corresponding ZrO_2 contents

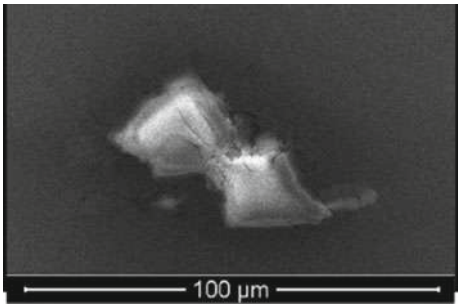

Fig. 8.35 SEM image of the interphase ceramic/steel at a ZrO_2 content of 10% (HV: 20 kV; WD: 10; and Mag.: 2000)

The microstructures in the shear zone of the specimens show a fixed bond between the reinforcing particle and the matrix for the specimens with 5, 10 and 15% ZrO_2. In addition, no pores or cracks are visible. In the specimen with 20% ZrO_2, pores or holes in the steel matrix are visible at the poles of the particles. Thus, there is no 100% binding of the reinforcing particles to the matrix. Smaller and isolated particles are fully bound to the matrix, whereas large particles or whole particle clusters show corresponding pores in the matrix.

The images in the forging cross of the specimens show that the specimens with ZrO_2 contents of 5, 10 and 15% also exhibit a firm bond between the reinforcing particle and the matrix. The specimen with 20% ZrO_2 also shows pores in the matrix and in the shear zone. However, the pores are more frequently found in the matrix than in the shear zone.

Images from a light microscope indicate that the specimens with a low particle content show a good phase bonding between matrix and reinforcing particles. This good phase bond is also visible during scanning electron microscopy (SEM) observations, as shown in Fig. 8.35. This finding confirms the assumptions from the light microscope images.

However, fewer pores are present in the specimens in the shear zone than in the specimens in the forging cross. This discrepancy can be explained by the hydrostatic stress field and the yield stress. As the ZrO_2 content increases, stresses form in the matrix that counteract the hydrostatic stress, thereby preventing the specimen from compacting. These yield stresses become particularly large in clusters of reinforcing particles. These stresses can become so great that they completely stop the flow of material. The difference in the residual porosity between the shear zone and

the forging cross is mainly to be found in the forming or the material flow. Since the specimens in the shear zone undergo a large deformation due to the shear and the associated shear strain, there is a greater yield stress in this section, as shown in Sect. 8.4.1; thus, a greater material flow occurs due to the compression of the specimen. In the case of the specimens in the forging cross, no correspondingly high shear strain occurs due to the lack of a strong material flow, which can also be seen from the only slightly distorted grid on the specimen in Fig. 8.21. As a result, the yield stress is sufficiently large to counteract the hydrostatic stress field and to subsequently counteract full compaction. This assertion is supported by the increased occurrence of pores in places where many particles meet. Detailed and further information can be found in the literature [52].

8.4.4 Mechanical Properties

When considering the hardness distribution within the different dies, as shown in Fig. 8.36, the highest density is achieved in die 2, whereas die 1 produces the lowest hardness.

These results can be explained by the density of the specimens. The higher the density of the specimen is, the better the mechanical properties and the higher the hardness of a powder-forged specimen. The highest compaction was achieved in die 2. The hardness measurements showed that the hardness of the specimens increased with increasing ZrO_2 content. This increase in hardness can be explained by the fact that the reinforcing particles counteract the deformation caused by the hardness tester.

It is possible to calculate the tensile strength of a material from the hardness of the material [53]. According to this model, the data from Fig. 8.37 were collected.

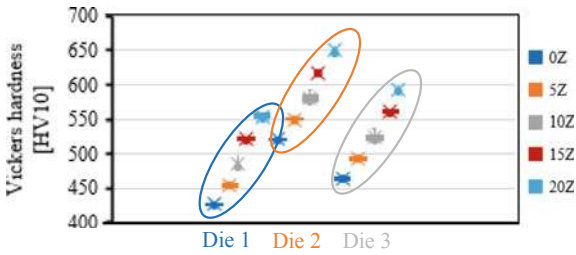

Fig. 8.36 Hardness distribution at different ZrO_2 contents in the different dies

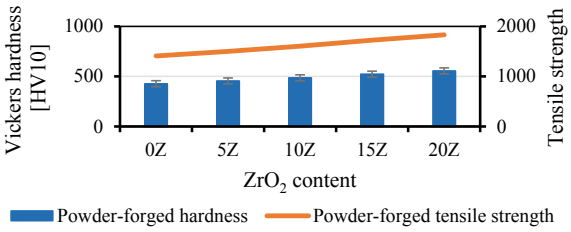

Fig. 8.37 Hardness and tensile strength after powder forging in die 2

8.4.5 *Shear Strength of the Layers with a Graded Layer Structure*

The adhesion of the layers of the graded layer structure was measured in the graded material systems to determine the shear strength of the individual layers and to be able to make possible predictions for the failure location. When measuring the shear strength of the individual layers, it was found that with increasing ZrO_2 content in the individual layers, the shear strength generally decreases, as shown in Fig. 8.38.

With increasing ZrO_2 content, the shear strength decreases on average by 17% with increasing ZrO_2 content, both in forged and sintered specimens. In addition, the shear strength of forged specimens is significantly higher than that of sintered specimens. On average, the shear strength of forged specimens is 72% higher than that of sintered specimens.

This phenomenon can be explained by the increase in reinforcing particle fractions and the fact that as the number of particles contained in the matrix increases, the amount of matrix present at the interface of two layers decreases. Similarly, the poles represent flaws where crack initiation begins. These flaws also increased with increasing ZrO_2 content.

When comparing the shear strength of the individual layers with data from similar cladding processes used to coat materials onto a steel sheet, the values of the layers of the graded layer structure appear to be on the same level or higher than the values in the literature, as shown in Fig. 8.39. Only the stainless steel cladded on a steel sheet achieved an adhesive strength of 200 MPa [54–56].

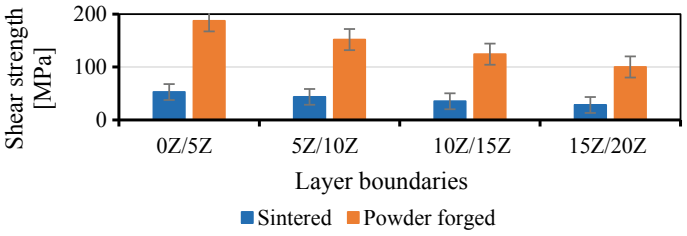

Fig. 8.38 Adhesion of individual layers before and after powder forging

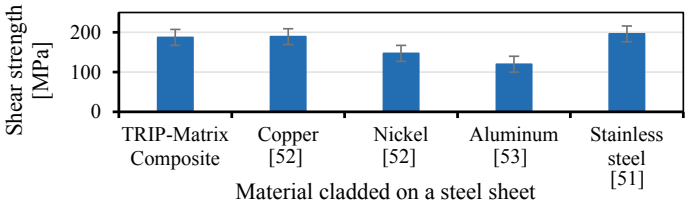

Fig. 8.39 Shear strength of materials cladded on a steel sheet

The shear strength in relation to the compaction ratio, as shown in Fig. 8.40, indicates that the shear strength of the layers increases with increasing compaction ratio. In addition, increasing the compaction ratio increases the shear strength of the forged specimens more than that of the sintered specimens. This phenomenon can be described by the following equation:

$$S = \Phi_{\rho}(c \cdot \rho_0) \tag{8.6}$$

where c is a material constant with a value of 2013 and ρ_0 is the relative density. Due to the differences in density between powder-forged and sintered specimens, the relative density of the specimen plays a decisive role in the equation, as does the compression ratio. This equation has a determination coefficient of 0.98 with the experimentally determined data.

These results can be explained by the compression itself. In the case of the specimens prior to powder forging, only sintered necks hold the specimen together, whereas the powder-forged specimens have a microstructure. The force required to break a sintered neck is much less than the force required to introduce sufficient energy into the matrix to maintain crack initiation and propagation.

Fig. 8.40 Comparison of adhesive strength and compaction degree

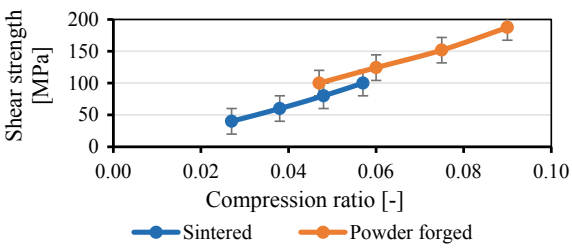

8.5 Conclusions

In general, this study showed that ZrO_2 particle-reinforced TRIP steels can be produced via the powder metallurgical route and that the produced samples achieved solid material densities and exhibited enhanced mechanical properties.

In addition, this same production approach can produce components with graded particle reinforcements and compact the components to a density of solid material without losing the graded structure. The following process parameters were the most successful for the process route. The highest obtained density was achieved in dies with compensating gaps, in which shearg occurred immediately during forming. If the compensating gaps are arranged in such a way that only a pure compression followed by shear occurred, a compact material was not produced; the same phenomenon occurred when no compensating gaps were used. In addition, the highest densities were achieved at a temperature of 1000 °C and a strain of 0.5 in the same die. In addition, up to a reinforcement particle content of 10%, excellent bonding was observed between the reinforcement particles and the matrix.

Acknowledgements This work was funded by the Deutsche Forschungsgemeinschaft (DFG, German Research Foundation), project number 54473466—SFB 799, subproject A6.

References

1. W. König, R.S.G. Röber, Umformtechnikmagazin **426** (1992)
2. G. Röber, Powder forging of gearwheels in layered composite technology—stress-compliant production and component behaviour, Doctorate thesis, RWTH Aachen, 1991
3. K. Vossen, Powder forging of spur and helical cylindrical gears, Doctorate thesis, RWTH Aachen, 1987
4. M. Abdel-Rahman, M.N. El-Sheikh, J. Mater. Process. Technol. **97** (1995)
5. T. Nakagawa, T. Amano, K. Obara, Y. Nishino, Y. Maeda, in *13th International Machine Tool Design and Research Conference* (1972), p. 455
6. A. Salak, Hutnicke Listy 418 (1990)
7. G. Zapf, *Engineering Handbook. Primeval Forming* (Carl Hanser Verlag, München, 1981)
8. H.A. Kuhn, B. Lynn, Metal Powder Industries (1990)
9. H.E. Exner, H. Danninger, *Gmelin Handbook of Inorganic Chemistry, Metallurgy of Iron. Powder Metallurgy of Steel*, 10th edn. (Springer, Berlin, Heidelberg, 1992)
10. F.J. Esper, *Powder Metallurgy. The Flexible and Advanced Method for Economical and Reliable Components; with 15 Tables* (Expert-Verlag, 1996)
11. G. Durrant, V.D. Scott, Compos. Sci. Technol. **49**, 153 (1993)
12. G. Eberhardt, *Powder Forging. Manufacturing Technology* (Hochschule, Pforzheim, 2013)
13. W. Schaub, M. Stilz, R. Geiger, *Forming technology—Handbook for Industry and Science. Volume 4: Special Processes, Process Simulation, Tool Technology, Production*, 2nd edn. (Springer, Berlin, 1993)
14. P.B. Prangnell, S.J. Barnes, S.M. Roberts, P.J. Withers, Mater. Sci. Eng., A **220**, 41 (1996)
15. B.-A. Behrens, N. Vahed, H. Brand (eds.), *Powder Metallurgical Production of Graded Tool Materials* (Verlag Meisenbach, Bamberg, 2013)
16. F. Klocke, W. König (eds.), *Fertigungsverfahren 5, Gießen, Pulvermetallurgie, Additive Manufacturing*, 4. Auflage (Springer Vieweg, Berlin, Heidelberg, 2015)

17. F. Klocke in *Fertigungsverfahren 5. Gießen, Pulvermetallurgie, Additive Manufacturing*, ed. by F. Klocke, W. König (Springer Vieweg, Berlin, Heidelberg, 2015), p. 39
18. M. Krehl, *Einführung in die Pulvermetallurgie* (FPM, 2019)
19. G. Arth, A. Samoilov, Berg Huettenmaenn Monatsh **157**, 306 (2012)
20. D. Rogowski, Process for the preparation of preforms for metal matrix composites, Patentschrift: DE 10 2008 054 561 A1 (2009)
21. H. Engel, *Sintered Materials from Non-ferrous Metals* (Springer, Berlin, Heidelberg, 1993)
22. I. Lenke, *Metall Matrix Composits* (Thinking Ceramics, CeramTec, Plochingen, 2002)
23. G. Zapf, Mater. Sci. Technol. **171** (1979)
24. R.L. Coble, *Reactive Sintering* (MIT, Cambridge, MA, 1984)
25. V.V. Skorokhod, *Mechanism for Improving the Mechanical Properties of Sintered Iron–Copper Composites Alloyed with Molybdenum*
26. S. Mäkipirtti, On the sintering of W-Ni-Cu heavy metal. Zugl.: Helsinki, Inst. of Technology, Diss., 1959 (The Finnish Acad. of Technical Sciences, Helsinki, 1959)
27. V. Pavlov, M. Nosenko, B. Popov, S. Jakunin, Poroshkovaja metallurgija **20** (1987)
28. TU Graz (ed.), *The Physical Properties of Steels „The 100 Steels Programme"*, Part I: Tables and Figures (Graz) (1994)
29. U. Frank, The Piosson's ratio of plastics, illustrated by the example of amorphous thermoplastics, Dissertation, Universität Stuttgart, 1984
30. H.A. Kuhn, C.L. Downey, Int. J. Powder Metall., **15** (1971)
31. W. Schatt, K.-P. Wieters, B. Kieback, *Powder Metallurgy. Technologies and materials*, 2., bearbeitete und erweiterte Auflage (Springer, Berlin, Heidelberg, 2007)
32. H.A. Kuhn, M.M. Hagerty, H.L. Gaigher, A. Lawley, (New York, Plenum Press, 1971), p. 463
33. N. Nguyen, Influence of process parameters in powder forging on the properties of the finished workpieces, Doctorate thesis, TU Bergakademie, Freiberg, 1995
34. B. Lorenz, A contribution to the theory of forming powder metallurgical initial forms, Habilitation thesis, TU Freiberg, 1995
35. L. Ceschini, G. Minak, A. Morri, F. Tarterini, Mater. Sci. Eng., A **513–514**, 176 (2009)
36. J.C. Halpin, S.W. Tsai, Air Force Materials Laboratory (1967)
37. W. Bleck, S. Münstermann, *Einflußgrößen auf den Elastizitätsmodul von Stählen für den Fahrzeugbau,* Forschungsvereinigung Automobiltechnik, 182 (2004)
38. H. Foell, *Elastische Module*, Material Science 1, Universität Kiel, (2015)
39. D. Hünert, *Corrosion processes and carburization of ferritic-martensitic steels in H2O-CO2 atmospheres*. Doctorate thesis TU Bergakademie Freiberg, 2010 (Bundesanstalt für Materialforschung und -prüfung (BAM), Berlin, 2010)
40. R. Viscorová, Investigation of the heat transfer during splash water cooling under consideration of the influence of scaling, Doctoral thesis, TU Clausthal (2007)
41. Y.V.R.K. Prasad, K.P. Rao, S. Sasidhara, *Hot Working Guide. A Compendium of Processing Maps*, 2nd edn. (ASM International, Materials Park, OH, 2015)
42. M. Kirschner, Mater. Sci. Forum **2019**, 15 (2019)
43. M. Kirschner, R. Eckner, S. Guk, L. Krüger, R. Kawalla, U. Prahl, Deformation behavior of particle reinforced TRIP steel / Mg PSZ composite at hot working temperatures. Steel Res. Int. (2018). https://www.doi.org/10.1002/srin.201800334
44. B.-A. Behrens, T. Yilkiran, N. Vahed, C. Frischkorn (eds.), *Influence of Material Flow on Compaction During Sinter Forging* (2014)
45. F. Li, J. Yi, J. Eckert, Metall. Mat. Trans. A **48**, 6027 (2017)
46. H. ElRakayby, H. Kim, S. Hong, K. Kim, Adv. Powder Technol. **26**, 1314 (2015)
47. G.-S. Shim, M.S. Kim, W.Y. Kim, H. Yamagata, MSF **439**, 40 (2003)
48. A. Salak, M. Selecká, Powder Metall. Prog. **3** (2005)
49. M. Kirschner, S. Guk, Beitrag zur Bewertung des Verdichtungsgrades mittels Visioplatsizität. Kongress & Fachmesse Werkstoffwoche 2019, Dresden, den 18–20.09.2019, Dokumenten-Bibliothek der Deutsche Gesellschaft für Materialkunde e.V. (2019)
50. A. Flodin, M. Andersson, A. Miedzinski, Met. Powder Rep. **72**, 107 (2017)

51. K.K. Deng, X.J. Wang, W.M. Gan, Y.W. Wu, K.B. Nie, K. Wu, M.Y. Zheng, H.G. Brokmeier, Mater. Sci. Eng., A **528**, 1707 (2011)
52. M. Kirschner, S. Guk, R. Kawalla, U. Prahl, Forming complex graded and homogeneous components by joining simple presintered parts of TRIP-matrix composite through powder forging. Metals (2020)
53. R.J. Meyer, E. Pietsch (eds.), *Eisen - Härteprüfverfahren*, Beziehung zwischen Härte und Zugfestigkeit, Achte Völlig neu Bearbeitete Auflage (Springer, Berlin, Heidelberg, s.l., 1974)
54. W. Rädeker, Steel and Iron (1938)
55. H. Schaumburg, *Materials* (Vieweg + Teubner Verlag, Wiesbaden, 1990)
56. M. Schmidtchen, R. Kawalla, in *Rolling of Flat Products*, ed. by H.G. Bauer, W. Schadt (Springer, Berlin, 2017), p. 87